Sonar Systems for Object Recognition

Yan Pailhas

Ocean Systems Laboratory, School of EPS
Heriot-Watt University

A thesis submitted for the degree of

Doctor of Philosophy

August 2012

Abstract

The deep sea exploration and exploitation is one of the biggest challenges of the next century. Military, oil & gas, offshore wind farming, underwater mining, oceanography are some of the actors interested in this field. The engineering and technical challenges to perform any tasks underwater are great but the most crucial element in any underwater systems has to be the sensors. In air numerous sensor systems have been developed: optic cameras, laser scanner or radar systems. Unfortunately electro magnetic waves propagate poorly in water, therefore acoustic sensors are a much preferred tool then optical ones. This thesis is dedicated to the study of the present and the future of acoustic sensors for detection, identification or survey. We will explore several sonar configurations and designs and their corresponding models for target scattering. We will show that object echoes can contain essential information concerning its structure and/or composition.

I would like to dedicate this thesis to Simona, *la mia bella*...

Acknowledgements

And I would like to acknowledge Prof. Yvan Petillot, Dr. Chris Capus, Dr. Keith Brown, Prof. Dave Lane, Prof. Bernie Mulgrew, Len MacLean, Dr. Clement Petres, Dr. Bertrand Lucotte, Dr. P.Y. Mignotte, Dr. Pedro Patron, Dr. Maiwenn Kersaudy Kerhoas, Istvan Csajaghy, Jamil Sawas, Nicolas Valeyrie, Reg Hollett, Gaetano Canepa, Dr. DJ. Tang, Dr. Ryan Goldhahn, Dr. Hans Groen, Dr. Violetta Sanjuan, Dr. Samantha Dugelay, Dr Duncan Williams and so many others...

ACADEMIC REGISTRY
Research Thesis Submission

Name*:*	Yan Pailhas		
School/PGI:	OSL, School of EPS		
Version: *(i.e. First, Resubmission, Final)*	Final	Degree Sought (Award **and** Subject area)	PhD

Declaration

In accordance with the appropriate regulations I hereby submit my thesis and I declare that:

1) the thesis embodies the results of my own work and has been composed by myself
2) where appropriate, I have made acknowledgement of the work of others and have made reference to work carried out in collaboration with other persons
3) the thesis is the correct version of the thesis for submission and is the same version as any electronic versions submitted*.
4) my thesis for the award referred to, deposited in the Heriot-Watt University Library, should be made available for loan or photocopying and be available via the Institutional Repository, subject to such conditions as the Librarian may require
5) I understand that as a student of the University I am required to abide by the Regulations of the University and to conform to its discipline.

* *Please note that it is the responsibility of the candidate to ensure that the correct version of the thesis is submitted.*

Signature of Candidate*:*		Date:	

Submission

Submitted By *(name in capitals):*	
Signature of Individual Submitting:	
Date Submitted:	

For Completion in the Student Service Centre (SSC)

Received in the SSC by *(name in capitals):*			
Method of Submission *(Handed in to SSC; posted through internal/ external mail):*			
*E-thesis Submitted (**mandatory for final theses)***			
Signature:		Date:	

Contents

List of Figures

List of Tables

Nomenclature

Roman Symbols

α	Sound attenuation coefficient in water
ΔF	Notches feature space projection
$\hat{T}_n$	Estimated target
λ	Acoustic wave wavelength
λ_n	Lamé first parameter
μ_n	Lamé second parameter
ρ	Density material
ρ_n	Material density
τ	Pulse duration
$\tau_{rl}(X_q)$	Propagation time delay between scattering point X_q and receiver l
$\tau_{tk}(X_q)$	Propagation time delay between transmitter k and scattering point X_q
Θ_{target}	Target subspace
$\vec{u^n}$	Displacement
ζ_q	Reflectivity coefficient of the scattering point q
a	Typical object dimension (Ex. radius for sphere)

c	Sound speed in water
c_l	Longitudinal sound speed
c_L^n	Longitudinal sound speed
c_t^n	Transversal sound speed
D	Depth
DI	Directivity Index
DT	Detection Threshold
EL	Echo Level
f	Acoustic wave frequency
F^α	Fractional Fourier transform
f_∞	Form function
G_{ij}	Green function
h_l	Spherical Hankel function
J_1	Bessel function of the first kind
j_l	Spherical Bessel function of the first kind
k	Acoustic wave wavenumber
M_i	Target image
n_l	Spherical Bessel function of the second kind
NL	ambient Noise Level
p	Total pressure
p_i	Pressure of the incoming wave
P_n	Legendre polynomial

p_s	Pressure of the scattering echo
r	Range
RL	Reverberation Level
S	Salinity
$s_k(t)$	Pulse sent by the transmitter k
S_s	Bottom scattering strength
SL	Source Level for the projector
T	Temperature
TL	Transmission Loss
TRN	Target Radiated Noise
TS	Target Strength
XS	Excess Level
$z_{lk}(t)$	Signal emitted by transmitter k and received by receiver l
dA	Elementary surface
dV	Elementary volume
F	Spectrum of the broadband echo

Chapter 1

Introduction

There is nothing new to be discovered in physics now,
All that remains is more and more precise measurement.
Lord Kelvin (1900)

1.1 Thesis motivations

The oceans cover around 72% of our blue planet. The sea has always been a source of fear and fascination for mankind. And yet we know better the surface of Mars than the bottom of the oceans. Certainly the challenges faced in the deep sea exploration are tremendous: the extreme pressure at high depth is one of many. Notwithstanding the difficulties to access and operate underwater the stakes are crucial for the future:

- **Military:** Harbour access, surface vessels protection and safe transit in costal area have always been a priority for any navy in the world. Identifying threats such as underwater mines is still a fully unsolved problem.
- **Oil & gas:** the recent disaster in the Golf of Mexico emphasises the issues of underwater interventions. New systems are needed for underwater structure installation, maintenance or intervention. Integrity management of these structures also represents a key element for continued, safe operation of offshore installations, especially with many fields coming to the end of their useful lives.

- **Clean energy:** the need for clean energy has pushed the development of massive offshore wind farms spread over hundreds of km^2. The monitoring of the underwater structures along with the huge network of power cables lying on the seabed is a requirement to the power companies.
- **Oceanography:** recent studies in climate change show that oceans play a central role in the climate regulation. Monitoring oceans is crucial to be able to protect and preserve them. Deep water corals for instance are good sensors to monitor fluctuations (Henry et al. [2010]; Roberts et al. [2009]).

The engineering and technical challenges to perform any complex tasks underwater are great but the most crucial element in any underwater systems has to be the sensors. In air a numerous sensor systems have been developed: optic cameras, laser scanner or radar systems. Unfortunately EM waves propagate poorly in water. Visible light does not travel further than few metres underwater. So cameras can to used for close inspection at the cost of carrying lighting systems and the batteries to go with them.

Considering the impedance of water compared to air sound suffers less attenuation and therefore travels further underwater. For this reason acoustic sensors are a much preferred tool then optical ones. In this thesis we study the present and the future of acoustic sensors for detection, identification or survey.

1.2 Thesis architecture

This thesis is organised as follows: In chapter 2 we pose the basics of the underwater acoustics. The sonar equation proposed by Urick in Urick [1975] explains from an energetic point of view how an acoustic pulse is sent, propagates in the water, interacts with the seafloor, the surface or an object and is backpropagated towards the receiver. This elegant formulation stipulates the fundamental for sonar systems and allows us in chapter 3 to fully explain the formation of a sidescan image and the various phenomena related to it. Inversely by solving the sonar equation we were able to build a realistic sidescan image simulator. This

simulator turns out to be a great tool to test ATR (automatic target recognition) algorithms, and thanks to its flexibility we could demonstrate the importance of the resolution for sonar image processing tasks. In particular we explain why the centimetric precision of the new generation of sonar known as SAS (synthetic aperture sonar) is needed to extract useful information from target highlights.

Chapter 4 focuses on synthetic aperture sonar. The general trend for imaging sonars is to use relatively high frequencies (>100kHz). The reason behind this choice is the linear dependancy between wavelength and resolution: higher frequency, greater resolution. In this chapter we will look in the opposite direction and try to answer the question: what will be the advantages of a low frequency SAS system? The sonar equation shows its limitation in answering this question, and we will have to introduce new tools and solve the acoustic wave equation to understand the SAS image formation and the influence of the frequency.

Chapters 3 and 4 are dedicated to two configurations of imaging sonars. Our most developed sense is sight for humans, and it is no surprise that we chose images for data display and representation. That is why we want to see what is below the surface rather than hearing it. In chapter 5 we demonstrate that by imaging the sound, so in other words by using an incoherent process to map a coherent one, a tremendous quantity of information is lost. In this same chapter we propose a biomimetic sonar system design based on observations of bottlenose dolphins. A biosonar prototype has been built and we were able to demonstrate in real environments its capability in term of detection, classification and identification of such system. Finally in chapter 6 we explore the potential of MIMO (multiple input multiple output) broadband sonar systems. We will describe in particular how the multiview aspect of MIMO systems with widely spaced antenna increases detection rate and reduces false alarm rate.

Figure 1.1 displays the architecture of this thesis and the chapters' dependancy.

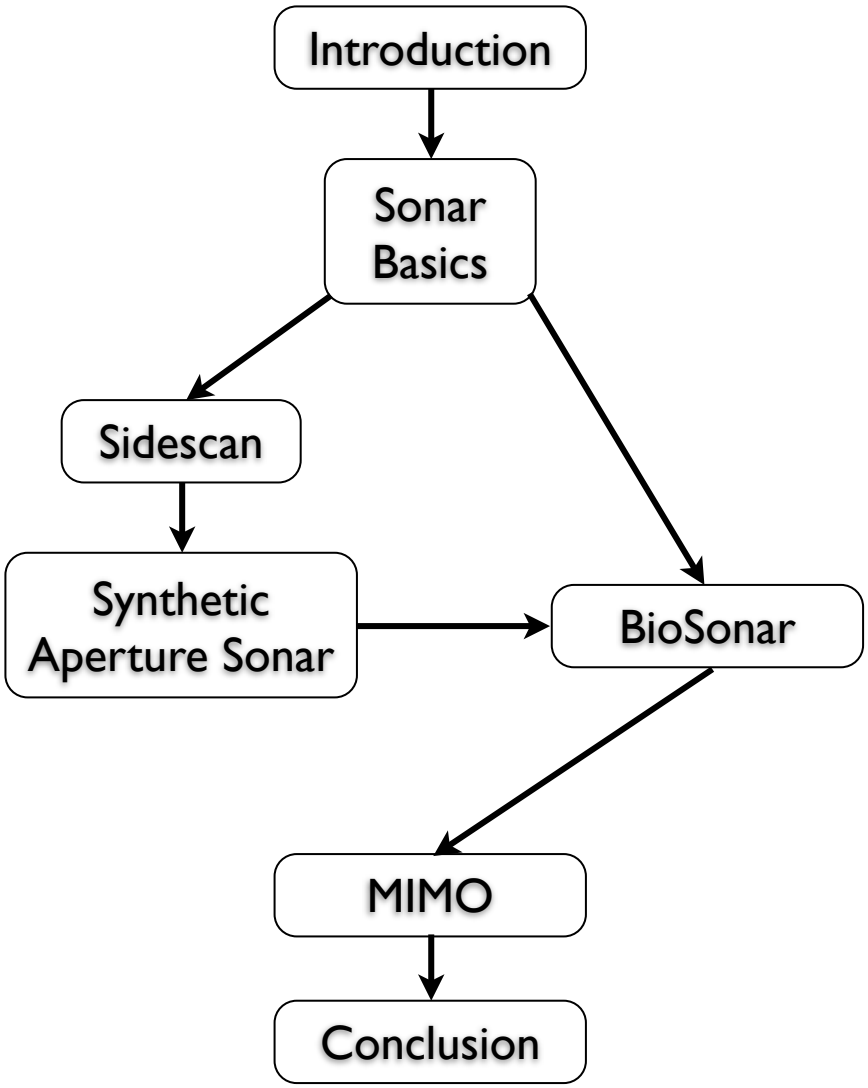

Figure 1.1: Thesis architecture.

1.3 Contributions

The main contributions to this thesis are:

- **Sidescan Simulator:** we have developed a sidescan sonar simulator that is both realistic and computationally efficient. The simulator can generate realistic synthetic sidescan images of various seabed types. Mine-like targets can also be added to the environment. The simulator is using a pseudo ray tracing algorithm minimising the computation requirements. This sidescan simulator offers a great tool for ATR (automatic target recognition) or seabed segmentation algorithm testing. It has also been successfully integrated through the ROS (Robot Operating System) platform into an AUV (autonomous underwater vehicle) simulator.

- **Study on the resolution:** taking advantage of our sidescan image simulator we propose a study on the pixel resolution needed to carry out ATR on sonar images. We demonstrate that using the commercially available sidescan systems (with an average of 10 cm pixel resolution) the main extractable information lies in the shape of the shadow. We show as well that in order to extract information from the highlights a greater resolution is needed (less than 3 cm pixel resolution) and systems such as SAS are required.

- **Design of low frequency SAS and its advantages:** we propose a design for a LF-SAS (low frequency synthetic aperture sonar) and emphasise its advantages compared to a high frequency system. We demonstrate that with such design it is possible to image the inner of a target and by doing so drastically reduce the false alarm rate.

- **SAS image formation:** the synthetic aperture algorithm (for radar or sonar) is based on the strong hypothesis that the area to be imaged is composed of a finite number of scattering points. In fact each pixel in the SAR/SAS image represents one of these scattering points. We demonstrate that not only the direct scattering from an object is part of the synthetic aperture image but most importantly its reflection from the seabed (*i.e.* its virtual image) contributes greatly to the image formation.

- **Analysis of broadband echoes:** broadband sonar systems demand understanding of the full echo structure and the understanding of the echo formation. We present the physics underlying acoustic backscattering, focusing mainly on cylindrical and spherical shells. We link the interferences in the echo spectra to the shape and material properties of the target of interest. Few models for broadband echo formation are proposed and validated by both analytical solution of the theory and simulations. Finally we propose an algorithm to classify and identify ensonified target based on its broadband echo.

- **Biomimetic sonar development:** we have built an AUV ready biomimetic sonar system. The frequency band of our biosonar matches the one used by the *Tursiops truncatus* bottlenose dolphins known for their excellent performances in target (fish) detection and identification. Our system leads us to several successful MCM (mine counter measure) trials demonstrating in real environments the capabilities of biomimetic sonar systems and the performance of our algorithms.

- **MIMO sonar formulation:** we propose a formulation adapted to sonar MIMO (multiple input multiple output) and show that a MIMO system benefits greatly from the target multi-aspect it provides both for detection and identification. We also demonstrate that using time reversal techniques we can automatically steer the overall beam pattern of the MIMO system toward the target increasing the SNR (signal to noise ratio) and then the detection rate.

- **Models for target scattering:** target scattering modelling is the underlying core of this thesis. Throughout this thesis we explore different sonar systems and configurations, each of which requires different scattering models. We show that if a simple energetic equation can explain most of the sidescan imaging process, we need to dig deeper into the acoustic wave interaction with matter to understand more complex systems such as broadband sonar. The Lambertian model, the Kirchhoff approximation, the wave equation analytical solution, the geometrical optics analogy, the

finite point model and the virtual scattering point theory are only a few different target scattering models presented in this work.

1.4 Publications

The research performed during those three years along with various collaborations lead to the following publications:

1.4.1 Journal papers

1. Yan Pailhas, Chris Capus and Keith Brown, Dolphin-inspired sonar system and its performance, IET Radar, Sonar & Navigation, *accepted*, 2012.

2. Yan Pailhas, Chris Capus, Keith Brown and Yvan Petillot, Design of artificial landmarks for underwater SLAM, IET Radar, Sonar & Navigation, *accepted*, 2012.

3. Yan Pailhas, Chris Capus, Keith Brown and Yvan Petillot, BioSonar: a biomimetic approach to sonar systems, Concepts and Applications, INTECH, chapter of "Biomimetic", ISBN 978-953-307-271-5, 2011.

4. Yan Pailhas, Yvan Petillot, and Chris Capus, High-Resolution Sonars: What Resolution Do We Need for Target Recognition?, EURASIP Journal on Advances in Signal Processing, vol. 2010, Article ID 205095, 13 pages, 2010. doi:10.1155/2010/205095

5. K. Brown, C. Capus, Y. Pailhas, Y. Petillot and D. Lane, The Application of Bio-inspired Sonar To Cable Tracking on the Seafloor, EURASIP Journal on Advances in Signal Processing Volume 2011 (2011), Article ID 484619.

6. Pailhas Y., Capus C., Brown K. and Moore P., Analysis and classification of broadband echoes using bio-inspired dolphin pulses Journal of the Acoustical Society of America, 127(6), pp. 3809-3820, June 2010.

1.4.2 Conferences

1. Capus, C., Pailhas, Y., Brown, K. and Evans J., Bio-inspired cable tracking using autonomous underwater vehicles, Institute of Acoustics Bioacoustics Conference 2009, Loughborough, U.K.

2. Petillot Y., Pailhas Y., Capus C., and Brown K., Underwater target detection and classification using high resolution sensors and wide band sonar, J. Acoust. Soc. Am. Volume 125, Issue 4, pp. 2577-2577, April 2009

3. Pailhas Y., Petillot Y., Capus C. and Brown K., Real-time Sidescan Simulator and Applications, IEEE Oceans 2009 Europe Conferences, Bremen, Germany, May 2009.

4. Pailhas Y., Petillot Y., Capus C. and Brown K., Broadband MIMO sonar system: a theoretical and experimental approach, *invited paper*, UAM 2009, 3rd International Conference and Exhibition on Underwater Acoustic Measurements: Technologies & Results, Nafplion, Greece, June 2009.

5. Capus C., Pailhas Y., Brown K., Evans J. and Willins D., Underwater Detection Classification and Tracking Using Wideband Sonar, UAM 2009, 3rd International Conference and Exhibition on Underwater Acoustic Measurements: Technologies & Results, Nafplion, Greece, June 2009.

6. Capus C., Pailhas Y., Brown K., Detection of Buried and Partially Buried Objects Using Wideband Sonar, ICTCA, 9th International Conference on Theoretical and Computational Acoustics, Dresden, Germany, September 2009.

7. Y. Pailhas, Y. Petillot, C. Capus, Time Reversal Techniques for Broadband MIMO Sonar Systems, *invited paper*, ICTCA, 9th International Conference on Theoretical and Computational Acoustics, Dresden, Germany, September 2009.

8. Chris Capus, Yan Pailhas, Keith Brown, David Lane, Application of Bioinspired Wideband Sonar to Detection and Tracking of Underwater Targets

from Autonomous Platforms, NATO Workshop on Machine Intelligence For Autonomous Operations, Lerici, Italy, October 2009.

9. Yvan Petillot, Pedro Patron and Yan Pailhas, Towards robust autonomous underwater target detection and identification using AUVs, NATO Workshop on Machine Intelligence For Autonomous Operations, Lerici, Italy, October 2009.

10. Chris Capus, Yan Pailhas, Keith Brown, David Lane,Detection of Buried and Partially Buried Objects Using A Bio-inspired Wideband Sonar, OCEANS'10 IEEE Conference, Sydney, Autralia, May, 2010.

11. Yan Pailhas, Yvan Petillot, Chris Capus, Reg Hollett, Bernie Mulgrew, Target Imaging with Low Frequency SAS, *invited paper*, European Conference on Underwater Acoustics, ECUA'10, Istanbul, Turkey, July, 2010.

12. Yvan Petillot, Yan Pailhas, Chris Capus, Jamil Sawal, Nicolas Valerie, *invited paper*, Review on ATR, European Conference on Underwater Acoustics, ECUA'10, Istanbul, Turkey, July, 2010.

13. Jamil Sawas, Yvan Petillot, Yan Pailhas, Target detection and classification using cascades of boosted classifiers, European Conference on Underwater Acoustics, ECUA'10, Istanbul, Turkey, July, 2010.

14. Yvan Petillot, Yan Pailhas, Jamil Sawas, Nicolas Valeyrie, Target detection and identification in Synthetic Aperture Sonar using AUVs, 2010 International Conference on Synthetic Aperture Sonar and Synthetic Aperture Radar (SAS/SAR 2010), Lerici, Italy, September 2010.

15. Yan Pailhas, Yvan Petillot, Chris Capus, Reg Hollett, Bernie Mulgrew, Study, design and concept of low frequency SAS, 2010 International Conference on Synthetic Aperture Sonar and Synthetic Aperture Radar (SAS/SAR 2010), Lerici, Italy, September 2010.

16. Yan Pailhas, Pedro Patron, Joel Cartwright, Francesco Maurelli, Yvan Petillot, Jamil Sawas & Nicolas Valeyrie, Fully integrated multi-vehicles mine countermeasure missions, *invited paper*, UAM 2011, 4rd International

Conference and Exhibition on Underwater Acoustic Measurements: Technologies & Results, Kos, Greece, June 2011.

17. Yan Pailhas, Yvan Petillot, Chris Capus, Man-made objects vs natural objects in SAS data., *invited paper*, UAM 2011, 4rd International Conference and Exhibition on Underwater Acoustic Measurements: Technologies & Results, Kos, Greece, June 2011.

18. Nicolas Valeyrie, Yan Pailhas, Yvan Petillot, Texture recognition in synthetic aperture sonar images with scattering operators, *invited paper*, UAM 2011, 4rd International Conference and Exhibition on Underwater Acoustic Measurements: Technologies & Results, Kos, Greece, June 2011.

19. Yan Pailhas, Chris Capus, Keith Brown, BIO-INSPIRED SONAR, DSP 2011, 17th International Conference on Digital Signal Processing, Corfu, Greece, July 2011.

20. Yan Pailhas, Chris Capus, Keith Brown, MCM trials with Biosonar system, *invited paper*, European Conference on Underwater Acoustics, ECUA'12, Edinburgh, UK, July, 2012.

21. Yan Pailhas, Chris Capus, Keith Brown, Permanent scatterers detection using raw SAS data, *invited paper*, European Conference on Underwater Acoustics, ECUA'12, Edinburgh, UK, July, 2012.

22. Yan Pailhas, Yvan Petillot, Chris Capus, Bernie Mulgrew, Target detection using statistical MIMO, *invited paper*, European Conference on Underwater Acoustics, ECUA'12, Edinburgh, UK, July, 2012.

Chapter 2

Sonar Basics

2.1 A bit of history

> *"If you cause your ship to stop and place the head of a long tube in the water and place the outer extremity to your ear, you will hear ships at a great distance from you."* Leonardo da Vinci (1490)

With this observation made in 1490, Leonardo da Vinci revealed for the first time the potential of passive sonar systems. Three points are noticeable in the da Vinci's quote: objects moving in water generate acoustic noise, sound travels in water and it travels far. Despite the simplicity of the proposed device, similar configurations based on air-filled tubes were used until World War I in order to detect ships and submarines.

The first issue to solve to develop active sonars was to generate sound in water. The high impedance of water compared to air (about 3500 times higher) made sound generation underwater challenging. Daniel Colladon and Charles Sturm in an experiment in Lake Geneva in Switzerland in 1827 managed to estimate the velocity of sound in water using an underwater bell as a pulse generator (Colladon [1893]). But the real breakthrough was the discovery of piezoelectricity by Pierre and Jacques Currie in 1880 (Lippman [1881]). Certain crystals such as quartz have the ability to generate electricity under physical stress and conversely are deformed when an electrical charge is applied.

In 1917 Charles Langevin and Constantin Chilowsky used the piezoelectric effect of quartz to build the first active sonar. It has been reported that this first sonar system was able to detect submarine at 1500 metres of distance. Today the vast majority of sonar systems are equipped with piezoelectric transducers. The interwar period was very prolific for sonar development. New synthetic crystals with higher efficiency soon replaced the traditional quartz crystals as acoustic transducers. Thanks to progress in electronics, filtering, amplification and processing were integrated into sonar systems increasing drastically the SNR (signal-to-noise ratio) and then as a direct consequence the detection rate of these systems. In parallel theoretical studies on the propagation medium have given the sonar community a better understanding of sound propagation in the oceans. Phenomena such as the "shadow zone" has been explained with the depth dependant water temperature of the oceans.

The last breakthrough came during the 1960s with the digital age. The rapid evolution of computer technology along with digital processing has enabled a drastic gain in term of performance, portability and versatility of sonar systems.The civilian use of sonar had spread in many applications such as fishery, bathymetry etc... Many engineering efforts have been put into imaging sonars and new sonar configurations. Forward looking sonar and sidescan sonar were born during this period. The latest imaging sonar system to date is based on synthetic aperture antenna. SAS system (synthetic aperture sonar) has been developed during the last 20 years and inherits from the SAR (synthetic aperture radar) technology. One of the main advantages of SAS systems is its constant resolution over range and very large swath.

2.2 The transducers

The transducers represent the central part of any sonar system. The introduction of the piezoelectric transducer in the early 1900s solved the problem of the very high acoustic impedance of water.

2.2.1 The piezoelectric effect

The piezoelectric effect is the ability for certain materials to generate electricity under mechanical stress. This effect is reversible meaning that a piezoelectric material generates mechanical strain under an electrical charge (Lippman [1881]). The principle of piezoelectricity can be described mathematically thanks to the following coupled equations:

$$S = \quad s^E T \quad + d^t E \tag{2.1}$$

$$D = \quad dT \quad + \epsilon^T E \tag{2.2}$$

where S is the strain vector or relative deformation vector, S is a normalized measure of displacement and therefore dimensionless , T the mechanical stress vector is the force per unit area applied to the piezoelectric and it is expressed in Newton per m^2, E the electric strength vector is expressed in Newton per Coulomb and D the electric displacement vector is expressed in Coulomb per m^2. s^E represents the compliance matrix or elasticity matrix, d is the direct piezoelectricity effect matrix, d^t is the converse piezoelectricity effect matrix and ϵ^T the permittivity matrix (for T constant).

Using the Voigt notations, the piezoelectricity effect matrix $d = (d_{ij})_{i,j\in[1,3]}$ can be re-written as:

$$d_{ij} = \left(\frac{\partial S_j}{\partial E_i}\right)^T \tag{2.3}$$

where the symbol ^{T} means at T constant. Conventionally the polarisation $\vec{P}$ of the piezoelectric crystal is collinear to axis 3. So by integrating Eq. (2.3) along the thickness of the piezoelectric component parallel to its polarisation, we obtain:

$$\Delta S_3 = d_{33}\ U_{\text{in}} \tag{2.4}$$

U_{in} represents the charge applied to the piezoelectric component and ΔS_3 the resulting physical deformation along axis 3. Figure 2.1 illustrates the physical interpretation of Eq. (2.4) at the macroscopic scale. Figure 2.2 shows the crystal configuration of a piezoelectric and its deformation along the polarisation axis.

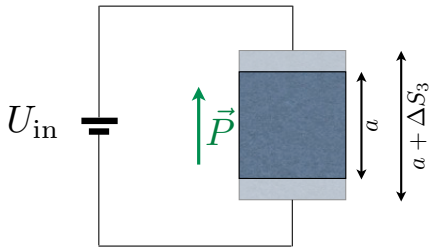

Figure 2.1: Schematic representation of the deformation ΔS_3 of a piezoelectric component under an electric charge U_{in}.

2.2.2 The piezoelectric components

In the early days sonar engineers were using quartz because of their natural piezoelectric capabilities. Quartz has been replaced latterly by synthetic piezoceramics. These synthetic piezocrystals present higher piezoelectric effects than the natural ones. In particular the direct piezoelectric term d_{33} which links linearly the displacement to the electric charge (cf. Eq. (2.4)) is much higher (around 10 times higher). This property induces a much higher electromechanical efficiency.

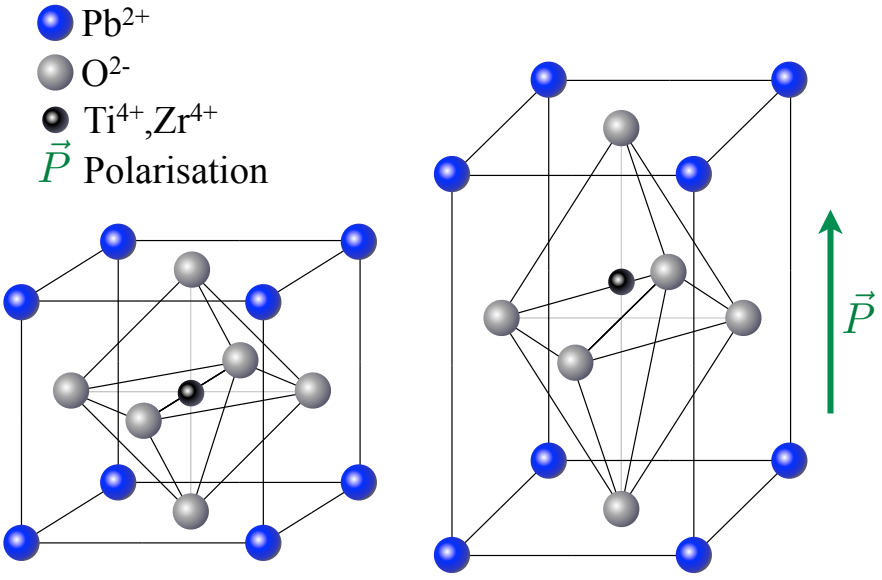

Figure 2.2: Crystal configuration of PZT above Curie temperature *(left)* and below the Curie temperature *(right)*.

Lead zirconate titanate ($Pb[Zr_xTi_{1-x}]O_3$, $0 \leq x \leq 1$) or PZT is the most widely used piezoceramic for underwater acoustic transducers. The metals are mixed at high temperature (higher than the Curie temperature). A voltage field is then applied to polarise the crystal in one specific direction. A remnant polarisation is then *recorded* into the intrinsic nature of the piezoceramic. Figure 2.2 displays the crystal configuration of the PZT with its remnant polarisation $\vec{P}$.

2.3 Electronics

The piezoelectric transducer's ability to be driven by electricity facilitates their integration into an electronic system. The electronic revolution of the XX$^{\text{th}}$ century developed sonar as a useful tool. For active sonar, amplifiers drive the transmitters at higher voltages increasing linearly the output power in the water. From a receiver point of view, filters can filter the out of band noise and amplifiers increase the SNR. Figure 2.3 illustrates the basic features of an active sonar system.

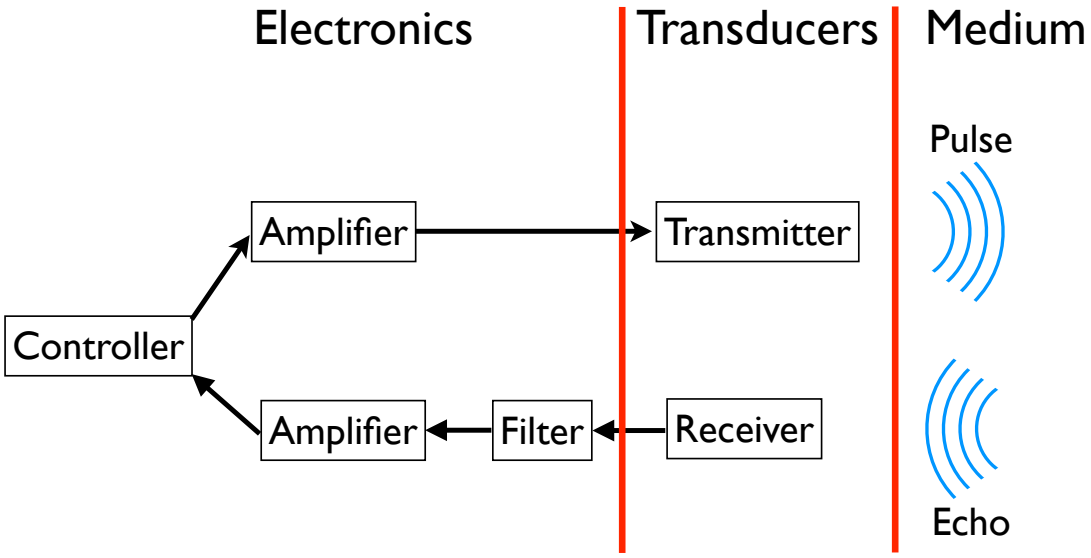

Figure 2.3: Active sonar functional schematic.

2.4 The Sonar Equation

The sonar equation formulated by Urick [1975] describes in a simple manner and from an energetic point of view the basic sonar principles. It relates the energy sent into the water by the transmitter to the energy received by the receiver.

The sonar equation is defined in terms of the following parameters:

- SL: Source Level for the projector
- DI: Directivity Index
- TL: Transmission Loss
- NL: ambient Noise Level
- RL: Reverberation Level
- TS: Target Strength
- DT: Detection Threshold

All are measured in decibels (dB) relative to the standard reference intensity of a 1μPa plane wave. Two simple forms of the sonar equation are commonly used:

(1) in the ambient noise limited situation,

$$SL - 2TL + TS = NL - DI + DT \tag{2.5}$$

(2) and with reverberation level dominant,

$$SL - 2TL + TS = RL + DT \tag{2.6}$$

These two equations can be reformulated as follow:

$$SL - 2TL + TS = NL - DI + RL + DT \tag{2.7}$$

Note that this equation is suitable for an active, monostatic sonar under certain conditions for validity, principally:

- only direct paths are considered: multipath and diffusion phenomena are not taken into account.
- this formulation of sound propagation is strictly energetic in the basic form, the shape of the signal does not enter into the equation.

One can read Eq. (2.7) as the sound *history* of an active sonar: a pulse is first emitted by the transducer with a certain energy SL. The transmitted pulse propagates into the medium, its energy decreases along the propagation $-TL$. The acoustic wave interacts with a target and a part of the energy is reflected back toward the sonar TS. And finally the target echo propagates back to the receiver losing energy along the path $-TL$.

The Echo Level EL which can be seen as the signal level from a sonar point of view can be written as:

$$EL = SL - 2TL + TS \tag{2.8}$$

This echo level is then balanced against the noise level $(NL - DI)$ which includes ambient noise and self noise and against the reverberation level (RL) due to the interaction between the outgoing pulse and the seafloor.

From Eq. (2.7) it is relatively easy to deduce the sonar equation for the passive case. In passive acoustics, the signal is produced by the target itself. The target radiated noise (TRN) serves the purpose of emitter. The sound emitted by the target propagates from the target to the receiver. Considering one-way propagation and suppressing the reverberation level (an intrinsic parameter of active systems), the sonar equation becomes:

$$TRN - TL = NL - DI + DT \tag{2.9}$$

It is interesting to link the sonar equation previously described with the radar equation (cf. Blake [1969]; Kerr [1951]). The radar equation is traditionally written as follows:

$$P_r = \frac{P_t G_t A_r \sigma F^4}{(4\pi)^2 R^4} \tag{2.10}$$

where P_t is the transmitter power, G_t the gain of the transmitting antenna, A_r the aperture of the receiving antenna, σ the radar cross section of the target, F the propagation factor, and R the distance between the radar and the target. The radar equation in Eq. (2.10) describes fundamentally the same energetic dependency between transmit and receive power as the echo level equation in Eq. (2.8).

The sonar equation despite its simplicity is a powerful tool in order to predict and evaluate the performance of a given sonar. One of the main applications of sonars developed during the 2$^{\text{nd}}$ World War was the detection of submarines. For ASW (anti-submarine warfare) detection range is a critical parameter. The detection range can be evaluated by solving the transmission loss TL into Eq. (2.7). The sonar equation can also be used during the sonar design process. Given a particular application the future sonar has to fulfil, for example be able to detect a certain target at a given range, the design engineer will be able through the sonar equation to compute the source level SL, directivity index DI and frequency band suitable for this particular application.

The following sections describe the different models needed to compute each of the parameters of the sonar equation.

2.4.1 Sound speed

Sound speed in seawater is given by Mackenzie's equation (Mackenzie [1981]). Mackenzie's equation is a nine-term equation based on empirical measurements. It is a function of the temperature T in °C, the salinity S in ppt and the depth D in metres.

$$
\begin{aligned}
c = \quad & 1448.96 + 4.591T - 5.304.10^{-2}T^2 + 2.374.10^{-4}T^3 \\
& +1.340(S-35) + 1.630.10^{-2}D + 1.675.10^{-7}D^2 \\
& -1.025.10^{-2}T(S-35) - 7.139.10^{-13}TD^3
\end{aligned} \tag{2.11}
$$

The degree of uncertainty in this equation is around $\pm$ 0.07 m.s^{-1}. The valid range is:

$$
\begin{array}{ccccc}
-2°\text{C} & \leq & \text{T} & \leq & 30°\text{C} \\
30\text{ppt} & \leq & \text{S} & \leq & 40\text{ppt} \\
0\text{m} & \leq & \text{D} & \leq & 8000\text{m}
\end{array}
$$

Operating conditions in certain parts of the Persian Gulf or the Mediterranean Sea could potentialy exceed some of these levels.

The sound speed in fresh water is given by the empirical equation of Grosso and Mader [1972]:

$$
\begin{aligned}
c = \quad & 1402.388 + 5.03711T - 0.0580852T^2 \\
& +3.342.10^{-4}T^3 - 1.478.10^{-6}T^4 + 3.15.10^{-8}T^5
\end{aligned} \tag{2.12}
$$

T represents the temperature in °C.

2.4.2 The Source Level

Table 2.1 gives reported source level values for several manmade and biological sonars. The figures given for the marine mammal sonars are collated over several experiments in different locations. These sonars are highly adaptive and the preferred peak frequency for an individual dolphin can differ by as much as 40 kHz depending on location and task (Au [1993]). The 3 dB bandwidths are similarly adaptive for many marine mammal species. The source levels given for the marine mammals are at the upper end of a range. The source level of a

	Sonar	Frequency (in kHz)	Source Level (in dB)
Manmade Sonars	Tritech SeaKing Obstacle Avoidance Sonar	325; 675	235
	Reson SeaBat 8101 Multibeam	240	217
	GeoAcoustics Dual Frequency Sidescan	114; 410	223
	Didson Detection Sonar Acoustic Camera	1100; 1800	205
	HWU Biosonar (prototype)	30 $\rightarrow$ 150	200
Biological Sonars	Bottlenose dolphin (Turiops truncatus)	30 $\rightarrow$130	228
	False killer whale (Pseudorca crassidens)	100 $\rightarrow$ 130	228
	Harbour porpoise (Phocoena phocoena)	120 $\rightarrow$140	162

Table 2.1: Examples of operating frequencies, bandwidths and reported Source Levels for several manmade and biological sonars

particular pulse is dependent on task and conditions. For example in performing an echolocation task, target strength, target range and ambient noise all directly influence the signal power used. The peak-to-peak source level may give an over-estimate of the signal power used by marine mammals when compared to the CW devices in the table above, the latter having a much longer pulse length. Accepting the argument that measures based on the Energy Flux Density are better suited to the description of very short-duration transient signals these values would be revised down by as much as 40 - 50 dB.

2.4.3 The Transmission Loss

In a wide range of cases a good approximation to transmission loss can be made by considering the process as a combination of free field spherical spreading and an added absorption loss. As noted above, this working rule can be expressed as,

$$TL = 20 \log r + \alpha r \tag{2.13}$$

where r is the transmission range and α is an attenuation coefficient expressed in dB/m. For low frequency models, at short ranges (< 100 m), the absorption coefficient has only a small impact on transmission loss and it may be sufficient to consider spherical spreading alone. Note that assuming a monostatic system, the range r will be twice the distance between sonar and target allowing for there-and-back transit.

The attenuation coefficient can be expressed as the sum of two chemical relaxation processes and the absorption of pure water.

$$\begin{matrix}\text{Total} \\ \text{Absorption}\end{matrix} = \begin{matrix}\text{BoricAcid} \\ \text{Contribution}\end{matrix} + \begin{matrix}\text{MgSO4} \\ \text{Contribution}\end{matrix} + \begin{matrix}\text{PureWater} \\ \text{Contribution}\end{matrix} \tag{2.14}$$

The formula is given by:

$$\alpha = \frac{A_1 P_1 f_1 f^2}{f_1^2 + f^2} + \frac{A_2 P_2 f_2 f^2}{f_2^2 + f^2} + A_3 P_3 f^2 \tag{2.15}$$

where f is the sonar frequency in kHz, f_1 and f_2 are the relaxation frequencies, as defined below. The Francois and Garrison [1982a,b] formula gives a numerical value for the coefficients:

$$A_1 = \frac{8.86}{c} 10^{0.78pH-5} \tag{2.16}$$

$$P_1 = 1 \tag{2.17}$$

$$f_1 = 2.8\sqrt{S/35}\ 10^{4-1245/(T+273)} \tag{2.18}$$

$$A_2 = 21.44\frac{S}{c}(1 + 0.025T) \tag{2.19}$$

$$P_2 = 1 - 1.37 \times 10^{-4} D + 6.2 \times 10^{-9} D^2 \tag{2.20}$$

$$f_2 = \frac{8.17 \times 10^{8-1990/(T+273)}}{1 + 0.0018(S - 35)} \tag{2.21}$$

$$A_3 = 4.937 \times 10^{-4} - 2.59 \times 10^{-5}T + 9.11 \times 10^{-7}T^2 - 1.5 \times 10^{-8}T^3 \quad (2.22)$$

$$P_3 = 1 - 3.83 \times 10^{-5}D + 4.9 \times 10^{-10}D^2 \quad (2.23)$$

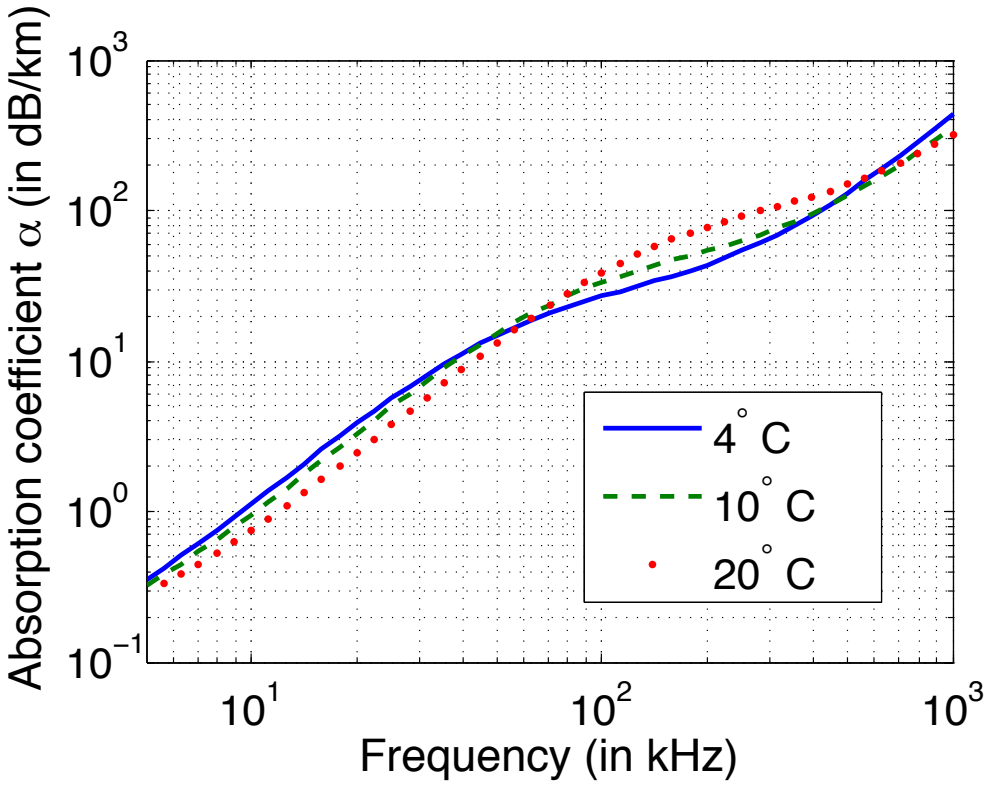

Figure 2.4: Absorption coefficient in sea water as a function of sonar frequency for three temperatures (4°C, 10°C and 20°C). Depth is set at 0m, salinity = 35ppt and pH = 8.

Figure 2.4 shows the variation of the α coefficient as a function of frequency. Note that above 10kHz the absorption coefficient begins to be significant and must be taken into account.

2.4.4 The Target Strength

The term target strength refers to the echo returned by a target. Several definitions are used. The most common, peak-to-peak, is based on measurement of

the ratio between the incident peak signal strength and the return peak signal strength. This is the simplest form and is used widely making it most appropriate for comparisons between the widest range of figures given in the literature. Alternative definitions, such as that based on the ratio of incident and return energy flux density, may be more appropriate for wideband signals and have been developed primarily to account for the integration over time that seems to be a feature of signal processing in certain marine mammals. We concentrate here on the first measure and target strength (TS), measured in decibels (dB), is defined as,

$$TS = 10 \log \left(\frac{I_r}{I_i} \right) \tag{2.24}$$

where, I_r is the intensity of the return measured at a distance of 1m from the target, and I_i is the incident intensity. Intuitively we may assume that this value depends on the shape of the target, the wavelength of the incident sound wave and the target material properties.

The following two subsections describe the Target Strength computation of two simple targets:

- an isotropic target: a rigid sphere
- an anisotropic target: a rigid finite cylinder with flat end caps

2.4.4.1 Spherical target

Early calculations of target strength were performed by Rayleigh [1945] using simple cylindrical and spherical targets. Note that the sphere is considered as rigid. The sphere model has become a standard reference and simplifies calculations through its symmetry properties. For a large sphere, defined for ka $\gg 1$, where k is the wave number ($2\pi/\lambda$) and a is the radius of the sphere, the target strength is given by:

$$TS = 10 \ \log \frac{a^2}{4} \tag{2.25}$$

2.4.4.2 Cylindrical target

A cylindrical target shape is shown in Figure 2.5. From a model viewpoint it is composed of two principal components: the finite cylinder, and the two circular endcaps. The cylindrical part can be modeled using the formula (Kerr [1951]):

$$TS_{\text{cylinder}} = 10 \log \left[\frac{aL^2}{2\lambda} \left(\frac{\sin \beta}{\beta} \right)^2 \cos^2 \theta \right] \tag{2.26}$$

where a and L are respectively the radius and the length of the cylinder, λ the wave length, θ the angle of view and $\beta = kL \sin \theta$

The circular endcap contribution is given by Kerr [1951]:

$$TS_{\text{disk}} = 10 \log \left[\left(\frac{\pi a^2}{\lambda} \right)^2 \left(\frac{2J_1(\hat{\beta})}{\hat{\beta}} \right)^2 \cos^2 \hat{\theta} \right] \tag{2.27}$$

where a is the radius of the circular plate, $\hat{\theta} = \pi/2 - \theta$, $\hat{\beta} = 2ka \sin \hat{\theta}$ and J_1 is the Bessel function of the first kind.

The resultant Target Strength of the cylindrical target is the maximum of the two components:

$$TS = \max(TS_{\text{cylinder}}, TS_{\text{disk}}) \tag{2.28}$$

Figure 2.6 shows the angular dependency of the target.

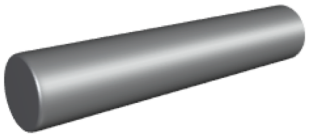

Figure 2.5: Shape of the cylindrical target.

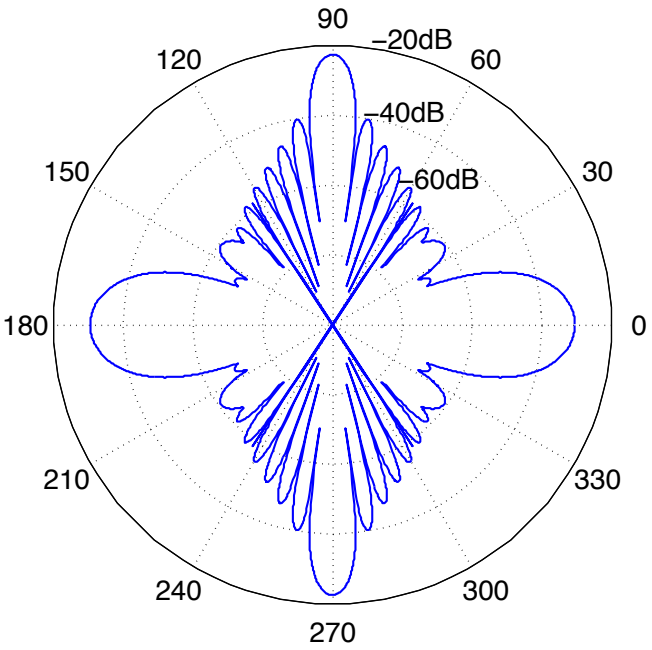

Figure 2.6: The angular dependency of the Target Strength of the cylindrical target.

2.4.5 The Reverberation Level

The volume reverberation level, working from the notion of a volume scattering element (dV), can be defined as follows:

$$\mathrm{d}V = \frac{c\tau}{2} r^2 \mathrm{d}\Omega \tag{2.29}$$

where c is the sound speed, τ the pulse duration, r the range and $\mathrm{d}\Omega$ the elementary solid angle. The elementary volume, dV, is defined such that scattering by the front end of the pulse by the rear scatterers in dV will arrive back at the source at the same time instant as scattering of the rear end of the pulse by the front scatterers in dV. Thus the difference in two-way transit time between the front and rear scatterers must equal the pulse length.

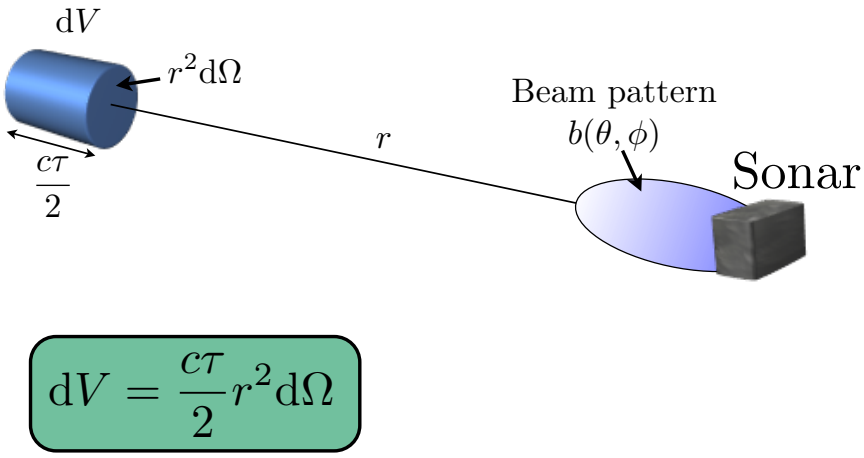

Figure 2.7: Notations for the definition of volume reverberation.

These definitions allow us to cast the volume contribution to reverberation level in the following form,

$$RL = SL - 2TL + S_v + 10 \log \frac{c\tau}{2} \psi r^2 \tag{2.30}$$

where, SL is the source level, r is the distance between the sonar and the reflector, S_v is the ratio of the energy reflected by the surface/volume, τ is the pulse length and ψ is the solid angle derived from the ideal beam equivalent of the complex beam pattern, b(θ,ϕ). This formula describes the acoustic energy integrated over all of the volume elements, dV, ensonified by the active sonar at range r.

Figure 2.8 illustrates how the definition of an elementary surface scattering element can be derived. The surface reverberation definition is similar to that for volume reverberation and can be developed as follows:

$$dA = \frac{c\tau}{2} r^2 d\Phi \tag{2.31}$$

dA defines the elementary surface subtended by horizontal angle dϕ. These are the equivalents of dV and d in the volume reverberation definition. Once

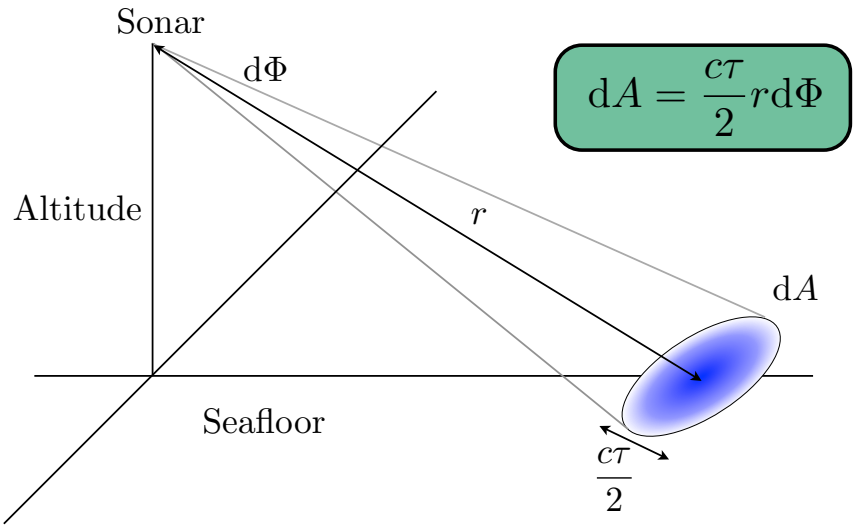

Figure 2.8: Definitions for surface reverberation modelling.

again simultaneous returns from the front and rear ends of the pulse determine the size of the elementary surface element, dA. So, for the surface contribution to reverberation level, we can write,

$$RL = SL - 2TL + S_s + 10 \log \frac{c\tau}{2} \phi r \tag{2.32}$$

The Reverberation Level represents the most significant 'noise' factor at short range especially for imaging systems such as sidescan sonar systems. The computation of the Bottom Scattering Strength has created a lot of interest in the underwater acoustic community. APL-UW [October 1994] proposed different models for the S_s coefficient. Figure 2.9 shows the Bottom Scattering Strength as a function of the grazing angle for the three different seabed types (very fine sand, sandy gravel and rough rock) at a frequency of 30kHz.

2.4.6 The Noise Level

Deep water noise spectra are easier to characterise than those for shallow water. Figure 2.10 is based on deep water ambient noise spectra published by Urick [1975], updated with comparative measurements taken more recently on the Con-

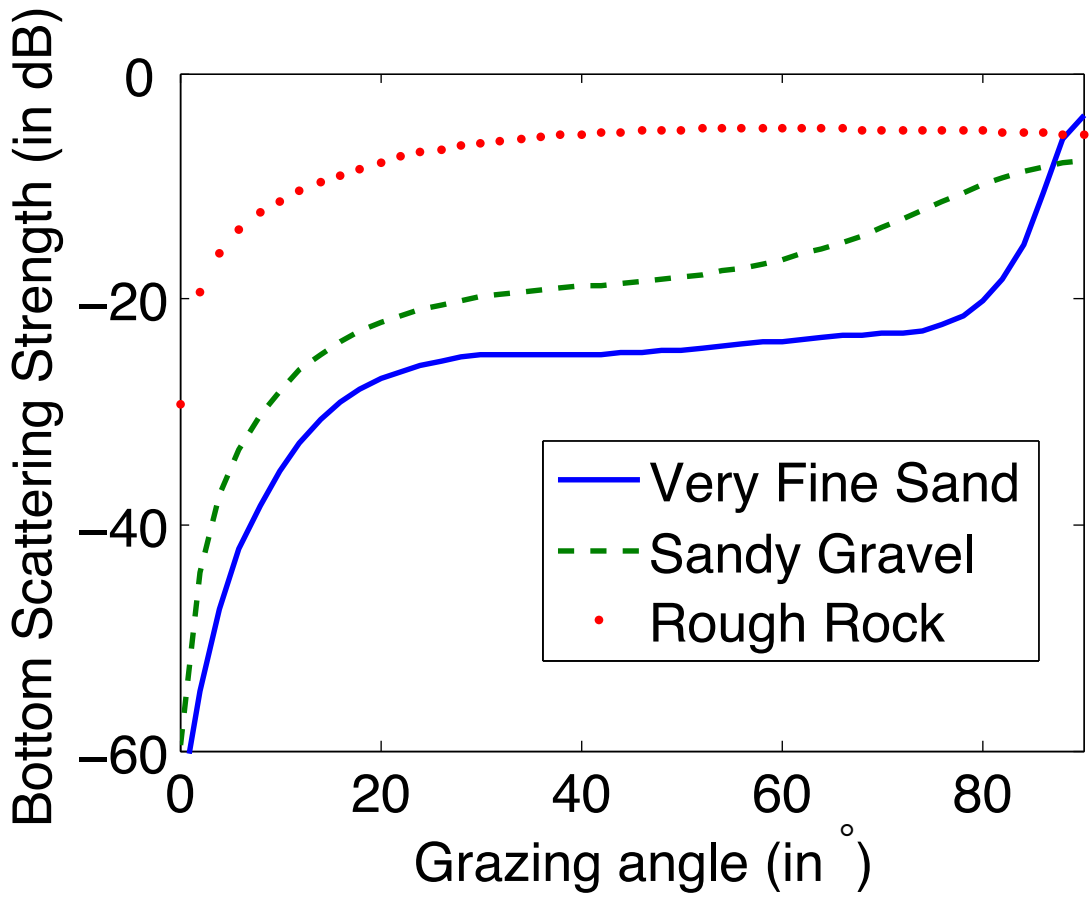

Figure 2.9: Variation in bottom scattering strength with grazing angle for three seabed types (very fine sand, sandy gravel and rough rock) at 30kHz.

tinental slope off Point Sur, California. These figures indicate a rise in ambient noise over the last 30-40 years predominantly due to shipping activity. The increase is of the order of 10dB in the range 10-500Hz. At higher frequencies, more applicable to modern detection sonar systems, major noise sources are due to wind and sea state, and thermal agitation (>100kHz).

1. < 10Hz the main contribution to the ambient noise spectrum comes from ocean turbulence

2. 10Hz – 100Hz predominantly shipping noise

3. 100Hz – 100kHz noise coming from the air-water interface (this kind of noise depends primarily on wind strength) characterised by the Knudsen spectra
4. 100Hz – 20kHz rain
5. 10kHz – 200kHz biological noise main contribution from snapping shrimp; also whales, dolphins etc.
6. $>$ 100kHz, major contribution is from molecular thermal agitation

Figure 2.10 illustrates the different contributions to the noise spectra. The black dash line at the lower frequencies represents the deep water noise spectra. The green curves and the red curves represent respectively theoretical and empirical shipping noise. And finally the blue curves represent air-water interface noise at different sea states.

For the range of frequencies from 10kHz to 400kHz, only two contributions for the Ambient Noise Level can be considered: the noise generated by the sea state and the thermal noise.

For thermal agitation, the equivalent noise spectrum level is given by the formula introduced in Mellen [1952]

$$NL_{th} = -15 + 20\log f \qquad \text{with } f \text{ in kHz} \tag{2.33}$$

A simple model for the noise related to the sea state is given by the model from Knudsen et al. [1948]:

$$NL_{sea} = A - 17\log f \qquad \text{with } f \text{ in kHz} \tag{2.34}$$

where A, the spectral noise at 1 kHz, is function of the sea state. Table 2.2 gives the A Knudsen parameter in function of the sea state.

Note that the attenuation due to depth can be taken into account as shown in Figure 2.11. Deeper in the sea, the Ambient Noise generated by the sea state decreases due to the sound absorption.

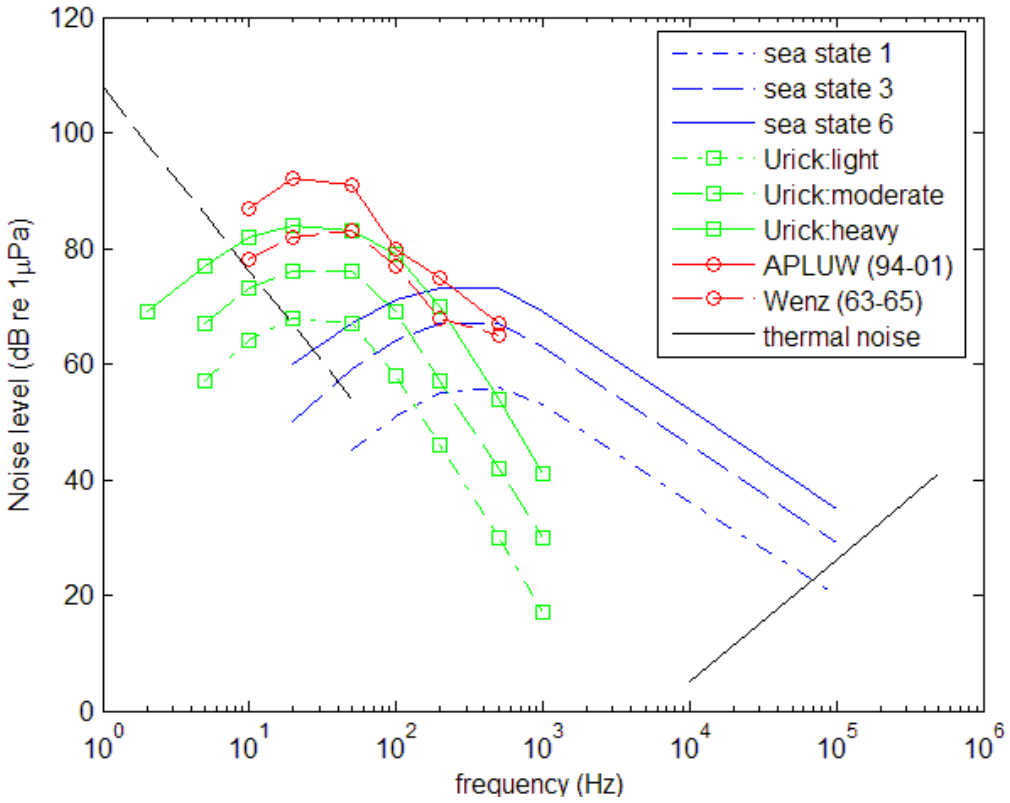

Figure 2.10: Deep water noise spectra: below 10Hz ocean turbulence predominant; 10-150Hz shipping noise is major contributor; 0.1-10kHz dominated by the Knudsen spectra mainly due to wind and wave action; 10-100kHz thermal noise is significant.

Sea state	0	0.5	1	2	3	4	5	6
A	44.5	50	55	61.5	64.5	66.5	68.5	70

Table 2.2: Spectral noise level @ 1kHz.

The resulting Ambient Noise NL for the frequency band 10 kHz to 400 kHz can be written:

$$NL = NL_{sea} + NL_{th} \tag{2.35}$$

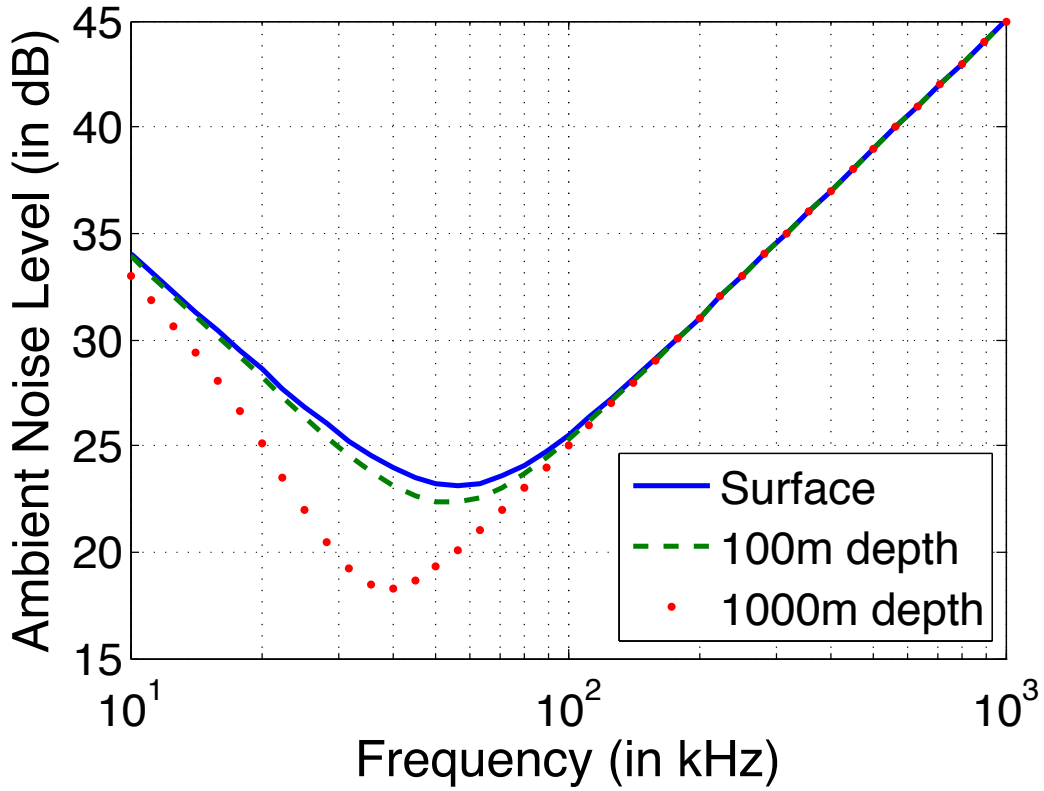

Figure 2.11: Influence of depth on the Ambient Noise Level (sea state 1).

2.4.7 The Beam Pattern and the Directivity Index

The Directivity Index (DI) is a sonar dependent factor associated with directionality of the transducer system. The projector/transmitter stage will have a characteristic beam pattern describing any angular dependency in output power. Similarly there will be a receiver beam pattern. Beam forming array configurations are built both to increase signal to noise ratio and to provide better target localisation. Sonar beam patterns are typically multi-lobed and sensitive to changes in frequency.

As an example one can derive the beam pattern from a continuous line array model of length l. The beam pattern function can be computed thanks to the

next formula. Note this case is valid only if $l \ll \lambda$.

$$B(\theta) = \left[\frac{\sin(\pi l/\lambda)\sin\theta}{(\pi l/\lambda)\sin\theta)} \right]^2 \tag{2.36}$$

The Directivity Index, DI, is found by integration over angles:

$$DI = 10 \ \log\left(\frac{2L}{\lambda}\right) \tag{2.37}$$

Figure 2.12 puts the sonar into the scene geometry. As noted earlier, the sonar beam pattern contains lobes and nulls which can drastically affect the range profile. For example considering the following configuration: $f = 30$kHz, $d = 30$m, $l = 0.1$m and $\theta_2 = 22.5°$, the beam pattern presents a null at $\approx 29.6°$. In the range profile, the data at the corresponding range (≈ 38m) will also be nulled.

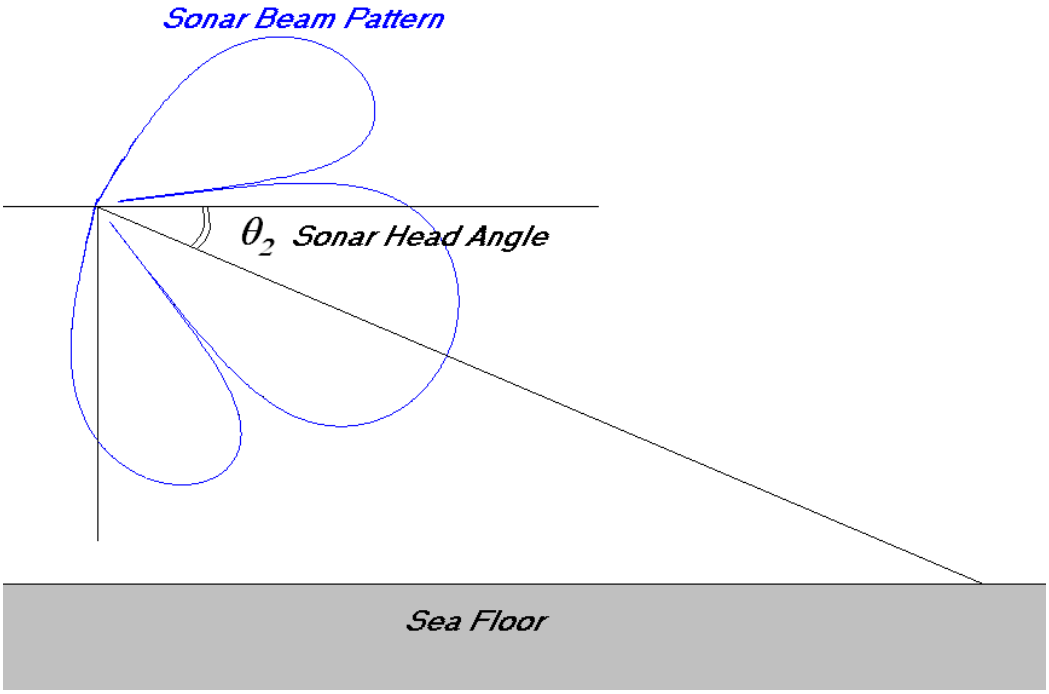

Figure 2.12: Example of sonar configuration with its beam pattern.

2.5 Conclusions

A lot of progress have been made during the last 60 years in sonar technology. Sonar's applications now stretch from military to biomedical, from environmental surveys to oil and gas. Sonar is also widely used for navigation and fishery. The sonar equation presented in the second half of this chapter gives a first order approximation of the echo formation for active sonar. It explains in simple terms the history of a pulse send into the medium, hitting a target and reflected back the to sonar sensor. Despite its simplicity we will see in chapter 3 that the sonar equation explains most of the phenomenas occurring in a sidescan image. In the same chapter we will also see that it can used as a model to produce synthetic sonar data.

The limitations of the sonar equation came mainly from the fact that this equation is based on energy and not the acoustic wave itself. Therefore acoustic phenomena such as multipath, target resonances, *et cetera* cannot be explained properly. The wave equation resolution and several other models will be presented in the following chapters to give a deeper understanding on the interaction between acoustic wave and matter.

Chapter 3

Sidescan Sonars

3.1 Sidescan systems

3.1.1 Sonar configurations

Sonar systems have evolved dramatically from the simple ranging system built by Langevin to complex sonar imaging systems. Several configurations for underwater sonars are now available (cf. figure 3.1) and the most popular are:

- profiler: the sonar is usually mounted vertically on a vehicle (boat, AUV...) and ensonifies the seabed just beneath it. It gives, as its name indicates, a 3D profile of the seabed or bathymetry.
- sidescan: sidescan sonars ensonify perpendicular to the trajectory of the vehicle (sideways). The port and starboard pings are stacked to form an image. They provide sonar images of the survey area.
- forward-looking: the sonar is pointing forward. Forward-looking sonars are usually used for mid-water object detection and obstacle avoidance. The bearing angle is given thanks to a mechanical scan or electronic beam forming.

In recent years, manufacturers developed in the imaging systems both in the sidescan and the forward-looking sonars focusing on providing very high resolution sonar images. The latest sonar technology developed is the SAS system

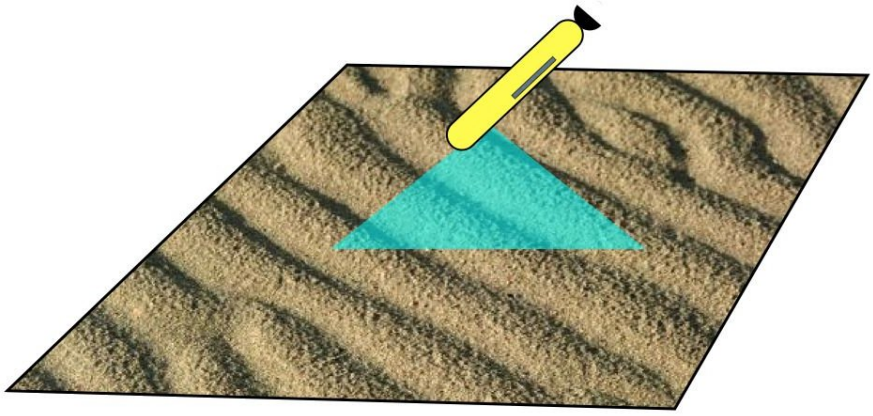

(a)

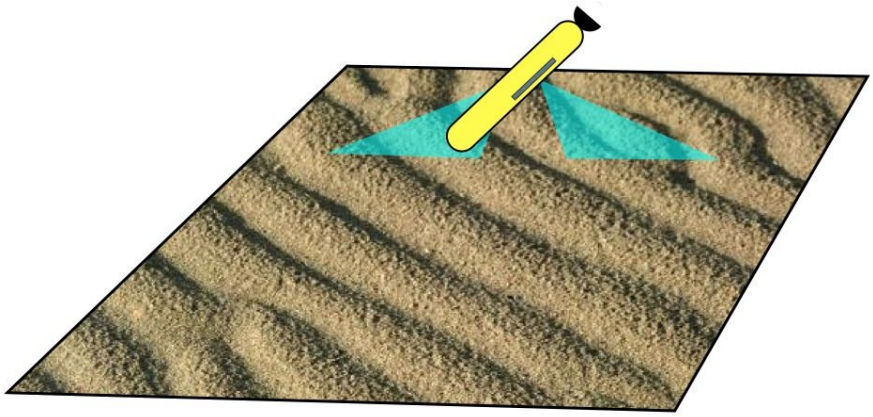

(b)

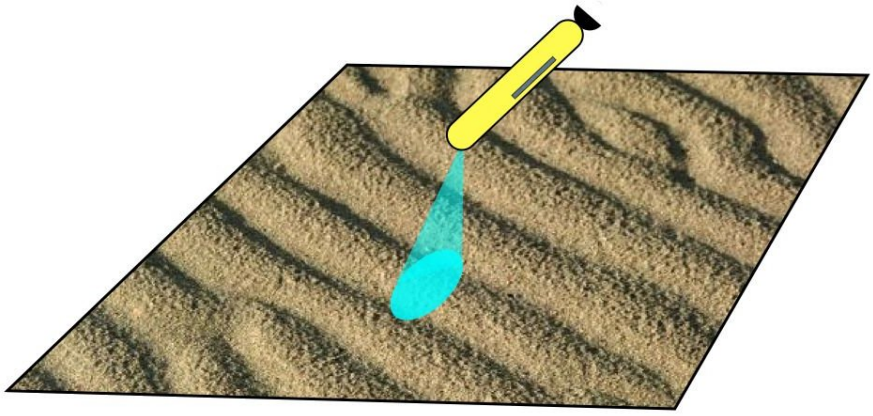

(c)

Figure 3.1: Classical sonar configurations: *(a)* profiler, *(b)* sidescan and *(c)* foward looking.

(Synthetic Aperture Sonar) which is based on the ideas from SAR (Synthetic Aperture Radar) technology. SAS systems provide sidescan-like images with a constant centimetric resolution over the whole range. SAS systems will be the subject of chapter 4.

3.1.2 The sidescan configuration

In this chapter, we focus our attention on sidescan sonar systems. The basic principle of sidescan sonar is simple and yet very effective to provide sonar images of the seabed. Sidescan systems are usually mounted on towfish and towed by a boat or directly mounted on a AUV. It consists of two acoustic arrays mounted on each side of the system and ensonifying respectively the port and starboard side perpendicularly to the trajectory. Figure 3.2 draws the insonification principle of sidescan sonar systems.

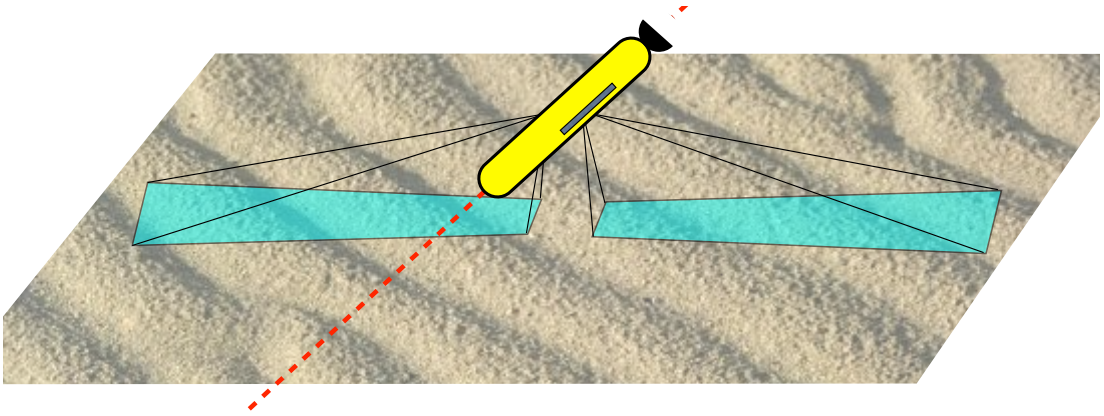

Figure 3.2: Sidescan sonar configuration.

In order to produce good quality images, the beam pattern of the antennas should follow two main criteria: the vertical beam pattern should be very wide (usually around 80°) in order to maximize the range of the sonar, and the horizontal beam pattern should be extremely narrow (usually between 0.1° and 0.5°) to have the best across range resolution possible. For these reasons sidescan arrays are typically long rectangular arrays.

In order to increase the sonar resolution and by doing so the overall quality of sonar images, manufacturers have chosen to increase the frequency. The resolution is linearly dependant on the wavelength λ ($\lambda = c/f$ where c is the sound speed in water and f the frequency). For this reason, the frequencies used for sidescan systems are generally relatively high (in the order of hundreds kHz).

3.1.3 Sidescan sonar image formation

As the sidescan sonar flies above the seabed, it pings and records the echo. A certain number of operations are applied to the echo at the reception including TVG (time varying gain) correction to compensate the energy loss due to the propagation, bandpass filtering or match-filtering to increase the SNR and suppress out of band noise, digitalization, envelope detection of the signal, downsampling of the signal amplitude and storage. The pings are then stacked together to form the sidescan image.

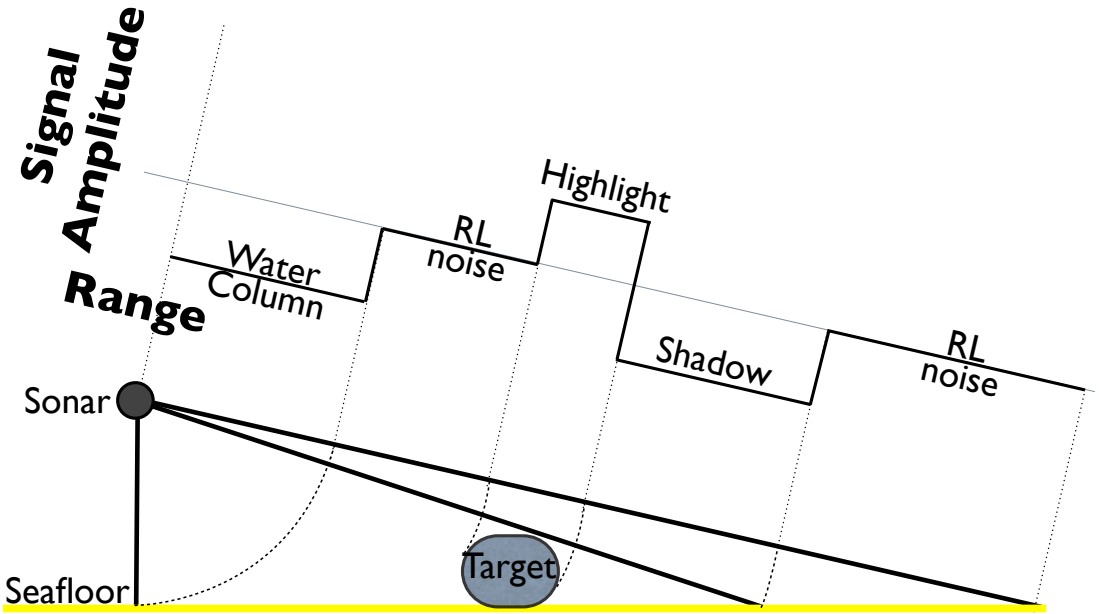

Figure 3.3: Sidescan sonar insonification principle.

Because of the high frequencies used in sidescan systems and the relatively short range of such sonars, geometric acoustics can be used to understand sidescan

images. As a first approximation the sound can be modelled by rays. It is important to note that a sonar image differs from an optical image because the resulting image is fundamentally a range image and NOT an angular image. Figure 3.3 explains the sidescan echo formation of a target lying on a flat seabed. The sound hitting an object on the seafloor will generate a highlight in the echo amplitude, this is mainly due the rapid change in the grazing angle. The area just below the object is not reached by the sound and will create a drop in the echo amplitude. This region is called *target shadow*.

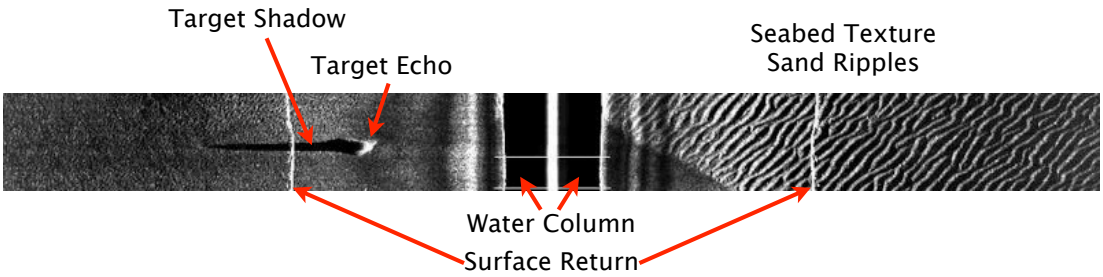

Figure 3.4: Sidescan sonar images featuring a mine-like object lying on a flat seabed. The echo of the target and its shadow are clearly visible on the starboard side of the sidescan image.

In figure 3.4 an example of target highlight and shadow is presented. Note that by using simple geometry, it is possible to estimate the height h of the object knowing the sonar altitude H, the range of the object r and the length of the shadow s. The height h is given by the following formula:

$$h = H\frac{s}{r+s} \tag{3.1}$$

Figure 3.5 displays two examples of the Marine Sonic sidescan images recorded with the AUV REMUS 100 from Hydroid. Figure 3.5(a) shows the coral reef of Loch Crehran (Scotland) on a flat environment. Figure 3.5(b) shows the terrain diversity of the seabed offshore of the Isola d'Elba (Italy) with sand ripples and seaweeds. Sidescan sonar systems provide useful acoustic images of the seafloor. These images can be interpreted properly by trained operators. It is important to note here that it is the stacking of the quasi-parallel pings when the sidescan

sonar flies over the scene which gives coherence to the overall acoustic image. Seabed 2D textures then became *visible*.

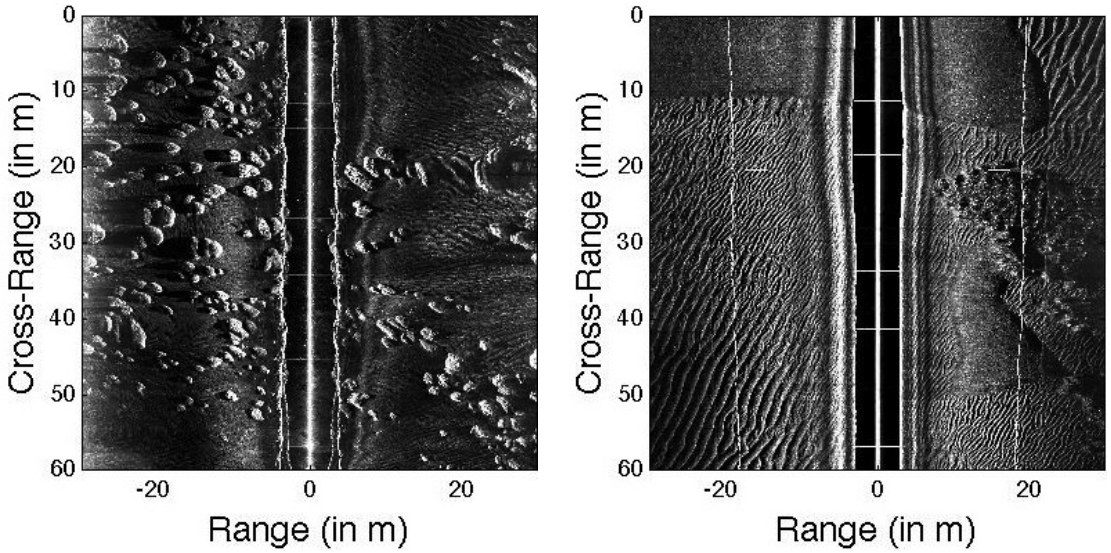

Figure 3.5: Examples of the Marine Sonics sidescan images taken with a REMUS 100. (*a*) corals on flat seabed, (*b*) mixed terrain with flat seabed, sand ripples and *posidonia* (seaweed).

The main limitation of such a system is that the resolution is not constant along the range. The ensonified area increases linearly with the range. And the along track resolution δx is:

$$\delta x = r\Phi \tag{3.2}$$

where r is the range, and Φ the horizontal beam aperture of the sonar. This can result a blurring of the sidescan image at long ranges.

3.2 Sidescan simulator

3.2.1 Motivations

Sonar images are difficult and expensive to obtain. A realistic sonar simulator offers an alternative for developing and testing image processing algorithms. High-frequency sonars increase the resolution of the sonar image from tens of cm to a few cm (3 to 5 cm). The resulting sonar images become closer to optical images. By increasing the resolution of the image the objects become sharper. The objective here is to produce a simulator that can realistically reproduce such images in real time.

There is an existing body of research into sonar simulation (e.g. Bell [1995]; Hunter et al. [2003]). The simulators are generally based on ray tracing techniques (Bell [1997]) or on a solution to the full wave equation (Elston and Bell [2004]). SAS simulation takes into account the SAS processing and is, in general, highly complex (cf. Hunter et al. [2003]). Critically, in all cases, the algorithms are extremely slow (one hour to several days to compute a synthetic sidescan image with a desktop computer). When high frequencies are used, the path of the acoustic waves can be approximated by straight lines. In this case, classical ray-tracing techniques combined with a careful and detailed modelling of the energy-based sonar equation can be used. The results obtained are very similar to those obtained using more complex propagation models. Ray tracing methods are much faster and still produce very realistic images.

Note that the simulator developed here is a high precision sidescan simulator, which can be equally well applied to forward looking sonar. SAS images differ from sidescan images in two main points: a constant pixel resolution at all ranges and a blur in the object shadows (see Pinto [2006]). The simulator can cope with the constant range resolution so synthetic target highlights will appear similar. A fully representative SAS shadow model remains to be implemented, but the analyses are still relevant for identification of targets from highlights in SAS imagery.

3.2.2 Simulator

The simulator presented here first generates a realistic synthetic 3D environment. The 3D environment is divided into three layers: a partition layer which assigns a seabed type to each area, an elevation profile corresponding to the general variation of the seabed, and a 3D texture that models each seabed structure. Figure 3.6 displays snapshots of four different types of seabed (flat sediment, sand ripples, rocky seabed and a cluttered environment) that can be generated by the simulator. All these natural structures can be modelled well using fractal representations. The simulator can also take into account various compositions of the seabed in terms of scattering strengths. The boundaries between each seabed type are also modelled using fractals.

Objects of different shapes and different materials can be inserted into the environment. For MCM algorithms, several types of mines have been modelled such as the Manta (truncated cone shape), Rockan and cylindrical mines.

The resulting 3D environment is an heightmap, meaning that to one location corresponds one unique elevation. So objects floating in mid-water for example cannot be modelled here. The sonar images are produced from this 3D environment, taking into account a particular trajectory of the sensor (mounted on a vessel or an autonomous platforms). The seabed reflectivity is computed thanks to state-of-the-art models developed by APL-UW [October 1994] in the High-Frequency Ocean Environmental Acoustic Models Handbook and the reflectivity of the targets is based on a Lambertian model. A pseudo ray-tracing algorithm is performed and the sonar equation is solved for each ensonified area giving the backscattered energy. Note that the shadows are automatically taken into account thanks to the pseudo ray-tracing algorithm. The processing time required to compute a sonar image of 50 m by 50 m using a 2 GHz Intel Core 2 Duo with 2 GB of memory is approximately 7 seconds. The remainder of this section details each of the modules required to perform the simulation.

Figure 3.7 displays the overall functional structure of the sidescan simulator. The user enters a series of parameters relative to the underwater environment

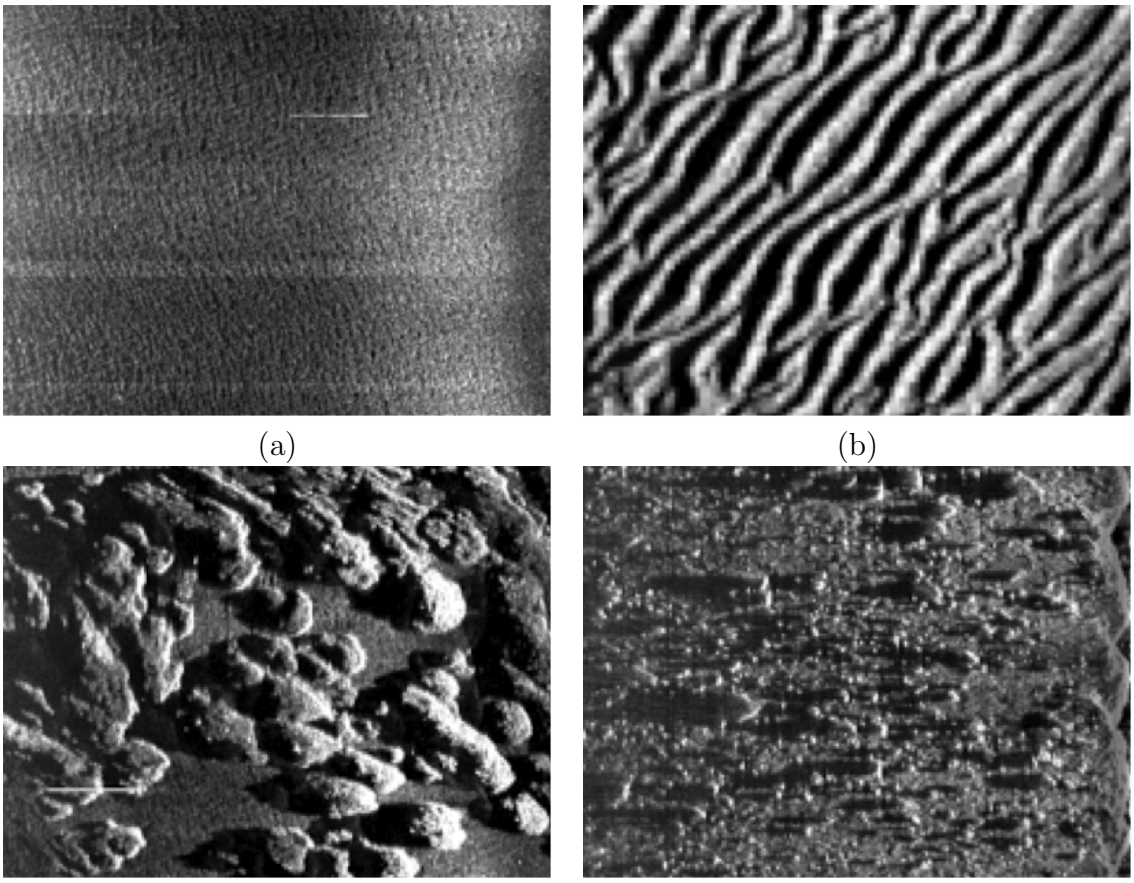

Figure 3.6: Snapshots of four different types of seabed: (a) flat seabed, (b) sand ripples, (c) rocky seabed and (d) cluttered environment.

to be modelled, the target to be put into that environment and the trajectory of the AUV inside this environment. First the 3D terrain is generated and the target is put into this environment. The 3D trajectory of the AUV relative to the synthetic seabed in then generated. Finally the sidescan simulator bloc solves the sonar equation for each point of the trajectory for a perpendicular insonification of the seafloor. As the AUV flies above the scene the A-scans stack together and form the synthetic sidescan image of the seabed. The computation of the different blocs are explained in the next subsections.

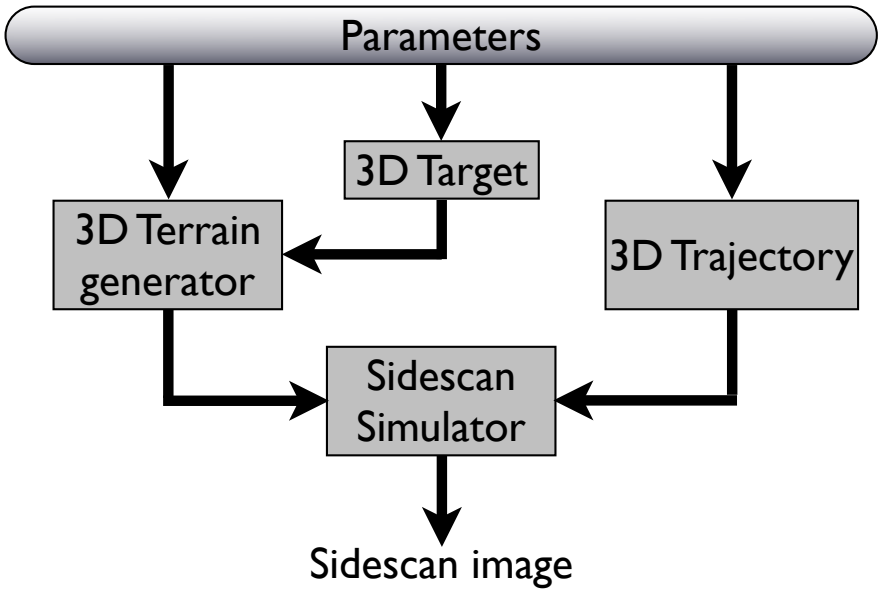

Figure 3.7: Functional structure of the sidescan simulator.

3.2.2.1 3D Digital Terrain Model Generator

The aim of this module is to generate realistic 3D seabed environments. It should be able to handle several types of seabed, to generate a realistic model for each seabed type, and to synthesize a realistic 3D elevation. For these reasons, the final 3D structure is built by superposition of three different layers: a partition layer, an elevation layer and a texture layer. Figure 3.8 shows an example of the three different layers which form the final 3D environment.

In the late seventies, mathematicians such as Mandelbrot [1982] linked the symmetry patterns and self-similarity found in nature to mathematical objects called fractals (Burrought [1981]; Lovejoy [1982]; Pentland [1984]; Voss [1985]). Fractals have been used to model realistic textures and heightmap terrains (cf. Voss [1985]). A quick way to generate realistic 3D fractal heightmap terrains is by using a pink noise generator (Voss [1985]). A pink noise is characterized by its power spectral density decreasing as $\frac{1}{f^\beta}$, where $1 < \beta < 2$.

The Partition Layer

In the simulator, various types of seabeds can be chosen (up to three for a given image). The boundaries between the seabed types are computed using fractal borders.

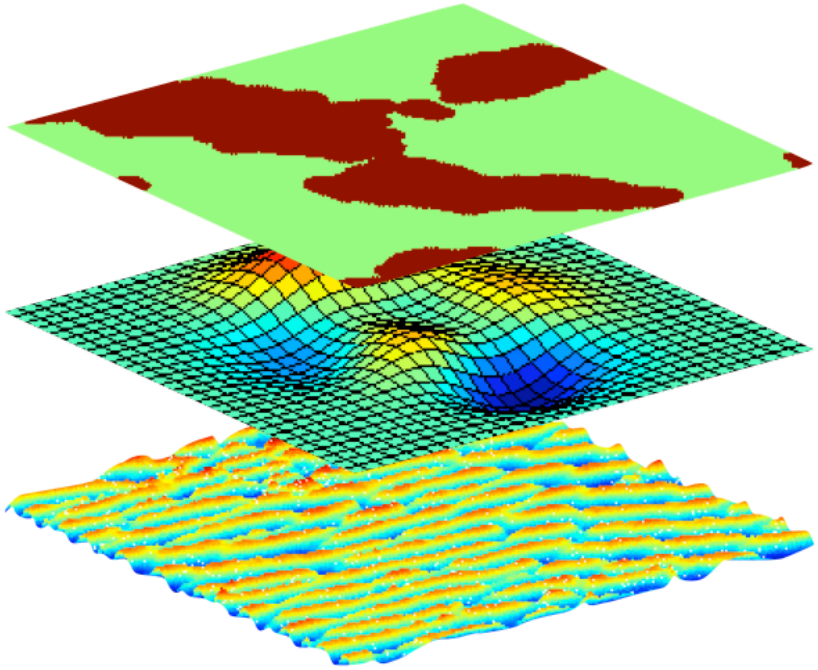

Figure 3.8: Decomposition of the 3D representation of the seafloor in 3 layers: partition between the different types of seabed, global elevation, roughness and texture.

Elevation Layer

This layer contains two types of possible elevation: a linear slope characterizing coastal seabeds and a random 3D elevation. The random elevation is a smoothing of a pink noise process. The β parameter is used to tune the roughness of the seabed.

Texture Layer

Four different textures have been created to model four kinds of seabed. Once again the textures are synthesized by fractal models derived from pink noise models.

Flat Seabed: A simple flat floor is used for the flat seabed. No texture is needed in this case. Differences in reflectivity and scattering between sediment types are handled by the Image Generator module.

Sand Ripples: The sand ripples are characterized by the periodicity and the direction of the ripples. A modified pink noise is used here. In this case the frequency decay is anisotropic. The amplitude of the magnitude of the Fourier transform follows Eq. (3.3). The frequency of the ripples is given by $F_{ripples} = \sqrt{f_{xpeak}^2 + f_{ypeak}^2}$ and the direction is given by $\theta = \tan^{-1}\left(\frac{f_{xpeak}}{f_{ypeak}}\right)$. The phase is modeled by a uniform distribution.

$$F(f_x, f_y) = \frac{1}{(f_x - f_{xpeak})^\beta} \frac{1}{(f_y - f_{ypeak})^\beta} \tag{3.3}$$

Rocky seabed: The magnitude of the Fourier transform of the the rocky seabed is modeled by Eq. (3.4). The factor α models the anisotropic erosion of the rock due to underwater currents.

$$F(f_x, f_y) = \frac{1}{\left(\sqrt{\alpha.f_x^2 + f_y^2}\right)^\beta} \tag{3.4}$$

Cluttered Environment: The cluttered environment is characterized by a random distribution of small rocks. A poisson distribution has been chosen for the spatial distribution of the rocks on the seabed as the mean number of occurrences is relatively small.

3.2.2.2 Targets

A separate module is provided for adding targets into the environment. Figure 3.9 displays the 3D models of 6 different targets. Location, size and material composition can be adjusted by the user. The resulting sidescan images offer a large data base for detection and classification algorithms.

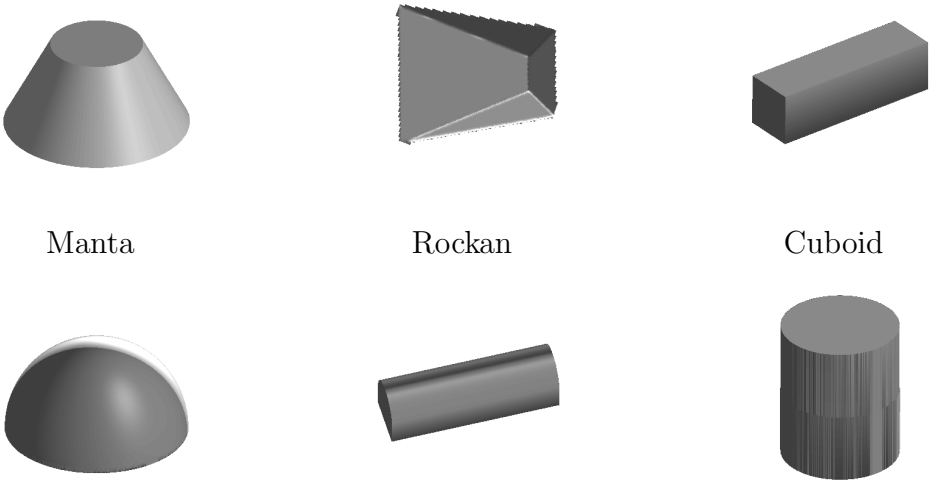

Figure 3.9: 3D models of the different targets and mine-like objects.

Non-mine targets can also be generated by varying parameters in this module. Several are used to test the algorithms with the results presented in Section 3.4.1.2.

3.2.2.3 Sonar Image Generator

The sonar module computes the sidescan image from a given 3D environment. The simulator is ray-tracing based and basically solves each parameter of the sonar equation that we described in detail in chapter 2 to compute the excess level (*i.e.* the backscattering energy) XS in Eq. (3.5). Because Eq. (3.5) is an energetic equation, phenomena such as multipaths are not taken into account. For a monostatic sonar system, the sound propagation can be expressed from an energetic point of view as:

$$XS = SL - 2TL + TS + DI - NL - RL \tag{3.5}$$

All the parameters are measured in decibels (dB) relative to the standard reference intensity of a 1 μPa plane wave. Values for the Source Level SL can be found in Table 2.1. The computation of the Transmission Loss TL, the Reverberation

Level RL and the Noise Level NL is done using respectively Eq. (2.13), Eq. (2.32) and Eq. (2.35). The Directivity Index DI is associated with directionality of the transducer system and computed using the beam pattern of a long rectangular array as described in Eq. (2.36). In our model, the targets form part of the 3D environment. The Target Scattering Strength TS is computed using a Lambertian model. The reflectance factor in the Lambertian law is associated to the acoustic impedance. The simulator takes into account the acoustic impedance of the target given by $Z = \rho.c_l$, where ρ is the density of the material, and c_l the longitudinal sound speed in the material.

The trajectory of the sonar platform is tuneable (as shown in Figure 3.10). This allows multiview sidescan images of the same environment. Figure 3.11 displays sonar images of the same scene with two different angles of view. Further examples of typical images obtained for the various types of seabed are shown in Figure 3.12. Note that if the sonar range exceed the dimension of the digital terrain the XS is set to zero (black in figures 3.10 and 3.11(*bottom*)).

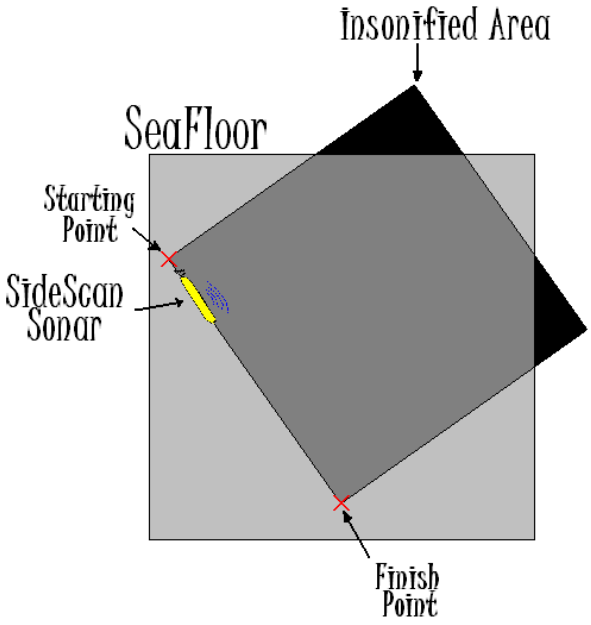

Figure 3.10: Plan view of the trajectory of the sonar platform can be placed into the 3D environment.

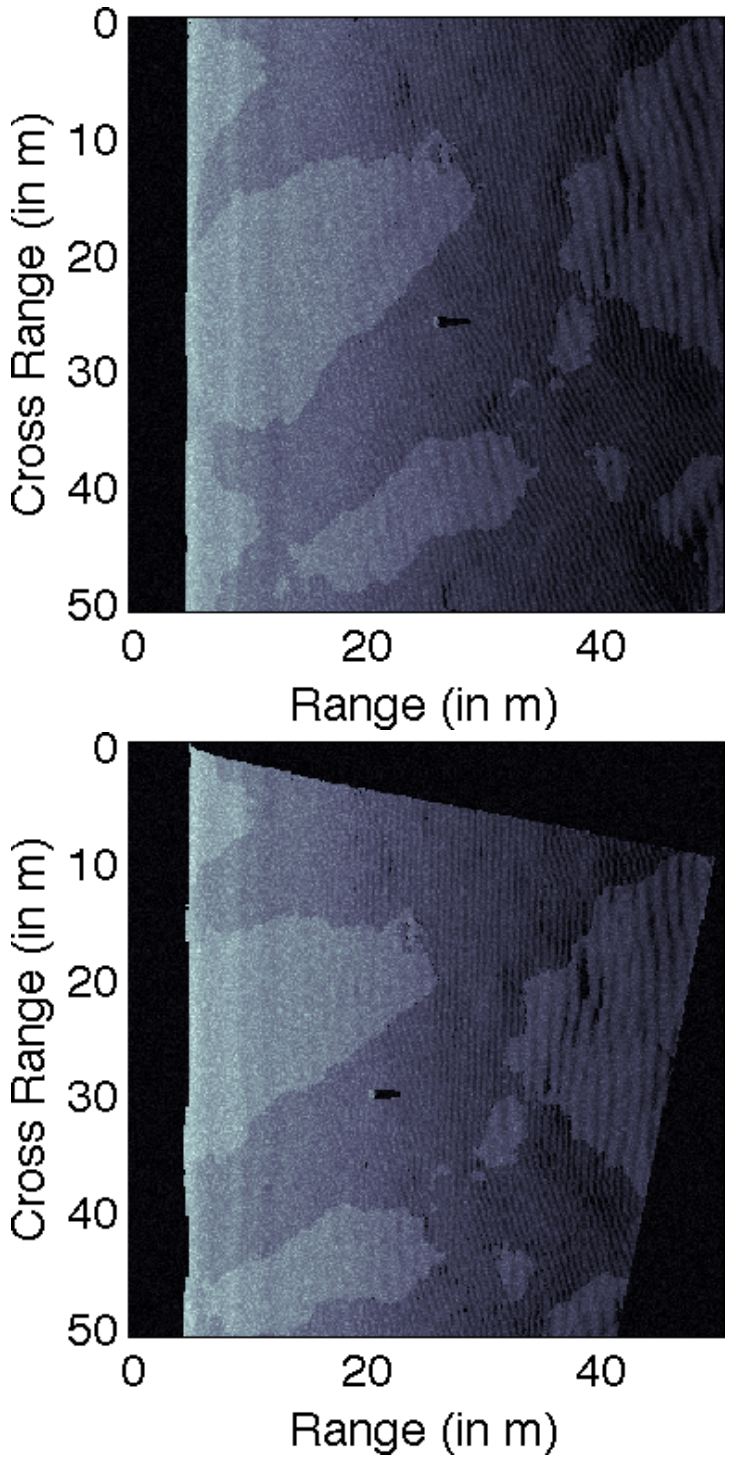

Figure 3.11: Display of the resulting sidescan images of the same scene with different trajectory. The seafloor is composed with two sand ripples phenomena at different frequencies and different sediments (VeryFineSand for the high frequency ripples and VeryCoarseSand for the low frequency ripples). A manta object has been put in the centre of the map.

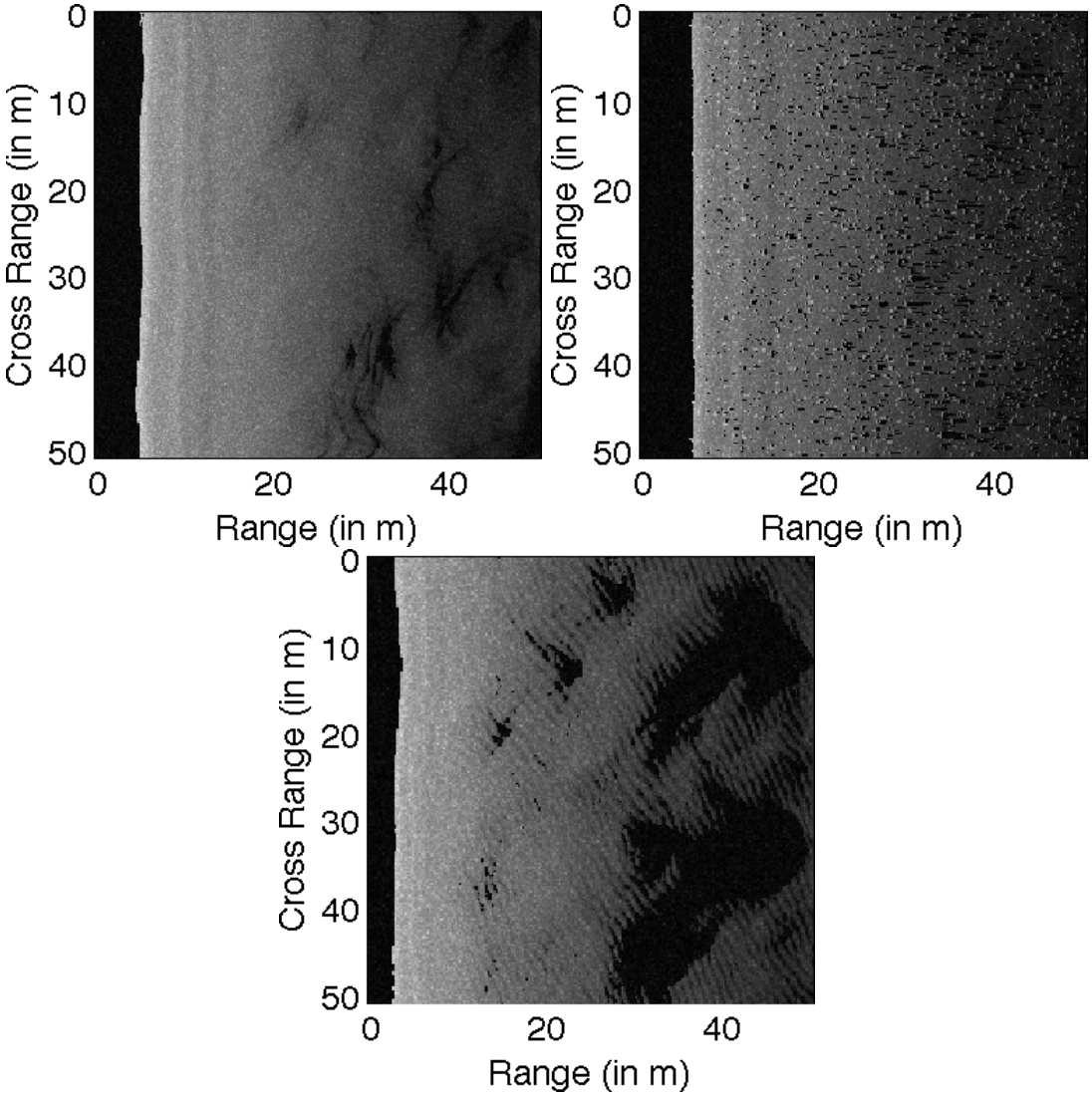

Figure 3.12: Examples of simulated sonar images for different seabed types (clutter, flat, ripples), 3D elevation and scattering strength. (a) represents a smooth seabed with some small variations, (b) represents a mixture of flat and cluttered seabed and (c) represents a rippled seabed

3.3 Application: the ATR problem

3.3.1 ATR problem in sonar images

Automatic target recognition (ATR) in sonar imagery has long been an active research area in the maritime domain. Recently, however, it has received increased attention, in part due to the development of new generations of sensors with increased resolution and in part due to the emergence of new threats to critical maritime assets and a new paradigm for target recognition based on autonomous platforms. The recent introduction of operational Synthetic Aperture Sonar (SAS) systems (Belletini and Pinto [2009]; Ferguson and Wyber [2009]) and the development of ultra high resolution acoustic cameras (Belcher et al. [1999]) have increased tenfold the resolution of the images available for target recognition as demonstrated in Figure 3.13. In parallel, traditional dedicated ships are being replaced by small, low cost, autonomous platforms easily deployable by any vessel of opportunity. This creates new sensing and processing challenges, as the classification algorithms need to be fully automatic and run in real time on the platforms. The platforms' behaviours also require to be autonomously adapted online, to guarantee appropriate detection performance is met, sometimes on very challenging terrains. This creates a direct link between sensing and mission planning, sometimes called active perception, where the data acquisition is directly controlled by the scene interpretation.

Detection and identification techniques have tended to focus on saliency such as global rarity or local contrast (Calder et al. [1997]; Goldman and Cohen [2005]; Maussang et al. [2007]), model based detection (Balasubramanian and Stevenson [2001]; Calder [1997]; Calder et al. [1998]; Dobeck et al. [1997]; Dura et al. [2008]; Mignotte et al. [2000]; Quidu et al. [2000a]; Reed et al. [2004a,b]) or supervised learning (Azimi-Sadjadi et al. [2001]; Ciany and Huang [2000]; Ciany and Zurawski [2001]; Fawcett [2001]; Perry [2001]; Quidu et al. [2000b]; Zerr et al. [2001]). Alternative approaches to investigate the internal structure of objects using wide-band acoustics (Capus et al. [2007]; Pailhas et al. [2010]) are showing some promises, but it is now widely acknowledged that current techniques are reaching their limits. Yet, their performance does not enable rapid and effective

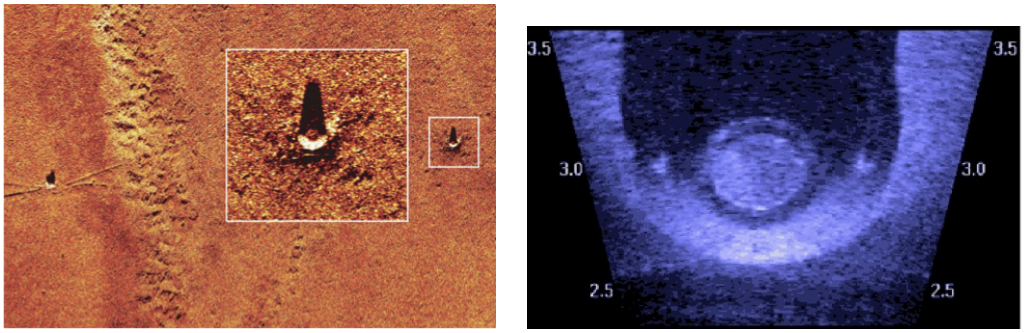

(a) (b)

Figure 3.13: Example of Target in Synthetic Aperture Sonar (a) and Acoustic Camera (b). Images are courtesy of the NATO Undersea Research Centre (a) and Soundmetrics Ltd (b).

mine clearance and false alarm rates remain prohibitively high (cf. Azimi-Sadjadi et al. [2001]; Balasubramanian and Stevenson [2001]; Calder [1997]; Calder et al. [1997, 1998]; Ciany and Huang [2000]; Ciany and Zurawski [2001]; Dobeck et al. [1997]; Dura et al. [2008]; Fawcett [2001]; Goldman and Cohen [2005]; Maussang et al. [2007]; Mignotte et al. [2000]; Perry [2001]; Quidu et al. [2000a,b]; Reed et al. [2004a,b]; Zerr et al. [2001]). This is not a critical problem when operators can validate the outputs of the algorithms directly, as they still enable a very high data compression rate by dramatically reducing the amount of information that an operator has to review. The increasing use of autonomous platforms raises fundamentally different challenges. Underwater communication is very poor due to the very low bandwidth of the medium (the data transfer rate is typically around 300 bits/s) and it does not permit online operator visualisation or intervention. For this reason the use of collaborating multiple platforms requires robust and accurate on-board decision making.

In order to improve the ATR performances, the MCM (Mine and Counter Measures) community has focused on improving the resolution of the sensors and high resolution sonars are now a reality. The counterpart is that these sensors are very expensive and very limited data (if any) are available to the research community. New high resolution sonars such as SAS produce images which get

closer to traditional optical imagery. This is also opening a new era of algorithm development for acoustics, as techniques recently developed in computer vision become more applicable. For example, the SAS system developed by NURC (MUSCLE) can achieve a 5 to 3 cm pixel resolution, almost independent of range. Thanks to this resolution, direct analysis of the target echo rather than traditional techniques based on its shadow become possible.

3.3.2 Highlight-based classifier using PCA

The algorithm presented here for classification is based on the eigenfaces algorithm. The PCA based eigenfaces approach has been used for face recognition purposes (Kamran and Chellappa [1997]; Sirovich and Kirby [1987]) and is still close to the state of the art for this application (cf. Wright et al. [2009]).

Assuming the training set is composed of k images of a target. Each target image M_i is an $n \times m$ matrix. The M_i are converted into vectors $\tilde{M}_i$ of dimension $1 \times n.m$. A mean image of the target is computed using Eq. (3.6).

$$M_{\text{mean}} = \frac{1}{k} \sum_{i=1}^{k} \tilde{M}_i \tag{3.6}$$

The training vectors $\tilde{M}_i$ are centred and normalized according to Eq. (3.7). In the training set, the target is selected from various ranges (from 5m to 50 m from the sonar). The contrast and illumination change drastically through the training set. The normalization by the standard deviation of the image reduces this effect. Let std $\tilde{M}_i$ be the standard deviation of $\tilde{M}_i$.

$$T_i = \frac{\tilde{M}_i - M_{\text{mean}}}{\text{std } \tilde{M}_i} \tag{3.7}$$

Let $T = [T_i]$ be the preprocessing training set of dimension $k \times n.m$. The covariance matrix $\Omega = T.T^T$ is calculated. The p largest eigenvalues of Ω are computed, and the p corresponding eigenvectors form the decomposition base of

the target. The subspace Θ_{target} formed by the p eigenvectors is called target space. The number p has been chosen such as the projection of the target into Θ_{target} represents in average more than 95% of the signal.

The classifier projects the test target image I_n to each target space. We denote $P_{\Theta_{\text{target}}}(I_n)$ the projection of I_n in the target space Θ_{target}. The estimated target $\hat{T}_n$ is the target corresponding to the minimum distance between I_n and $P_{\Theta_{\text{target}}}(I_n)$ as expressed in Eq. (3.8).

$$\hat{T}_n = \min_{\text{target}} \parallel I_n - P_{\Theta_{\text{target}}}(I_n) \parallel \tag{3.8}$$

$P_{\Theta_{\text{target}}}(I_n)$ with the minimum distance represents the most compact space which represents the object under inspection.

3.4 Results

In previous works (Dura et al. [2008]; Myers [2001]; Reed et al. [2003a]; Zerr et al. [2001]), target classification algorithms using standard sidescan sonars have mainly been based on the analysis of the targets' shadows. With high resolution sonars, we note that more information should be exploitable from the target's highlight. In this section, we investigate the resolution needed for the PCA image-based classifier described in section 3.3.2 to classify using only the information carried by the highlight.

The sidescan simulator presented in section 3.2.2 will provide synthetic data in order to train and to test the PCA image-based classifier. All the sidescan images are generated with a randomly selected seafloor (from flat seabed, ripples and cluster environment), random sonar altitude (from 2 to 10 metres altitude) and random range for the targets (from 5 to 50 metres range).

For each experiment, two separate sets of sonar images have been computed, one specifically for training (in order to compute the target space Θ_{target}) and one

specifically for testing. At each sonar resolution and for each target, 80 synthetic target images at random ranges, random altitude and with a randomly selected seafloor have been used for training. A larger set of 40000 synthetic target images are used to test the classifier. The classifier is trained and tested according to the algorithm described in section 3.3.2.

3.4.1 What precision is needed?

The question of resolution has been raised again by the advent of very high resolution sidescan, forward-look and SAS systems. These change the quality of the images markedly producing near-optical images. In this section we investigate whether the resolution is now high enough to apply optical image processing techniques to take advantage of advances made in other fields.

The limitations of current sidescan technology are highlighted in figure 3.14. It would seem from this figure that only SAS systems can give large area coverage and still give high resolution needed for identification. However the boundaries drawn between detection and identification are more the results of general wisdom than solid scientific evidence.

Identifying the resolution required to perform target classification is not a simple problem. In sonar, this has been attempted by various authors: Florin et al. [2003]; Kessel [2002]; Myers and Pinto [2007]; Pinto [1997], generally looking at the minimum resolution required to distinguish a sphere from a cube and using information theory approaches. These techniques provide a lower bound on the minimum resolution required but tend to be over optimistic. We focus here on modern subspace algorithms (described in section 3.3.2) as a mechanism to analyze the resolution needs for classification. Why focus on such techniques? The main reason is that they are very versatile and have been applied successfully to a variety of classical target identification problems. This has been demonstrated recently on face recognition in Wright et al. [2009] and land-based object detection problems (Nayak et al. [2008]).

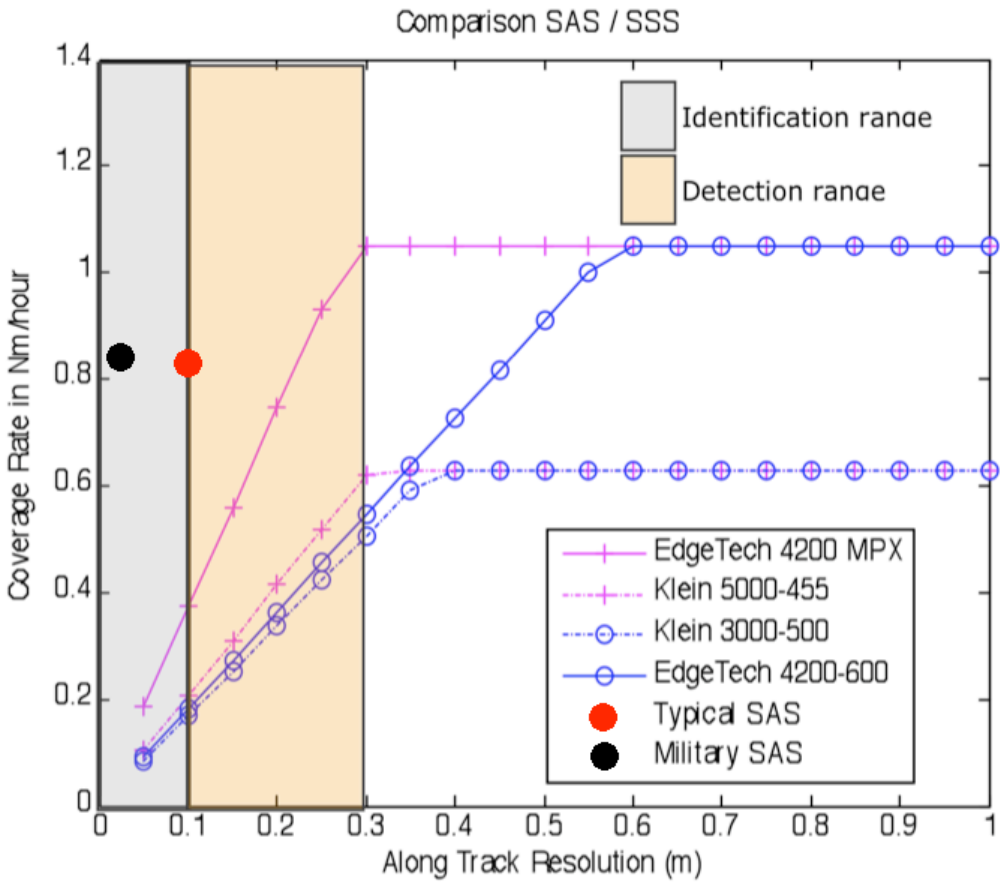

Figure 3.14: Ability to detect and identify targets as a function of resolution and coverage rate (Nm/h: nautical mile per hour) for the best side-scan and synthetic aperture sonars. The SAS sonars here are a typical 100 - 300 kHz sonar in optimal conditions for synthetic aperture.

3.4.1.1 Identification

In this first experiment the PCA classifier is trained for identification. Assuming a mine-like object has been detected and classified as a mine, the algorithm identifies the kind of mine the target is. Four targets have been chosen: a Manta mine (truncated cone with dimensions 98 cm lower diameter; 49 cm upper diameter; 47 cm height), a Rockan mine (L×W×H: 100 cm × 50 cm × 40 cm), a cuboid with dimensions 100 cm × 30 cm × 30 cm and a cylinder 100 cm long and 30 cm in diameter. Figure 3.15 displays snapshots of the four different targets for a 5 cm sonar resolution.

The pixel resolution is tunable in the simulator. Sidescan simulation/classification processes have been run for 15 different pixel resolutions from 3 cm (high resolution sonar) to 30 cm (low resolution sonar) covering the detection and classification range of side looking sonars. Figure 3.16 displays the misidentification % of the four targets against the pixel resolution.

As expected, the image-based classifier fails at low resolutions. Between 15 and 20 cm resolution, which corresponds to the majority of standard sonar systems, classification based on the highlights is poor (between 50% and 80% correct classification). The results stabilize at around 5 cm resolution to reach around 95% correct classification.

In previous work involving face recognition, it has been shown that PCA techniques are not very robust to rotation (Turk and Pentland [1991]). The algorithm can be optimized using multiple subspaces for each non-symmetric target, each of the subspaces covering a limited angular range.

3.4.1.2 Classification

Here we extend the PCA classifier for underwater object classification purposes. A larger set of seven targets have been chosen with three mine-like objects: the Manta, the Rockan, a cylinder 100 cm long and 30 cm diameter and four non-mine objects: a cuboid with dimension 100 cm × 50 cm × 40 cm, two hemispheres

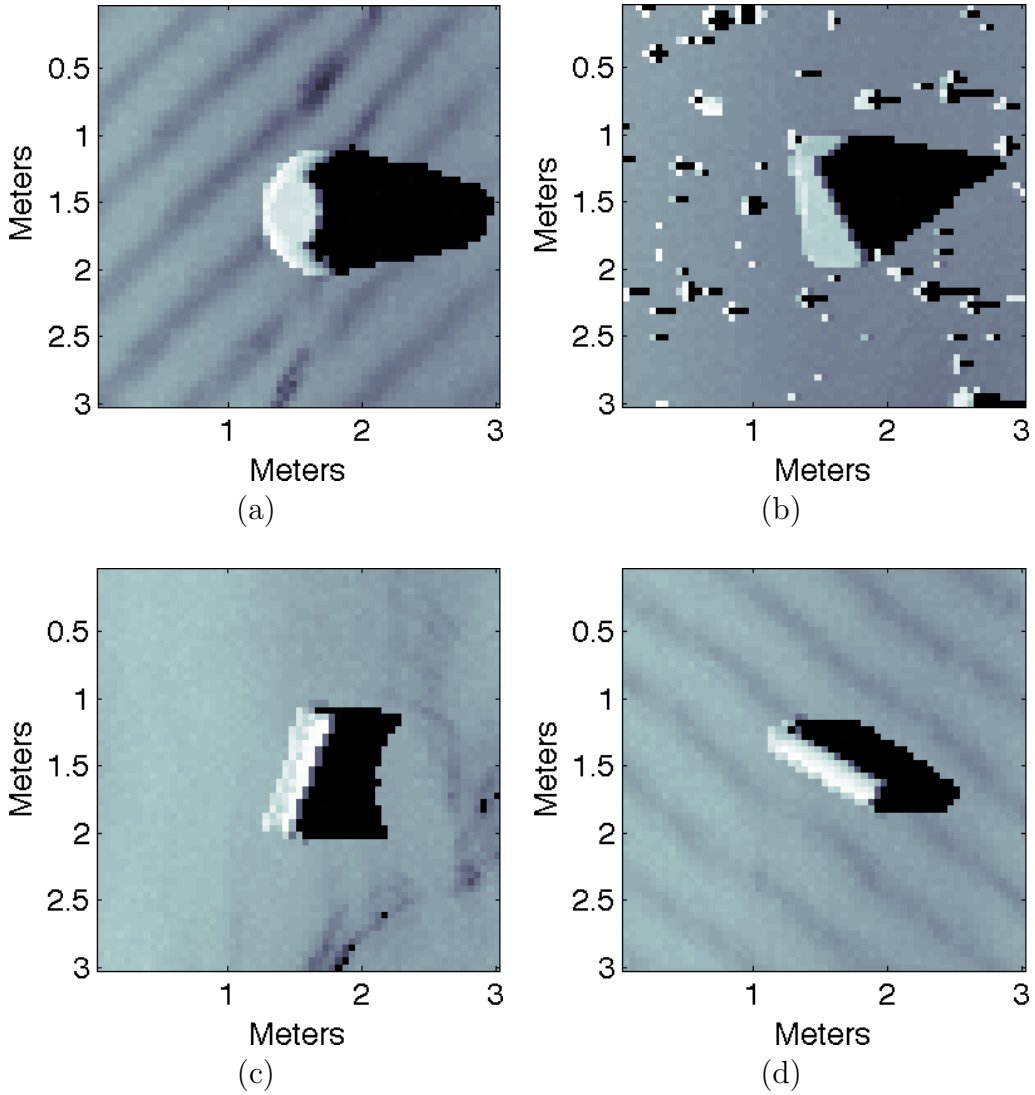

Figure 3.15: Snapshot of the four targets. (a) Manta, on sand ripples, (b) Rockan on cluttered environment, (c) Cuboid on flat seabed, (d) Cylinder on sand ripples. The pixel size in these targets images is 5 cm.

with diameters respectively 100 cm and 50 cm and a box with dimension 70 cm $\times$ 70 cm $\times$ 40 cm. Note that the non-mine targets have been chosen such as the dimension of the big hemisphere matches with the dimension of the Manta, and the dimension of the box matches with the dimension of the Rockan. Figure 3.17 provides snapshots of the different targets.

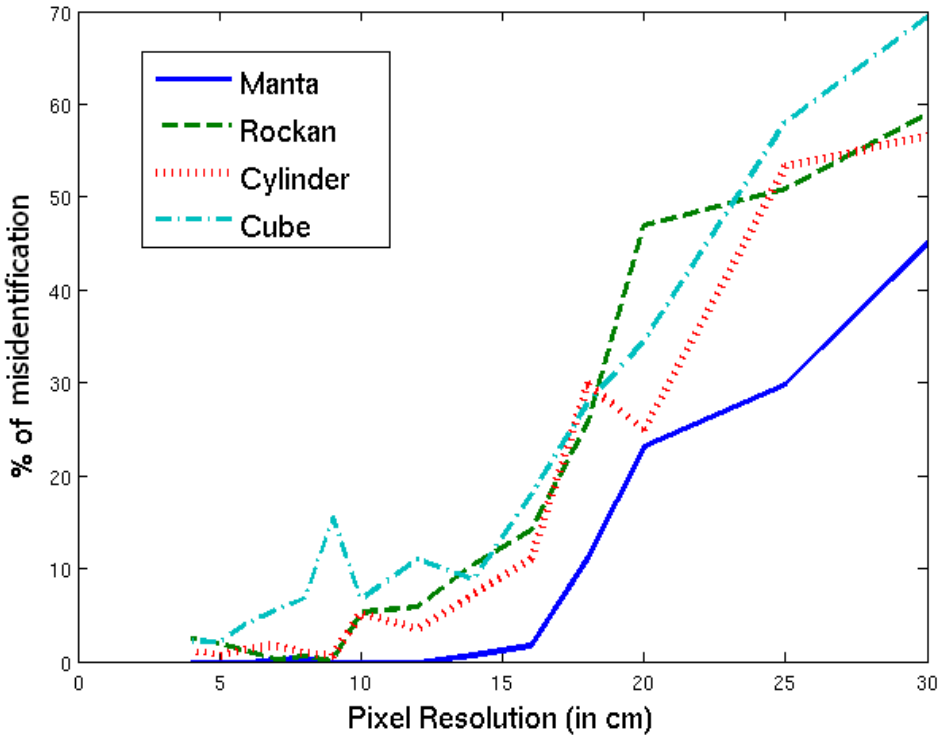

Figure 3.16: Misidentification of the four targets as a function of the pixel resolution. This is considering the highlight of the targets.

As described in section 3.4.1.1, two data sets for training and testing have been produced. The target classification relies on two steps: at first the target is identify following the same process as section 3.4.1.1 and then classified into two classes $mine - like$ and $non - mine$ Figure 3.18*(top)* displays the results of the identification step. the curves of misidentification for each target follow the general pattern described earlier in section 3.4.1.1 with a low misidentification (below 5%) for a pixel resolution lower than 5 cm. In figure 3.18*(bottom)*, the results of the classification between $mine - like$ and $non - mine$ is showed. Contrary to the identification process, the classification curves stabilise at higher pixel resolution (around 10 cm) to 2-3% misclassification.

In these examples we show that the identification task needs a higher pixel resolution that the classification task to match the same performance of 95%

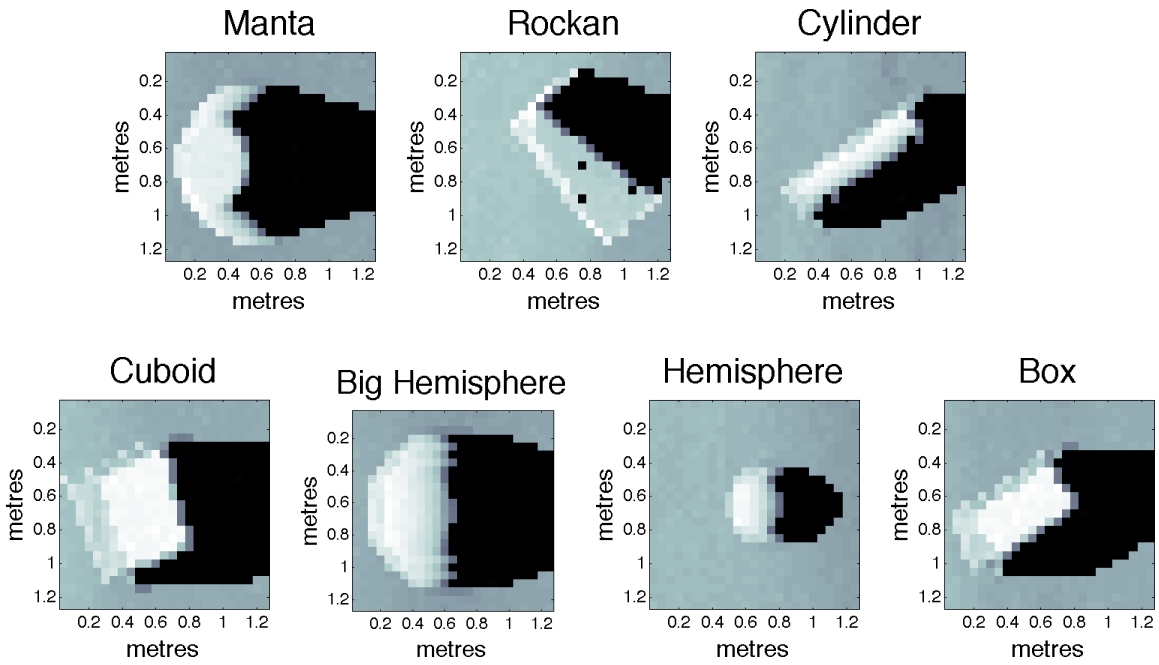

Figure 3.17: Snapshot of the targets used for classification. On the first line, the mine-like targets with the Manta, the Rockan and the cylinder. On the second line, the non-mine targets with the cube, the two hemispheres, and the box shape target. The pixel size in these targets images is 5 cm

correct identification/classification.

3.4.2 Identification with shadow

As mentioned earlier, current sidescan ATR algorithms depend strongly on the target shadow for detection and classification. The usual assumption made is: *at low resolution the information relative to the target is mostly contained in its shadow*. In this section we aim to confirm this statement by using the classifier described in 3.3.2 directly on the target shadows. We study here the quantity of information contained into the shape of the shadow, and how this information is retrievable depending on the pixel resolution.

Shadows are the result of the directional acoustic illumination of a 3D target. They are therefore range dependent. For the purposes of this experiment, in order to remove the effect of the range dependence of the shadows, the targets

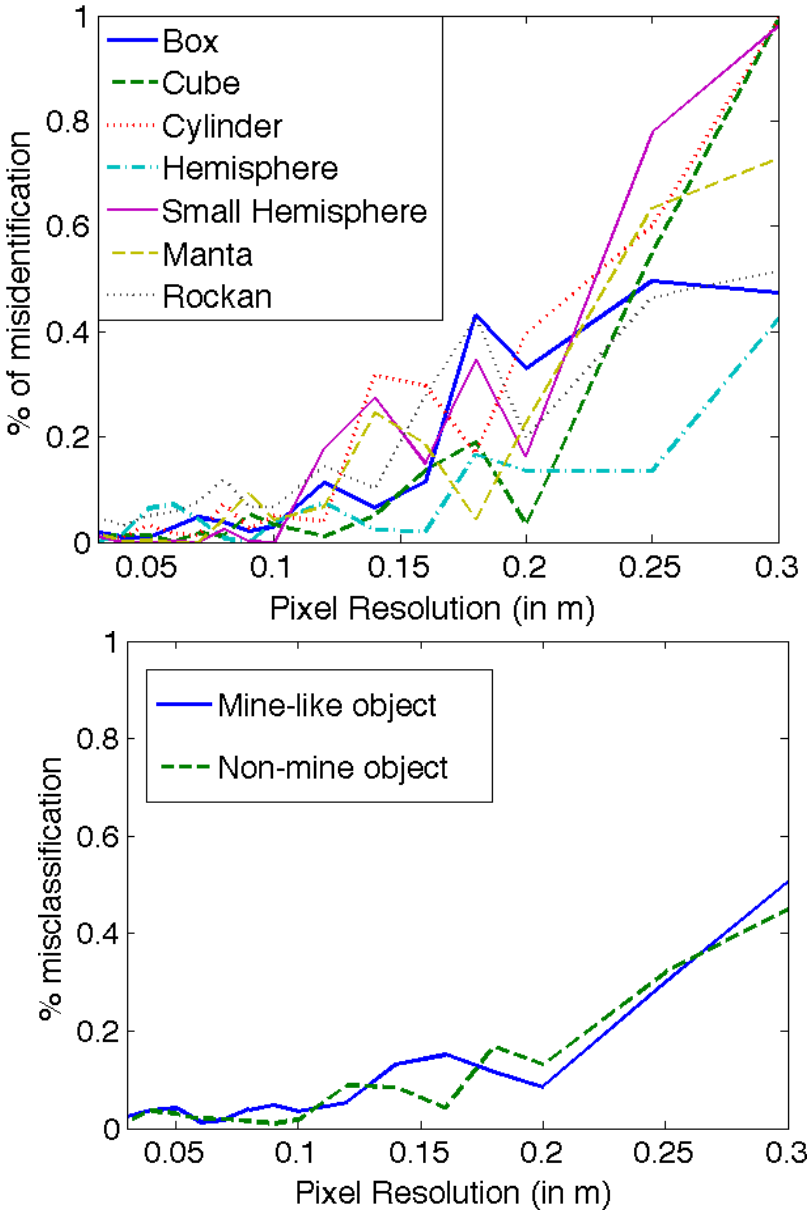

Figure 3.18: *(top)* Misidentification of the seven targets as a function of the pixel resolution. *(bottom)* Misclassification of the target as function of the pixel resolution.

are positioned at a fixed range of 25 m from the sensor. Image segments containing the target shadows are extracted from the data. Figure 3.19 displays snapshots of target shadows with different orientations and backgrounds for a 5 cm pixel

resolution. We process the target shadow images in exactly in the same way as we did for the target highlight images in the previous sections. For each sonar resolution, 80 target shadows per object are used for training the classifier, and a set of 40000 shadow images is used for testing.

Figure 3.19: Snapshot of the shadow of the four targets (from left to right: Manta, Rockan, Cube and Cylinder) to classify with different orientations and backgrounds. The pixel size is these target images is 5 cm. The size of each snapshot is 1.25 m $\times$ 2.75 m.

In total 15 training/classification simulations have been performed for 15 sonar pixel resolutions (from 5 cm to 30 cm). Figure 3.20 shows the percentage of misclassification versus the pixel resolution for various target types.

Concerning the Cylinder and Cuboid targets, their shadows are very similar due the similar geometry. In Figure 3.19 it is almost impossible to distinguish visually between the two objects looking only at their shadows. In broadside for example, the two shadows have exactly the same rectangular shape, explaining why the confusion between these two objects is high.

For the Manta and Rockan targets, the misidentification curves stabilize near 0 % misidentification below 20 cm sonar resolution. Therefore, for standard sidescan

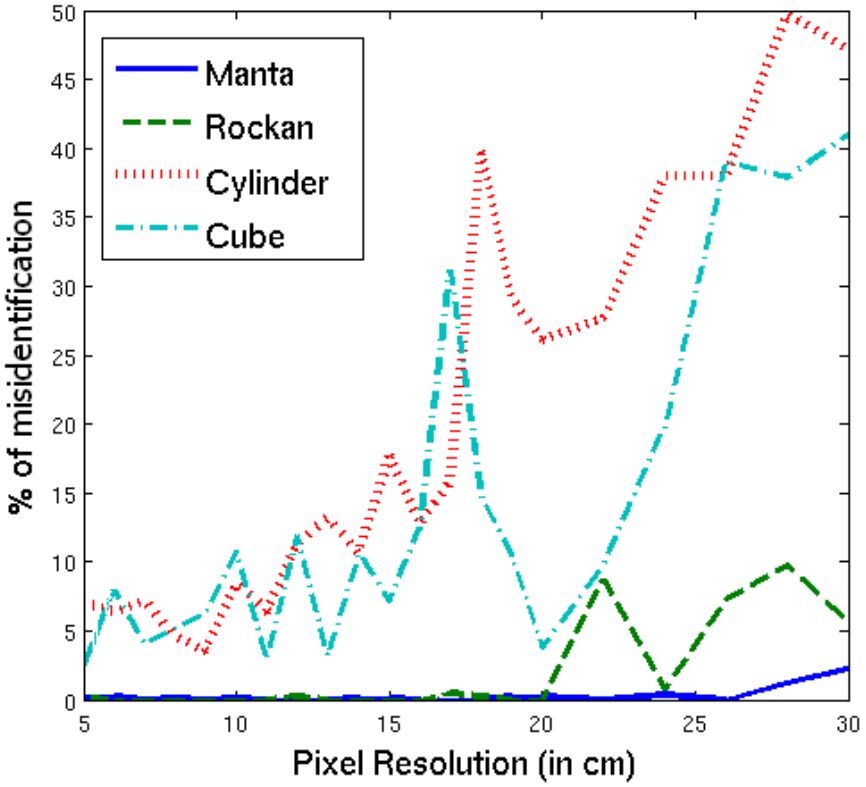

Figure 3.20: Percentage of misidentification versus the pixel resolution for various target types. This considers the shadow of the target and not its echo.

systems with a resolution in the 10 - 30 cm range, the target information can be extracted from the shadow with an excellent probability of correct identification. In comparison, correct identification using the target highlights at 20 cm resolution is about 50% (cf. Figure 3.16)

3.5 Conclusions

Sidescan sonar is now a mature technology, and despite its limitations it still offers a cheap and convenient sensor for seabed survey. The results of section 3.4.2 processing shadow images back up the widely accepted idea that identification from current sonars at 10 - 20 cm resolution is reaching its performance limit.

The advent of much higher resolution sonars has now made it possible to bring in and apply techniques new to the field from optical image processing. The PCA analyses presented here, operating on highlights as opposed solely to shadow, show that these can give a significant improvement in target identification and classification performance opening the way for reinvigorated efforts in this area. From an ATR point of view, we have indeed demonstrated that as the sonar resolution increases the information level contained in the shadow stagnates below 10 - 15 cm and that the information level contained in the highlight becomes extractable below 5 cm resolution. New advanced target identification techniques will emerge with the new generation very high resolution sonar systems such as SAS (which is the subject of the next chapter) and acoustic cameras.

Chapter 4

Synthetic Aperture Sonar

4.1 Introduction

In chapter 3 we emphasised the importance of the resolution in sonar images in order to properly extract significant and meaningful information from them. Considering the problem of automatic target recognition in the context of MCM, we determined the sonar image resolution has to be on the order of few centimetres. For this reason, the MCM community has put a lot of effort in improving imaging systems specially in high frequency sonar.

The last generation of sonar, SAS (Synthetic Aperture Sonar) systems, have been developed in the last 15 years embracing this vision. The centrimetric resolution of SAS systems provides a new powerful tool for mine detection, identification and classification. The main advantages of SAS systems are: a resolution close to the wavelength even at long range and a constant resolution across range. A high frequency SAS system has been developed at NURC (Belletini and Pinto [2009]; Pinto [2006]; Pinto and Bellettini [2007]), the MUSCLE vehicle (300kHz centre frequency) but despite the extremely good quality of the SAS images, ambiguities between mine-like objects cannot always be overcome.

In this chapter we investigate low frequency SAS systems (LF-SAS) in order to address the two main limitations of the present systems linked essentially to the sound absorption at high frequencies: providing imagery inside the target and

detecting buried targets. Synthetic SAS images have been generated and studied in order to demonstrate the capability of LF-SAS to provide information of the inside of targets. We demonstrate that the inner resonances of objects are visible and exploitable in these LF-SAS images. Most of the time the reverberation level (RL) of the seafloor is the main limitation factor in sonar images. In order to take into account the RL limitation and buried targets, we have introduced the seafloor boundary into the problem. The backscattering echo can be computed thanks to an approximation of the Helmholtz-Kirchhoff equation. The synthetic SAS images have been compared to real SAS images produced in the HWU (Heriot-Watt University) test tank.

4.2 SAS Principles

SAS stands for Synthetic Aperture Sonar and has been developed over the last 15 years. It inherits the technologies developed for SAR (Synthetic Aperture Radar) over the last 40 years (Tomiyasu [1978]). The main idea relies on the fact that for a standard sidescan sonar the along track (cross range), resolution is the ratio between the acoustic wavelength and the length of the antenna. In order to increase the resolution in cross range typical sidescan manufacturers have chosen to work at higher frequencies despite the increased sound attenuation in water at high frequency.

The principle of SAR/SAS is to artificially increase the length of the antenna thanks to the synthetic aperture antenna algorithm in order to increase the cross range resolution. Contrary to sidescan systems where the horizontal beampattern aperture is as narrow as possible to improve the cross-range resolution, SAS systems use a wide beampattern. Every point in the seabed is then seen several times. The synthetic aperture algorithm fuses these multi-views coherently. The synthetic aperture algorithm is explained in more details in section 4.2.1. SAS systems use broadband pulses (essentially chirps) in order to increase the range resolution.

SAS was seen at its beginning as the *"little sister"* of SAR (Cutrona [1975, 1977]). But due to the challenges encountered in order for SAS systems to work properly, SAS has become a subject and a community in itself. The two main unique challenges that the SAS community has to solve are: the relatively slow velocity of the sound speed in water (around 1500 m.s^{-1}) compared to the speed of light (around 3.10^8 m.s^{-1}) and the uncertainty on the underwater navigation.

The relative slow speed of sound in water jeopardises the formation of a synthetic coherent aperture antenna. Assuming for example a SAS system with a central frequency of 300 kHz mounted on a vehicle flying at 3 knots, assuming that the maximum range is 200 m, during the time for the sound to travel back and forward the maximum range, the SAS system will have moved of 40 cm, which is way above the traditional $\lambda/2 = 2.5$ mm that beam forming required. The under-sampling along the cross-range has been first solved in Huxtable and Geyer [1993] by using a single transmitter and a coherent array of receivers. In order to form the synthetic aperture antennas, consecutive sub-antenna (determined by the ping rate) have to overlap.

The second challenge that the SAS community had to overcome is related to the uncertainty of the navigation. As we will see in section 4.2.1, the image formation is performed coherently meaning that the relative position of the SAS during the synthetic aperture has to be known with a precision lower than the wavelength (typically few millimetres). The estimation of the trajectory is done in two steps: a gross estimate is first given by the navigation sensors typically combining INS (inertial navigation systems) with DVL (Doppler velocity logs). A finer estimate is then computed using autofocus algorithms (Belletini and Pinto [2002]; Lurton [2000]).

4.2.1 SAS image formation

From the raw SAS data, two compression algorithms are performed to obtain the SAS image. Let $s(t, u)$ be the raw signal. t representing the time, and u the along track parameter. The first compression takes advantage of the broadband

pulse used by SAS systems. This compression is a range compression and is computed through matched filtering of the echo (see Eq. (4.1)).

$$s_M(t,u) = s(t,u) * p^*(-t) \tag{4.1}$$

where $p(t)$ represent the SAS broadband pulse. Note that the incoming pulse is usually a chirp, which maximizes the achievable compression by matched filtering (cf. Turin [1960]).

Several algorithms can be used to obtain the cross-range resolution. We will be using the backpropagation algorithm as explained in Seydel [1982]. Each pixel (x,y) in the resulting SAS image is computed using to Eq. (4.2)

$$f(x,y) = \int_u s_M \left[t, \frac{\sqrt{x^2 + (y-u)^2}}{c} \right] \mathrm{d}u \tag{4.2}$$

where c represents the speed of sound in water and s_M is the matched filter echo obtained in Eq. (4.1). This compression technique takes advantage of the wide beamwidth of SAS system. A single scatterer is represented in the raw SAS image as a parabola assuming the SAS system flies along a linear track. The backpropagation algorithm sums coherently all the contributions of the scatterer along this parabola.

A SAS system has been developed at NURC called MUSCLE. This SAS operates at a central frequency of 300 kHz with around 60 kHz bandwidth. The beamwidth is 7°. The system gives a range of 2 × 200 m with a fixed precision of around 3 cm. Figure 4.1 displays a picture of the NURC SAS system MUSCLE and an example of a MUSCLE SAS image.

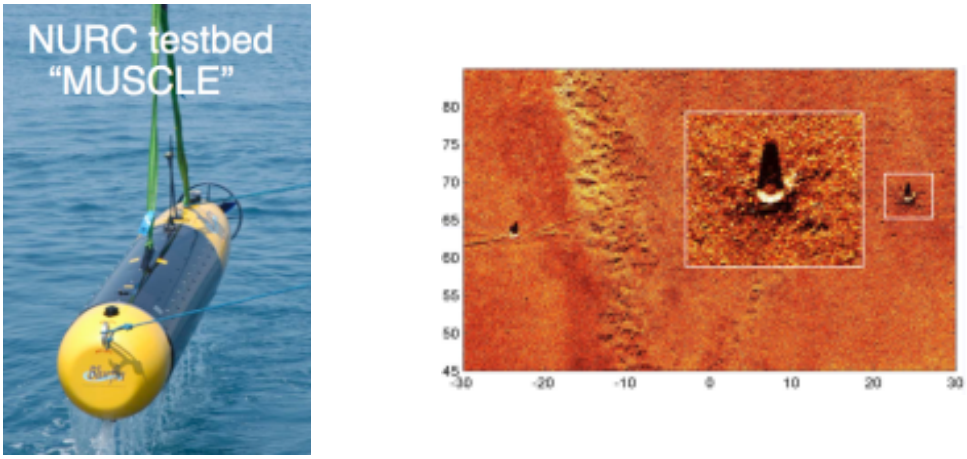

Figure 4.1: (*left*) MUSCLE NURC SAS mounted on the Bluefin. (*right*) MUSCLE SAS image of a mine-like object at 65 m range.

4.2.2 Why a low frequency SAS system?

The images produced by high frequency SAS such as the NURC-MUSCLE are able to provide a centimetric resolution over a range of 200 m. The quality of these images visually are close to optical images which allows difficult tasks such as identification and classification (Courmontagne [2008]; Jonsson et al. [2005]; Matthews et al. [2006]; Pinto et al. [2002]). Despite the extremely good quality images provided by high frequency SAS, ambiguity between objects can still exist in certain cases. In the context of MCM (Mine Counter Measure), even with high frequency high resolution systems distinctions between a sea-mine and a rock can be sometimes difficult. Working with low frequency will inevitably lead to a decrease in resolution, but on another hand, low frequencies suffer less absorption. By studying a low frequency SAS system, we aim for two main goals:

- produce an internal image of the target
- detect buried targets

The LF-SAS studied in the next sections have the following characteristics:

- Bandwidth: 5 - 50 kHz
- Beamwidth: 90°

According to the RST (resonance scattering theory) Gaunaurd and Strifors [1993]; Gaunaurd and Uberall [1983]; Hasan and Azimi-Sadjadi [1996], the inner resonances of an object are strong when the factor $k.a$ is between 1 and 60. $k = \frac{2\pi f}{c}$ represents the wavelength, and a represents a characteristic dimension of the object (example: the diameter in the case of a sphere). In our case, we are interested in mine-like objects with a dimension of around 50 cm. The factor $k.a$ of these targets using the LF-SAS frequency band will be included between 10 and 100. We expect strong characteristic resonances.

4.3 Synthetic SAS Images of Simple Targets

In this section, we explain how to produce synthetic SAS images of simple targets. Analytical solutions for the back-scattering problem are typically not available due to the complexity of the sound propagation equations. The problem has been solved only for simple geometrical shaped objects such as spheres (Goodman and Stern [1962]) or cylinders (Doolittle and Uberall [1966]). In this section we will extend the theory of spherical shell to multi-layer spheres, compute synthetic SAS images and compare LF-SAS images with HF-SAS images. Old sea mines can often be modelled using a concentric sphere structure. Figure 4.2 displays a picture of old MK 14 british sea mine.

Figure 4.2: MK 14 sea mine. (*Courtesy to Oxyman*)

4.3.1 Scattering theory of concentric spheres

Faran [1951] proposed an analytical solution for solid sphere echo. Next Goodman and Stern [1962] extend the solution to the spherical shell problem. In this section we extend the results of Goodman to the multi-layer sphere problem.

4.3.1.1 Incoming pulse: Spherical wave & plane wave

We consider a multi-layered sphere in free water. Each layer can be solid or fluid. The spherical coordinates are a natural choice here. In order to solve the problem, a modal decomposition of the parameters such as pressure or displacement is necessary. The modal decomposition is achieved thanks to the Jacobi-Anger expansion of the exponential function (cf. Abramowitz and Stegun [1965]). Note that in all the equations, the term $\exp(i\omega t)$ is ignored.

The co-centrical spheres are centered at the origin. We consider a source point situated at a distance r_0 of the sphere, coordinates $(r_0, \pi, 0)$. The pressure p_i induced by the source at any point (r, θ, ϕ) outside the target can be computed thanks to Eq. (4.3):

$$\begin{aligned} p_i &= P_0 \exp(i.k.D)/D \quad \text{with } D = r_0^2 + r^2 + 2rr_0\cos\theta \\ &= ikP_0 \sum_{n=0}^{+\infty}(2n+1)(-1)^n P_n(\cos\theta) j_n(k.r) h_n(k.r_0) \end{aligned} \tag{4.3}$$

where P_0 is the amplitude of the pulse at the emission point, P_n the Legendre polynomial, j_n the spherical Bessel function of the first kind, and h_n the spherical Hankel function.

At long range (above 30 m) and for a target of 50 cm, we can assume a plane wave hypothesis. In this case, Eq. (4.3) becomes:

$$\begin{aligned} p_i &= P_0 \ \exp(ikr\cos\theta) \\ &= P_0 \sum_{n=0}^{+\infty}(2n+1) i^n P_n(\cos\theta) j_n(k.r) \end{aligned} \tag{4.4}$$

The total pressure p in the free water space is the sum of the incoming wave p_i coming from the source and the scattering echo p_s from the object. It can be

written as:

$$p = p_i + p_s \tag{4.5}$$

4.3.1.2 Wave equations

The main equation to solve is the wave propagation equation of the displacement $\vec{u^n}$ (for each layer n). It can written as follows:

$$(\lambda_n + 2\mu_n)\vec{\nabla}.\vec{\nabla}.\vec{u^n} - 2\mu_n\vec{\nabla} \times \vec{\nabla} \times \vec{u^n} = \rho_n \frac{\partial^2 \vec{u^n}}{\partial t^2} \tag{4.6}$$

λ_n and μ_n represent the Lamé parameters, and ρ_n is the material density for the layer n. By taking the divergence of Eq. (4.6), we arrive to:

$$\vec{\nabla}^2 \left(\vec{\nabla}.\vec{u}\right) = \frac{\rho_n}{\lambda_n + 2\mu_n} \frac{\partial^2 \left(\vec{\nabla}.\vec{u}\right)}{\partial t^2} \tag{4.7}$$

In a same manner, by computing the curl of Eq. (4.6):

$$\vec{\nabla}^2 \left(\vec{\nabla} \times \vec{u}\right) = \frac{\rho_n}{\mu_n} \frac{\partial^2 \left(\vec{\nabla} \times \vec{u}\right)}{\partial t^2} \tag{4.8}$$

By using the notations $c_L^n = \sqrt{\frac{\lambda_n + 2\mu_n}{\rho_n}}$ and $c_T^n = \sqrt{\frac{\mu_n}{\rho_n}}$, Eq. (4.7) and Eq. (4.8) suggest that the displacement $\vec{u^n}$ is derived from two potential fields. We are looking for solutions such as:

$$\vec{u^n} = -\vec{\nabla}\Phi^n + \vec{\nabla} \times \vec{\Psi^n} \tag{4.9}$$

Using Eq. (4.9) into Eq. (4.6) and Eq. (4.8), it is possible to re-write Eq. (4.6) and Eq. (4.8) as follows:

$$\vec{\nabla}^2\Phi^n = \frac{1}{(c_L^n)^2}\frac{\partial^2\Phi^n}{\partial t^2} \tag{4.10}$$

$$\vec{\nabla}^2\vec{\Psi^n} = \frac{1}{(c_T^n)^2}\frac{\partial^2\vec{\Psi^n}}{\partial t^2} \tag{4.11}$$

We recognize in Eq. (4.10) and (4.11) the classical wave equations. c_L^n is the longitudinal sound speed and c_T^n is the transversal sound speed. In the case of a fluid layer, the Lamé parameter μ_n is null as well as the transversal sound speed c_T^n and the potential vector field $\vec{\Psi^n}$ does not exist.

So the potential field solutions of the multi-layer sphere scattering problem can be written as:

$$\Phi_i = \sum_{l=0}^{+\infty} i^l(2l+1)P_l(\cos\theta)j_l\left(k_L^{(1)}r\right) \tag{4.12}$$

$$\Phi_1 = \sum_{l=0}^{+\infty} P_l(\cos\theta)A_l^{(1)}h_l\left(k_L^{(1)}r\right) \tag{4.13}$$

$$\Phi_n = \sum_{l=0}^{+\infty} P_l(\cos\theta)\left[A_l^{(n)}j_l\left(k_L^{(n)}r\right) + B_l^{(n)}n_l\left(k_L^{(n)}r\right)\right] \tag{4.14}$$

$$\Psi_n = \sum_{l=0}^{+\infty} \frac{\partial P_l(\cos\theta)}{\partial\theta}\left[C_l^{(n)}j_l\left(k_T^{(n)}r\right) + D_l^{(n)}n_l\left(k_T^{(n)}r\right)\right] \tag{4.15}$$

where n_l is the spherical Bessel function of the second kind, $k_L^{(n)}$ and $k_T^{(n)}$ the wave number associated to the longitudinal and transversal sound speed (c_L^n and c_T^n) of the nth layer. $A_l^{(n)}$, $B_l^{(n)}$, $C_l^{(n)}$ and $D_l^{(n)}$ are the unknown variables associated with the layer n and the mode l. For the outer fluid ($n = 1$), Eq. (4.12) is related to the incoming pulse and a plane wave hypothesis has been assumed (cf. Eq. (4.4)). Note that for a fluid layer $\Psi_n = 0$. For the core layer n containing the origin, the two variables $B_l^{(n)}$ and $D_l^{(n)}$ are null.

To solve the problem, we need to find the coefficients $A_l^{(n)}$, $B_l^{(n)}$, $C_l^{(n)}$ and $D_l^{(n)}$. These coefficients are linked through the limit conditions at the interface of each layer.

4.3.1.3 Limit conditions

Let r_n be the radius of the interface between the layer n and the layer $n+1$. In order to find the relations between the unknown coefficients, we have to express the limit conditions at the interface of the layers n and $n+1$.

Fluid/Fluid interface

Let us suppose that layer n and $n+1$ are fluid. The interface is defined by $r = r_n$. Let $x_L^{(n)} = k_L^{(n)} r_n$ and $y_L^{(n)} = k_L^{(n+1)} r_n$. Two limit conditions can be written at this interface:

- continuity of pressure.
- continuity of the normal component of displacement.

These two limit conditions are expressed in Eq. (4.16) and (4.17)

$$p_n(r_n^+) = p_{n+1}(r_n^-) \tag{4.16}$$

$$\vec{u}^n(r_n^+).\vec{r} = \vec{u}^{n+1}(r_n^-).\vec{r} \tag{4.17}$$

The pressure p_n in a fluid is proportional to the potential field Φ_n:

$$p_n = \omega^2 \rho_n \Phi_n \tag{4.18}$$

And the normal component of displacement can be found through Eq. (4.9):

$$\vec{u}^n.\vec{r} = -\vec{\nabla}\Phi^n.\vec{r} = -\frac{\partial \Phi_n}{\partial r} \tag{4.19}$$

Using Eq. (4.18) in Eq. (4.16) and Eq. (4.19) in Eq. (4.17) leads to the following system of equations:

$$\begin{array}{lllll} \rho_n j_l(x_L^{(n)}) & A_l^{(n)} + \rho_n n_l(x_L^{(n)}) & B_l^{(n)} = \rho_{n+1} j_l(y_L^{(n)}) & A_l^{(n+1)} + \rho_{n+1} n_l(y_L^{(n)}) & B_l^{(n+1)} \\ x_L^{(n)} j_l'(x_L^{(n)}) & A_l^{(n)} + x_L^{(n)} n_l'(x_L^{(n)}) & B_l^{(n)} = y_L^{(n)} j_l'(y_L^{(n)}) & A_l^{(n+1)} + y_L^{(n)} n_l'(y_L^{(n)}) & B_l^{(n+1)} \end{array} \tag{4.20}$$

Fluid/Solid interface

Let us suppose that layer n is fluid, and layer $n+1$ is solid. Let $y_T^{(n)} = k_T^{(n+1)} r_n$. Three limit conditions exist at this interface:

- continuity between the pressure of fluid and the normal component of stress
- continuity of the normal component of displacement
- perpendicular component of shearing stress is null

These three limit conditions can be written as:

$$p_n(r_n^+) = -\lambda_{n+1} \vec{\nabla}^2 . \Phi_{n+1} - 2\mu_{n+1} \frac{\partial u_r^{n+1}}{\partial r} \tag{4.21}$$

$$u_r^n(r_n^+) = u_r^{n+1}(r_n^-) \tag{4.22}$$

$$\frac{\partial u_\theta^{n+1}}{\partial r} - \frac{u_\theta^{n+1}}{r} + \frac{1}{r} \frac{\partial u_r^{n+1}}{\partial \theta} = 0 \tag{4.23}$$

with $u_r^{n+1} = \vec{u}^{n+1} . \vec{r}$ and $u_\theta^{n+1} = \vec{u}^{n+1} . \vec{\theta}$

After computation Eq. (4.21), (4.22) and (4.23) become:

$$\begin{array}{lll} \frac{\rho_n}{\rho_{n+1}} j_l(x_L^{(n)}) A_l^{(n)} + \frac{\rho_n}{\rho_{n+1}} n_l(x_L^{(n)}) B_l^{(n)} = & \frac{1}{\lambda+2\mu} \left[2\mu j_l''(y_L^{(n)}) - \lambda j_l(y_L^{(n)}) \right] & A_l^{(n+1)} + \\ & \frac{1}{\lambda+2\mu} \left[2\mu n_l''(y_L^{(n)}) - \lambda n_l(y_L^{(n)}) \right] & B_l^{(n+1)} + \\ & \frac{2l(l+1)}{(y_T^{(n)})^2} \left[y_T^{(n)} j_l'(y_T^{(n)}) - j_l(y_T^{(n)}) \right] & C_l^{(n+1)} + \\ & \frac{2l(l+1)}{(y_T^{(n)})^2} \left[y_T^{(n)} n_l'(y_T^{(n)}) - n_l(y_T^{(n)}) \right] & D_l^{(n+1)} \end{array} \tag{4.24}$$

$$\begin{array}{lll} x_L^{(n)} j_l'(x_L^{(n)}) A_l^{(n)} + x_L^{(n)} n_l'(x_L^{(n)}) B_l^{(n)} = & y_L^{(n)} j_l'(y_L^{(n)}) & A_l^{(n+1)} + y_L^{(n)} n_l'(y_L^{(n)}) \quad B_l^{(n+1)} + \\ & l(l+1) j_l(y_T^{(n)}) & C_l^{(n+1)} + l(l+1) n_l(y_T^{(n)}) \quad D_l^{(n+1)} \end{array} \tag{4.25}$$

$$
\begin{array}{ll}
2\left[y_L^{(n)} j_l'(y_L^{(n)}) - j_l(y_L^{(n)})\right] & A_l^{(n+1)} + \\
2\left[y_L^{(n)} n_l'(y_L^{(n)}) - n_l(y_L^{(n)})\right] & B_l^{(n+1)} + \\
\left[y_T^{(n)} j_l''(y_T^{(n)}) + (l+2)(l+1) j_l(y_T^{(n)})\right] & C_l^{(n+1)} + \\
\left[y_T^{(n)} n_l''(y_T^{(n)}) + (l+2)(l+1) n_l(y_T^{(n)})\right] & D_l^{(n+1)} = 0
\end{array}
\tag{4.26}
$$

4.3.1.4 Resolution

Let consider a multi-layer sphere with N layers. Over these N layers, P of them are solid. Let assume that the core layer (the one containing the origin) is fluid. And lets assume that the interfaces are only fluid/fluid or fluid/solid type.

Considering the system of equations Eq. (4.12) to (4.15), there is one unknown variable in the outer fluid, $A_l^{(1)}$, and one unknown variable in the core layer $A_l^{(N+1)}$. In the inbetween layers, there are 2 unknown variables for each fluid layer, and 4 for each solid layers. So in total there are $2+2(N-1)+2P = 2(N+P)$ unknown variables. A concentric sphere with N layers has N interfaces. At each interface, there are 2 equations related to the continuity of pressure and continuity of the normal component of displacement. Each solid layer offers one equation at each of its two interfaces. So in total there are $2N + 2P = 2(N + P)$ equations.

So for each mode l, we have a linear system of $2(N+P)$ equations with $2(N+P)$ unknown variables. By using the Cramer determinant method, it is possible to find every variable and in particular $A_l^{(1)}$ which is related to the scattering echo.

Note that if the core layer is solid, the result is similar: there is still one unknown variable for the outer fluid, $A_l^{(1)}$, and now two variables for the core layer $A_l^{(N+1)}$ and $C_l^{(N+1)}$. In the inbetween layers, there are 2 unknown variables for each fluid layer, and 4 for each of the $P-1$ inbetween solid layers. So in total there are $3+2(N-1)+2(P-1) = 2(N+P)-1$ unknown variables. A concentric sphere with N layers has N interfaces. At each interface, there are 2 equations related to the continuity of pressure and continuity of the normal component of displacement. Each inbetween solid layer offers one equation at each of its two

interfaces. The solid core layer has only one interface so only one equation is added for it. So in total there are $2N + 2(P-1) + 1 = 2(N+P) - 1$ equations. We then have a linear system of $2(N+P)-1$ with the same number of unknown variables. The resolution using Cramer determinant is also possible .

4.3.1.5 Backscattering echo in the time domain

For the backscattering problem $\theta = \pi$. So the Legendre polynomial $P_n(\cos\theta) = (-1)^n$. Assuming a far field configuration ($k_L^{(1)}.r \gg 1$), the scattering echo p_s is simplified to:

$$p_s \approx P_0 \frac{\mathrm{e}^{ik_L^{(1)}r}}{k_L^{(1)}r} \sum_{l=0}^{+\infty} i^{l+3} A_l^{(1)} = P_0 \frac{\mathrm{e}^{ik_L^{(1)}r}}{k_L^{(1)}r} f_\infty \tag{4.27}$$

$f_\infty = \sum_{l=0}^{+\infty} i^{l+3} A_l^{(1)}$ is called the form function. From the form function f_∞ and the out going pulse $s(t)$, the echo in the time domain of the multi layer sphere can be computed thanks to Eq. (4.28) from Hickling [1962].

$$p_s(t) = \mathrm{FT}^{-1}\left[\frac{\mathrm{e}^{-2jk_L^{(1)}r}}{|k_L^{(1)}|r^2}\mathrm{FT}[s(t)]f_\infty(k)\right] \tag{4.28}$$

FT is the Fourier transform and r the range of the sphere. Figure 4.3 displays the computed echo of the PVC spherical shell (Ø: 30cm) situated at 30 m from the source. The incoming pulse is a gaussian windowed chirp (5 - 50 kHz). Several echoes corresponding to the different bounces are clearly visible. The secondary echo is stronger: the sphere acts as convex mirror and focusses the sound.

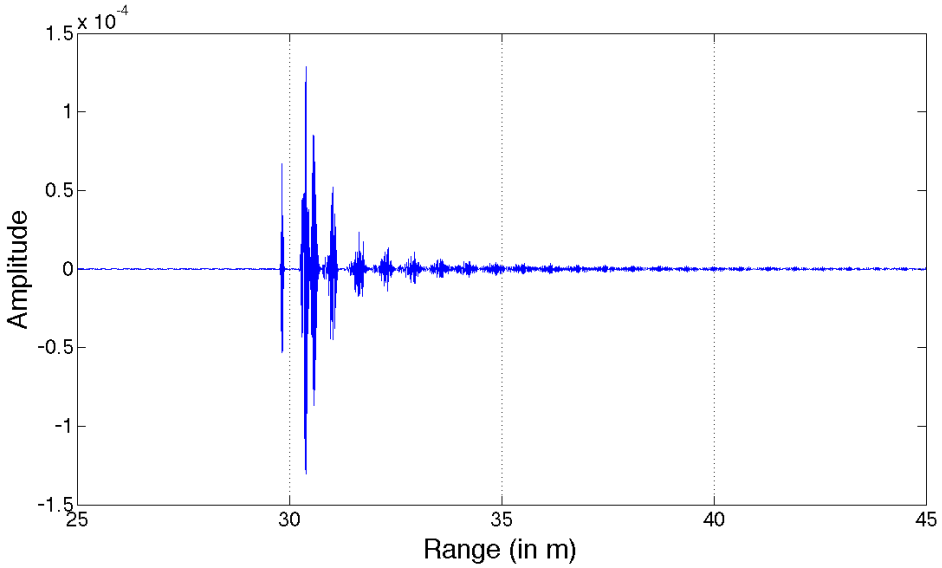

Figure 4.3: Echo in the time domain of a 30 cm diameter PVC spherical shell situated at 30 m from the source.

4.3.2 Synthetic SAS image computation

In order to compute synthetic SAS images of multilayer spheres in free water, the first step is to compute the form function f_∞ as explained in Section 4.3.1. From the form function, the echo in the time domain is computed thanks to Eq. (4.28). Assuming a linear trajectory of the SAS system, the target is viewed in the the raw SAS data (*i.e.* before compression) as a parabola. Note that the extension of the parabola depends on the beamwidth of the system. Figure 4.5 displays the three processing steps explained earlier.

Once the raw SAS data has been computed, the algorithms of compression explained in Section 4.2.1 are applied to obtain the synthetic SAS image. Figure 4.4 show an example of synthetic SAS image of a PVC spherical shell (Ø: 50 cm , wall thickness: 1cm). In figure 4.6, we modelled a four layers structure: 2 co-centrical spherical shells made of PVC ($Ø_1$: 50 cm, $Ø_2$: 15 cm) filled with water. The backscattered echo has been computed thanks to the results from section 4.3.1. Figure 4.6*(bottom)* displays the resulting synthetic SAS image of the 4 layer structure.

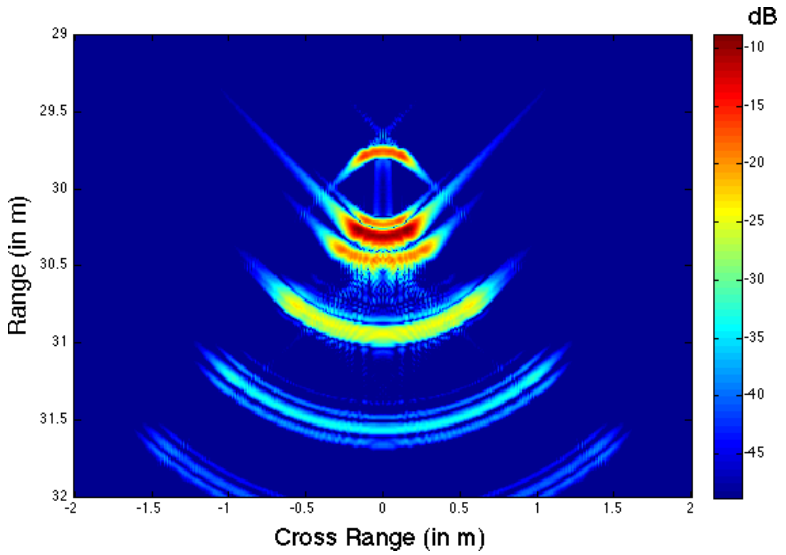

Figure 4.4: Synthetic SAS image of a PVC spherical shell (Ø: 50 cm) with the SAS design proposed in Section 4.2.2.

4.3.3 Comparison between HF-SAS & LF-SAS

In this section we compare synthetic SAS images between a high frequency system and a low frequency system with and without the effects of sound absorption.

4.3.3.1 A world without sound attenuation

In an ideal world, we can consider that the absorption is negligible. Figure 4.7 displays two SAS images from the same target, a PVC spherical shell with 50 cm diameter and 1 cm shell thickness. The low frequency system is the same as described earlier. The high frequency system has the same beamwidth and a frequency band from 250 kHz to 350 kHz. The pulse for both systems is a 100 μs chirp covering the respective frequency band of the two systems.

Comparing the two SAS images, the high frequency SAS offers better imagery for several reasons. At higher frequency, the target strength (TS) of the sphere increases. For example the TS of the PVC spherical shell at LF is 50 dB lower than at HF. At higher frequency, more internal waves are exited Tesei et al. [1998]

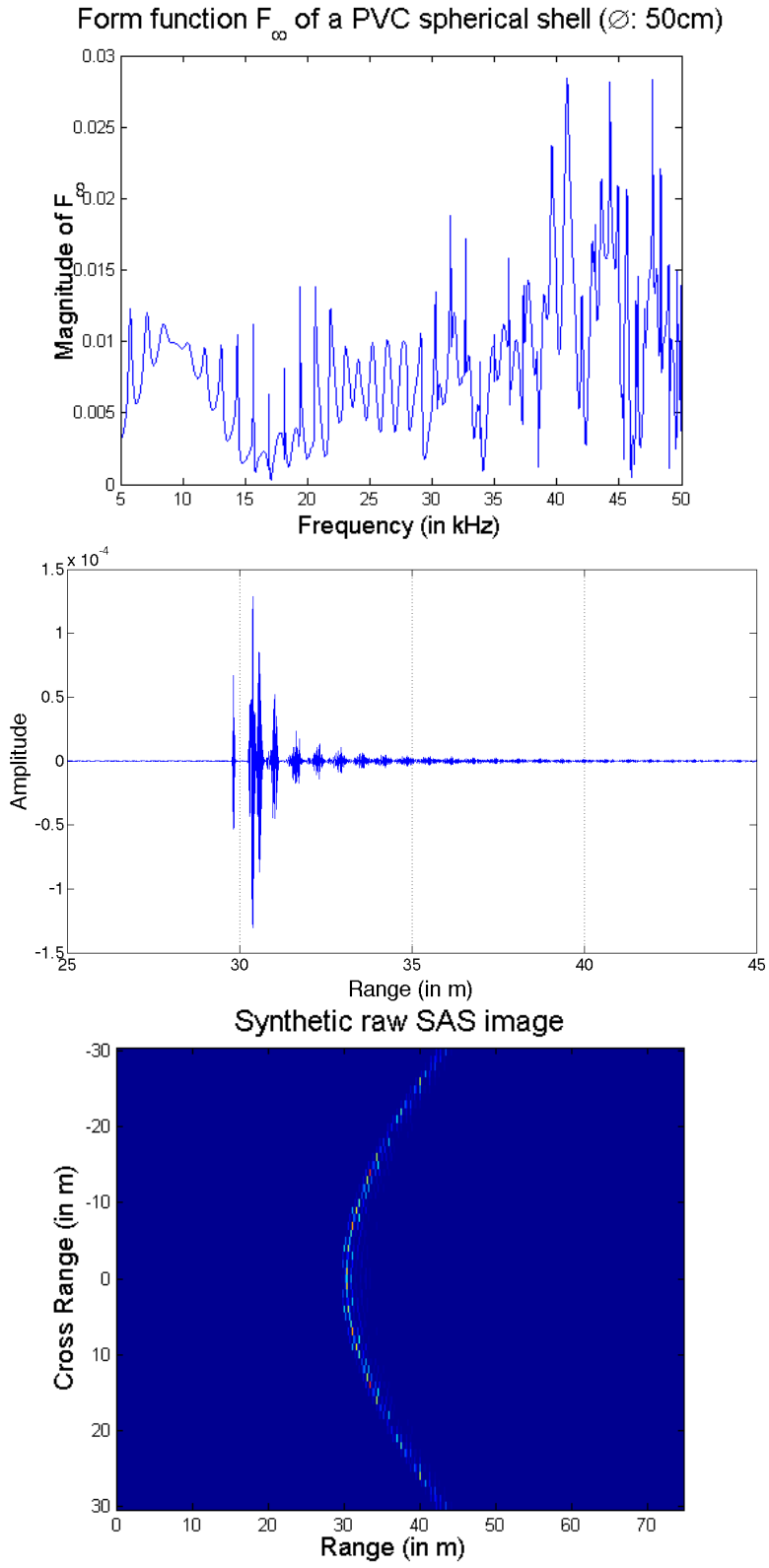

Figure 4.5: From *top* to *bottom*: Amplitude of the form function of a PVC spherical shell, its echo in the time domain, synthetic raw SAS data of the target.

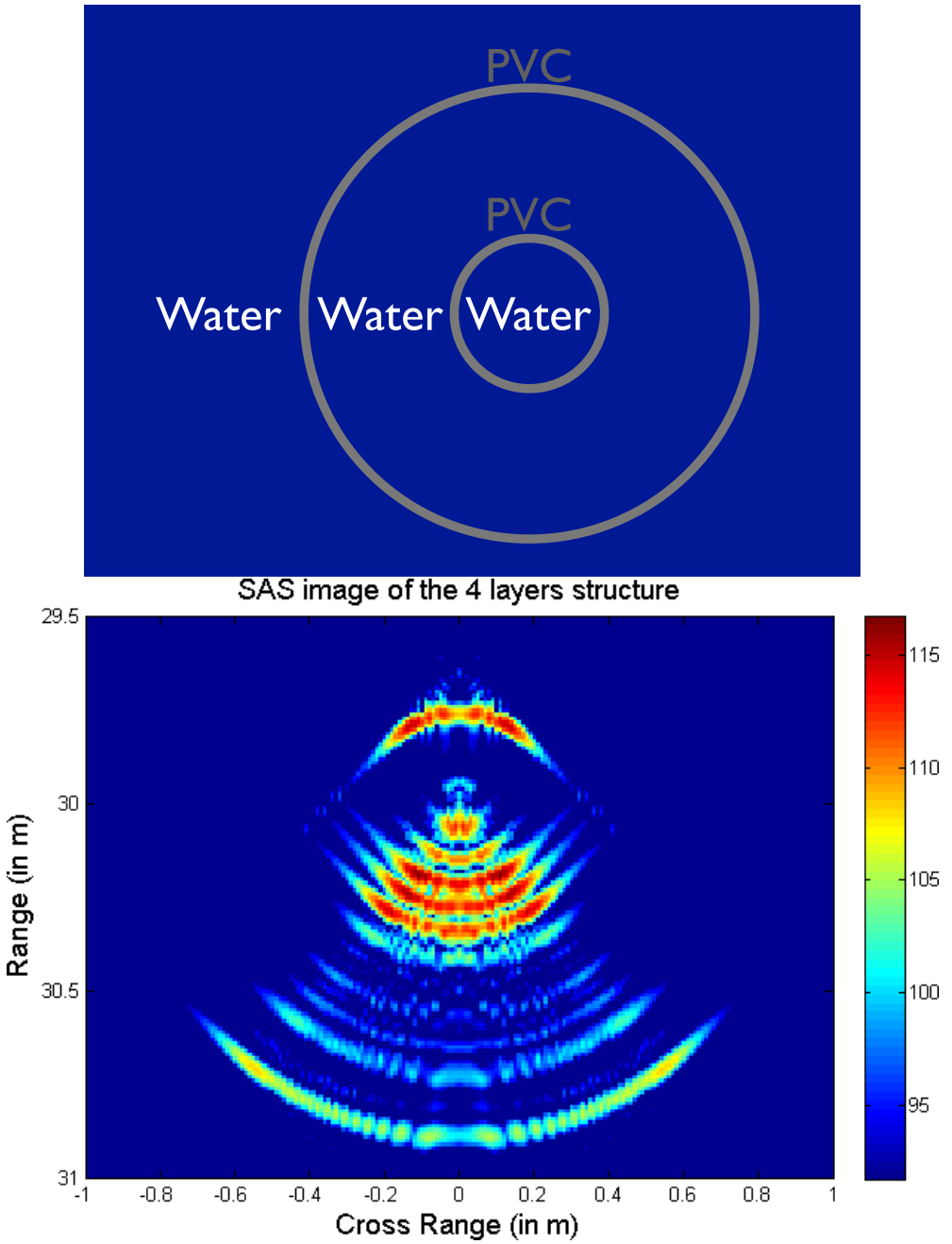

Figure 4.6: (*top*) 4 layers co-centrical sphere structure. (*bottom*) SAS image of the multi-layer sphere.

which offer more characteristics for classification and/or identification.

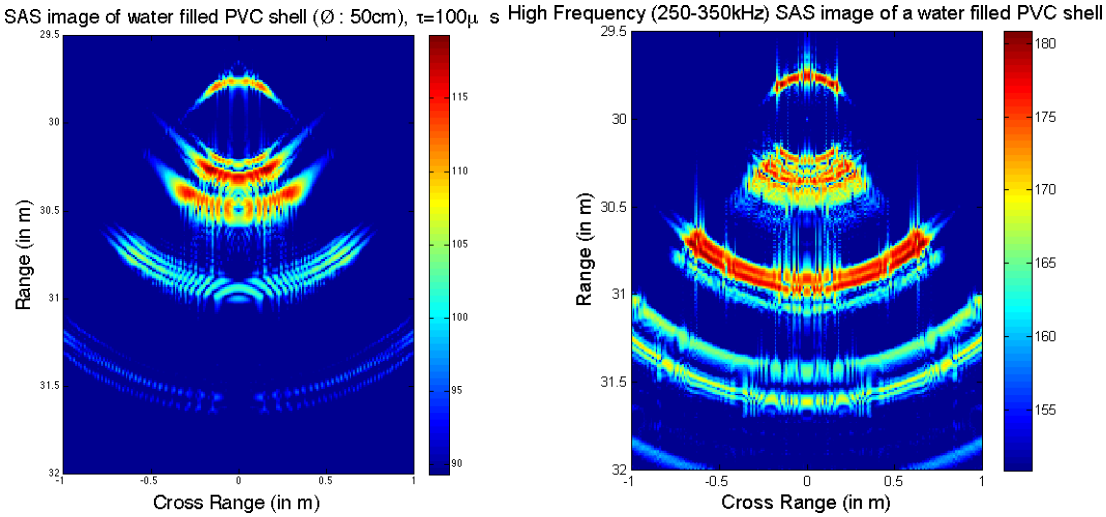

Figure 4.7: (*left*) low frequency SAS image of a spherical PVC shell (Ø: 50 cm, wall thickness: 1cm). (*right*) high frequency SAS image of the same target.

4.3.3.2 Sound attenuation

The sound suffers from attenuation, specially when it propagates into the seabed or material. At high frequency (above 100 kHz), the main factor for sound attenuation is due to friction Marston [1988]. This attenuation can be introduced in the wave equations by considering a complex sound speed.

Let $p(x)$ be a plane wave:

$$\begin{aligned} p(x) &= \mathrm{e}^{ikx} \text{ with } k = k_r + ik_i \\ &= \mathrm{e}^{ik_r x}.\mathrm{e}^{-k_i x} \end{aligned} \tag{4.29}$$

In Eq. (4.29), the first term $\mathrm{e}^{ik_r x}$ corresponds to the equation of a plane wave, and the second term $\mathrm{e}^{-k_i x}$ is a decreasing exponential and models the attenuation of the acoustic wave. Assuming that the amplitude of the imaginary sound speed c_i is much lower than the real part c_r ($|c_i| \ll c_r$), k the wave number can be

written as:

$$k = k_r + ik_i = \frac{\omega}{c_r} - i\frac{\omega c_i}{c_r^2} \tag{4.30}$$

Note that c_i is negative.

The attenuation factor k_i' is usually expressed in dB/λ. It is linked to the imaginary sound speed c_i by:

$$c_i = -\frac{k_i' c_r}{40\pi \log_{10} \mathrm{e}} \tag{4.31}$$

For example, epoxy-resin has the following longitudinal and transversal sound speeds and the corresponding attenuation coefficients found in Tesei et al. [2008]:
$c_L = 3000$ m.s^{-1} $\quad \alpha_L = 0.8$ dB/λ
$c_T = 1550$ m.s^{-1} $\quad \alpha_T = 1.8$ dB/λ
thanks to Eq. (4.31), we can compute the imaginary longitudinal and transversal sound speeds:
$c_L^i =$ -43.98 m.s^{-1}
$c_T^i =$ -51.12 m.s^{-1}

A typical value for the attenuation coefficients is 1 dB/λ, and is frequency independent. So for this reason, low frequency systems suffer less from the sound attenuation than high frequency systems. The next table compares the -20 dB attenuation length for a HF (300 kHz) and a LF (5 kHz).

Frequency	λ	-20 dB attenuation
300 kHz	5 mm	10 cm
5 kHz	30 cm	6 m

Table 4.1 displays the acoustic parameters used for the simulations of section 4.3.3.3.

4.3.3.3 LF-SAS vs HF-SAS

As we saw in Eq. (4.29), the sound attenuation is directly integrated in the wave propagation equations by introducing a complex sound speed (computed thanks to Eq. (4.31)). In order to demonstrate the potential of LF-SAS to image

parameters for epoxy-resin	
$c_L = 3000$ m.s^{-1}	$c_L^i =$ - 43.98 m.s^{-1}
$c_T = 1550$ m.s^{-1}	$c_T^i =$ - 51.12 m.s^{-1}
parameters for fibreglass	
$c_L = 3000$ m.s^{-1}	$c_L^i =$ - 19.24 m.s^{-1}
$c_T = 2550$ m.s^{-1}	$c_T^i =$ - 20.00 m.s^{-1}

Table 4.1: Acoustic parameters used for the simulations.

inside of the target, a series of simulations has been computed. In this section, two results are discussed.

In the first experiment, we produce a SAS image of a epoxy-resin shell. The outer diameter of the shell is 50 cm, and the inner diameter is 10 cm. The shell is filled with air. The drawing in figure 4.8 shows the configuration and the geometry of the target. SAS images have been computed using the algorithm discussed in section 4.3.2. The sound attenuation has been taken into account according to the equations introduced in section 4.3.3.2, as well as the values for the imaginary longitudinal and transversal sound speed for the epoxy-resin.

LF-SAS images and HF images have been computed. The LF-SAS system is similar to the one described in LF-SAS design section. The HF-SAS system has the same beamwidth as the LF-SAS system, and it covers the frequency band of 250 kHz - 300 kHz. The reason for using in this section a slightly lower frequency band than the LF-SAS described in section 4.3.3.1 is linked to the computational instability of the Bessel functions for high values.

The resulting synthetic HF-SAS and LF-SAS images displayed in figure 4.8 show the capability for LF-SAS to image inside the target. The air inside the epoxy-resin sphere is acoustically very reflective, but because of the strong attenuation of the high frequencies, the HF-SAS cannot image inside the sphere, and only the front face of the sphere appears in the SAS image. On another hand, the LF-SAS image shows the inside of the target and its resonances. The difficult part here is to be able to interpret this image. As it is easy to see in Eq. (4.2), the reconstructed image (which is a range image) is based on the hypothesis of

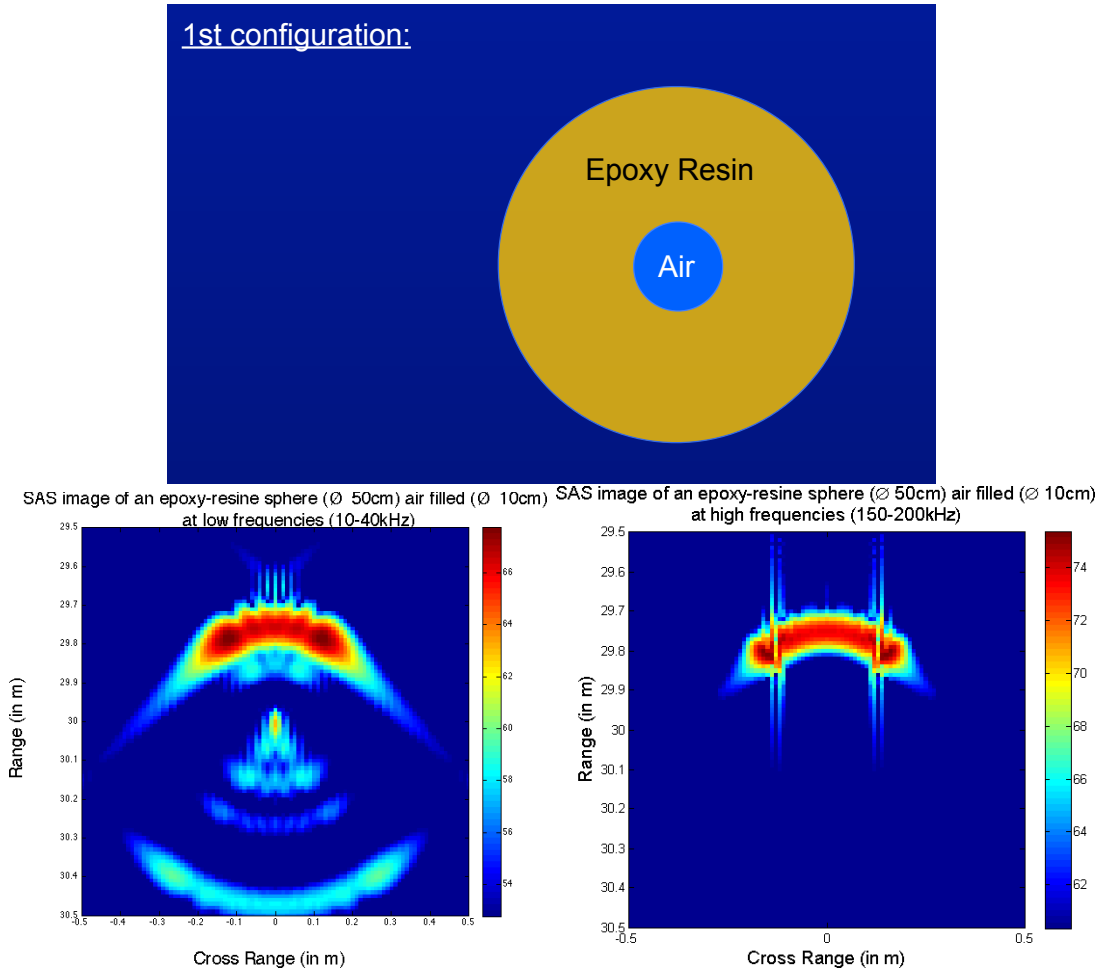

Figure 4.8: (*top*) Geometry of the epoxy-resine spherical shell (outer Ø: 50 cm, inner Ø: 10 cm), the sphere is filled with air. (*bottom-left*) LF-SAS image of the sphere. (*bottom-right*) HF-SAS image of the same target.

a constant sound speed c, which is the sound speed in water. Inside the sphere, the sound travels faster (around 3000 m.s^{-1} for the longitudinal wave). In this case the target in the image is deformed and loses its circular shape. What is appearing to be the centre of the sphere is in fact the back face of the target. The air structure inside the object is situated between the front and back echoes.

The second simulation tries to model more accurately a mine like object. A shell of fibreglass of 1 cm thickness surrounds a layer of water, and the explosive part is modelled by a a layer of epoxy-resin. The electronic box is represented by

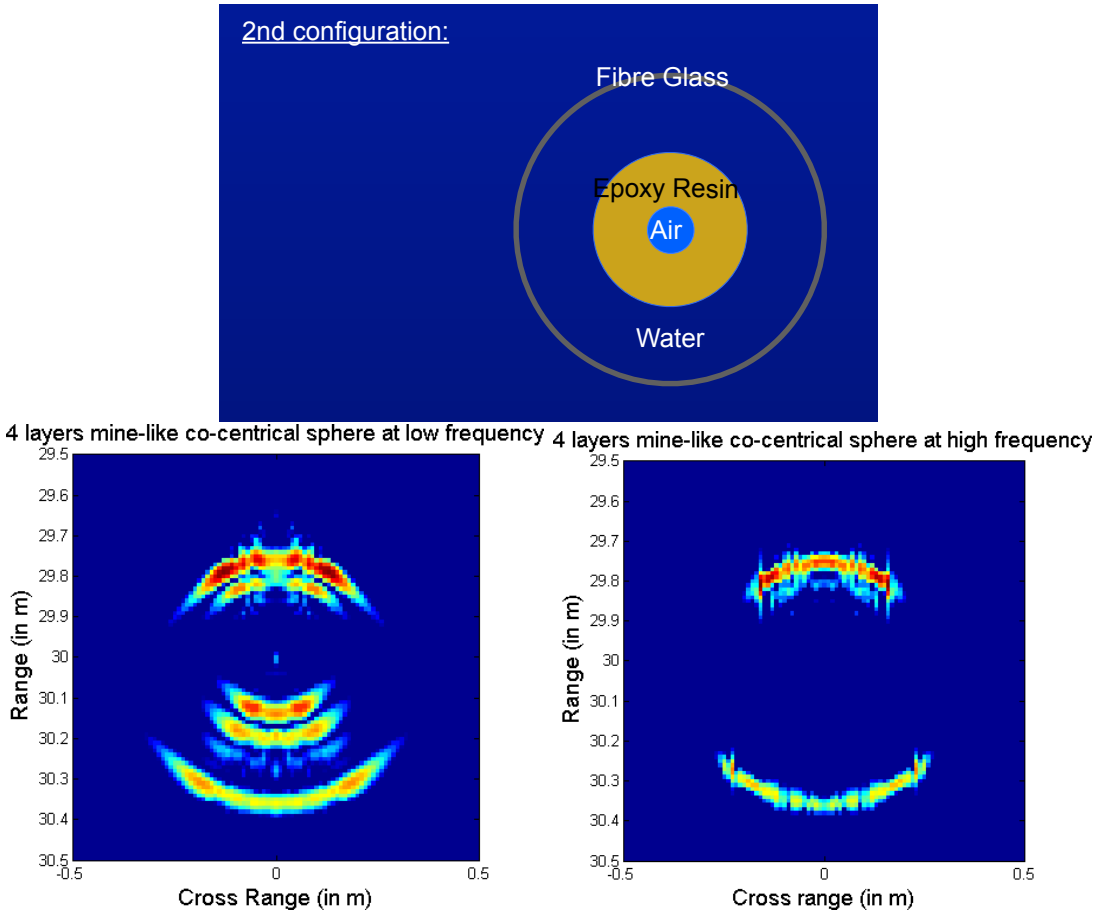

Figure 4.9: (*top*) Geometry of the co-centrical *"mine-like"* spheres. (*bottom-left*) LF-SAS image of the target. (*bottom-right*) HF-SAS image of the same target.

a inner core layer of air. A drawing of this model is shown in Fig. 4.9 (*top*). In this simulation, the sound absorption within the fibreglass and the epoxy-resin has been taking into account. In the HF-SAS image (Fig. 4.9 (*bottom-right*)), the sphere appears to be empty. The LF-SAS system produces an image of the inside the target. The echoes of the core structure of the *mine-like* object are clearly visible.

4.3.3.4 Discussion and Results

Sonars manufacturers have been mainly considering high frequency for imaging systems. The reason behind this choice is clearly the resolution gain. The

resolution is indeed directly linked to the wavelength (inversely proportional to the frequency). HF-SAS, such as the NURC-MUSCLE system, provides sonar images with a cm resolution.

As discussed in section 4.3.3.2, the main disadvantage of high frequencies is the strong attenuation within solid materials or even from the seabed. LF-SAS systems on the contrary can provide images of the resonances of the targets and can image the inner of the ensonified objects (cf. discussion in section 4.3.3.3). Using the same argument about sound absorption, buried targets can be detected using a low frequency system.

One of the disadvantages of the LF-SAS is a lower quality image compared to a HF-SAS system. A second disadvantage will be the difficult interpretation of LF-SAS images. As seen in 4.3.3.3, the LF-SAS image of a particular target will be distorted by the difference between the sound speed in water and within the target. Because the sound speed of the material is *a priori* unknown, the right geometry of the inner of the target is not available. However it will be possible to distinguish between an empty object and a non-empty object. Future generations of sonar may use both high and low frequencies for respectively high quality images and inner target insonification.

4.4 Reverberation Level in SAS Images

In the previous sections, echoes of multi-layer spheres have been computed in free water. However in sidescan sonar or SAS systems, the main limitation in terms of noise comes from the reverberation level (RL). The RL is not noise in the sense that it contains information relative to the reflectivity and the geometry of the seabed. But it represents a coherent noise from a signal processing and image processing point of view. In this section, a model of RL suitable for SAS is studied. The main idea is to compare the SAS reverberation level to the level of the secondary echoes for the simple targets studied in section 4.3.

4.4.1 Different theories for seabed scattering behaviour

Jackson and Richardson [2007] divide the theories for seabed acoustic scattering behaviour into three main classes depending on the model chosen for the seabed. The seabed can indeed be modelled as fluid, as a solid with elastic properties or as a poroelastic medium. The three classes are then the fluid theory, the elastic theory and the poroelastic theory. It is noted that all these models and theories are perfectly valid and depend only on the type of seabed to be modelled.

In the fluid theory the seabed is considered as a fluid. Three main parameters are necessary to model the seabed: the bulk density, the compressional sound speed and sound attenuation. This theory models very well very fine and fine sediments such as silt, clay or fine sand.

In the elastic theory the seabed is modelled as a solid and then it supports shear stress as well as compressional waves. This model has mainly been developed by geophysicists to understand sound propagation into stratified solid media. Compared to fluid theory, two other parameters are needed: the shear velocity and the shear attenuation. This theory models well solid sediments such as a rocky seafloor.

The poroelastic theory is based on the observation that sediments have a two phase structure: particles which are considered as solid saturated with fluid (in

our case water). The sediment particles constitute the *porous frame*, and the pore space is filled with water. Biot's theory of porous media Biot [1956a,b] has been widely applied in seabed acoustic behaviour.

4.4.2 Small Perturbation Fluid Model

The model chosen here is based on the small perturbation fluid model of Jackson and Richardson [2007]. The interface between the water and the sediment is denoted as $\zeta(x, y)$. ζ represents the roughness of the seabed. The seabed is considered as flat meaning that $\zeta(x, y)$ has zero mean. The term *"small perturbation"* relates to a rough flat seabed hypothesis. The roughness of the interface ζ is supposed to be smaller than the wavelength. Note that for a 10 kHz frequency, the wavelength corresponds to 15 cm.

The water column (represented by the half-space: $\{z > \zeta(x, y)\}$) is considered as homogeneous. Let c_1 be its sound speed, and ρ_1 its density. The sound attenuation in water is neglected. The bottom (represented by the half-space: $\{z \leq \zeta(x, y)\}$) is considered as a homogeneous fluid with a sound speed c_2 and a density ρ_2. The sound attenuation in the sediment δ is supposed to be linear function of frequency, so it can be expressed as dB/λ.

Let k_1 and k_2 be respectively the wave number in water and in the sediment.

$$k_1 = \frac{2\pi f}{c_1} \tag{4.32}$$

$$k_2 = \frac{2\pi f(1 + i\delta)}{c_2} \tag{4.33}$$

Using a first order perturbation, the scattered field ϕ can be expressed as:

$$\phi(f) = -S(f)\frac{k_1^2}{2\pi}\iint_{(x',y')} B(x', y')\tau(x', y')\zeta(x', y')\frac{1}{r_s r_r}\mathrm{e}^{ik_1(r_s+r_r)}dx'dy' \tag{4.34}$$

where $S(f)$ is the Fourier transform of the outcoming pulse, B represents the cross beampattern (transmitter/receiver), r_s and r_r are respectively the distance

between the point in the interface $(x', y', \zeta(x', y'))$ and the source and the distance between the same point $(x', y', \zeta(x', y'))$ and the receiver. The scalar τ is the first order perturbation scattering parameter, and its expression is:

$$\tau(x, y) = \frac{1}{2}(1 + V_s)(1 + V_r)G \tag{4.35}$$

with

$$\begin{aligned}
\kappa &= (1 + i\delta)\frac{c_1}{c_2} \\
\rho &= \frac{\rho_2}{\rho_1} \\
G &= \left(\frac{1}{\rho} - 1\right)\left(\cos\theta_r \cos\theta_s \cos\phi - \frac{P_r P_s}{\rho}\right) + 1 - \frac{\kappa^2}{\rho} \\
P_{s,r} &= \sqrt{\kappa^2 - \cos^2\theta_{s,r}} \\
V_{s,r} &= \frac{\rho \sin\theta_{s,r} - \sqrt{\kappa^2 - \cos^2\theta_{s,r}}}{\rho \sin\theta_{s,r} - +\sqrt{\kappa^2 - \cos^2\theta_{s,r}}}
\end{aligned}$$

ϕ is the bistatic angle, where $\phi = \pi$ corresponds to the back-scattering case, $\phi = 0$ to the forward-scattering case.

The advantage of this model is its simplicity. The scattered field in Eq. (4.34) is the integration through the ensonified interface of geometrical parameters and works directly with 3D surfaces. The computation is very quick in comparison to trying to solve the wave equation at an interface for example.

In order to compute a SAS image of a particular seafloor, we first generate the rough surface between the water column and the sediment. Since the mid-seventies, it has been shown that many natural structures can be well represented by fractal models, Mandelbrot [1982]. For this reason, the model used to generate the seafloor is based on fractals. The generation of the 3D rough seabed surface is performed using a pink noise method Pentland [1984]. Figure 4.10 displays an example of a rough surface generated using fractals.

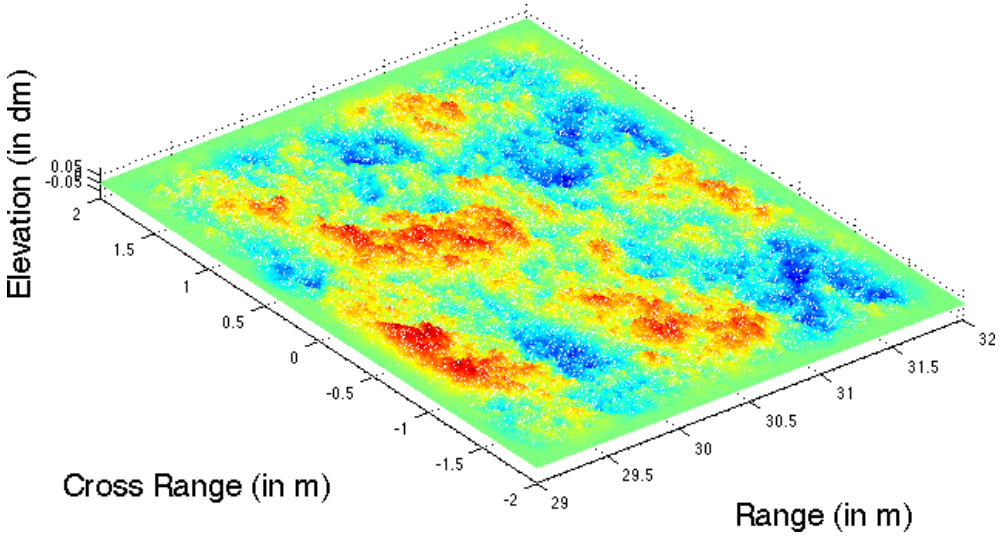

Figure 4.10: Example of rough surface generated using a pink noise method.

Once the roughness ζ is computed, Eq. (4.34) is solved for all the frequencies within the bandwidth used by the SAS system. The time domain echo is obtained by applying the inverse Fourier transform to $\phi(f)$. This process is repeated along the trajectory of the SAS system in order to synthesise the raw SAS data. The algorithms explained in §.4.2.1 are applied to the raw data to construct the final SAS image.

4.4.3 Results

4.4.3.1 Reverberation Level and SNR estimation

Figure 4.11 displays the roughness ζ computed from a fractal generator, and the resulting SAS image from the rough surface. Figure 4.11 (*bottom*) displays the histogram associated to the patch of seabed imaged with the SAS system.

The histogram of the patch of synthetic SAS image has been computed in order to evaluate the RL and RL distribution. The synthetic RL distribution follows a Rayleigh distribution. This first texture feature matches with the real SAS-RL. A more advanced study is done in the section 4.4.3.2 on synthetic and real SAS images based on texture comparison.

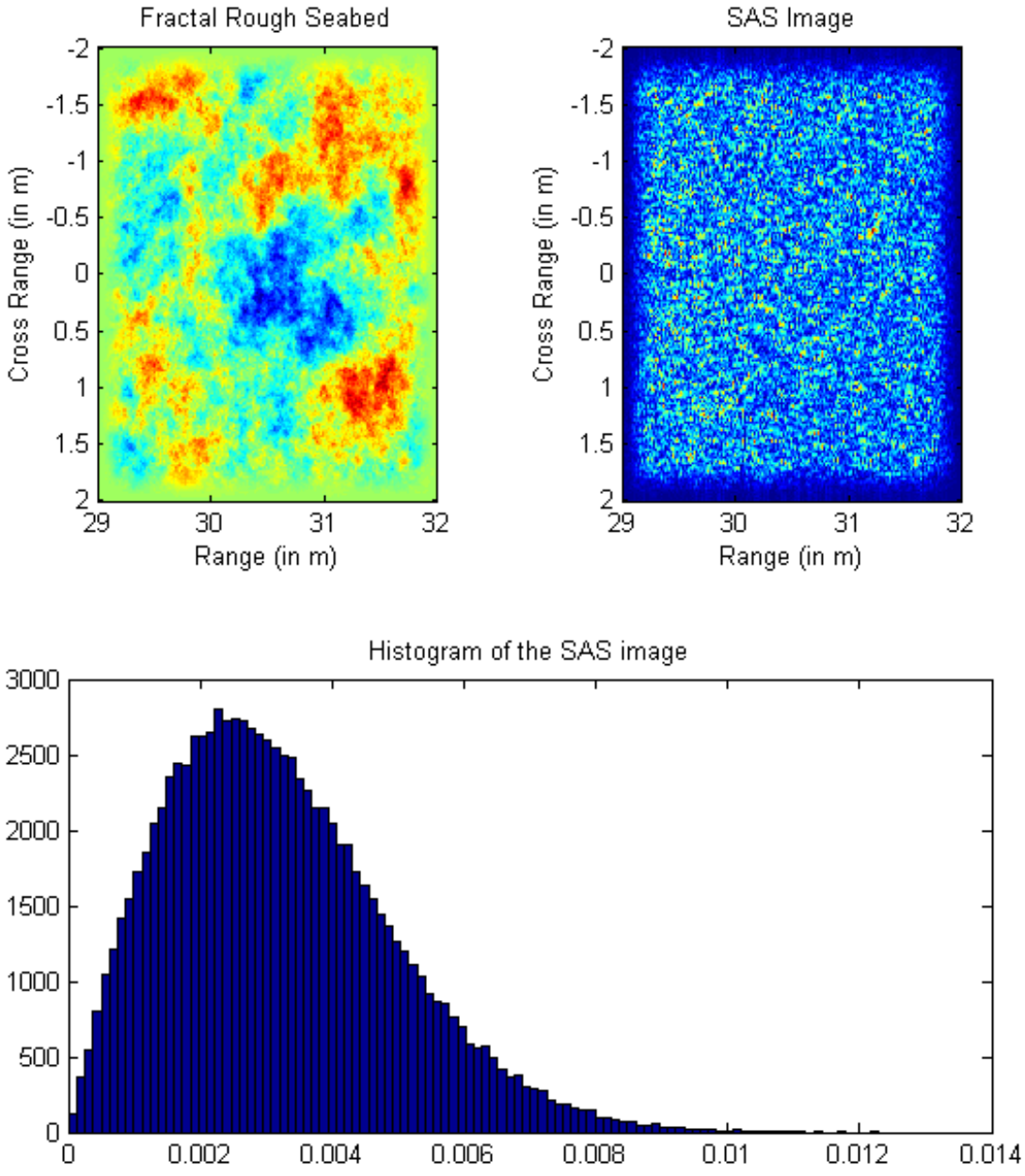

Figure 4.11: *(top-left)* Example of rough surface generated using a pink noise method. *(top-right)* SAS image computed from the rough seabed. *(bottom)* Histogram associated to the seabed SAS image.

We want here to compare the RL to the level of the different secondary echoes of a target of interest. As an example we will work here with the PVC spherical shell

(Ø: 50 cm, wall-thickness: 1 cm) we have already studied earlier (in section 4.3). In figure 4.12 the synthetic SAS image of the PVC spherical shell in free water (*left*) and the histogram the RL and the different part of the highlights of the object are displayed.

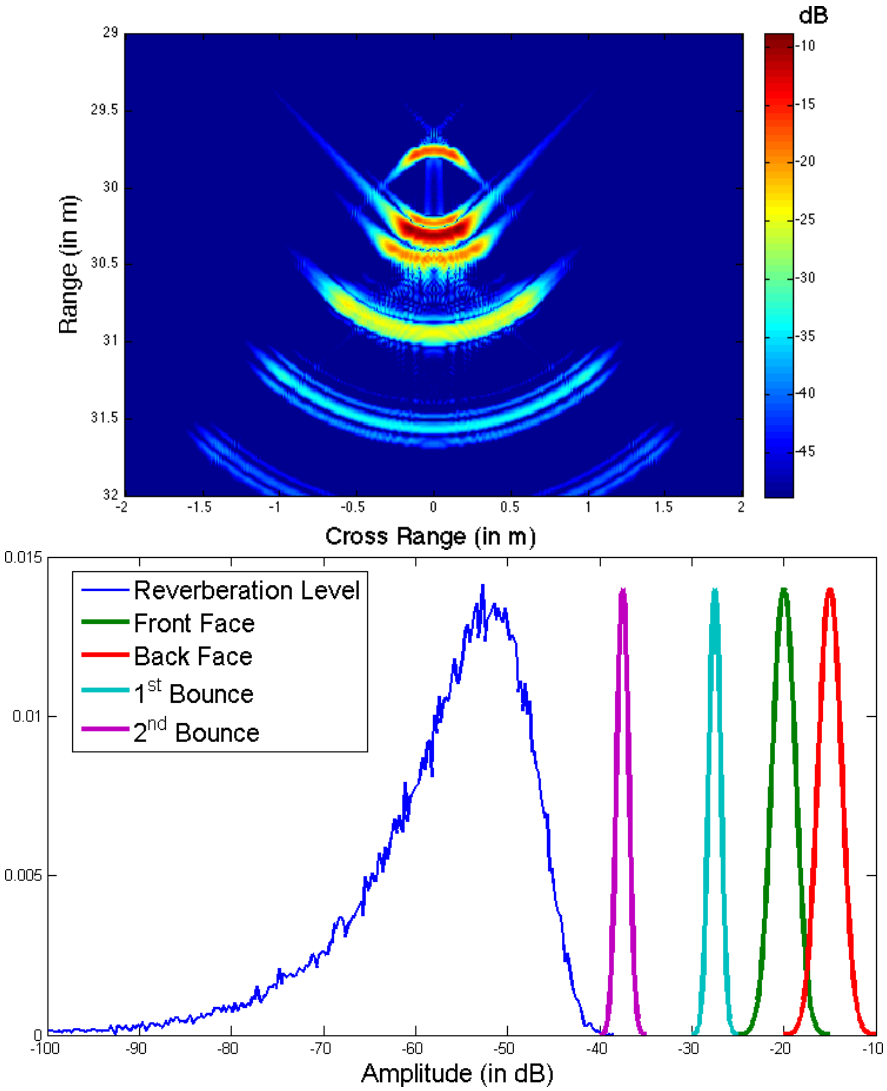

Figure 4.12: Synthetic SAS image of a PVC spherical shell (*top*) . Histogram of the SAS reverberation level using the small perturbation fluid model and the several echoes of the PVC spherical shell (*bottom*).

We are comparing here a target in free water and the RL from a flat featureless seabed. For this PVC target, and as shown in figure 4.12, the highlights from the front face and back face are clearly visible (more than 30 dB above the RL mean value). The first two secondary echo are visible as well (respectively 20 and 10 dB above the RL). The following resonating echoes disappear into the reverberation level noise.

In conclusion, with a LF-SAS the structure of the highlight of the target, induced by its geometry, is highly visible with respect to the reverberation level. But equally some of the secondary echoes coming a resonating target can be imaged. This will be a strong feature for detection, classification and identification.

4.4.3.2 Comparison between synthetic and real SAS bottom echo

In this section we aim to validate the numerical model of the SAS Reverberation Level computation by comparing it with real SAS images of seabed. Figure 4.13 displays two seafloor SAS images coming from the numerical model (*left*) and the real SAS data (*right*). Visually the texture appears similar in both images.

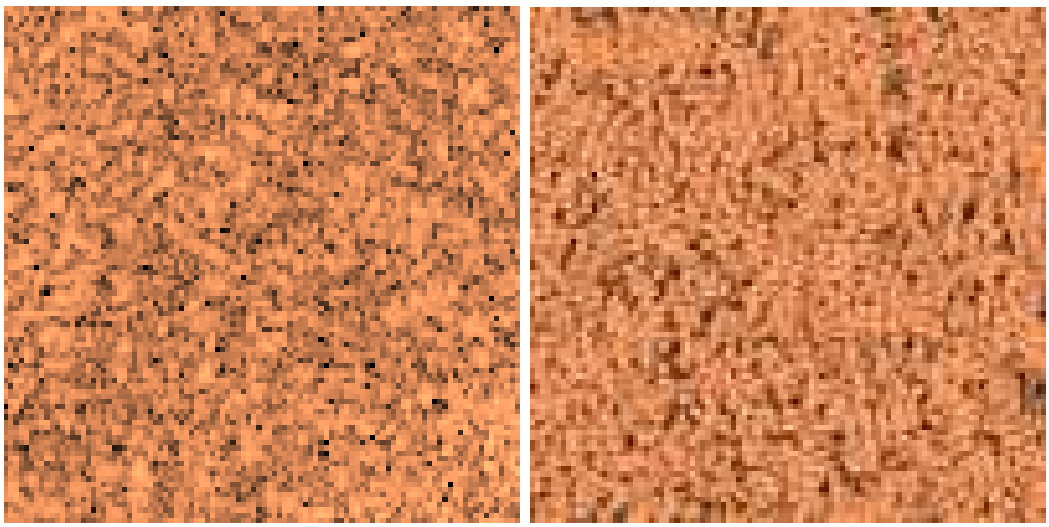

Figure 4.13: (*left*) Synthetic seafloor SAS image computed according to §. 4.4.1. (*right*) Snapshot of flat and featureless seabed recorded with the NURC-MUSCLE SAS system.

In section 4.4.3.1, the histogram of the synthetic SAS-RL has been studied. And it has been shown that the histogram of the synthetic SAS-RL follows a Rayleigh distribution similar to real SAS images. However, the histogram is not a good feature for texture characterisation.

In order to compare the two reverberation level textures we compute the grey level co-occurence matrices introduced by Haralick et al. [1973]. The co-occurence matrix compute the joint probability $p(i, j)$ that 2 pixels separated by a displacement vector $\vec{d}$ have their grey level respectively equal to i and j. Figure 4.14 displays the two grey level co-occurence matrices $p(i, j)$ of a synthetic SAS RL and of a real SAS RL. The two distributions are geometrically relatively close.

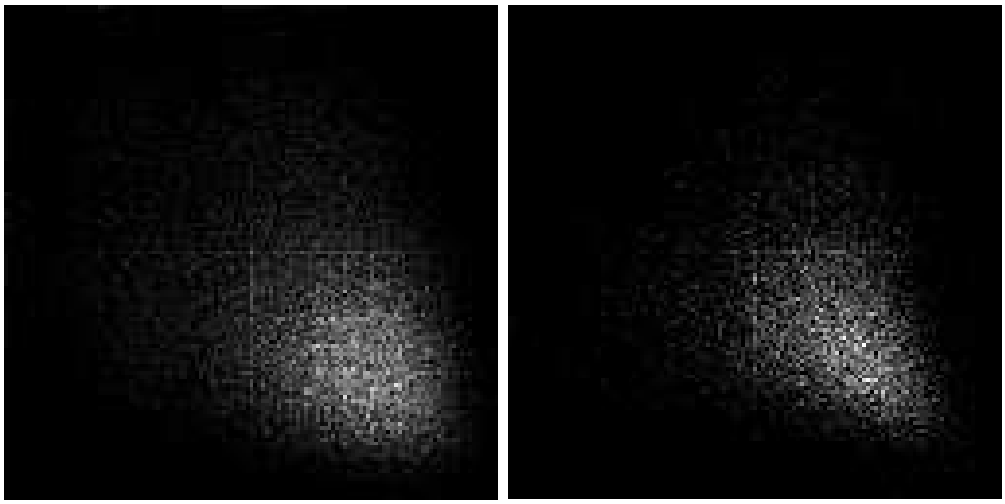

Figure 4.14: Grey level co-occurence matrix of the synthetic RL (*left*) and of real SAS data (*right*).

From the grey level co-occurence matrix, Haralick et al. [1973] proposes 14 textural features. Here we consider only the 4 most common:

Energy	$\sum_{i,j} p(i,j)^2$
Contrast	$\sum_{i,j} \lvert i-j \rvert p(i,j)$
Correlation	$\sum_{i,j} \frac{(i-\mu_i)(j-\mu_j)p(i,j)}{\sigma_i \sigma_j}$
Homogeneity	$\sum_{i,j} \frac{p(i,j)}{\lvert i-j \rvert +1}$

We computed these textural features for the two RL textures. The table 4.2 compares the Haralick's textural features of the two reverberation textures. The two textures which appear very similar visually from figure 4.13, share roughly the same geometry through their co-occurence matrices. And it is not a surprise that their textural features are very similar.

	Real SAS RL	Synthetic SAS RL
Energy	$1.9\ 10^{-4}$	$1.1\ 10^{-4}$
Contrast	$1.7\ 10^{3}$	$2.2\ 10^{3}$
Correlation	0.313	0.366
Homogeneity	0.0867	0.0703

Table 4.2: Haralick's textural features for real and synthetic SAS reverberation.

4.5 Half-Space Interaction

4.5.1 Resolution of the Helmholtz-Kirchhoff integral

Let's consider the backscattering of a multi-layer sphere problem as described in section 4.3, and add an interface (typically a seabed). Adding a simple simple interface to the problem breaks the spherical symmetry of the free water problem and no closed form solution appears possible. In order to solve the problem approximations are needed.

As in section 4.4, the space is divided into two half-spaces: $\{z > 0\}$ corresponds to the water column, and $\{z \leq 0\}$ corresponds to the sediment. Both half-spaces are considered as homogeneous. The sediment is considered as a fluid. The scalars c_1 and c_2 are respectively the sound speed in water and in the sediment, while ρ_1 and ρ_2 are respectively the density of the water and the sediment. Let S be the wet-surface surrounding the target, and $\{\tilde{r}_j\}_{j\in[1,M]} \in S$ a discrete representation of S. The Helmholtz-Kirchhoff theorem (Pierce [1991]; Schmidt [2004]) stipulates that the acoustic far-field can be found by solving the Helmholtz-Kirchhoff equation (equation introduced by Kirchhoff [1876]). A discrete approximation of the Helmholtz-Kirchhoff equation is given by Schmidt [2004] and can be written as follows:

$$p(r_i) \approx \sum_{j=1}^{M} \left(\frac{\partial G_{ij}}{\partial n_j} p(\tilde{r}_j) - \rho(\tilde{r}_j)\omega^2 G_{ij} u_n(\tilde{r}_j) \right) \mathrm{d}A_j \tag{4.36}$$

where $p(\tilde{r}_j)$ represents the pressure at $\tilde{r}_j$, $u_n(\tilde{r}_j)$ the normal displacement at $\tilde{r}_j$, and G_{ij} is the Green's function. The operator $\partial/\partial n_j$ is the derivative in the direction of the outward-pointing normal vector at the point $\tilde{r}_j$ on the wet-surface. A_j is the surface area associated to $\tilde{r}_j$ and $\omega = 2\pi f$ is the angular frequency.

Zampolli et al. [2008, 2009] propose an approximation of the Green's function G_{ij} for a two layer fluid media. Zampolli derives two expressions for the Green's function depending on which layer the target is located. Figure 4.15 displays the geometry and configuration for both cases.

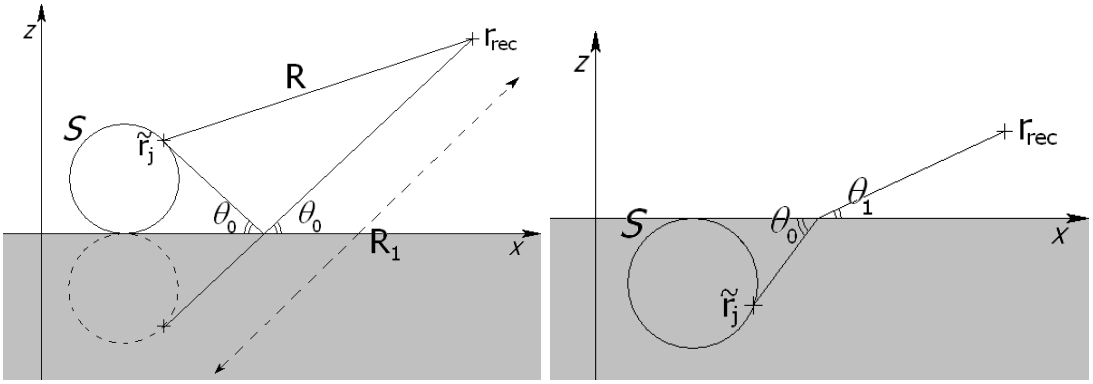

Figure 4.15: (*left*) Geometry, configuration and notations for an object situated in the water column. (*right*) Geometry, configuration, and notations for an object buried into the sediment.

4.5.1.1 Target in the water column

For a target in the water column, the Green's function G_{ij} can be written as:

$$G_{ij} = \frac{\mathrm{e}^{ik_1 R}}{R} + \frac{\mathrm{e}^{ik_1 R_1}}{R_1}\left[V(\xi) - i\frac{N}{kR_1}\right] \tag{4.37}$$

k_1 is the wavenumber in the water column, k_2 is the wavenumber in the sediment, V is the plane-wave reflection coefficient and is expressed as:

$$V(\xi) = \frac{m\mu_1 - \mu_2}{m\mu_1 + \mu_2}$$

where $\xi = k_1 \cos\theta_0$, $\mu_1 = \sqrt{k_1^2 - \xi}$, $\mu_2 = \sqrt{k_2^2 - \xi}$ and m is the density ratio ρ_2/ρ_1. N is given by:

$$N = \frac{1}{2}\left(\frac{\partial^2 V}{\partial\theta^2} - \frac{\partial V}{\partial\theta}\tan\theta\right)_{\theta=\theta_0} \tag{4.38}$$

4.5.1.2 Buried target

If the target is buried, G_{ij} can be approximated by:

$$
\begin{aligned}
G_{ij} &= \sqrt{\frac{\cos\theta_0 \sin\theta_0}{r(\tilde{z}_j + z_{rec}\sin^3\theta_0/(n\sin^3\theta_1))}} \\
&\quad \times \exp\left[ik_2\left(\frac{\tilde{z}_j}{\sin\theta_0} + \frac{nz_{rec}}{\sin\theta_1}\right)\right] \\
&\quad \times \left[W(\cos\theta_0) + \frac{iN_t\sin^3\theta_0}{2k_2(\tilde{z}_j + z_{rec}\sin^3\theta_0/(n\sin^3\theta_1))}\right]
\end{aligned} \tag{4.39}
$$

where n is the speed ratio c_2/c_1. The plane-wave transmission function W can be written as:

$$
W(q) = \frac{2\sqrt{1-q^2}}{\sqrt{1-q^2} + m\sqrt{n^2-q^2}} \tag{4.40}
$$

and

$$
N_t = \frac{3\cos\theta_0}{\sin^2\theta_0}\left(\frac{\tilde{z}_j + z_{rec}\sin^5\theta_0\ n^{-3}\sin^{-5}\theta_1}{\tilde{z}_j + z_{rec}\sin^3\theta_0\ n^{-1}\sin^{-3}\theta_1} - \frac{1+\cos^2\theta_0}{3\cos^2\theta_0}\right)\frac{\partial W}{\partial q} - \frac{\partial^2 W}{\partial q^2} \tag{4.41}
$$

Full details and notations of Eq. (4.37) and Eq. (4.39) can be found in Zampolli et al. [2008].

4.5.2 LF-SAS images of targets with seabed interaction

In this section, we apply the results from § 4.5.1 to our initial problem: target imaging with LF-SAS system. The targets considered here are the multi-layer spheres studied in section 4.3.

The Green's function expressions in Eq. (4.37) and Eq. (4.39) are only functions of the geometry of the configuration and physical parameters such as sound speed and density. The terms of pressure p and normal displacement u_n in Eq. (4.36) can be computed on the wet-surface of the sphere by using the exact expression of the scattering problem expressed in Eq. (4.13). The pressure p is related to the potential field ϕ_1 by: $p = \omega^2\rho_1\phi_1$. And the displacement u_n is computed thanks to: $u_n = \omega^2\rho_1\frac{\partial\phi_1}{\partial r}$.

By putting Eq. (4.37) (on the surface case) or Eq. (4.39) (buried case) and the analytical solution for multi-layer sphere into Eq. (4.36), the far-field scattering echo of the target can be computed for each frequency. Repeating the previous process for all the frequencies covered by the LF-SAS system, it is possible to recover the time domain echo at any location in the far field. The raw SAS data can then be computed by computing the time domain echo along the SAS trajectory. The final LF-SAS image is finally obtained using the compression algorithms described in section 4.2.

The next two sections present the numerical results of a PVC sphere put on the surface of a sandy seafloor and totally buried in mud. In both experiments, the SAS system runs at an altitude of 5 m and at 30 m range from the target. This configuration has been chosen in order to accentuate the effect of bottom interface interaction.

4.5.2.1 On the seabed case

We consider a PVC spherical shell (Ø: 50 cm, wall-thickness: 1 cm) filled with water lying on a perfectly flat sandy seafloor. The configuration of this simulation is drawn in figure 4.16.

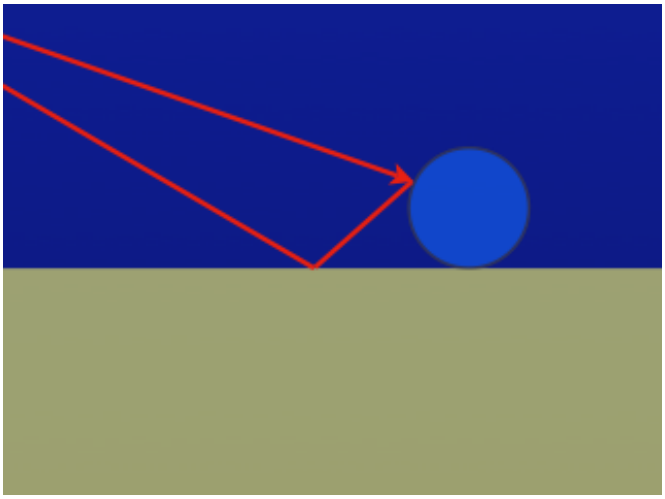

Figure 4.16: Configuration of the simulation. The PVC spherical shell is lying on the surface. The red arrows represent the sound trajectory.

On figure 4.16, the red arrows represent a sketch of the sound trajectory and its interaction between the object and the seafloor. Looking closer at Eq. (4.37), the Green's function is divided into two terms. The first one $\frac{e^{ikR}}{R}$ is the classical expression of the Green's function in free water. It corresponds to the sound wave directly hitting the target and coming back toward the receiver without any interaction with the seafloor. The second term $\frac{e^{ikR_1}}{R_1}\left[V(\xi) - i\frac{N}{kR_1}\right]$ can be approximated to the order by $\frac{e^{ikR_1}}{R_1}V(\xi)$. Note that $V(\xi)$ represents the plane-wave reflection coefficient. This term can be interpreted as one bounce on the seafloor.

So the main contributions to the backscattering echo are the free water echo, the two echoes involving one bounce on the surface (transmitter / target / bottom / receiver and transmitter / bottom / target receiver) and the echo involving two bounces on the seafloor (transmitter / bottom / target / bottom / receiver).

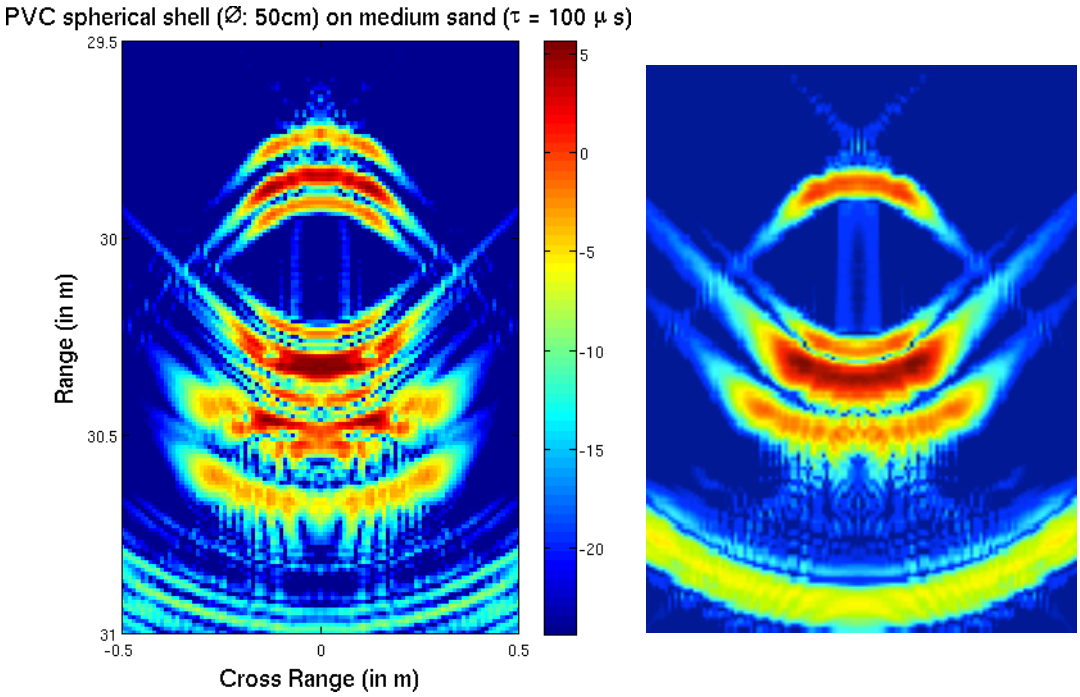

Figure 4.17: (*left*) Synthetic LF-SAS image of the PVC spherical shell lying on a flat sandy seafloor. (*right*) Synthetic LF-SAS image of the same target in free water.

Figure 4.17 displays the result of the simulation. The trajectory of the LF-

SAS has been set at 5 m altitude and 30 m range from the target. Note that this configuration is not optimal for imagery because of the high grazing angle, but it emphasises the different contributions in the echo by separating them in time.

The target LF-SAS image in free water (Fig. 4.17 (*right*)) is shown for comparison purposes. Looking at the contribution of the front face of the sphere, it is possible to distinguish between the three main contributions (free-water/one bounce/two bounces). The second arc corresponds to the one bounce contribution. Note that it is stronger in amplitude than the direct echo because it is the sum of the two one-bounce contributions which are exactly in phase and then sum coherently.

In a MCM context, the trajectory of the sonar tends to be much lower in order to increase the shadows. Using SAS systems, the range can be up to 200 m. For longer range and lower altitude, the time difference between the different contributions (free-water/one-bounce/two-bounces) is almost negligible (less than the resolution of the sonar) and they sum together.

4.5.2.2 Buried case

We consider the same target as in section 4.5.2.1, but fully buried in mud. The sound attenuation in the sediment has been taken into account thanks to a complex sound speed for the mud. Figure 4.18 shows the configuration of the simulation.

By contrast to the last simulation, one main contribution appears here, and the LF-SAS images of the target in free water and buried are much more similar. Note the arc representing the front face contribution has less aperture. This phenomenon is simply explained by the fact that away from the target, the sound travels futher into the sediment to reach the target and then it experiences more attenuation. Using LF-SAS, the sound attenuation into the sediment is not drastic especially when the object is situated just below the interface. By comparing the amplitude in figure. 4.17 and figure. 4.19, there are only a few dB difference between the maximum amplitudes. With 1dB attenuation per 3 mm of sediment

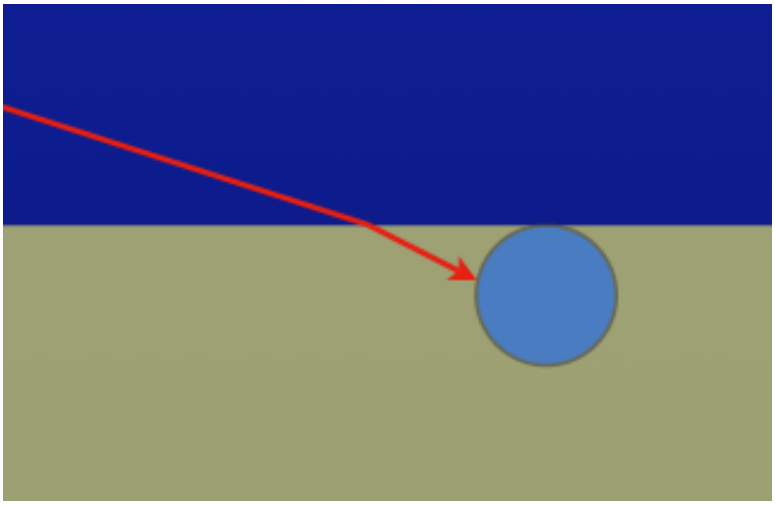

Figure 4.18: Configuration of the simulation. The PVC spherical shell is just below the seafloor. The red arrows represent the sound trajectory.

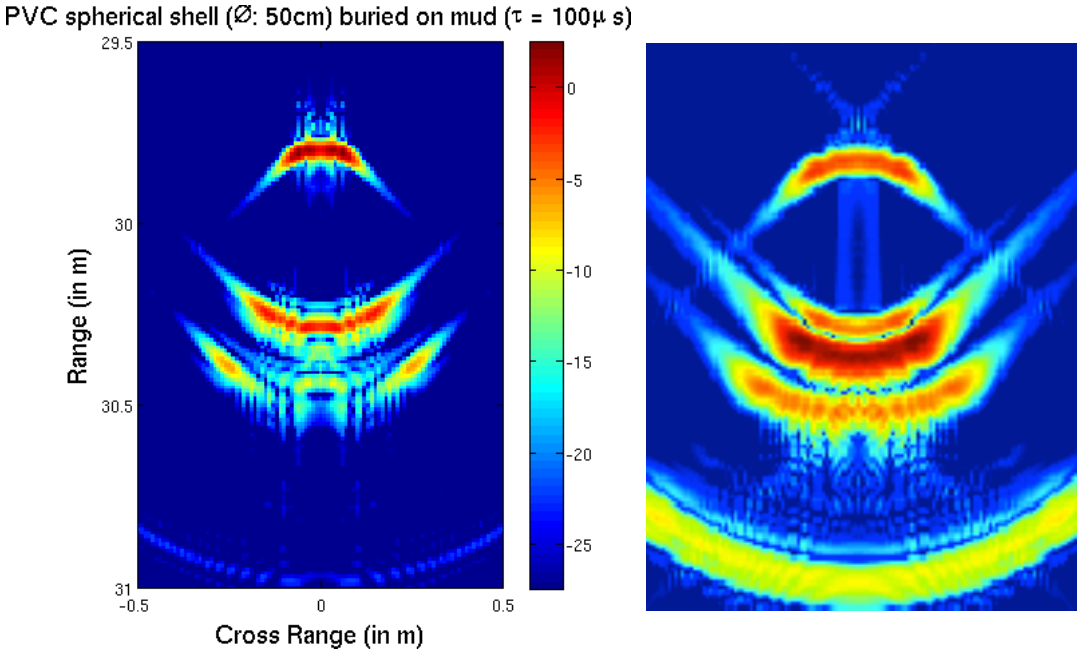

Figure 4.19: (*left*) Synthetic LF-SAS image of the PVC spherical shell lying under a flat muddy seafloor. (*right*) Synthetic LF-SAS image of the same target in free water.

the target echo using a HF-SAS is way below the reverberation level and therefore a HF-SAS simply cannot image buried targets.

4.6 Kirchhoff Model for Target Echoes

In previous sections, the study has focussed on simple targets (multi-layer spheres). The reason behind this choice is that only very simple shape objects, such as spheres or infinite cylinders, have an analytical solution to the scattering problem. Man-made objects often have more complex shapes. In this section, we study a Kirchhoff model to characterise target echoes for complex shaped targets.

Figure 4.20: Picture of a Manta underwater mine. (*courtesy of S.E.I.*)

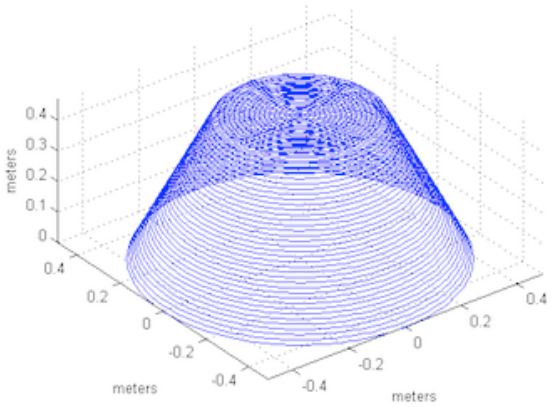

Figure 4.21: 3D model of a truncated cone.

The study here focusses on truncated cone objects. The truncated cone is a geometrical approximation to the well known Manta mine (cf. Fig. 4.20). Figure 4.21 displays the 3D model of a truncated cone matching the dimensions of the Manta. Because there is not an analytical solution to the scattering prob-

lem of a truncated cone, it is impossible to solve exactly the Helmholtz-Kirchhoff equation (cf. Eq. (4.36)).

For this reason, the following assumptions have been made:

1. the material is perfectly reflective
2. Kirchhoff approximation: each facet of the target acts as an infinite plane (Ponomarev and Yakubov [1976])

The consequences of these assumptions are: the pressure at the wet surface is equal to the incoming pressure (assumption 1.) and the normal displacement is null $u_n = 0$ (assumption 2.). So the pressure p in Eq. (4.36) is known. The Helmholtz-Kirchhoff equation becomes:

$$p(r_i) = \sum_j \frac{\partial G_{ij}}{\partial n_j} p(\tilde{r}_j) \mathrm{d}A_j \tag{4.42}$$

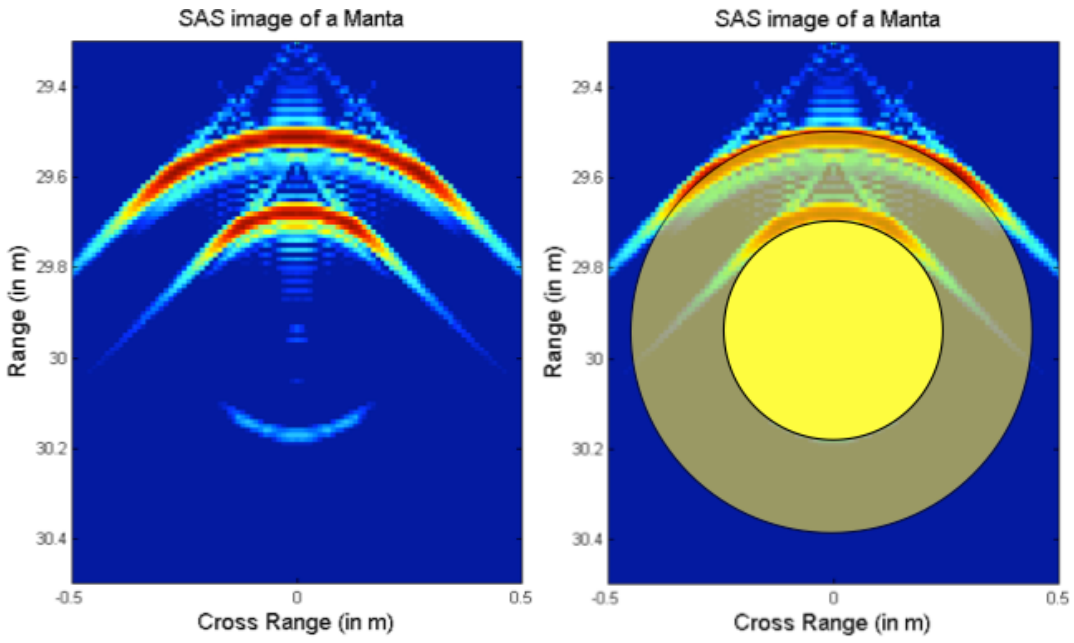

Figure 4.22: Numerical SAS image of a truncated cone shaped object using the Kirchhoff model.

4.7 Experiments

Two sets of experiments have been performed in the test tank at Heriot-Watt University. The aim of these experiments were to demonstrate the capabilities of a low frequency SAS system, and demonstrate the resonance target imaging and inner target imaging.

The sensors available do unfortunately not match the 5 - 50 kHz proposed for the LF-SAS design. Their frequency band is 30 - 130 kHz. The transmitted pulse used was a up-chirp from 30 to 130 kHz, with a time duration τ of 100 μs. The beamwidth of the transducer used for the experiments is 40°, which is about half of the design beamwidth.

The experiments took place in the test tank (dimensions: L $\times$ W $\times$ D: 4 m $\times$ 3 m $\times$ 2 m). The sensors (transmitter and receiver) were controlled by a cartesian robot which allowed us to simulate a perfect linear trajectory. The accuracy in location of the cartesian robot is sub-millimetric.

The first set of experiments investigate simple objects in free water. The second set aims to study the interaction with the bottom and the consequences for the imaging process.

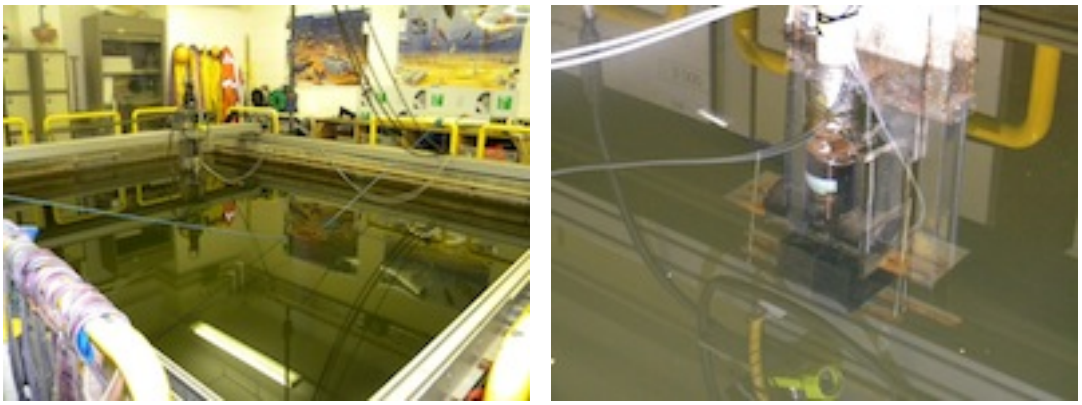

Figure 4.23: (*left*) HWU test tank with the cartesian robot. (*right*) Wideband transducer mounted on the cartesian robot.

Figure 4.23 shows a picture of the HWU test tank with the cartesian robot and a picture of the wideband transducers mounted on the cartesian robot.

4.7.1 Mid water experiments

In this first set of experiments, the targets are situated in mid water. The aim of this set of experiments is to validate the capability of LF-SAS systems to image resonances of the target and to show its capability to image inside the target. The two targets chosen for the mid-water experiments are a PVC cylindrical shell and the same PVC cylindrical shell with an aluminium cylindrical shell inside it. The two targets are shown in figure 4.24.

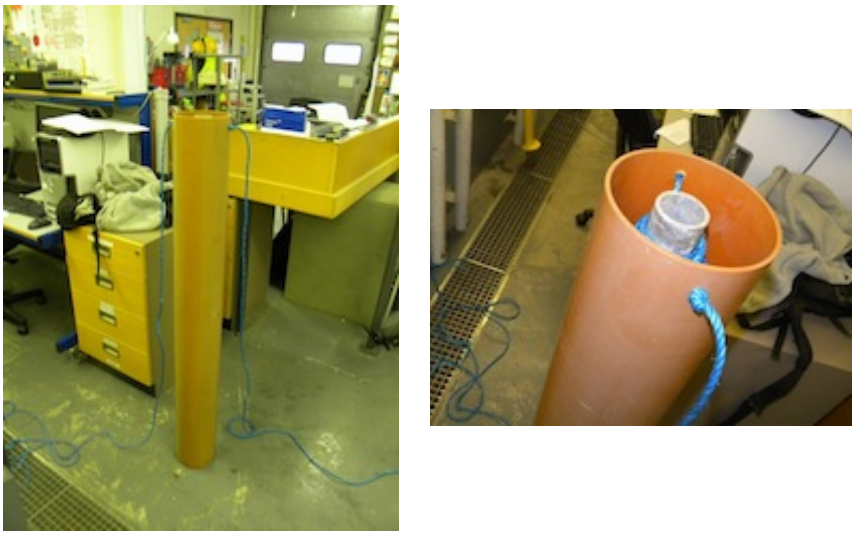

Figure 4.24: (*left*) Picture of the PVC cylinder target used for the free water experiments. (*right*) PVC cylinder with an aluminium cylinder inside.

The transducers are mounted in the cartesian robot 80 cm below the surface pointing horizontally to the water surface and perpendicularly to the linear trajectory. The targets are situated around 2 m from the synthetic antenna. The transducers send and record along the virtual trajectory every centimetre. The resulting SAS images are computed using the compressing algorithms described in section 4.2.

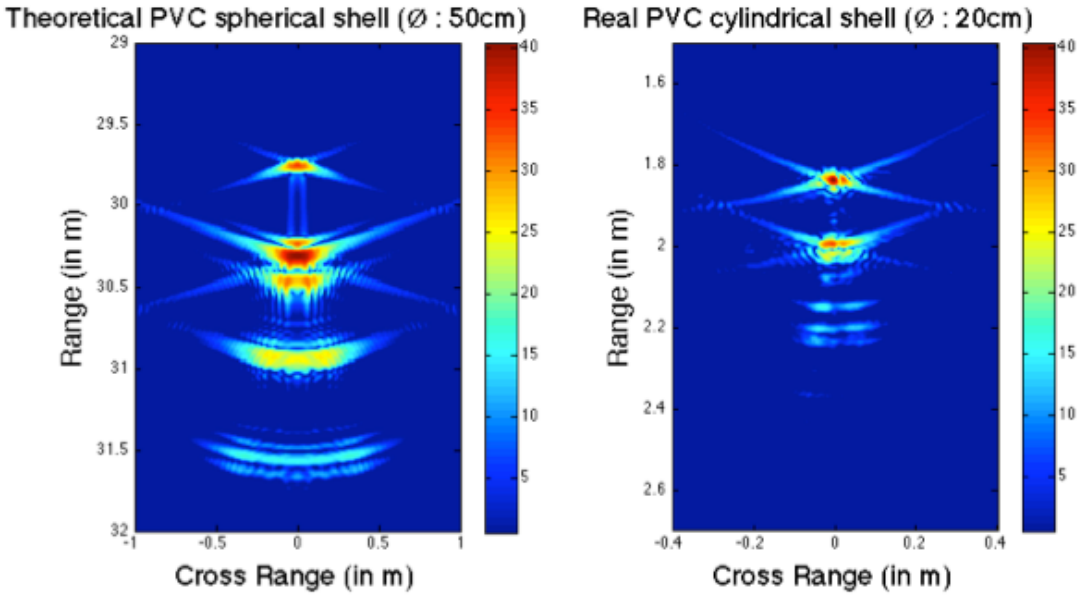

Figure 4.25: (*left*) Synthetic SAS image of a PVC sphere. (*right*) Empirical SAS image of the empty PVC cylinder.

Figure 4.25 (*right*) shows the SAS image of the empty PVC cylindrical shell. The front face and the back face of the cylinder are clearly visible. A few dB below, the secondary echoes of the target are also clearly visible. In figure 4.25 (*left*) a synthetic SAS image of a PVC sphere is displayed for comparison. Note that the secondary echoes of the sphere are stronger than the cylinder because its back face focuses the sound in a similar manner as a spherical mirror (Pailhas et al. [2010]).

Figure 4.26 shows the SAS images of the two targets of interest. The inner aluminium cylinder is clearly visible in figure 4.26 (*right*). These two experiments show the capability of LF-SAS systems to image the resonances of targets and to image inside the target.

4.7.2 On the bottom experiments

Dense objects tend to drawn and to lie on the sea bottom rather than floating in the sea. As mentioned in section 4.4, the reverberation level is generally the

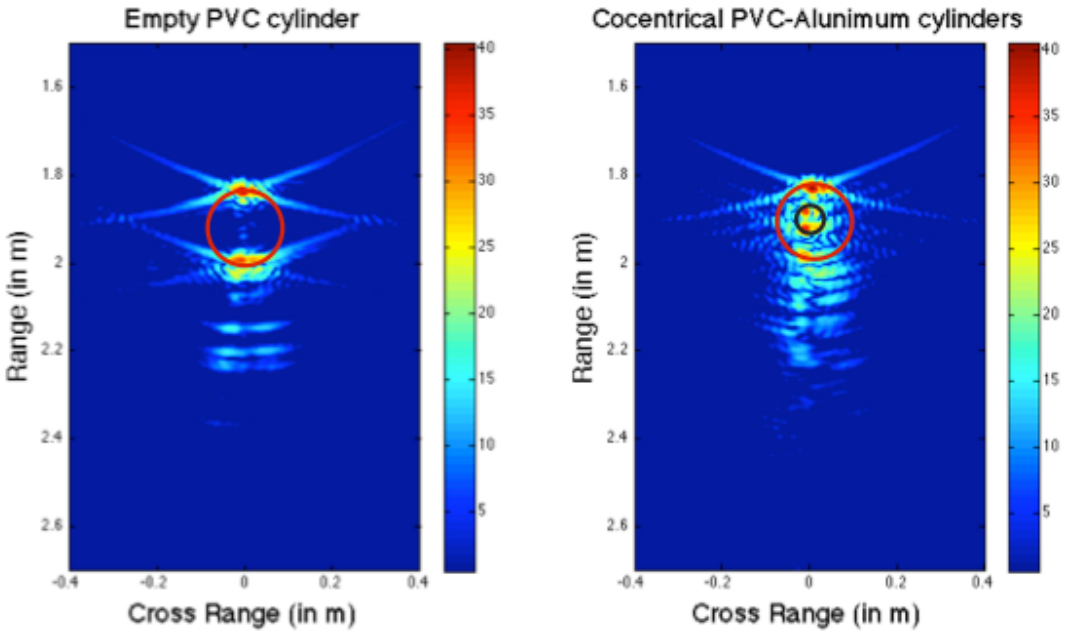

Figure 4.26: (*left*) SAS image of the empty PVC cylinder. The red circle indicates the cylinder position (*right*) SAS image of the PVC cylindrical shell with the aluminium cylinder inside. The red circle indicates the position of the PVC cylinder and the black circle indicates the position of the aluminium cylinder.

main source of noise from an image point of view and a limiting factor for tasks such as detection / identification / classification of man-made objects.

In this set of experiments, the targets have been put on the bottom of the test tank. To increase the realism of the experiments, 20 centimetres of fine sand covers the concrete floor of the tank.

For this set of experiments, spherical targets have been built: A steel spherical shell with 28 cm diameter and 1mm wall thickness, a PVC spherical shell with 28 cm diameter and 1 cm wall thickness and a plain concrete sphere of 25 cm diameter. Figure 4.27 displays a picture of the three spherical targets used.

As with the experiments described in section 4.7.1, the raw SAS data is generated along a linear trajectory using the cartesian robot for a sub-millimetric localisation precision. The altitude of the transducers is 1.2 metres and the tar-

Figure 4.27: Set of spherical targets used for the bottom experiments. From left to right: steel spherical shell (Ø: 38 cm), PVC spherical shell (Ø: 28 cm) and concrete sphere (Ø: 25 cm).

gets are located at around 2 metres ground range from the transducers. The heading of the transducers is 27°, which corresponds to a direct illumination of the target when the transducers are in line with the target.

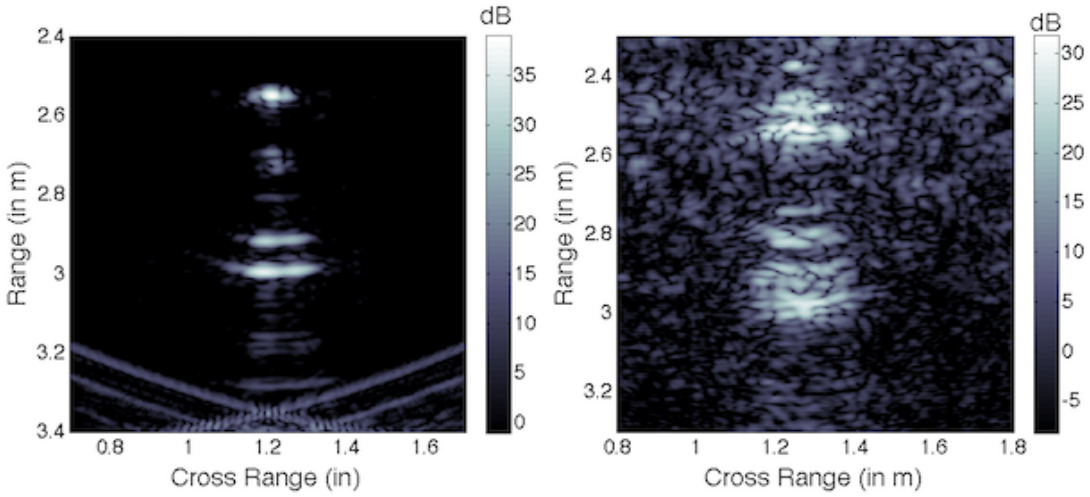

Figure 4.28: (*left*) SAS image of the steel spherical object in free water. (*right*) SAS image of the same target lying on the sandy tank floor.

Figure 4.28 displays the SAS image of the steel spherical shell in mid water (*left*) and lying on the tank bottom (*right*). As section 4.5 suggested, the two SAS images are not identical. The three main echo contributions for the steel sphere in mid water are visible in figure 4.28 (*left*): the specular echo at range 2.55 m and cross range 1.2 m, and the two Lamb waves S_0 and A_0 respectively at range 2.9 m and 3 m. Note that the aperture of the specular echo reflects the 20° beamwidth of the transducers.

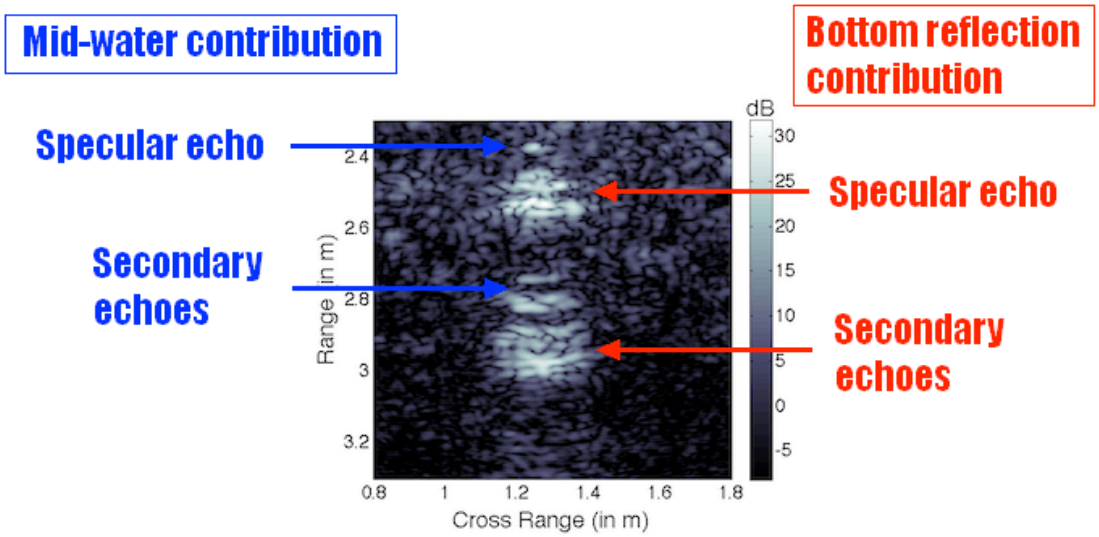

Figure 4.29: Experimental SAS image of the steel spherical shell.

Because of the set up of the experiment and especially the high grazing angle, the direct contribution and the bottom contribution to the target echo are spatially separated. As suggested in section 4.5, we can approximate the full echo as the sum of a mid-water only contribution and a bottom reflection contribution (where the acoustic wave interacts at least once with the bottom). Figure 4.29 displays the SAS image of the steel sphere. It appears clearly that the two contributions are spatially distinct. This is due to the path difference between the wave directly hitting the target, and the wave hitting the target after bouncing to the bottom.

It is interesting to compare this experimental result with the numerical result obtained in section 4.5.2.1. In figure 4.17, the specular echo from the bottom contribution as the same aperture than the specular echo from the mid-water contribution. The aperture of the specular echo from the bottom reflection contribution in the experimental SAS image is much higher than the mid-water specular echo (around 90° instead of the 20° of the transducers beamwidth). Another point of interest: the bottom reflection contribution echoes from the experiment are much more diffused and textured than the one predicted by the numerical simulation in 4.5.2.1.

The numerical results of section 4.5.2.1 and the experimental results described in this section confirm that the bottom interaction plays an active role in the image formation. Section 4.8 proposes several models to explain and simulate the bottom interaction in the SAS image formation.

4.8 On rough interface interactions

4.8.1 About the disagreement between numerical models and experimental results

In the previous sections of this chapter we developed models and algorithms to compute synthetic SAS images based on the exact analytical backscattering echo solution or Kirchhoff model for complex targets. With those simulations we were able to model and understand the formation of the specular echo and resonances of an object in a SAS image. Assuming a perfectly flat seabed an approximation of the Green's function taking into account the interaction with the interface can be computed. The synthetic SAS images computed highlight the active role that the seafloor is playing in the image formation.

However these models do not explain why the target echo in a SAS image is not confined to the horizontal beam aperture of the transducers. In figure 4.30 we compare a synthetic SAS image of a truncated cone (Manta mine-like object) obtained with our Kirchhoff model with a real SAS image of the same object. Note that in this simulated image we used the same aperture beam angle of 7° as the SAS MUSCLE system.

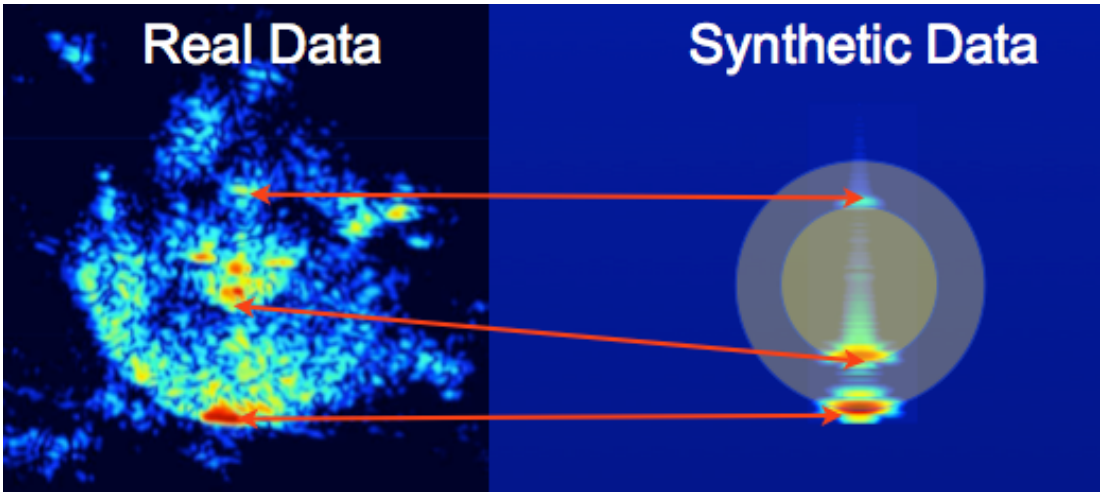

Figure 4.30: Comparison between NURC-SAS image of a Manta-like object and the numerical Kirchhoff model of the same object.

It appears the Kirchhoff model explains well the specular echoes of the target, but does not explain why the full object is visible in a real SAS image. This observation is similar with the one we have done in section 4.7.2 where we identify the different echo contributions in the experimental data.

In this section we take the hypothesis that the seafloor plays an even more important role in the image formation that the results of section 4.5. By assuming the seafloor rough instead of perfectly flat we aim to explain the virtual larger aperture of SAS system and explain the full image formation.

4.8.2 Models to simulate the bottom interaction

4.8.2.1 Kirchhoff approximation with rough seafloor hypothesis

The numerical simulations from section 4.5, based on the derivation of the Green's function, predict the bottom reflection contributions (cf. Eq. (4.37)) but cannot explain the aperture of the specular echo from the bottom reflection contribution nor its texture. In this section we propose a model to simulate the bottom reflection contribution.

We are focusing our study on the bottom reflection contribution of the echo. The notations and the configuration of the model is illustrated in figure 4.31. We assume that the sound is reflected by the rough seabed area situated in front of the target to the target itself and back propagated toward the transducer.

We chose a Kirchhoff approximation from Ponomarev and Yakubov [1976] to model the sound interacting with the target. The implications of this assumption is described in section 4.8.2.1. A small perturbation fluid model is used to model the reflection of the sound with the rough seabed (cf. section 4.4.2). As has been mentioned in section 4.5, there is no analytical solution to this scattering problem, and it is impossible to solve exactly the Helmholtz-Kirchhoff equation.

For this reason, the following assumptions have been made:

1. the material is perfectly reflective

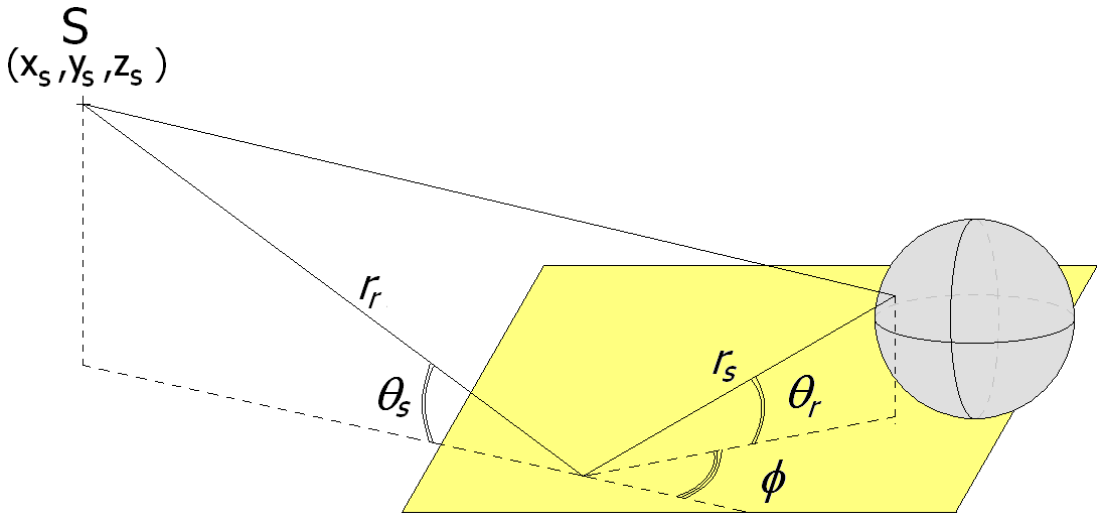

Figure 4.31: Notations and configuration of the Kirchhoff approximation with rough seafloor hypothesis model.

2. Kirchhoff approximation: each facet of the target acts as an infinite plane

The consequences of these assumptions are: the pressure at the wet surface is equal to the incoming pressure (assumption 1.), and the normal displacement is null $u_n = 0$ (assumption 2.). So the pressure p in Eq. (4.36) is known. The Helmholtz-Kirchhoff equation becomes:

$$p(r_i) = \sum_j \frac{\partial G_{ij}}{\partial n_j} p(\tilde{r}_j) \mathrm{d}A_j \tag{4.43}$$

Assuming the incoming pressure on the wet surface of the target is known, Eq. (4.43) allows the computation of the backscattering echo.

4.8.2.2 Results

A heightmap modelling the seabed interface has been generated using fractals. The target of interest here is a sphere of 50 cm diameter lying on sand, the sediment is modelled as a fluid. Eq. (4.34) gives the pressure field on the wet surface of the target. Finally Eq. (4.43) computes the backscattering echo.

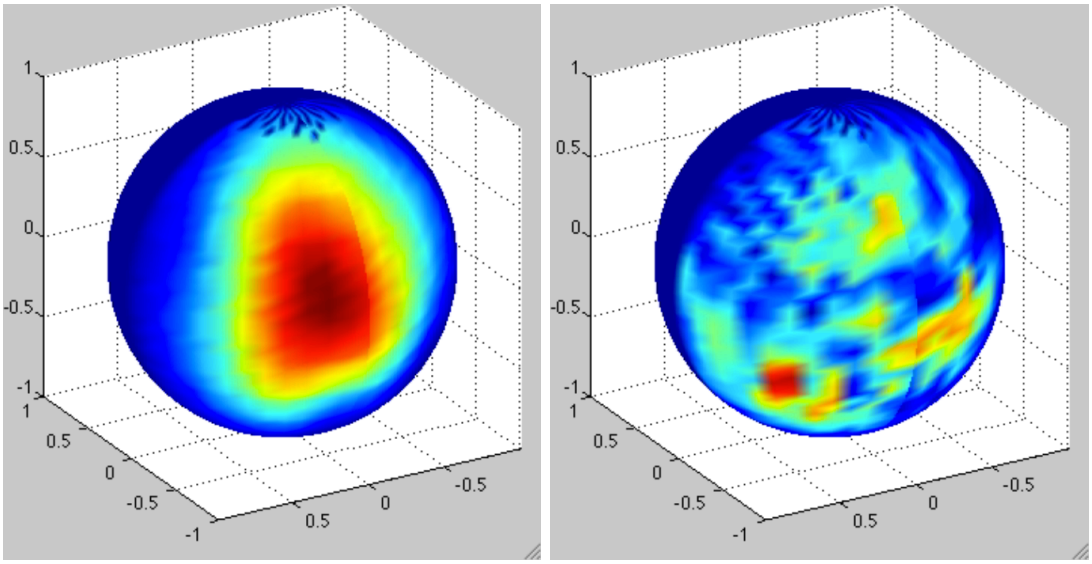

Figure 4.32: Magnitude of the scattered field $\phi(f)$ from the interface projected on the sphere target at (*left*) 5 kHz and (*right*) 50 kHz.

Figure 4.32 displays the normalised magnitude of the scattered field $\phi(f)$ from the interface projected on the sphere target at different frequencies. A 5 kHz frequency corresponds to a 30 cm wavelength. The wavelength is much larger than the roughness of the interface and the interface acts as a plane mirror. At 50 kHz frequency, the wavelength is 3 cm, close to the 1 cm roughness of the interface. The sound is diffracted by the interface. The texture of the seabed appears to be *projected* onto the target.

We assume here that the LF-SAS system has a beamwidth aperture of 20°. The sphere is located at 20 m ground range from the SAS trajectory, and the SAS system is flying at an altitude of 5 m.

Figure 4.33 (*right*) displays the synthetic SAS image of the bottom reflection contribution of the sphere using our model. A synthetic SAS image of the same sphere in free water (figure 4.33 (*left*)) is shown for comparison.

The Kirchhoff approximation with rough seafloor hypothesis model explains the aperture of the bottom reflection contribution of the specular echo. The synthetic

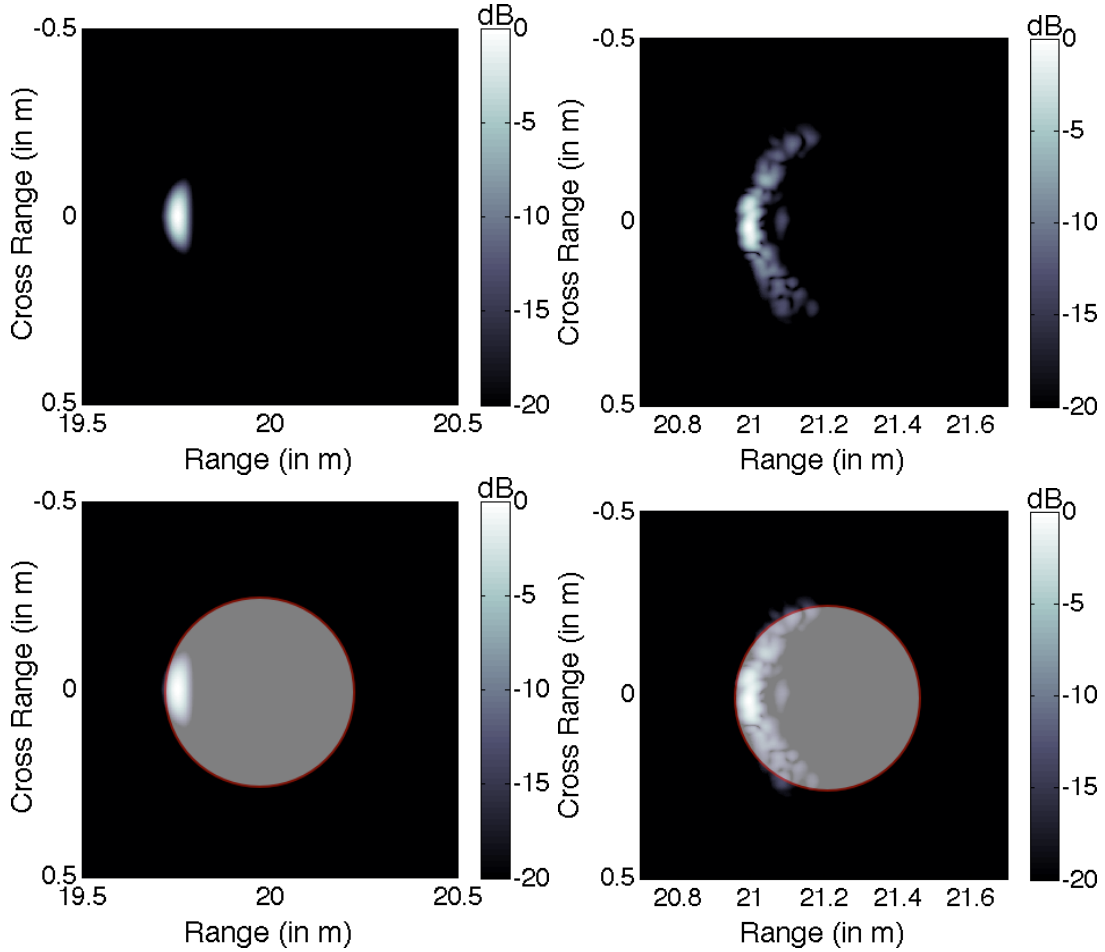

Figure 4.33: (*left*) SAS image of a perfectly reflective sphere in free water. (*right*) SAS image of a perfectly reflective sphere lying on the seabed computed using our model. On the bottom images we have just superimpose to the results above the shape of the target being imaged.

specular echo appears textured like in the experiments that are described in section 5.5.

It is interesting to compare the seabed reflection phenomena with the reflection of light that we can find in optical images. Figure 4.34 illustrates an example of a scene reflected in the water. Because this image is fundamentally an angular image, the real landscape and its virtual image are projected on two spatially distinct planes.

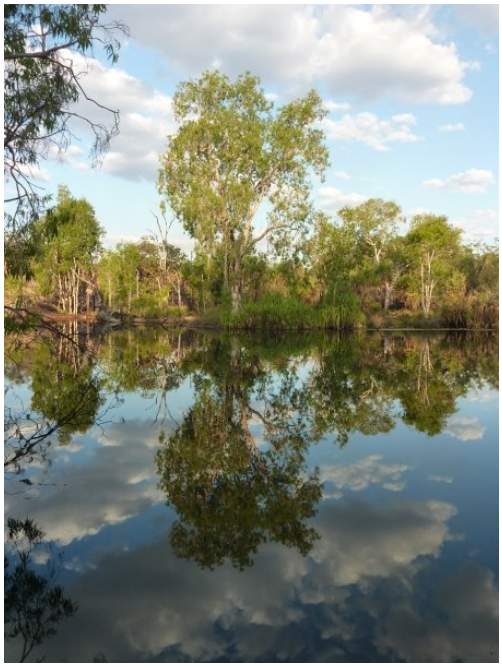

Figure 4.34: Photographic image picturing the sky and a forest reflected on a calm lake.

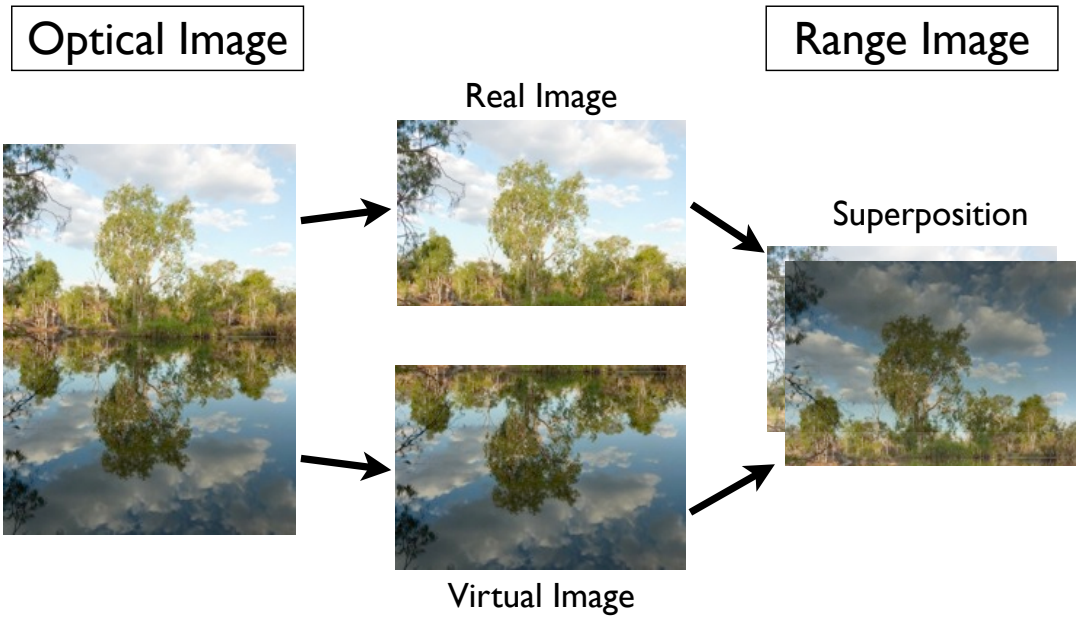

Figure 4.35: Photomontage featuring the superposition of the real image with the virtual image in a range projection.

Figure 4.35 is a photomontage featuring what figure 4.34 would look like if it were a range image. The figure considers the same scene but from a range point of view: using this analogy the real optical image corresponds to the direct path (*i.e.* the echo contribution going directly from the sensor to the target (here the tree) and back to the sensor). The optical virtual image (the reflection of the tree in the lake) corresponds to the indirect path. If the photo in figure 4.35 were a range image, the real image and the virtual image of the tree would superpose to each other in the range projection plane. The observer would effectively see one unique tree.

4.9 Conclusions

In this chapter we have proposed the design of a low frequency SAS system. We have demonstrated that with such system it is possible to image the inside of complex targets. This feature could greatly help to distinguish between rocks and mines. We propose several models and algorithms to synthesise artificial SAS images based on the analytical solution for the backscattering echo of simple targets or using the Kirchhoff model for more complex targets.

In parallel we have studied SAS image formation and have proved that the seabed reflection plays an active role during the imaging process. We have demonstrated that the specular echo, the diffracted echo and the backscattered resonances is the result of the direct path contribution. The shape and the texture of the target in a SAS image is however due to the reflection of the seabed. Finally we have proposed a method in order to simulate accurately SAS images of objects lying on the seabed.

Chapter 5

Bio-Inspired Sonar

5.1 Introduction

SONAR (SOund Navigation And Ranging) was invented and developed during the first world war based on observations of dolphins (in water) and bats (in air) with their capabilities to detect objects and navigate into a 3D world. Sonar systems have evolved dramatically since then from a simple ranging system to complex sonar imaging systems. The latest technology developed is the SAS system (Synthetic Aperture Sonar) which is based on the ideas from SAR (Synthetic Aperture Radar) technology. SAS systems provide sidescan-like images with a constant centimetric resolution over the whole range. In order to increase the sonar resolution and by doing so the overall quality of sonar images, manufacturers have chosen to increase the frequency. The resolution is linearly dependant on the wavelength λ ($\lambda = c/f$ where c is the sound speed in water and f the frequency). The final image is computed using only the amplitude of the signal. The main reason behind this is that we (humans) are more comfortable with an optic-like incoherent image. Sonar was inspired by dolphins and bats in its early stages, but now its practical engineering has evolved toward an imaging system.

The excellent acoustic target detection and identification capabilities of the bottlenose dolphin (*Tursiops truncatus*) are well documented (Au [1993]). Dolphins consistently outperform fabricated systems, especially in complex acoustic

environments such as shallow water or over cluttered seabeds. Working in these difficult environments the clicks and patterns of interpretation used must be robust to noise, and reverberation noise in particular. Compared to conventional narrowband sonar, wideband dolphin-like signals are expected to provide some improvement through pulse compression, and for certain difficult maritime targets have been shown to provide improved detection ranges (Lew [1996]; Pailhas et al. [2005]). Recognition is a more complex task and research has shown that dolphins can learn to distinguish objects' shapes, materials and contents acoustically (Nachtigall [1980]). Even though the interpretation and identification requires complex analysis, this shows that the information hidden in the return signal contains target parameters that are useful for classification purposes.

Chapters 2, 3 and 4 focussed on imaging sonars *i.e.* the amplitude of the backscattering echo. We demonstrate that as the sonar resolution increases the extractable information increases as well. Geometrical features of an object such as dimensions and shape can be extracted from a sidescan or a SAS image. In this chapter we step back from the classical imaging sonar systems and analyse why dolphin's sonars perform so well. In particular, we demonstrate that the phase of the backscattering echo contains useful information of the ensonified target such as structure, composition, thickness, *etc.*

Based on observations from dolphins we present our approach to a bio-mimetic sonar system. This approach (cf. section 5.2) focusses essentially on two points: a diversity of broadband outgoing pulses and a fine analysis of the backscattering echo. The echo analysis from broadband sonar demands an understanding of the echo structure and echo formation. Section 5.4 presents numerous models to interpret, analyse and synthesise broadband echoes. We present in section 5.5 experiments conducted with a bio-mimetic sonar which validate the models we introduced earlier. We propose in section 5.6 new features and metrics and show how a target can be identified unambiguously.

Finally in section 5.7 we present our prototype of an AUV ready bio-mimetic sonar: the BioSonar. We show two applications of the BioSonar and how it out-

performs traditional sonar. In section 5.7.2 we describe how a bio-mimetic sonar can be used in the MCM (mine counter measure) context. Then in section 5.7.3 we show its performance in cable tracking.

5.2 BioSonar

5.2.1 The dolphins' sonar

Dolphin sonar is the result of a million years of evolution. The dolphin echolocation systems are well known for their excellent performance and have been studied for decades (Au [1993]). They significantly outperform man-made sonars. They have shown excellent capabilities for object detection and identification, especially in complex environments such as very shallow water and cluttered locations. As an example, Moore et al. [1991] studied the capability of dolphins to identify the contents of an aluminium flask bottle suspended in mid-water. Because of their excellent capability and intelligence the US navy have trained dolphins for complicated tasks such as mine detection and harbour inspection.

5.2.1.1 The dolphins' click taxonomy

Based on observations of dolphins' echolocation clicks, Houser et al. [1999] introduced a taxonomy for the variety of clicks emitted based on their frequency content. The taxonomy is described in Table 5.1. This particular click taxonomy identified several click types based on distributions in two main spectral regions, one at low frequency (<70 kHz) and the other at higher frequency (>70 kHz).

In Martin et al. [2003] and Houser et al. [2005], the authors collect the echolocation clicks produced by dolphins while they are performing bottom-object searches in San Diego Bay. Two dolphins were trained specifically for this experiment. The echolocation clicks and their corresponding echoes were recorded using an instrumentation package, the biosonar measurement tool (BMT). The tool was carried by the dolphins.

A	unimodal, low frequency (<70 kHz)
B	unimodal, low frequency (<70 kHz); 2nd peak (>70 kHz) between -3 and -10 dB down
C	bimodal; low and high frequency peaks within -3 dB
D	unimodal, high frequency (>70 kHz)
E	unimodal, high frequency (>70 kHz); 2nd peak (<70 kHz) between -3 and -10 dB down
W	wideband; single continuous bounded region within -3 dB limit (freq. bandwidth >85 kHz)
M	multimodal; three or more distinctly bounded regions within -3 dB limit

Table 5.1: Click taxonomy from Houser et al. [1999]

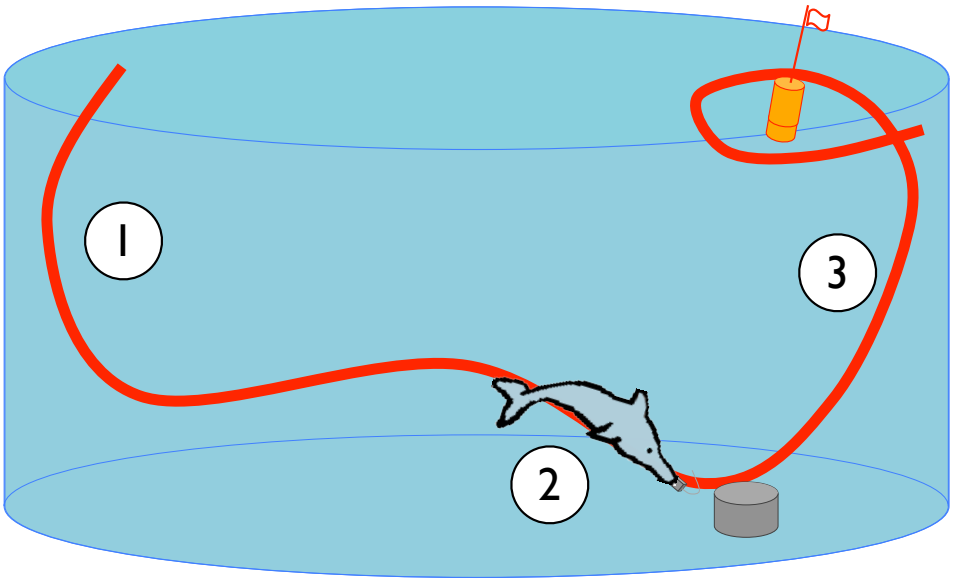

Figure 5.1: Dolphin's behaviour during the free-swimming experiment. **(1)** detection and localisation of the target, **(2)** target identification and **(3)** return to the boat.

Figure 5.1 shows a sketch of the dolphin's behaviour during the free-swimming experiment. During phases 1 and 3, the dolphin is respectively searching for the target on the seafloor and the boat at the surface. The clicks emitted during these detection phases are typically low frequency (predominantly type A). When the dolphin finds the target (phase 2), it starts an interrogation strategy, *pinging*

the target more frequently. The variety of clicks used during the interrogation is much larger than during the other phases, and the click pattern contains all of the click types described by Houser in the taxonomy.

5.2.1.2 Dolphins' click analysis

Dolphins' echolocation clicks are very short impulsive sounds. A typical click duration is around 80 μs (Au [1993]). For this reason, related to the uncertainty principle (Cohen [1995]), classical time frequency representations such as the spectrogram or Wigner-Ville distribution struggle to extract meaningful structure within the pulse without *prior* knowledge.

In Capus and Brown [2003] and Bultan [1999], the authors studied the echolocation clicks of the big brown bat (*Eptesicus fuscus*). Time-frequency analyses indicated that these signals are made up of three or four distinct downchirp components. By analogy we look for downchirps in the dolphin clicks. Linearisation of the problem leads to the emphasis of linear downchirp components in the dolphin clicks. This can be achieved by computing the fractional Fourier transform (FrFT) of the signal. The fractional Fourier transform of a function $f(x)$ is given by Eq. (5.1)

$$\begin{aligned} F^{\alpha}f(x) = \quad & \frac{\exp\left(-j\left(\frac{1}{4}\pi\hat{\phi}-\frac{1}{2}\phi\right)\right)}{2\pi|\sin\phi|^{1/2}}\exp\left(\tfrac{1}{2}jy^2\cot\phi\right) \\ & \times\int_{-\infty}^{+\infty}\exp\left(-\tfrac{jxy}{\sin\phi}+\tfrac{1}{2}jx^2\cot\phi\right)f(x)\mathrm{d}x \end{aligned} \tag{5.1}$$

where $\alpha \in [0,\ 1]$ represents the transform order, $\phi = \alpha(\pi/2)$ and $\hat{\phi} = \mathrm{sgn}(\phi)$.

Figure 5.2*(left)* displays the time representation of a type B dolphin click. In figure 5.2*(right)* the power spectra of the same click are computed using the classical Fourier transform and the fractional Fourier transform.

The two concentrations of energy in the FrFT representation of the type B click in figure 5.2*(right)* confirm the presence of two chirp components. Figure 5.3 displays a short-time FrFT of the same signal. A double downchirp structure

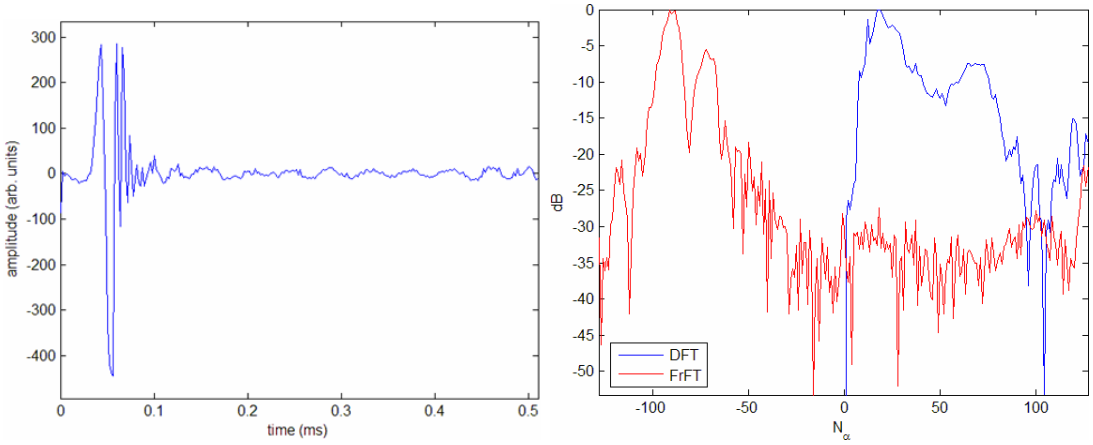

Figure 5.2: Representation of a type B dolphin click in the time domain *(left)* and Fourier and Fractional Fourier domain *(right)*.

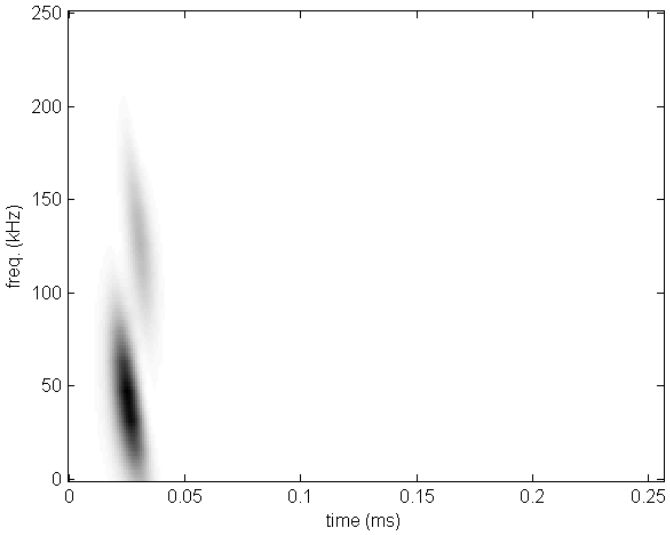

Figure 5.3: Time-frequency representation of the type B dolphin click from Fig. 5.2 using the squared modulus of the short-time fractional Fourier transform.

is clearly visible here. This observation matches with the echolocation pulses analysis from other mammals using sonar such as bats or whales.

5.2.2 BioSonar principles

So what makes dolphins' sonars so efficient? The short answer lies in the fact that they have a brain directly linked to their sonar system and are able to analyse directly the echoes. But one can argue that sonar experts struggle to find their objects of interest in a very cluttered environment even by analysing very high resolution images such as SAS images. Two elements of response to this question are given by analysing the dolphins' behaviour (especially their click pattern when they perform identification tasks) and the simplifications of man-made sonar systems:

- Complex broadband clicks: conventional sonars use narrowband transmitted pulses. Dolphins are using a variety of broadband clicks and studies show that the diversity of clicks is adapted to the current task and environment.

- Fine echo analysis (the forgotten phase): in classical sonar processing, we highlighted the fact that only the amplitude of the signal is usually used for the image processing. By doing so a tremendous amount of information is ignored.

Our approach to a bio-mimetic sonar system aims to resolve the two points previously highlighted:

- Biomimetic dolphin-like signals are built based on the analysis of real dolphins' clicks. We show in section 5.3 that we can reconstruct the whole click variety of the dolphins' clicks taxonomy.

- A fine echo analysis is proposed in order to take into account the forgotten phase of the signal. In section 5.4 we analyse the content of backscattering echoes and propose models to understand the echo formation. In particular we show that any object has characteristic acoustic resonances, which can be extracted and used as features for classification / identification.

5.3 Biomimetic pulses

The click taxonomy for dolphins described in section 5.2.1 has identified several click types based on distributions in two main spectral regions, one at low frequency (<70 kHz) and the other at higher frequency (>70 kHz) (Houser et al. [1999]). From these observations Capus et al. [2007] proposed a model for construction of bio-mimetic dolphin-like pulses based on double down-chirp components, overlapping in both the time and frequency domains (Capus et al. [2007]). An interesting parallel can be drawn with pulses used by the echolocating big brown bat (*Eptesicus fuscus*). Similar time-frequency analyses have indicated that these signals are made up of three or four distinct downchirp components (cf. Bultan [1999]; Capus and Brown [2003]).

Demands on transducer and processing hardware are mitigated to some degree by making the pulses around 50% longer than natural dolphin signals, with a time duration of 120 μs. The pulses cover a similar bandwidth to natural dolphin clicks ($30-130$ kHz) and the two downchirp components, each bounded by a Gaussian time window of $6\sigma = 100$ μs, are separated by 20 μs. Following from analyses of clicks emitted by real dolphins performing target detection and localization tasks, the higher frequency chirp is always delayed relative to the lower frequency one. The only difference between the pulses is the bandwidth covered by the individual chirp components. Figure 5.4 displays the chirp components for the bio-inspired double chirp signals in the time-frequency plane.

In total six bio-mimetic pulses have been designed and named DCn where n varies from 1 to 6. All the pulses are based on the same model described earlier, and they only vary in the chirp rate (increasing linearly from DC1 to DC6). Their parameters are given in Table 5.2.

The time signals and power spectra for DC1, DC3 and DC6 are displayed in figure 5.5. Note that for signal DC1 the two chirps have relatively high rates and are significantly overlapping. This pulse would be classified unimodal high frequency, type D, in the Houser et al. [1999] taxonomy. The DC3 pulse has a

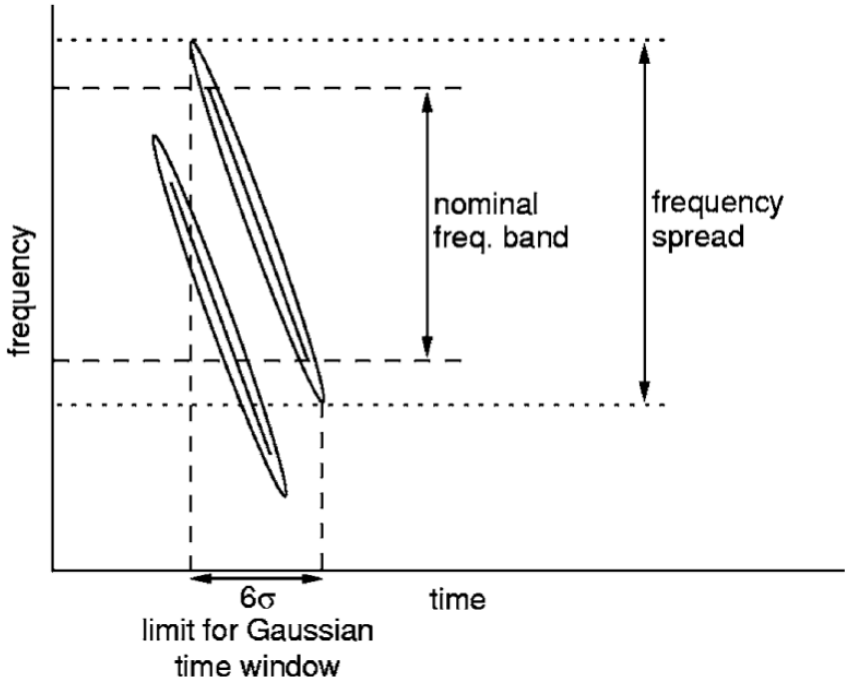

Figure 5.4: Time-frequency representation of the bio-inspired double chirp signals.

signal	Chirp rate (kHz.s^{-1})	Chirp 1	Chirp 2
DC1	-0.420 $\times$ 10^6	114 - 30 kHz	130 - 46 kHz
DC2	-0.375 $\times$ 10^6	105 - 30 kHz	130 - 55 kHz
DC3	-0.330 $\times$ 10^6	96 - 30 kHz	130 - 64 kHz
DC4	-0.300 $\times$ 10^6	90 - 30 kHz	130 - 70 kHz
DC5	-0.270 $\times$ 10^6	84 - 30 kHz	130 - 76 kHz
DC6	-0.240 $\times$ 10^6	78 - 30 kHz	130 - 82 kHz

Table 5.2: Set of the DCn pulses.

multimodal structure with three distinctly bounded regions and would be designated as type M. In DC6 the two chirp components are well separated and the frequency distribution is clearly bimodal, designated type C.

With only small changes in the chirp rate the double chirp structure of the bio-mimetic pulses present very different characteristics especially in the Fourier domain. Using a particular bio-mimetic pulse compared to another one focusses

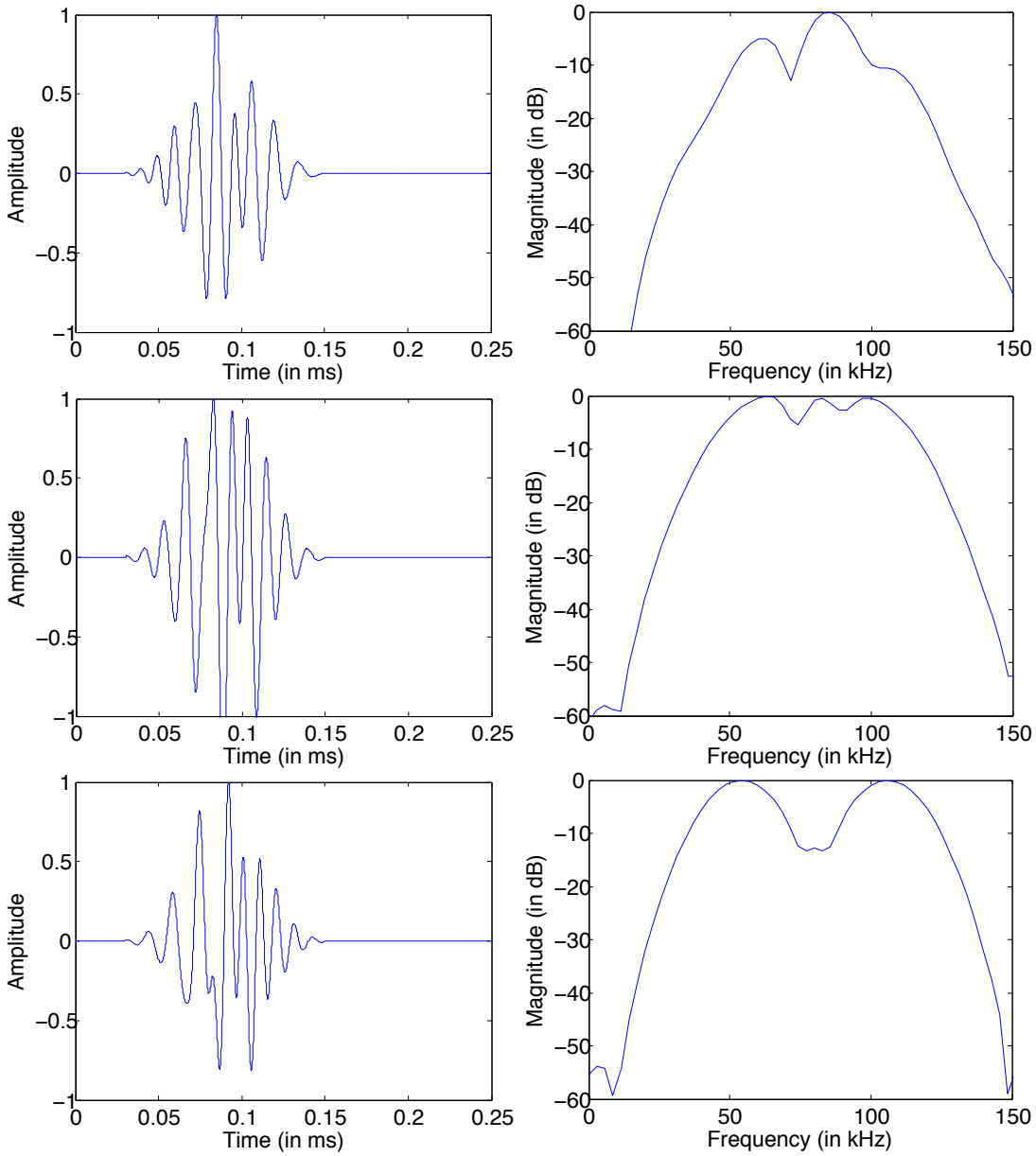

Figure 5.5: Examples of three bio-mimetic signals (from *top* to *bottom*): DC1, DC3 and DC6.

the energy on different frequencies. As we will demonstrate in the following sections an object can be characterised by the frequency content of its echo. We will see as well that the information relative to a particular ensonified object lies in a particular frequency band. Being able to steer the pulse energy on

certain frequency band increases the probability of identification of an object whose characteristic spectra lies inside this frequency band.

5.4 Broadband echo analysis

In previous chapters we highlighted the importance of acoustic modelling in order to understand, simulate or analyse any sonar data. In chapter 3 we studied sidescan sonar and we only needed the energetic expression of the sound to explain, model and synthesise sidescan images. In chapter 4 we explained that SAS images are formed from a coherent processing of the backscattered echo. So in order to compute synthetic SAS images we need the phase of the echo as well as its amplitude.

Biosonar systems demand the understanding of the full echo structure and the understanding of the echo formation. To aid understanding of the processes of echo formation in different sorts of targets, we provide here a brief discussion of the physics underlying acoustic backscattering from cylindrical shells, paying particular attention to the influence of different materials. We aim to link interferences in the echo spectra to the shape and material properties of the ensonified targets. Out of this study we propose models for the echo formation in section 5.4.3. Those models are then validated thanks to numerical simulations. A more general model for man-made object echo is then proposed in section 5.4.5.

5.4.1 Calculation of the Form Function

The main equation to solve is the wave propagation equation of the displacement $\vec{u}$ (see Rayleigh [1945]) . It can written as follows:

$$(\lambda + 2\mu)\vec{\nabla}.\vec{\nabla}.\vec{u} - 2\mu\vec{\nabla} \times \vec{\nabla} \times \vec{u} = \rho\frac{\partial^2\vec{u}}{\partial t^2} \tag{5.2}$$

where λ and μ represent the Lamé parameters and ρ the material density. Note that for a fluid the displacement $\vec{u}$ is linked to the pressure p through the following equation:

$$\vec{u} = -\frac{\vec{\nabla} p}{\omega^2 \rho} \tag{5.3}$$

where $\omega = 2\pi f$ represents the angular frequency.

An analytic solution for the pressure field scattered by simple shaped objects can be computed using a decomposition into individual modes. The case of the elastic cylindrical shell involves solving the system of equations by Cramer's rules, with the exact solution for an infinite cylindrical shell proposed by Doolittle and Uberall [1966]. This resolution comes from a modal decomposition, and in the case of far field backscatter we derive:

$$p_s = P_0 \sqrt{\frac{2}{\pi kr}} e^{jkr} e^{-j\pi/4} f_\infty e^{j\omega t} \tag{5.4}$$

Note that r represents the distance from the center of the cylinder to the receiver and k is the wavenumber. The form function f_∞ is given by: $\sum_{n=0}^{\infty} (-1)^n \epsilon_n b_n$. b_n is the solution of a system of equations and is determined by the ratio of two 6×6 determinants as suggested by Cramer. The scalar b_n is a function of the density and the compressional velocity of the two fluids inside and outside the cylinder, the dimensions (a and b respectively outer and inner diameters), the density, and the acoustic properties (c_l and c_s) of the cylinder material. As a result the form function f_∞ is a function of the frequency, the dimensions of the cylinder and its acoustic properties. To be more precise, the form function has the dependencies: $f_\infty(ka, k_L, k_T, a, b)$, where $k = 2\pi f / c_{water}$, $k_L = 2\pi f / c_l$ and $k_T = 2\pi f / c_s$. So for a given cylinder where dimensions and material are fixed, f_∞ is reduced to a function of the frequency alone. It is this dependency we will study in the following sections.

In our computation f_∞ is approximated by the truncated sum $\sum_{n=0}^{N} (-1)^n \epsilon_n b_n$ with $ka < N/2$. A justification of this approximation is given in appendix A. These results are defined for an incoming plane monochromatic sound wave. However an extension for any incoming pulse $g_i(t)$ was proposed by Hickling [1962]. This is a linear system resulting in the frequency representation of the

echo, $g_s(\omega)$ given in Eq. (5.5),

$$g_s(\omega) = \frac{a}{2r} f_\infty \int_{-\infty}^{+\infty} g_i(\tau) \mathrm{e}^{jka\tau} \mathrm{d}\tau \tag{5.5}$$

with $\tau = \frac{ct-r}{a}$. The theoretical echo in the time domain results from inverting this expression through the inverse Fourier transform.

5.4.2 Theoretical Predictions

We use the theoretical results from section 5.4.1 to calculate predicted echoes for two cylindrical shells: a PVC tube and a steel pipe. The cylinder parameters are taken from two real targets we have used extensively in experiments, see section 5.5.1. Stanton in Stanton [1989] has proposed some approximations derived from the ideal case to extend the formulae to finite and deformed cylinders. For the current case, finite straight cylinders, only a multiplicative factor depending on the length is required. The form function f_∞ does not change as long as the angle of incidence stays close to normal.

Material	Outer diameter a [m]	Inner diameter b [m]	Mass density ρ [kg.m^{-3}]	Compressional velocity c_l [m.s^{-1}]	Shear velocity c_s [m.s^{-1}]
PVC tube	0.170	0.164	1380	2380	1200
Steel pipe	0.168	0.142	7900	5900	3200
SIGG bottle (Aluminum)	0.0814	0.0798	2700	6420	3040

Table 5.3: Parameters used to compute the theoretical form functions of three cylindrical shells: a PVC tube; a steel pipe; and a thin walled aluminum flask (SIGG bottle). Note that all acoustical parameters can be found in Kino [1987]

The necessary parameters for the two cylinders and for a thin walled aluminium flask (SIGG bottle) used in some of the later experiments can be found in table 5.3. Figure 5.6 displays the form functions $|f_\infty|$ for the cylinders. We estimate from empirical data that the peak target strength of the steel pipe is approximately 1.6 dB above the target strength of the PVC tube. The theoretical computation gives a difference of 2 dB $\pm$ 1 dB in the range of 90 - 110 kHz, validating the measurement. An important point here is that at high frequencies (80

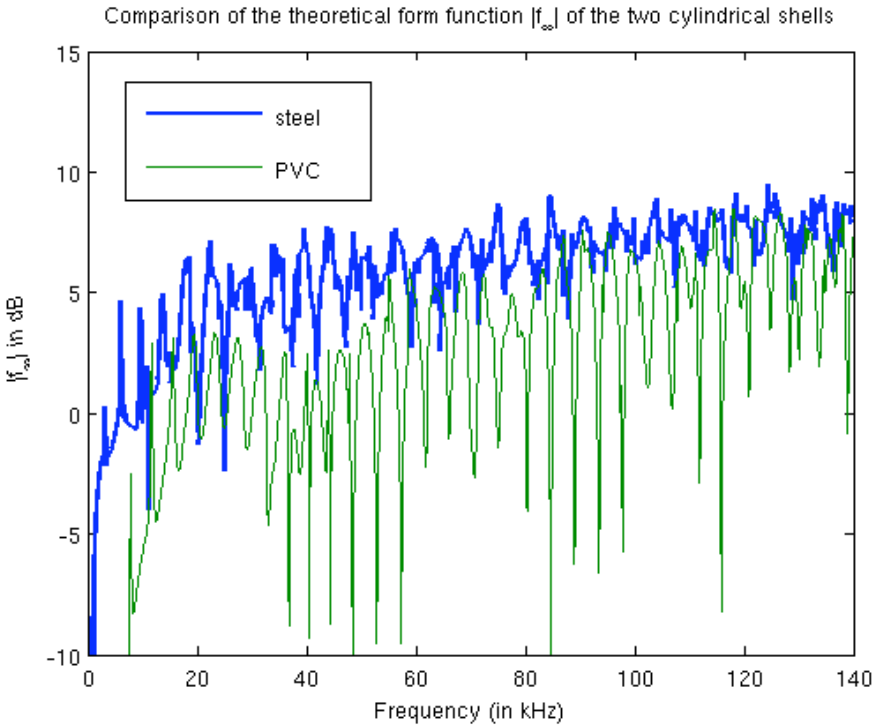

Figure 5.6: Theoretical form functions $|f_\infty|$ for the PVC tube and the steel pipe.

- 130 kHz) the peak values of $|f_\infty|$ for both materials are very similar. Conversely, at lower frequencies (30 - 80 kHz) the peaks are separated by 4.5 dB on average.

5.4.3 Echo structure modelling

The background acoustics theory presented in section 5.4.1 provides the basis for our target echo comparisons. For conventional narrowband sonar we would wish to avoid regions of the spectrum with strong oscillations in the form function since these could adversely affect detection of some objects. In the wideband case the oscillations will form the basis for classification and we target higher ka-values. Considering a bandwidth from 60 kHz to 130 kHz, with principal target dimensions of typically 10 - 20 cm, the investigation covers frequencies defined by the range ka from 10 to 50, where k is the wavenumber associated with wavelength λ and a is a key target dimension, e.g. radius for a cylinder. For these targets and frequency range, the Resonance Scattering Theory (RST) predicts the

presence of strong peaks and notches in the echo spectra (Gaunaurd and Strifors [1993]; Gaunaurd and Uberall [1983]; Hasan and Azimi-Sadjadi [1996]). The RST prediction simply stipulates that the distance between two principal scatterers in the target should be larger that one wavelength to create measurable interference effects and smaller than ten wavelengths for the interferences to be trackable.

The notches arise from destructiveinterference due to the integration in time of the different echoes. The first major contribution comes from the direct reflection and is called the specular echo. We are interested here in the time delay between the specular echo and large secondary echoes, since these time delays will determine the principal notch spacings.

5.4.3.1 Echo structure for cylindrical shell with low impedance material

Under the assumption that the first two major contributions to the echo are primarily due to reflections from the front and back walls of the PVC cylinder, the expected time spacing is approximated by,

$$\tau = 2\left(\frac{\delta}{c_{\text{cyl}}} + \frac{b}{c}\right) \tag{5.6}$$

where δ is the thickness of the wall, c_{cyl} the sound speed in the cylinder material, and b is the inner diameter.

This assumption is built on the observation that the tube wall is thin ($b/a \approx 0.96$), and the water/PVC impedance mismatch is small in comparison with metal. This allows acoustic transmission into the interior of the cylinder and the timing between the main echoes is expected to give a good approximation to the internal diameter: $b \approx \tau c/2$. Numerical simulation sheds more light on the processes of echo formation and allows us to develop a more accurate approximation based on an analogy with geometrical optics, see section 5.4.4.2.

5.4.3.2 Echo structure for cylindrical shell with high impedance material

In this case a purely geometrical interpretation of sound reflection cannot explain the echo structure. However the backscattering from the steel pipe can be predicted thanks to a generalization of the Geometrical Theory of Diffraction (GTD) in Kargl and Marston [1989]; Marston [1988]. Apart from the specular echo the return is mainly composed, at the frequencies of interest, by the asymmetrical A_0 and symmetrical S_0 Lamb waves. These are plane waves traveling around the wall of the cylinder and expressions for their phase velocities are given in Lamb [1917]. The group velocities can be derived directly from these expressions (Grigsby and Tajchman [1961]). Figure 5.7 plots the phase and group velocities matched to the thickness of the steel pipe.

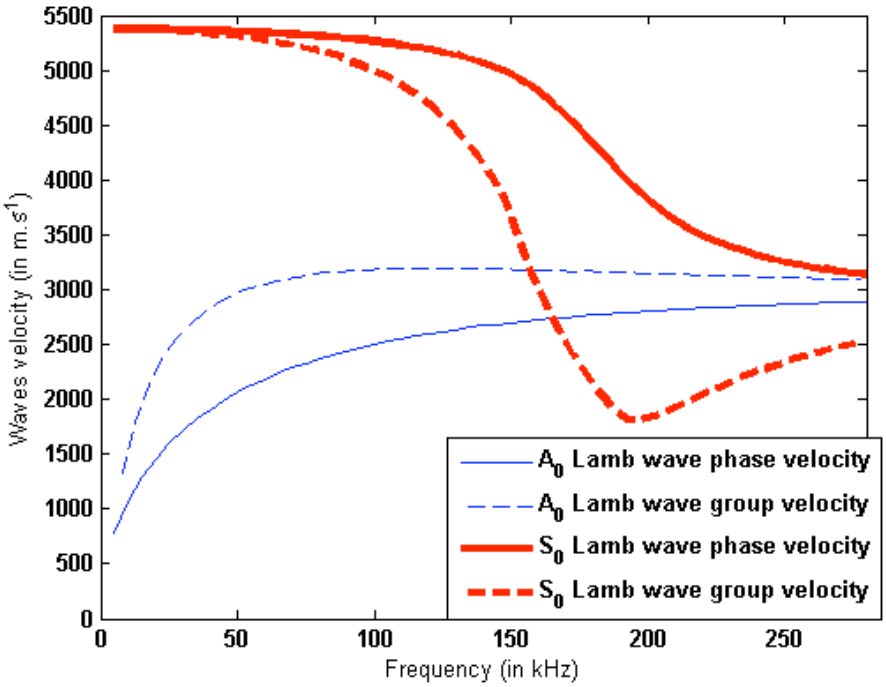

Figure 5.7: Dispersion plot of the phase and group velocities associated to the first Lamb waves A_0 and S_0 in a steel plate with 13 mm thickness.

According to the GTD, these plate waves are excited in the cylindrical shell close to the critical angle θ_c which refers to the relation:

$$\theta_c = \arcsin\left(\frac{c}{c_{plate}}\right) \tag{5.7}$$

where c_{plate} is the Lamb wave group velocity.

So the time delays between the specular echo and the Lamb waves can be evaluated by:

$$\tau = 2a\left(\frac{1-\cos\theta_c}{c} + \frac{\pi-\theta_c}{c_{plate}}\right) \tag{5.8}$$

The first term corresponds to the time difference between the specular reflection and the wavefront reaching the shell cylinder at the critical angle. The second term gives the time for the plate wave to go once around the cylinder and be diffracted again at $-\theta_c$ (cf. figure 5.8). Because of the range of frequencies we are working with (the majority of energy is condensed in the band 50 - 100 kHz), the group velocity of the Lamb wave is stable (less than 8% variation for both Lamb waves, cf. figure 5.7). This means that the propagation is relatively non-dispersive and the chirp rate and chirp duration for the secondary echoes are well preserved.

5.4.4 Numerical simulations

For more complex targets the theoretical analysis becomes intractable. In this section we demonstrate a numerical approach using a Finite Difference Time Domain (FDTD) simulator which provides a full wave equation solution as an alternative to analytic computation. The numerical model can also give new insights into the processes of echo formation to inform the development of new analytic solutions. Supported by simulations using FDTD, we propose a new model for the cylindrical shell with low impedance material based on an analogy with optical geometry.

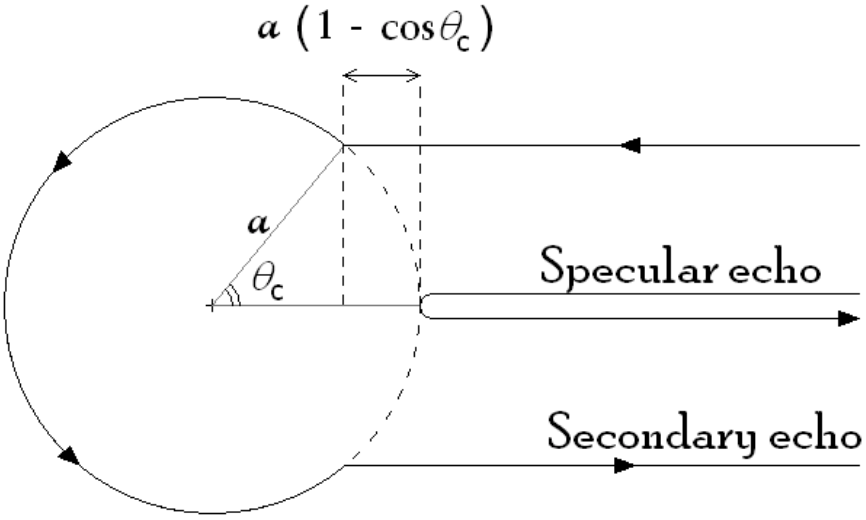

Figure 5.8: Echo formation for shell cylinder following the GTD. Display of the geometrical path taken by the specular echo and the secondary echo.

5.4.4.1 Numerical Approach: FDTD Simulator

The Finite-Difference Time Domain (FDTD) method solves the elastic wave equation by discretization of the time-space domain (Collatz [1966]). This method takes into account the shear velocity within a solid object and so is able to model target resonances (cf. Lianantonakis and Bell [2003]). For an idealised infinite cylindrical shell, simulations can be run in two dimensions. Visualised as a circular cross section, these provide a good approximation to the behaviour of the finite cylinder at broadside incidence.

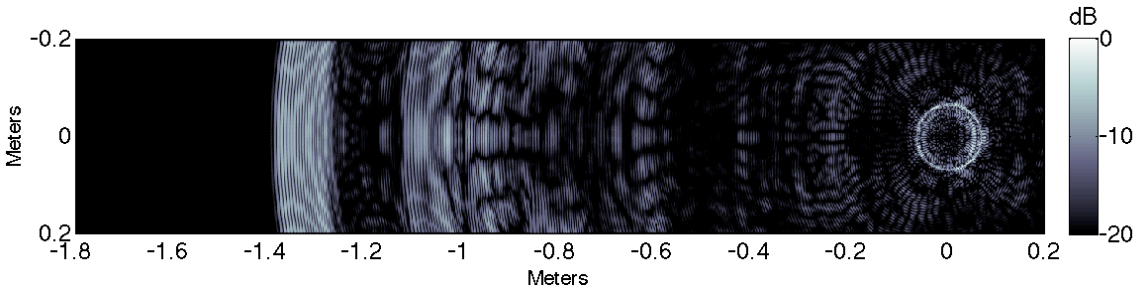

Figure 5.9: FDTD simulation showing the normalized sound pressure (in dB) for the echo of a PVC tube ensonified with a linear chirp.

Figure 5.9 provides a snapshot of the backpropagation of the simulated acoustic wave 1.1 ms after its interaction with the PVC tube, which is situated to the right of the image. The transmit signal is a linear chirp traversing 80 - 130 kHz over 0.06 ms. The simulated echo, traveling right to left, has the following structure in time: first there is a large reflection from the front of the tube, followed at a distance corresponding to approximately twice the diameter by a reflection from the rear wall. Then we see a dense tail related to strong resonances inside the tube.

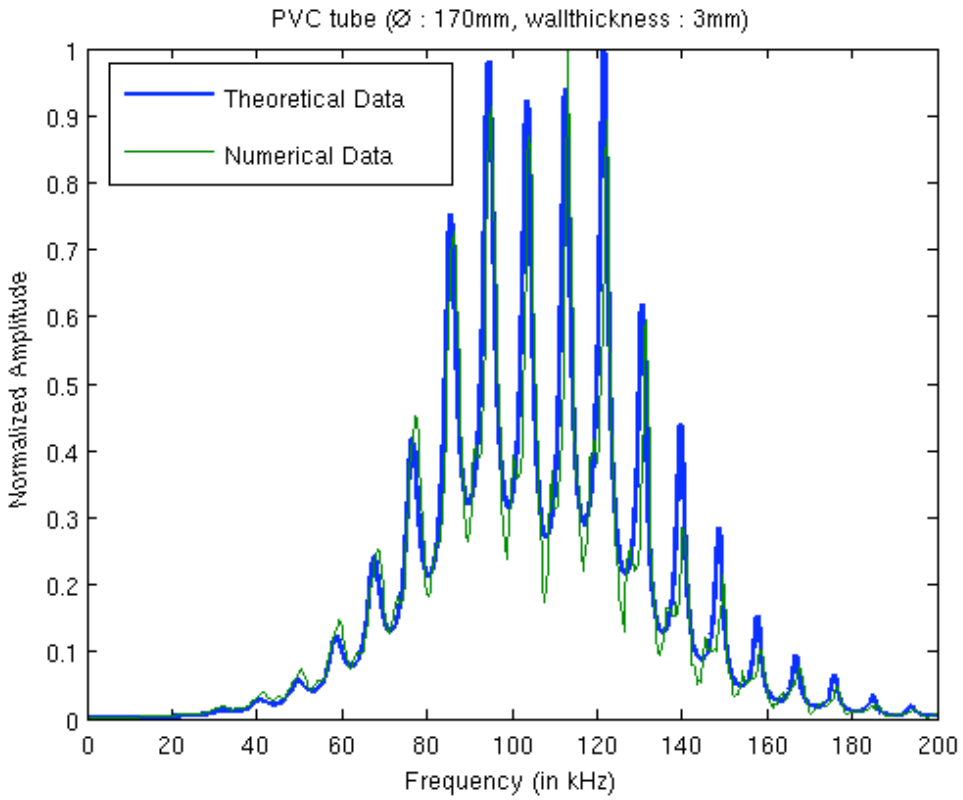

Figure 5.10: Matching between the analytical and numerical power spectra of the pressure field computed at the center of the PVC cylindrical shell.

The influence of the inner resonances on the power spectrum is illustrated in figure 5.10. This shows the power spectrum calculated at the centre of the modelled cylindrical shell for the numerical and theoretical approaches. The

numerical spectrum is calculated using a 0.7 ms integration time from first arrival of the pulse. The theoretical spectrum has been adjusted according to the spectral content of the transmit pulse. There is a high degree of concordance between the two with excellent agreement and colocation of peaks and troughs over the entire frequency range. This close agreement with the theoretical results for simple forms gives good confidence for the future value of numerical methods in estimating echoes from more complex targets.

5.4.4.2 Analogy with geometrical optics

For the PVC tube target, the simulator can also confirm that the first two main echo components are formed predominantly by reflections from the front and back of the cylinder. Figure 5.11 shows the interaction between the acoustic wave and the PVC tube and the formation of the echo structure. The incoming wave is seen passing beyond the cylinder to the right. The formation of the main echo fronts can be seen. The first, having reflected from the front face, is just approaching the left side of the image. The second is still forming within the pipe. The two echoes are cylindrical waves and the centres of these waves can be computed. The centre of the first echo is situated at ∼50 mm to the left of the cylinder centre. The source of the second echo is ∼45 mm to the right of the cylinder centre.

These observations can be understood using a spherical mirror analogy from geometrical optics. In the case of reflection at a spherical mirror the source image can be found using the formula given in Eq. (6.13). The notation is explained in figure 5.12 with reference to a concave mirror. $\mathbf{C}$ represents the centre of the sphere, $\mathbf{A}$ the source and $\mathbf{A}'$ the source image. Note that the formula is also valid for a convex mirror.

$$\frac{1}{\overline{\mathbf{SA}'}} + \frac{1}{\overline{\mathbf{SA}}} = \frac{2}{\overline{\mathbf{SC}}} \tag{5.9}$$

The argument readily generalises to the current case of a section through a cylinder with the images denoting line sources perpendicular to the plane of the page. We denote $\mathbf{A_1}$ the centre of the first echo, corresponding to the reflection

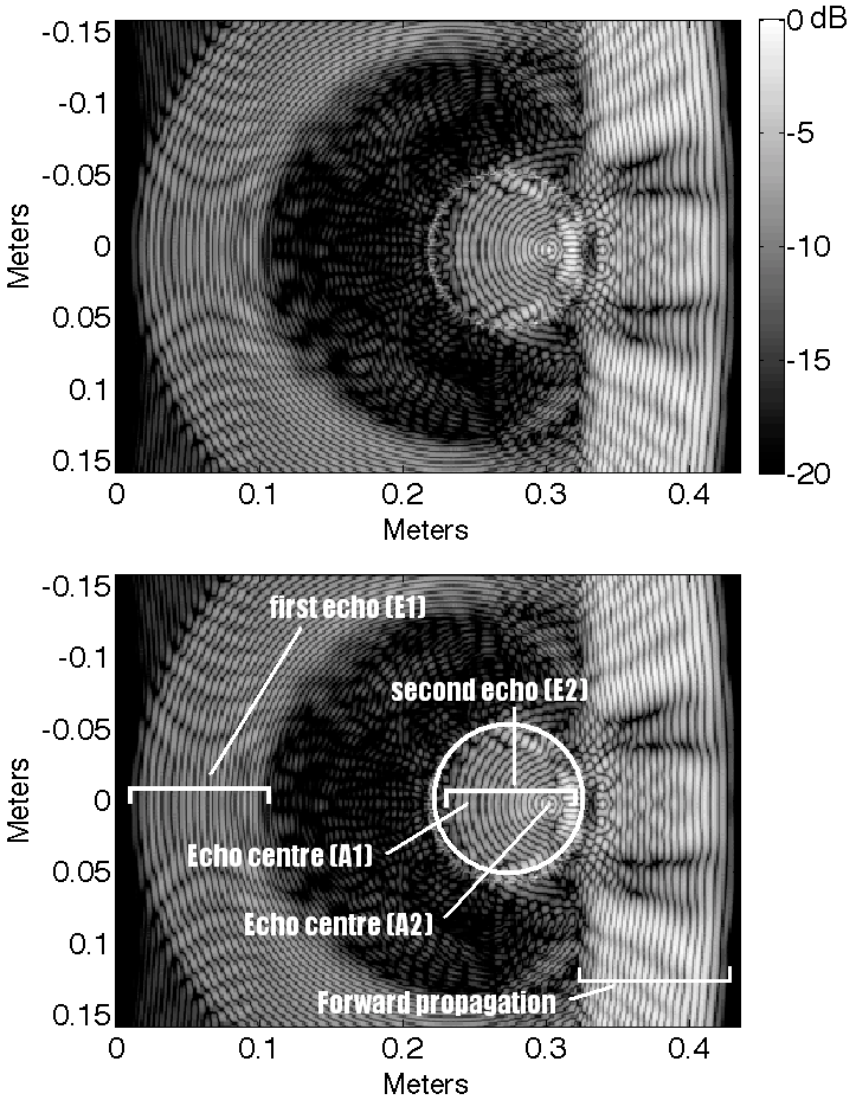

Figure 5.11: Display of the normalized sound pressure expressed in dB. Visualization of the interaction between the incoming acoustic wave and the PVC shelled cylinder and the echo formation inside the target. In the lower annotated diagram the position of the cylinder is indicated by the bold circle.

with a convex mirror of 170 mm diameter, and $\mathbf{A_2}$ the centre of the second echo corresponding to the reflection with a concave mirror of 164 mm diameter. The dimensions of the mirrors correspond to the dimensions of the cylinder.

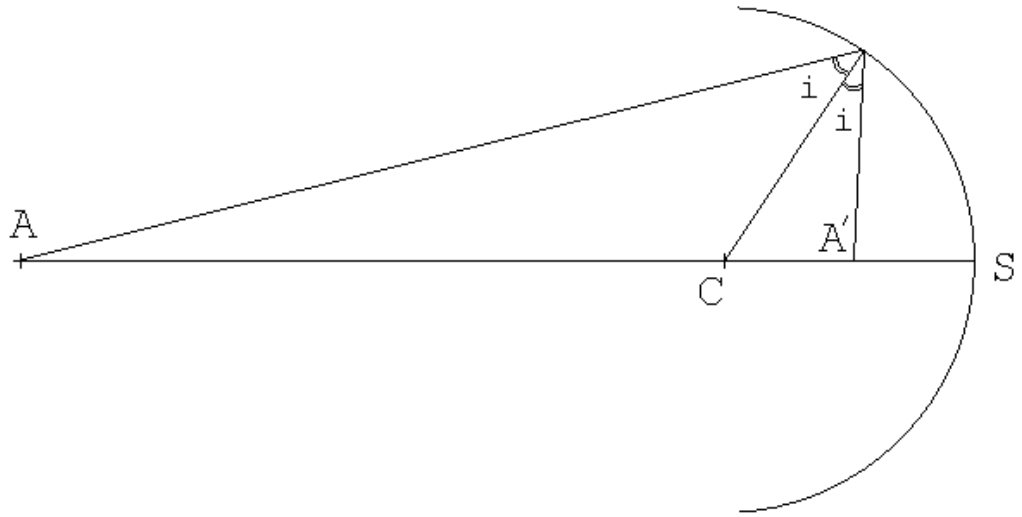

Figure 5.12: Reflection by a concave spherical mirror, construction of the source image $\mathbf{A}'$ from the source $\mathbf{A}$ in the axis $\mathbf{CS}$.

The values for $\overline{\mathbf{CA_1}}$ and $\overline{\mathbf{CA_2}}$ obtained using the acoustic response were given previously and were respectively -50 mm and $+45$ mm. Using the optical equation Eq. (6.13) the source image locations $\overline{\mathbf{CA_1}}$ and $\overline{\mathbf{CA_2}}$ are respectively -47 mm and +42 mm. The agreement between the results reinforces the assumption that the two first echoes are primarily due to reflections from the front and the back of the PVC tube.

5.4.5 Echo model of man-made objects

The backscatter can be computed by resolving the equation for the sound propagation integrated over the whole 3D object. Considering this integration over a continuous volume, the scattering points model proposed here is a discrete approximation of the echo process. We consider that the interaction between the incoming acoustic wave and a man-made object is reduced to the echo formation from a finite number of scatterers. To each scatterer we associate a beam pattern equivalent, the idea being to create one model valid for any angle of view. Two kinds of scatterers can be modelled:

(i) real scatterers (corresponding to a physical part of the object such as the water/material interface, corner reflectors or other strong discontinuities).

(ii) virtual scatterers (which can model phenomena such as Lamb waves).

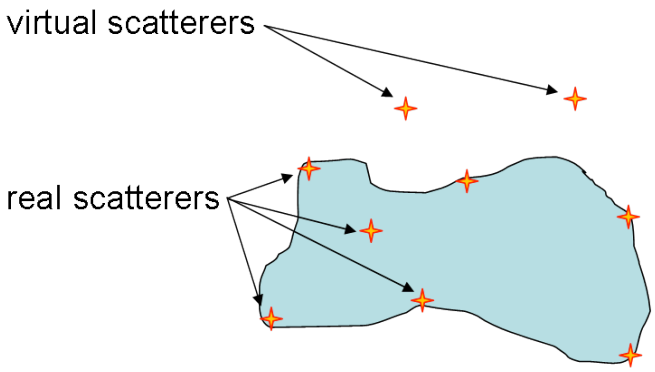

Figure 5.13: Scattering point model: a man-made object can be modelled by a finite number of real scatterers or virtual scatterers.

Figure 5.13 draws an object and its scattering point model including real and virtual scatterers. Beside the different models proposed in section 5.4.3 experimental evidences lead us as well to the scattering point model. Figure 5.14 displays the multiview aspect of a aluminium man-made conical object over 180° view angle. In the backscattering echo we can follow the trajectory of a few scattering points .

In figure 5.15 we apply the scattering point model to a PVC cylindrical shell and compare the experimental multiview data with the theoretical prediction. Figure 5.15 shows a very good match between the experimental and the theoretical data.

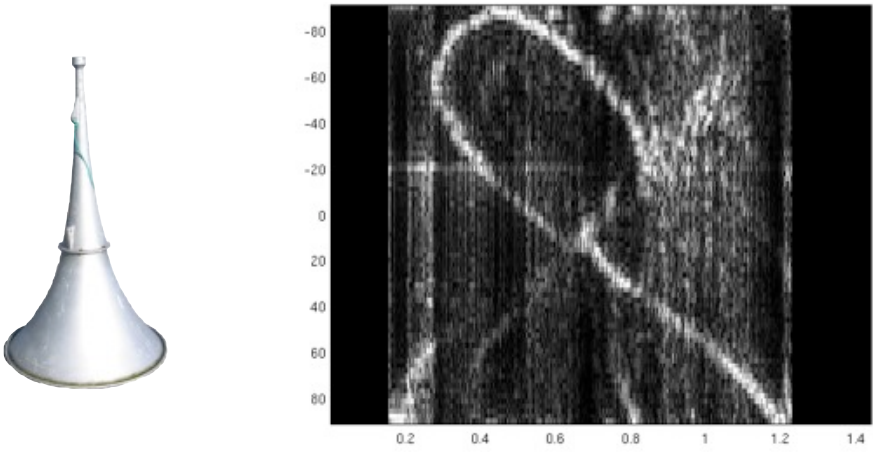

Figure 5.14: Backscattering echo of an aluminium man-made conical object over 180° view angle

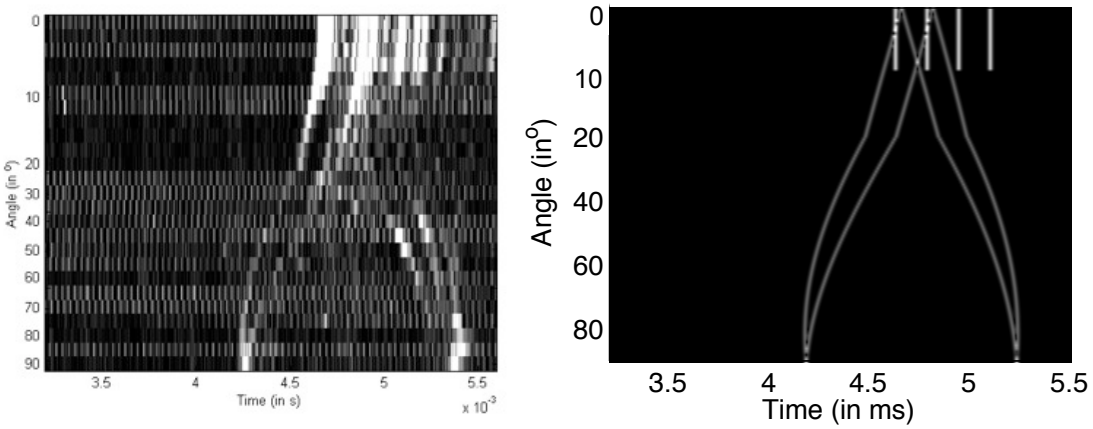

Figure 5.15: Comparison between experimental backscattering multiview of a PVC cylinder *left* and its theoretical model using the scattering point model *(right)*.

5.5 Experiments in controlled environment

The experimental program has been conducted using the biomimetic dolphin based sonar (DBS) developed jointly between the SPAWAR Systems Center, San Diego (SSC-SD) and the Applied Research Laboratory at the University of Texas (ARL-UT). The DBS has been designed to mimic both auditory and sound generation systems of the bottlenose dolphin with similar frequency bandwidths and sonar beamwidths (Houser et al. [2003]). The projector and paired laterally po-

sitioned receivers are constructed from 1-3 piezocomposite transducer material. The DBS sensitivity gives a -3 dB bandwidth of approximately 60 kHz to 130 kHz and it is capable of delivering a series of arbitrary waveforms within this range. The transducers are mounted on a pan-and-tilt unit allowing a mechanical scan of the area.

5.5.1 Tank experiments

Several tank experiments have been performed using the DBS with the synthetic dolphin-like pulses described above. These tests used the wave tank at Heriot-Watt University, which measures 12 m $\times$ 10 m $\times$ 4 m deep and is concrete lined. The tank incorporates a wave generator in one side wall with an absorbing beach structure along the opposite wall.

We are especially interested in the detailed spectral echo structures elicited using wideband pulses for discrimination purposes. The targets of interest here are the open-ended cylinders used for building the analytic and numerical models in sections 5.4.1 and 5.4.4. As previously noted, these objects have similar target strengths (e.g. 1.6 dB difference at 100 kHz) and similar dimensions (only 2 mm difference between the outer diameters, cf. table 5.3), making them very difficult to distinguish in intensity only data. However, they are made of different materials (steel and PVC) and, according to the models, are expected to have sufficiently different wideband echo structures for discrimination purposes.

The targets' responses were measured under identical conditions situated 8.90 m from the head of the DBS on the bottom of the test tank. In addition to the cylinder echoes the received signals contain significant reverberation returns from the surface water-air interface and from the tank floor.

5.5.1.1 Time-Frequency Observations and Echo Timings

Time-frequency representations offer a richer description for understanding echo phenomena than either time or frequency measures alone. Figure 5.16 displays spectrograms of the echoes from both tubes with signals DC1 and DC6

respectively. The spectrograms are computed with a Gaussian sliding window ($6\sigma = 100$ μs). The unimodal and bimodal characteristics of the transmit pulses can be seen in the horizontal banding in the reverberation returns.

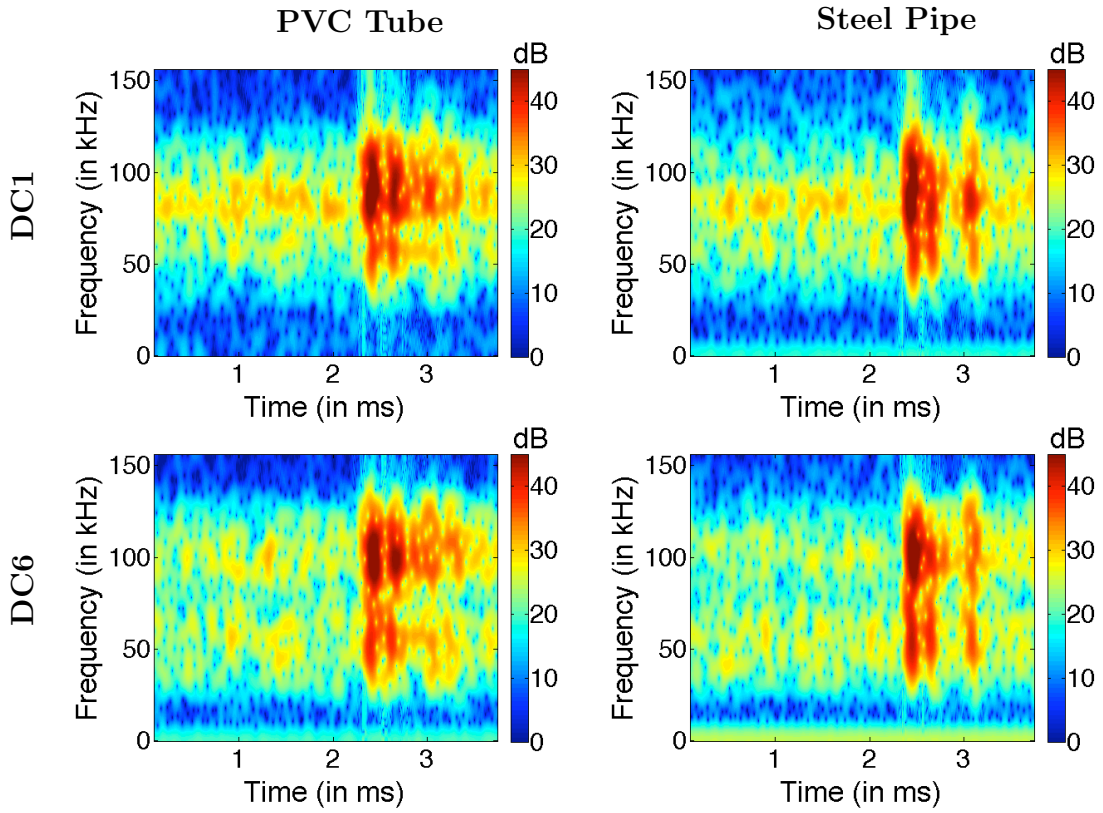

Figure 5.16: Spectrograms of PVC tube and steel pipe target echoes computed with a 100 μs sliding Gaussian window for pulses DC1 and DC6.

Comparing the PVC tube returns for both transmit signals, similar gross echo structures are seen. A first main echo front (specular echo) is followed by a second large reflection. In this case the second echo corresponds to the reflection of the sound wave from the back of the cylinder. The second strong echo is followed by a 'noisy' tail decreasing in amplitude over some 0.8 ms. Note that a similar pattern has been observed in the simulated echo in section 5.4.4.1. This general structure is characteristic over all of the transmit signals used during experimentation.

Values for the inter-arrival times for the first two echo fronts in each case have been evaluated theoretically (cf. Eq. (5.6)) and by empirical measurement as 221.2 μs and 220.8 μs respectively. These have been estimated from peaks in the matched filter returns for signal DC1, which has better pulse compression properties then DC6. In both cases the diameter of the PVC tube is estimated with a precision better than 1 mm (<1% error).

For the steel pipe target, time delays relative to the S_0 wave have been computed theoretically (cf. Eq. (5.8)) and empirically as 100.6 μs and 103.1 μs respectively. For the A_0 wave the results are respectively 153.3 μs and 152.4 μs. The theoretical time delays have been computed at 100 kHz. Once again the empirical time delays have been estimated from peaks in the matched filter returns for signal DC1.

5.5.1.2 Spectral Matching

Time-frequency representation is highly sensitive to the choice of windowing function and the selection made to provide sufficient resolution in echo timings above, loses oscillatory behavior in the spectrum. To regain this, the spectra must be calculated with a long enough window to integrate all of the key target echoes. Figure 5.17 shows the power spectral matching between the recorded echoes and the theoretical computations using a 0.6 ms gaussian window (long enough to include the main target echoes). The theoretical curves have been adjusted for the DBS transmitter and receiver sensitivities.

Despite the noted differences in scattering physics for the two targets, the responses match well with theoretical predictions. Both targets provide evidence of oscillatory behavior through the ka band from 10 to 50, indicating good discrimination potential from the wideband DBS responses. An indication of how well the curves match is given by colocation of the extrema, both maxima and minima, for each of the curves. Looking first at the PVC tube response, between 80 kHz and 130 kHz the maximum discrepancy in position for the peaks and troughs between the theoretical and empirical curves is approximately 1 kHz. The mean error is less than 0.1 kHz with variance of $\approx$ 0.5 kHz.

(a)

(b)

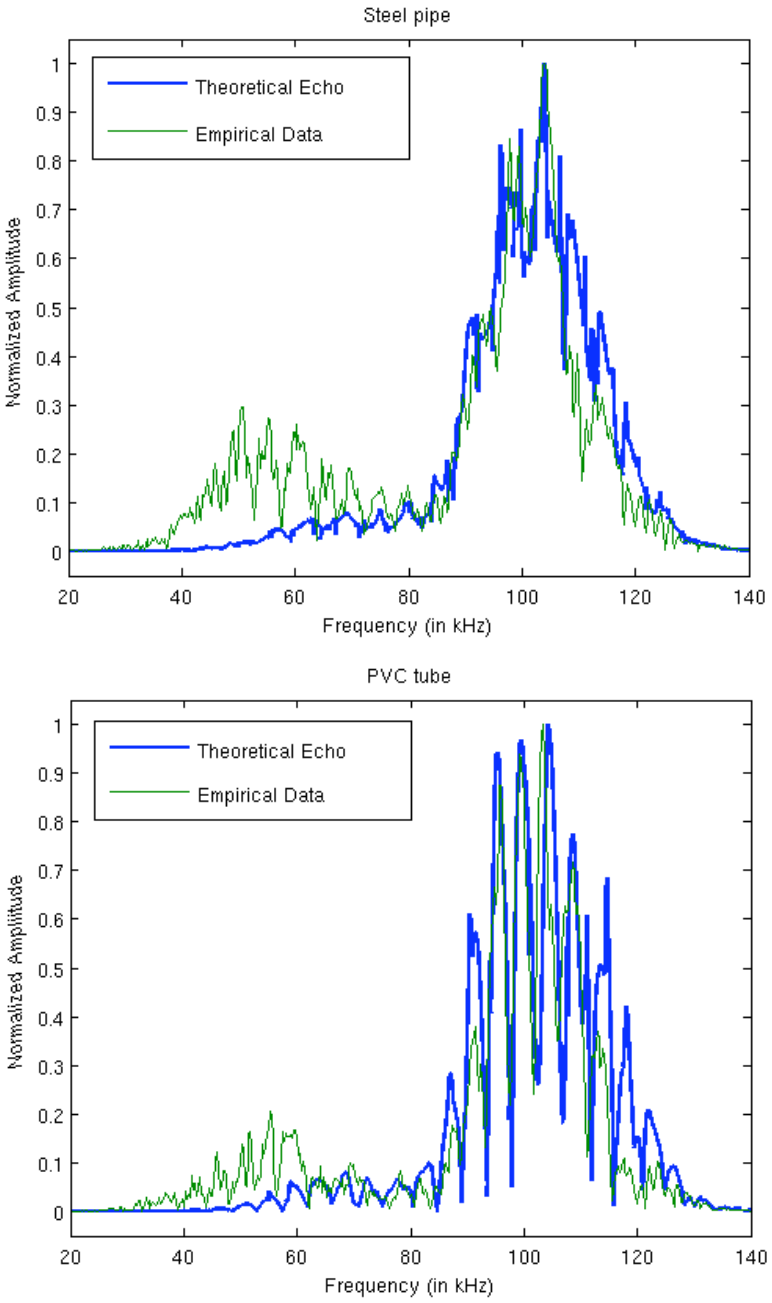

Figure 5.17: Matching between the theoretical and empirical DBS echoes power spectra for (a) steel pipe and (b) PVC tube. The high empirical response below 80 kHz due mainly to reverberation from the tank floor.

The heavily peaked form function for the PVC cylinder allows us to estimate parameters from the backscatter response curve in figure 5.17(b). The spectral notches are the strongest features and are the easiest to localize. An important consideration for discrimination of like targets is to relate the accuracy with which peak and notch positions can be determined to tolerances on physical parameters which influence the form function, f_∞. Processing the DBS returns with a time window ≥ 1 ms duration, we can readily measure spectral features with a precision of around 1 kHz. It is then possible to compute tolerances on various physical parameters which will keep the key resonance features within $\pm$ 1 kHz of the theoretical predictions for the exemplar target. The results are reported in table 5.4.

Cylinder Parameters	Tolerance
Outer Diameter	<1mm
Inner Diameter	<1mm
ρ	$\pm$10%
c_l	$\pm$4%
c_t	$\pm$2%

Table 5.4: Tolerances permitted in physical parameters of the PVC tube in order to keep the positions of resonance peaks and notches within $\pm$1 kHz band.

These values give an indication of the accuracy that can be achieved in parameter estimation given certain prior assumptions, such as possible target shape, size and material properties. Under the assumption of a cylindrical target, we can begin to extract size information from the wideband spectral response by relating the notch spacing Δf in the form function $|f_\infty|$ to the time spacing Δt between the two main echoes through the relation $\Delta f \Delta t = 1$ (cf. Gaunaurd et al. [1998]). In the case of the PVC tube we find a value of $\Delta f = 4.5$ kHz. The corresponding time spacing Δt_{PVC} is 222 μs equating to a cylinder diameter (cf. Eq. (5.6)) of 166 mm. These results are in line with expectations from the timing information given in section 5.5.1.1.

Note that the oscillations for the steel pipe are expected to be deeper over the bandwidth 40 - 80 kHz, facilitating feature extraction and improving accuracy.

5.5.2 Noisy Environment: Small Cylinder Responses in a Harbor Setting

The harbour experiments were carried out at Port Edgar, a working harbour and marina on the Forth Estuary near Edinburgh. This is a tidal site with a cluttered muddy seabed and shallow water, varying between two and eight meters in depth. In these experiments, the target under consideration is a one litre capacity aluminium SIGG bottle filled with seawater. The relevant target parameters concerning the SIGG bottle can be found in table. 5.3. The DBS was secured to a pontoon facing the target at 20 m range. The platform supporting the DBS was stable enough to ignore any Doppler effect. Even considering a 1 $m.s^{-1}$ velocity of the sonar relative to the target, and the smallest wavelength supported by the DBS (1.25 cm at 120 kHz), the maximum shift in frequency will be 80 Hz which is far below the 1 kHz precision of the sensor. In this sense, Doppler effects will not adversely affect the localisation of notches in the echo spectra of the target. Both sonar and target were 1 meter below the surface and the depth of the water at the time of the experiment was 3 meters. In addition to the shallow water setting, acoustic target detection and identification are made more difficult by the movement of boats, dredging and piling activity in the estuary, and with the influence of waves and prevailing weather conditions. The figures in table 5.4 show that even small changes in target parameters will modify the locations of the features we wish to use for classification. The current section demonstrates that it is still possible to extract these features even for a small target in a noisy shallow water environment and at ranges not achievable in the test tank.

Following our previous methodology, we model the SIGG bottle using a simplified, infinite cylindrical shell approximation. Given the short length of the cylinder (200 mm), artifacts from the bottle end caps and the low SNR, we cannot expect to achieve the same degree of correspondence between theoretical and empirical data as in the tank tests. However, the comparison between the model predictions and the measured response, figure 5.18, does show good agreement in principal peak and notch positions. For this target/environment combina-

(a)

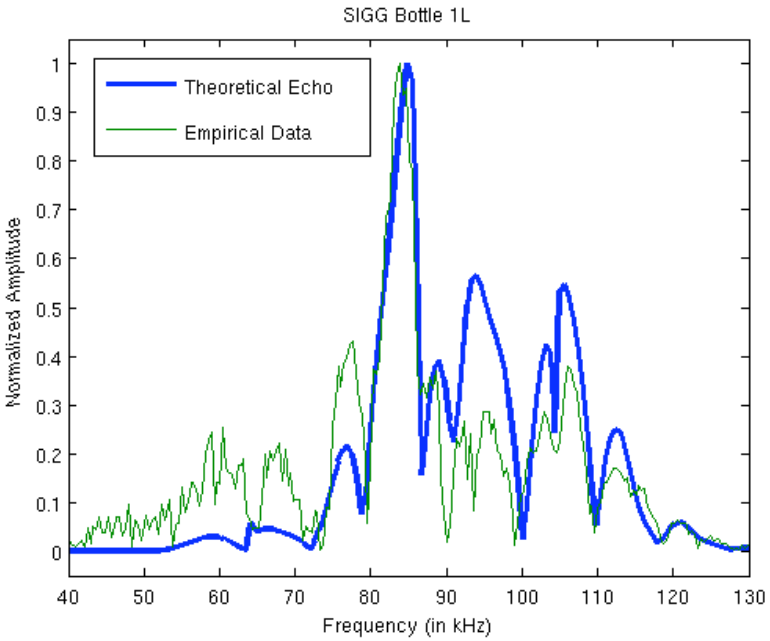

(b)

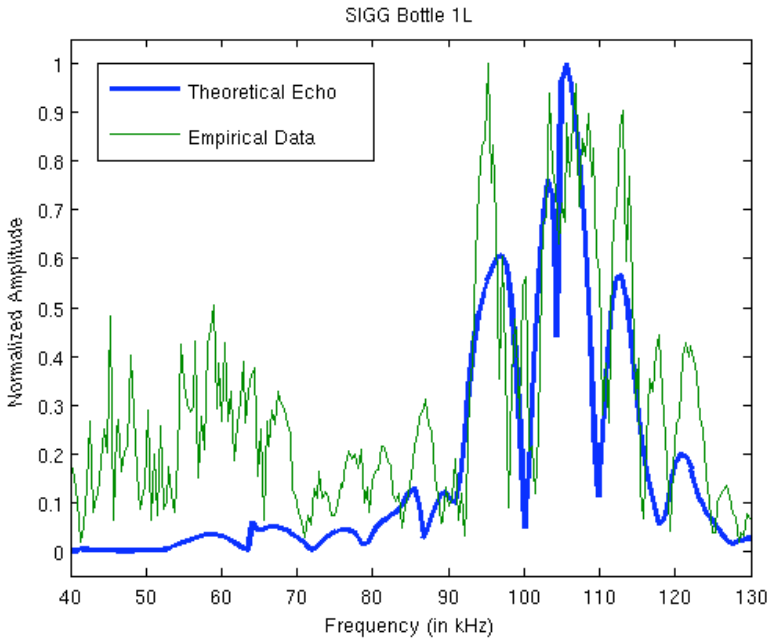

Figure 5.18: Matching between the theoretical and empirical DBS echoes power spectra for the SIGG bottle with (a) DC1 pulse and (b) DC6 pulse. The empirical spectrum has been computed using a single echo of the bottle.

tion, pulse DC1 gives consistently better results than DC6. A discussion of the influence of noise and required SNR for classification follows in section 5.6.2.

5.6 Classification

The models and empirical data presented above show that echoes from targets producing multiple returns are characterized by interferences in the spectra. For certain targets we can relate features of the spectra, particularly notch locations and spacings, to specific physical properties. In this section we propose a new metric for the classification of broadband echoes based on the localization of the interference notches.

5.6.1 Broadband features & classifier

Let F be the spectrum of the broadband echo. Let $\{\omega_i\}_{i\in[1,N]}$ be the location in frequency of the notches of F. To F we associate ΔF such that:

$$\Delta F(\omega) = \sum_{i=1}^{N} \delta_{\omega_i} * G_\sigma(\omega) \tag{5.10}$$

where $\delta_{\omega_i}(\omega) = \delta(\omega - \omega_i)$, δ represents the Dirac function, and G_σ is the centered Gauss function with a variance of σ. Given the capability of the sonar, we choose the value of parameter σ to match the 1 kHz precision we wish to achieve in notch location. The associated function ΔF is an irregular gaussian comb where the peaks represent the notch locations.

In this space we define the Euclidian distance between two elements ΔF and ΔG as:

$$d(\Delta F, \Delta G) = \left(\int_0^{+\infty} |\Delta F(\omega) - \Delta G(\omega)|^2 d\omega \right)^{\frac{1}{2}} \tag{5.11}$$

Classification using the distance metric has been tested using the PVC (tube) and steel (pipe) cylinders along with three other targets: an 800 mm long aluminium conical shell (cone) with diameter reducing from 500 mm to 20 mm along

its length, a solid aluminium nose cone (rocket head) 200 mm in height by 120 mm in diameter and a non-resonant concrete brick measuring 200 mm x 100 mm x 50 mm. The cone and the brick have been insonifed with two different orientations: vertical and tilted 8° for the cone and lengthways and widthways for the brick. As before the targets were placed on the tank floor approximately 8.90m from the centre of the DBS array. Although the tank floor is relatively flat compared to the minimum wavelength, the reverberation introduces coherent noise in the data. Each target has been ensonified 21 times with head angle varying from -10° to +10° in 2° intervals.

The echo corresponding to the target is extracted from each record, and the power spectrum is computed. The notches corresponding to local minima within a 2 kHz wide sliding window are extracted in the 60 - 130 kHz band, which corresponds to the most significant frequencies of the DBS. The 2 kHz sliding window just ensures that the notches do not overlap in the computation of the ΔF function.

From the location of the notches, the ΔF function is computed using Eq. (5.10) for each echo spectrum. In order to classify the targets one reference ΔF_{ref} is needed for each target. For the cone, tilted cone, rocket head, brick (length) and brick (width) target a single broadside echo has been recorded as the reference. The reference functions ΔF_{ref} for the PVC tube and steel pipe are computed from synthetic echoes. Thanks to the models proposed in section 5.4.3, the timing between the specular echo and the secondary echoes can be estimated with excellent precision. Synthetic echoes for these targets are built simply using the timing and the relative phase shift between the primary and the secondary echoes. Thus, the PVC tube and steel pipe ΔF_{ref} functions come solely from the notch locations given by analytical models.

The classifier uses a simple nearest neighbour algorithm. Table 5.5 displays confusion matrices for the two signals DC1 and DC6. In both cases the matrices demonstrate that this simple metric provides a good discriminant, but the two pulses do show different results. The pulses focus energy on different frequency

DC1	cone	cone 8° tilted	pipe	tube	rocket head	brick (length)	brick (width)
cone	**0.50**	0.26	0	0.06	0	0	0
cone 8° tilted	0.32	**0.56**	0.47	0.16	0	0	0
pipe	0.12	0.06	**0.43**	0	0	0	0
tube	0.06	0.03	0.05	**0.78**	0	0	0
rocket head	0	0.09	0	0	**1.00**	0.21	0
brick (long)	0	0	0.05	0	0	**0.79**	0
brick (large)	0	0	0	0	0	0	**1.00**

DC6	cone	cone 8° tilted	pipe	tube	rocket head	brick (length)	brick (width)
cone	**0.44**	0.44	0	0	0	0	0
cone 8° tilted	0.35	**0.44**	0.05	0	0	0	0
pipe	0.12	0	**0.81**	0.06	0	0	0
tube	0.09	0.12	0	**0.94**	0	0	0
rocket head	0	0	0.14	0	**1.00**	0	0
brick (long)	0	0	0	0	0	**1.00**	0
brick (large)	0	0	0	0	0	0	**1.00**

Table 5.5: *(top)* Confusion matrix relative to the DC1 pulse echoes, *(bottom)* confusion matrix relative to the DC6 pulse echoes. These matrices have been computed with 40 measurements per target.

bands and in this experiment DC6 proves more effective in classifying the full set of targets but DC1 shows better results in discriminating the cone orientation. Note that there is no misclassification between the resonant shelled targets and the solid concrete brick using DC6 and very little between solid and hollow target using either pulse. We can conclude that information related to the target structure is linked to the inner resonances of the target and that we can gain access to this information through the interference notches. Using several pulses with different frequency bands allows us to focus the classifier on relevant spectral regions for a particular target.

In the table 5.5 we computed the confusion matrices relative to the two bio-inspired pulses DC1 and DC6. A confusion matrix shows the performances of the classifier: it expresses the probability of an object A (column) to be classified

as an object B (line). The closest the confusion matrix is from the identity matrix, the better is the classifier. Another point of interest arises from those confusion matrices: the confusion between the two cone aspects is high (between 30% and 45%), because it is fundamentally the same target and the change of look angle is small (8°), so the resonances are expected to be similar. Note that the cone is classified correctly (independently of orientation) at 82.3% and 83.8% for DC1 and DC6 respectively. For the brick, the change of orientation is 90°, the scattering points are in a totally different configuration and the locations of the notches are significantly shifted. So there is no confusion between these two configurations.

DC1 & DC6	cone	cone 8° tilted	pipe	tube	rocket head	brick (length)	brick (width)
cone	**0.50**	0.21	0	0	0	0	0
cone 8° tilted	0.29	**0.59**	0.05	0	0	0	0
pipe	0.12	0	**0.81**	0.06	0	0	0
tube	0.09	0.12	0	**0.94**	0	0	0
rocket head	0	0.08	0.14	0	**1.00**	0	0
brick (long)	0	0	0	0	0	**1.00**	0
brick (large)	0	0	0	0	0	0	**1.00**

Table 5.6: Confusion matrix for the fusion system of the two classifiers relative to the two pulses

The results can be optimised with fusion algorithms. In our case we use the Dempster-Shafer theory of evidence from Shafer [1976], with confusion matrices for DC1 and DC6 giving an approximation of the belief functions. The final fusion decision is based on the rule of maximum belief. We run two classifiers, corresponding to pulses DC1 and DC6, for each view of a target. The belief functions are generated from the results of each classifier, given its expected performance estimated from the confusion matrix (the probability of correct classification). Over both belief functions, the maximum belief is chosen. Table 5.6 gives the confusion matrix fusing the results from both pulses. The fused result is better than either classifier operating independently. While DC1 performs better in classifying the cone, and distinguishing its two aspects, DC6 is better classifying

the pipe and tube. The fused classifier takes advantage of the best results of each classifier for each individual target.

5.6.2 Influence of the noise

In this section, we study the effect of noise and its limitations on the classifier. In sections 5.4.1 and 5.4.4, we explained the formation of characteristic spectral patterns from interference patterns between the primary and the secondary target echoes. The null estimator exploits these interference patterns for discrimination. Since both primary and secondary echoes are required, the strength of the secondaries is crucial in determining the performance of the classifier in noise. Defining SNR as the ratio of the peak of the secondary echoes to the noise level, Figure 5.19 displays the ΔF function for the PVC tube ensonified by pulse DC1 against an increasing levels of additive Gaussian white noise. With an SNR above 15 dB, the notches are well localised across the band. From 15 dB to -5 dB, the influence of the noise is apparent, but the frequency band 80-110 kHz, corresponding to the highest sensitivity of the DBS, remains stable and can be used for classification. At still lower SNR, with noise levels in excess of the peak secondary echoes, the target resonances are masked and the classifier will fail.

As we described earlier the presence of notches in the echo spectra is due to the interference of the different scatterers of the target. In the case of a large object with distant scatterers the oscillations in the spectra becomes intractable and the spectral feature extraction algorithm will inevitably fail. For this reason we developed a power spectrum filtering algorithm in to order to take into account only the interference between scatterers separated by a maximum distance d_{max}. The details and justification of this spectrum filtering algorithm is explained in appendix B.

5.7 Applications

In this section we discuss two applications of the BioSonar and how it outperforms traditional sonars. First we will describe how a bio-mimetic sonar can

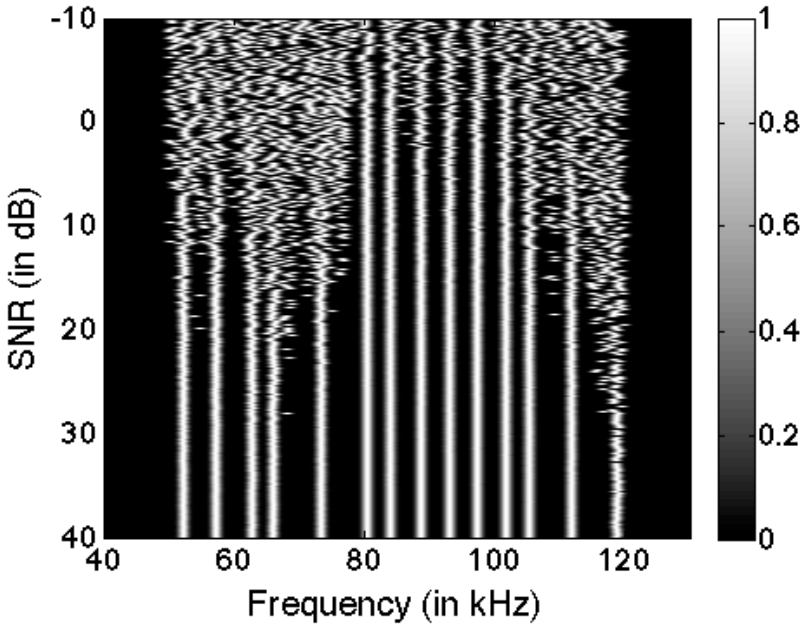

Figure 5.19: ΔF function of the echo of PVC tube with an increasing synthetic white noise.

be used in the MCM (mine countermeasures) context. Then its performance in cable tracking application is shown.

5.7.1 BioSonar for AUVs

In the early test experiments we used the DBS system built by SPAR-WAR at San Diego. The push for real applications of bio-mimetic sonars led us to build an AUV ready version of the BioSonar. Figure 5.20 displays the electronic bottle prototype which drives the transducers.

The electronic bottle includes a PC 104 which drives the data acquisition card (DAC). The present DAC system drive the transducers (transmitters and receivers). It records two channels at 800 kHz sampling rate at 16 bits and streams the data into disk. The backscattering echoes pass through anti-aliasing filters, high-pass filters and amplifiers before being digitalised. At the transmit side the output pulses are amplified thanks to an APEX 96 allowing us to drive the

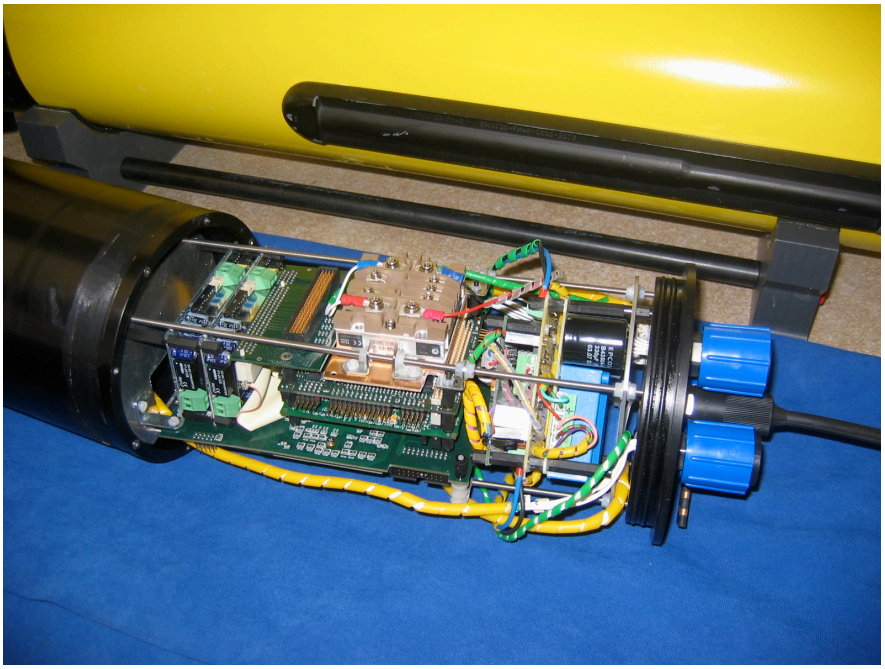

Figure 5.20: Electronic bottle of the BioSonar system.

transducers at ± 220 V.

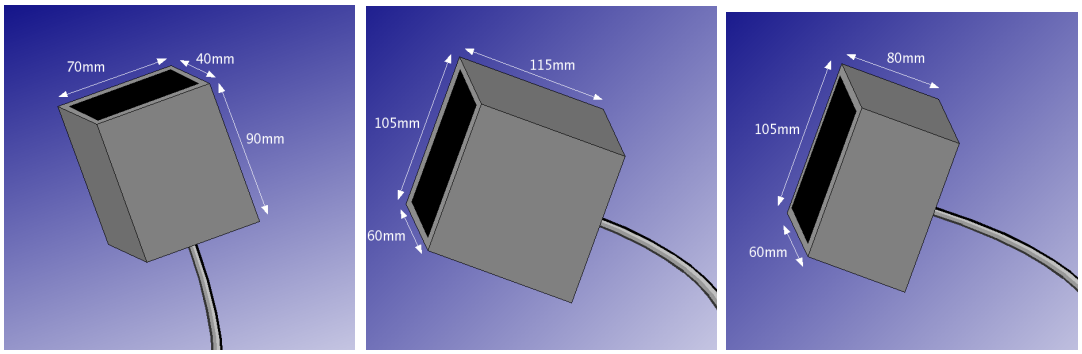

Figure 5.21: Schematics of the piezoelectric transducers designed and built by PCT Ltd. *(left)* high frequency projector, *(centre)* low frequency projector, *(right)* Receiver.

Figure 5.21 draws a schematic of the transducers we have been using. The transmitters have been designed and manufactured by PCT Ltd in Aberdeen. The desired bandwidth for the BioSonar (30 kHz to 130 kHz) is too wide to be covered by one transmitter. Two transmitters were then built: a low frequency transmit covering the frequency band 30 kHz to 90 kHz and a high frequency transmit covering the frequency band 60 kHz to 130 kHz.

To maximise the BioSonar coverage the transducers have been mounted in a sidescan configuration. Figure 5.22 shows two pictures of our BioSonar system mounted on a REMUS 100 (AUV from Hydroid) operating in Loch Earn (Scotland).

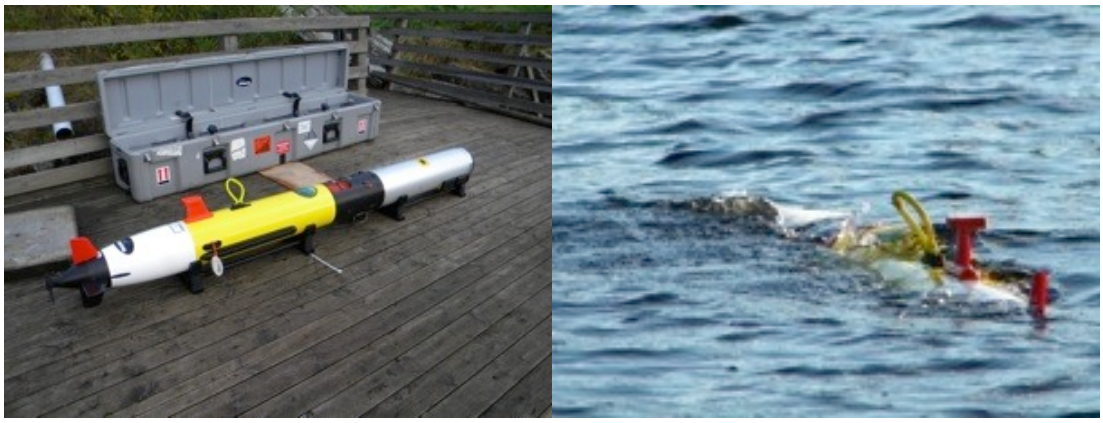

Figure 5.22: BioSonar system mounted on REMUS.

5.7.2 Mine countermeasures

Detection, classification and identification of underwater objects continues to be a major issue for the military. Mine countermeasures were traditionally performed by dedicated ships and trained divers. With the technology pushing forward, MCM evolves toward a greater autonomy including autonomous vehicles and autonomous algorithms to detect and identify underwater mines. The traditional approach to ATR (autonomous target recognition) is image based. Extensive research has been carried out on the subject. Calder et al. [1997]; Goldman and Cohen [2004]; Maussang et al. [2007] aim to detect global rarity

in the sonar image using the assumption that a mine is a rare event. In Calder et al. [1998]; Dobeck et al. [1997]; Dura et al. [2008]; Mignotte et al. [2000]; Reed et al. [2003a,b] a model base approach is considered. Using simulations, a model of the expected target is created and compared to the detected object. Classical approaches using supervised learning have also been considered by Azimi-Sadjadi et al. [2001]; Ciany and Huang [2000]; Fawcett [2001]; Perry [2001]; Zerr et al. [2001].

Despite the high performance of the new generation of imaging sonars (including SAS systems), ATR using imaging is still at this stage unreliable due to a high false alarm rate and poor performance in heavily cluttered areas (Petillot and Maurelli [2010]). In parallel, the US Navy Mammal Program had trained dolphins from the 60's to detect and identify underwater mines. Dolphins' capabilities for manmade object detection suggest that useful information for MCM can be extracted from broadband echoes.

The background research described earlier led us to build an AUV (autonomous underwater vehicle) ready BioSonar which can be plugged directly on a REMUS-100 AUV. The BioSonar prototype has been mounted in a side-looking configuration to facilitate gathering of collocated sidescan data using the vehicle's standard Marinesonics sonar at 900 kHz operating frequency.

A series of trials have been performed in Loch Earn (Scotland) in March 2010. The aim of these trials was to validate the capacity of the BioSonar for target recognition in a real environment operating from a reliable and commonly used autonomous vehicle. A set of spherical targets has been used for these trials (cf. Figure 5.23). Spheres provide a good reference target because of their rotational symmetries. The target itself will give a similar echo response at any angle of view, range or altitude. All the targets have a similar diameter (between 28 cm and 38 cm) and were made using different materials: stainless steel, concrete or plastic. Using conventional imaging sonar it is impossible to identify one target from another. Two experiments have been performed in two different area of the loch:

- Area 1 is a relatively flat region (depth around 38 metres) giving good conditions for multi-aspect survey of the full target set.
- Area 2 lies on a steeper slope near the mouth of a river which drains into the loch.The river has brought a considerable quantity of debris into the loch consisting primarily of rocks and tree trunks and branches. Consequently, this area is heavily cluttered.

Figure 5.23: Spherical target set used during the MCM trials.

In Area 1 we aim to demonstrate the capability to distinguish targets with the same shape and similar dimensions but constructed from different materials or to distinguish a solid target from a hollow target. These are fundamental capabilities for the recognition of manmade targets amongst natural clutter objects. In Area 2 we aim to demonstrate the capability to reject clutter returns on the strength of their spectral content and lack of any consistent match or similarity with the echo responses of the manmade test targets. Rapid rejection of clutter contacts is another fundamental requirement for the effective recognition of manmade targets in a highly cluttered environment.

Figures 5.24 and 5.25 show one parallel path past the targets at around 16 metres range. The sidescan maximum range is fixed at 30m and the BioSonar system is running at approximately 46m maximum range. The registered sidescan

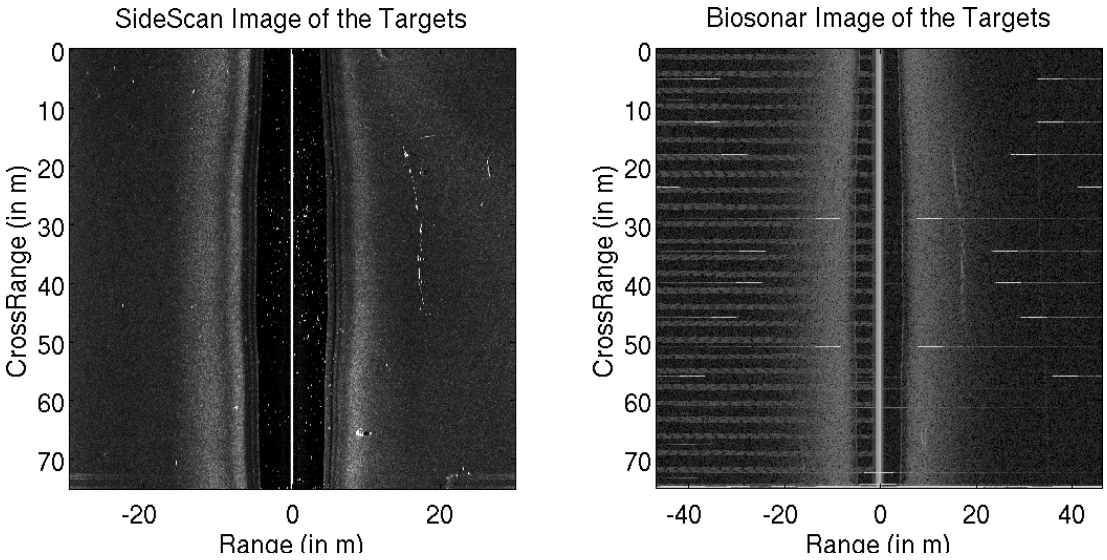

Figure 5.24: Display of the sidescan sonar image of the targets (on the left), and the BioSonar image of the targets (on the right).

image is displayed on the left, and the BioSonar image on the right. The BioSonar images are produced for visualisation purposes only from the envelope of the matched filtered echo.

Figure 5.25 shows close ups over the target set for both sensors. Note that the wide beamwidth of the BioSonar system leads to the target responses tracing arcs through the data, in a similar fashion to raw SAS images. The sidescan gives quite high resolution images allowing us to clearly locate each of the targets and gives a good response along the line connecting them (8mm braided polyethylene). Note that in the sidescan image, it is impossible to identify one target from another. Multiple responses at broadside do give some indication that certain targets are strongly resonant. Whilst precise location is more complicated working from the wideband returns, the resonances are more easily picked up in the parallel arcs associated with these targets.

In the following paragraphs we demonstrate an identification method using a time-domain Gaussian mixture model to represent the echo of the large steel sphere. Note that the time domain refers to the match filtered echo. The pa-

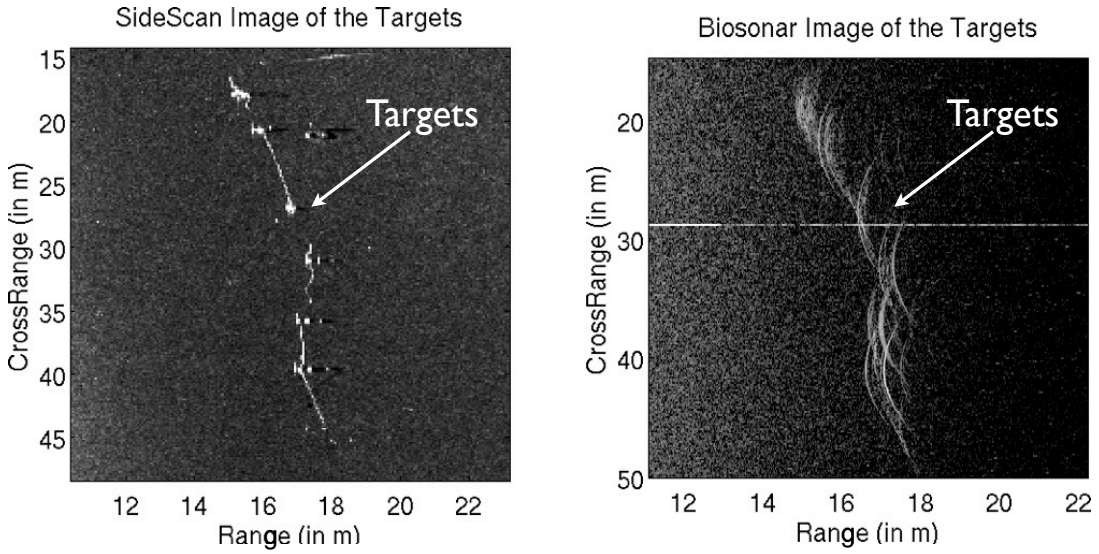

Figure 5.25: Spherical targets with roughly the same dimension (Ø: around 30 cm) but built with different materials (plastic, aluminium or concrete) have been put on the seafloor. The figure displays a close up of the targets using sidescan (on the left), and using BioSonar (on the right). All the targets appear very similar in the sidescan image and are impossible to differentiate. However in the BioSonar image, the characteristic resonances of the different targets are clear which make the identification possible.

rameter estimation for Gaussian mixture has been a subject of research for years from expectation maximisation (EM) algorithms (introduced by. Dempster et al. [1977]) to Probability Hypothesis Density (PHD) filters (cf. Clark and Vo [2007]). In our case the problem is greatly reduced assuming two hypothesis: the target echo at the frequencies we are working with is composed of the sum of its fundamental scatterers echoes, the separation between each scatterer is greater than the variance of the matched filter pulse. Under those conditions and knowing the variation of the matched filtered pulse, the missing Gaussian mixture parameters can be estimated by looking for the maxima in the time domain. A mixture of 4 gaussians has been chosen to model the envelope of the backscattering echo of the big steel sphere. Note that 4 gaussians were enough to model more than 90% of the signal.

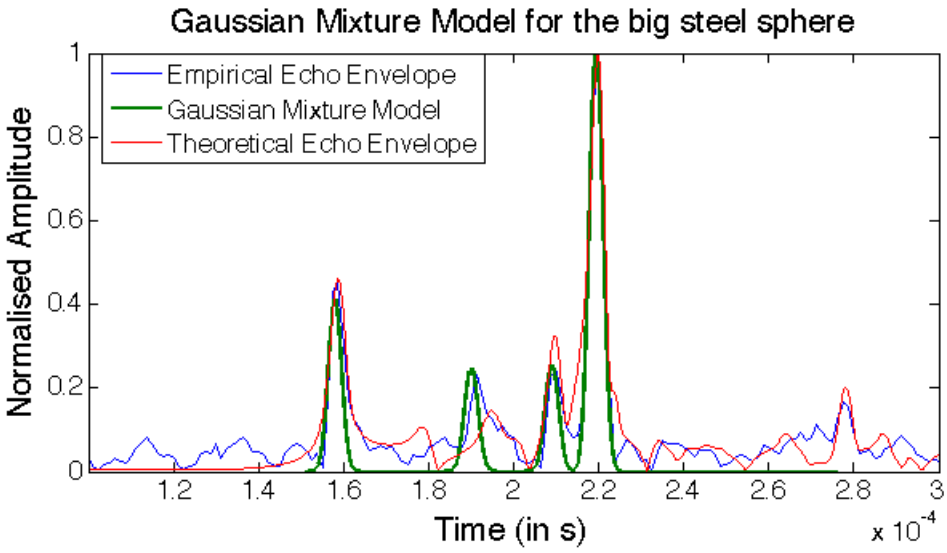

Figure 5.26: Echo of the big steel sphere in the time domain: empirical data, gaussian mixture model and theoretical echo.

The time domain methods suffer some limitations. In particular the match filtering in the time domain compresses the broadband pulses and tends to suppress the frequency dependance of single echo (especially the secondary echoes) and spread the envelope. An example of this statement can be found in figure 5.7: the velocity of the Lamb waves can vary significantly with frequency, this phenomena will cause deformation in the pulse shape. However the bandwidth used by the BioSonar provides relatively clear echo and almost linear echo in the frequency domain. For this reason the resulting match filtered echo exhibits strong and sharp specular and secondary echoes for the targets of interest. Figure 5.26 displays the match between the empirical sphere echo and the gaussian mixture model.

The Gaussian mixture model is then used as a template. A sliding window is applied to the BioSonar signal and the Euclidian distance is computed between the normalised extracted signal and the normalised template. Figure 5.27(*left*) shows a close-up of a BioSonar image of the five spherical targets. In figure 5.27(*right*) we display the result of the distance between the BioSonar image and the template. Note that the result in the figure is expressed in dB. As a reference point

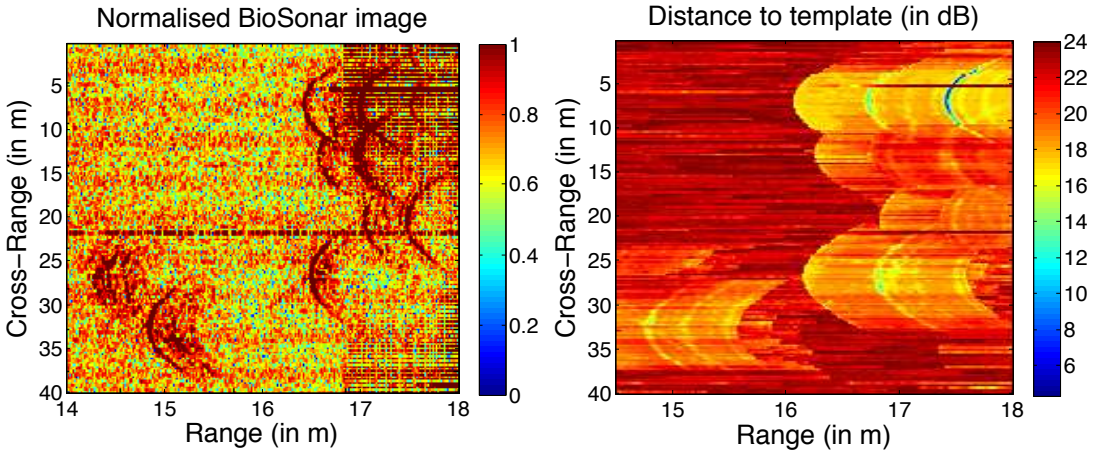

Figure 5.27: (*Left*) BioSonar image of the target set. (*Right*) Detection results.

the distance between the Gaussian mixture model and the big steel sphere echo with a SNR of 6 dB is around 4 dB. Figure 5.27(*right*) shows positive identifications (in blue) of the steel sphere amongst the other targets at various ranges and orientations relative to the direction of deployment. In all cases the lower distance values indicate higher confidence in recognition. The resonant targets similar to the large steel sphere such as the small steel sphere or the PVC sphere are 10 dB higher in the distance feature and the background is 20 dB higher.

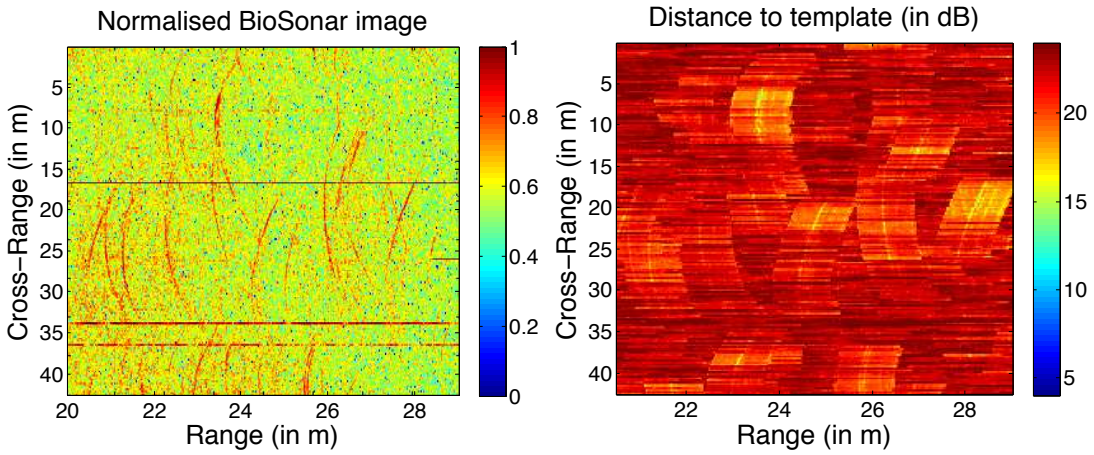

Figure 5.28: (*Left*) BioSonar image of a cluttered area. (*Right*) Detection results.

In figure 5.28, the algorithm has been run over the cluttered area (Area 2) with none of the prepared targets present. All the ATR algorithms failed in clustered area resulting in a very high number of false alarms (cf. Sawas et al. [2010]). Using the BioSonar however, no detections have been found in this area using this algorithm. This demonstrates the potential of the BioSonar system to drastically reduce false alarm rates even with relatively simple and efficient algorithms.

5.7.3 Cable tracking

Our research group has been running a wideband cable tracking project in parallel with the ongoing work on target detection and recognition. This culminated in a series of trials at Loch Earn in early January 2010, with a demonstration over a 500 m section of cable. An overview of the project and some results from the demonstrations are described in this section.

5.7.3.1 Background

The targets of interest in this project are US Navy range and communication cables. Samples of various types were provided, varying in external diameter from 32mm down to $16\frac{1}{2}$mm. All of the cable types comprised one or more continuous metallic layers with woven steel strain wires and a relatively low density plastic sheath. For the final sequence of trials, several substantial sections of a 17mm, polyethylene jacketed cable with a fibre optic core (SL17L) were deployed.

In Brown et al. [2011], the authors demonstrated the detectability of the SL17L cable using the BioSonar in a tank experiment. Figure 5.29 displays the match filtered echo of a section of SL17L cable lying on soft sediment (sand). The data were recorded using the DC3 bio-mimetic pulse. The cable is clearly visible at the centre of the image. In figure 5.30 a waterfall plot of the cable echo is shown. Despite the small diameter of the cable, the echo spectra shows strong consistency along its full length, even if a more reliable detector should be built by integrating over sequences of returns.

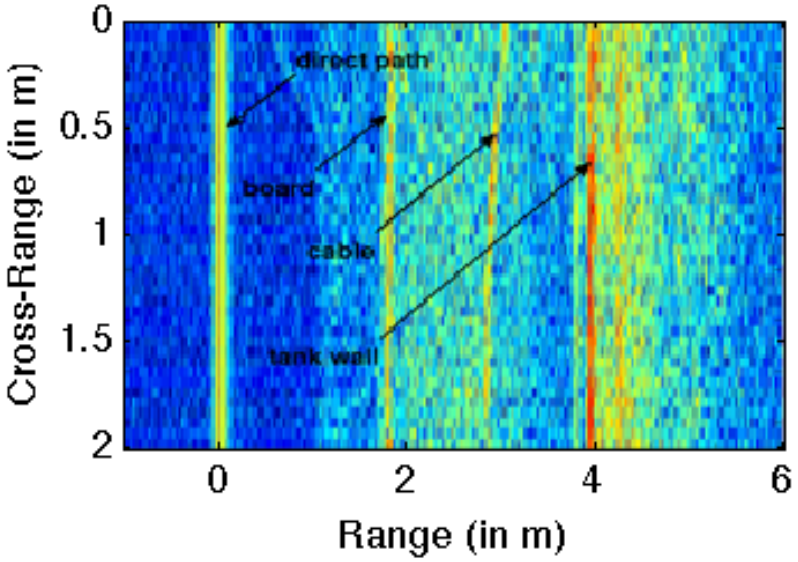

Figure 5.29: DC3 echoes at 5 cm intervals along 2 m section of SL17L cable (at 27° grazing angle).

For the real scale experiment, the BioSonar has been used in a side-looking configuration primarily to facilitate co-operation with the Marine Sonics sidescan unit. The transducer configuration comprises port and starboard projectors and receivers set at a depression angle of 25°.

The detector module operates on single wideband pings and port and starboard channels are treated independently. Visually the cable shows up clearly in imagery produced from the BioSonar system. However, with no hardware time-varying gain (TVG) correction, the background reverberation varies markedly over the sonar swath and simple thresholding cannot be applied. Rather than implement a software TVG, we downsample the data to reduce computational overheads and then estimate local reverberation statistics by fitting a Rayleigh distribution function to the backscatter intensity data. The Rayleigh is a simple, single parameter distribution well suited to modelling sonar intensity data, see Eq.5.12. Detection follows from the calculation of probabilities or likelihoods that a particular measured pixel value belongs to the estimated distribution. Low likelihoods indicate points that are not well represented by the seabed model and

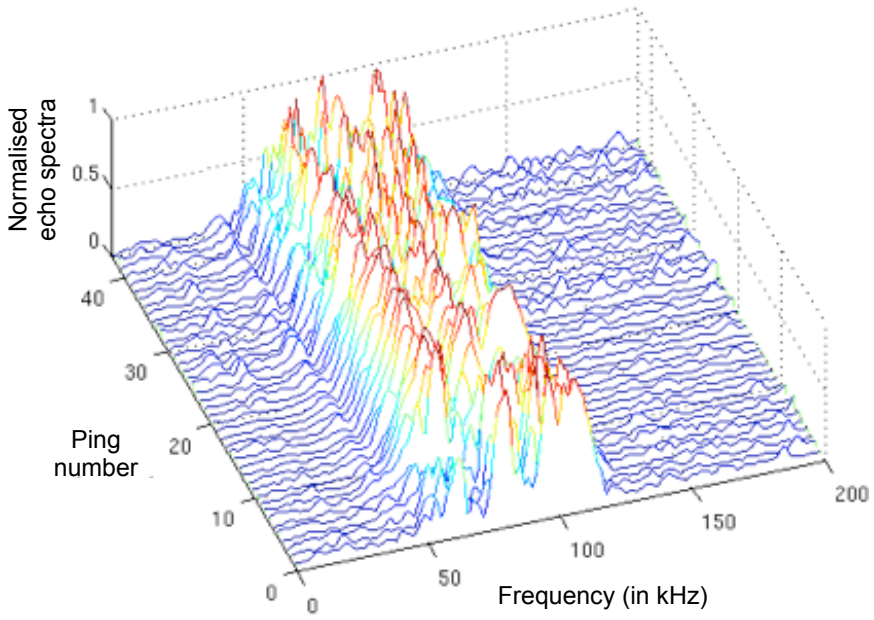

Figure 5.30: Waterfall plot of the cable normalised echo spectra whilst the general three-lobed pattern distinctive for this cable/pulse combination is strongly in evidence, variations would make discrimination from a single ping highly difficult and a more reliable detector will be built by integrating over the sequences of returns.

are therefore probable contacts.

$$\begin{aligned} p(\text{seabed}) &= \frac{x}{s^2}\exp\left(\frac{-x^2}{2s^2}\right) \\ p(\text{D}) &= 1 - p(\text{seabed}) \end{aligned} \tag{5.12}$$

For cable detection, running near parallel to the cable, this method benefits greatly from the wide beamwidth of the sonar. Returns are integrated over the full beamwidth, so that contributions are significantly enhanced for a long cable section compared to a more compact target. In this way the $p(\text{D})/p(\text{FA})$ ratio is maximized and a relatively simple detection algorithm can be employed. This is an important consideration given the large quantities of data collected at high data rates and consequent lengthy processing times. At the detector level, thresh-

olds have been set relatively high to ensure the system is not flooded with false alarms. The detections are therefore a little sparser than one would like visually, but provide plenty of information for the tracker to infill where a few pings are missed.

5.7.3.2 Sidescan and BioSonar sensor comparison

The sidescan and BioSonar sensors perform well in combination, often providing complementary information, and the best tracking results were obtained using both sensors together. For direct comparison, it is possible to generate imagery from the matched filtered wideband data that are similar to conventional sidescan images. These are useful for testing and visualisation, but we should note that they are not fully representative of the quality of the data generated by the sensor and that the wideband detector module is always fed the raw sensor data.

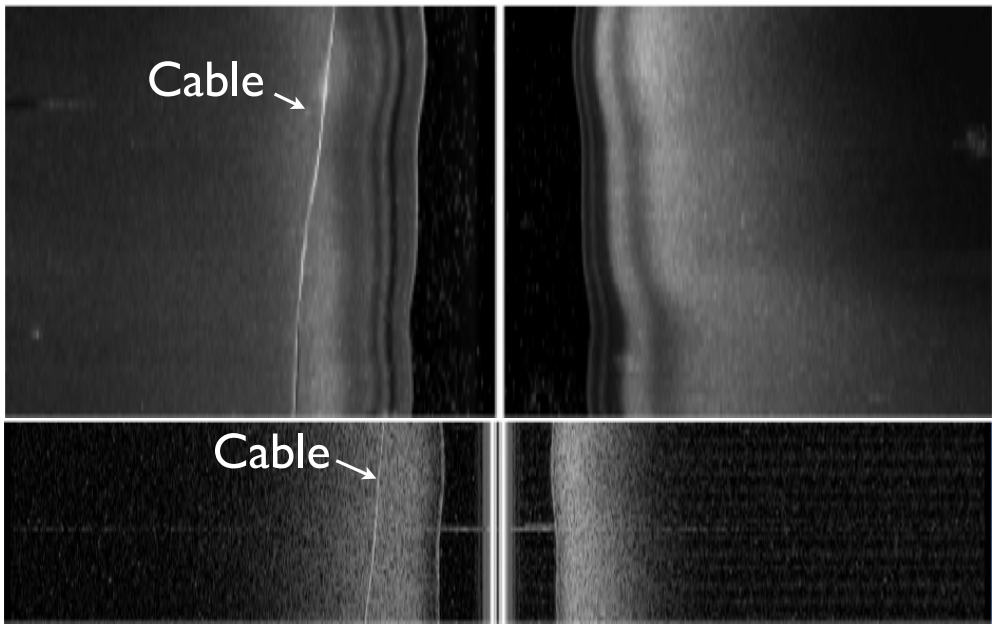

Figure 5.31: Top: Sidescan image showing cable in port channel. Bottom: BioSonar image of approximately half the duration with cable in port channel. Note the total swath width is 40m for the sidescan sensor is 75m for the BioSonar.

Figure 5.31 shows a section of sidescan sonar and a corresponding image produced from the BioSonar data. A section of cable shows well on the port side in

both sensors (cf. figure 5.31). The range is 20m for the sidescan, giving a total swath width of 40m and nearly twice this for the BioSonar.

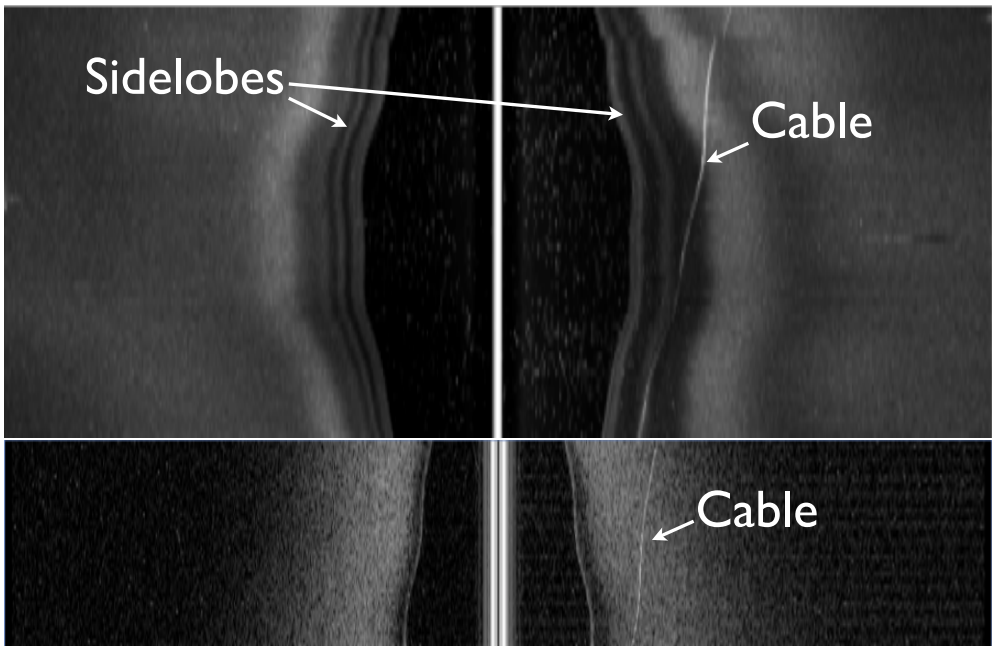

Figure 5.32: Top: Sidescan image showing cable in starboard channel. Bottom: BioSonar image of approximately half the duration with cable in starboard channel. The reduced beam pattern effects in the BioSonar data make tracking the cable much easier in these circumstances.

Figure 5.32 gives further samples of collocated sidescan and BioSonar data. The cable is clearly visible in the starboard channel for both sensors. When the cable deviates sharply bringing it closer to the vehicle, it is more difficult to track in the sidescan, because of the severe beam pattern characteristic of the MarineSonic sensor shown in figure 5.32(*top*). Consequently, the sidescan detector performance is poor in the beam pattern region of the image. Given that a very high frequency is required to generate the resolution required for detection in the imagery, this limits the effective channel for tracking to approximately 10 m. Here, the BioSonar has two inherent advantages. Firstly, the wide frequency band effectively smoothes out frequency dependent nulls in the beam pattern giving a much smoother beam profile and the potential to make continuous detections even when the cable passes beneath the vehicle. Secondly, the lower frequencies

available propagate far more effectively and we are able to get good detections beyond 25 m. Taken together, these mean that the effective channel width for tracking using the BioSonar is in excess of 50 m. In other loch tests stable detections at 40-50 m range have been noted where the cable is lying near parallel to the vehicle track. At a higher ping rate and with some parameter modification, the downsampled imagery could also provide a suitable input to the SS detector.

A further advantage in using the BioSonar for tracking is the ability to follow the cable through regions of partial and shallow burial. This is again related primarily to the difference in the operating frequencies between the two sonar systems, though the wide beam width of the BioSonar no doubt plays a role too. Figure 5.33 demonstrates the problem for the sidescan system. Where the cable goes into burial, detection probabilities are reduced. Furthermore, in maintaining a sufficient number of cable contacts to ensure robust tracking, a large number of false detections are generated. In the example shown, tracking is still possible due to the effectiveness of the particle filter tracking module used, but only a small increase in bottom clutter would lead to failure.

Both sensors struggle to detect a cable lying at a steep angle to the vehicle track. The wide beamwidth of the BioSonar works in its favour, but this is offset by the higher operating frequency of the MarineSonic system. Detection probabilities are significantly reduced at angles greater than 20°. This observation on detections can be seen in Figure 5.34. This shows cable detections over a c. 300 m length of cable. Given the difficulties in deploying the cable using only a small RIB, it was not possible to maintain tensions typical of marine installation. For this reason, the cable has a tendency to follow an elongated spiral trajectory over the loch bed. In places it goes into burial and its direction relative to the vehicle track is subject to large changes. For the BioSonar, burial is not a large problem. The dropped detections are correlated much more clearly with the cable angle. The greatest density of missed detections occurs in the centre of the image, corresponding to some gross vehicle movements, probably initiated by the obstacle avoidance systems. Even here, the remaining sparse detections are sufficient to maintain an active track and on this run a complete unbroken

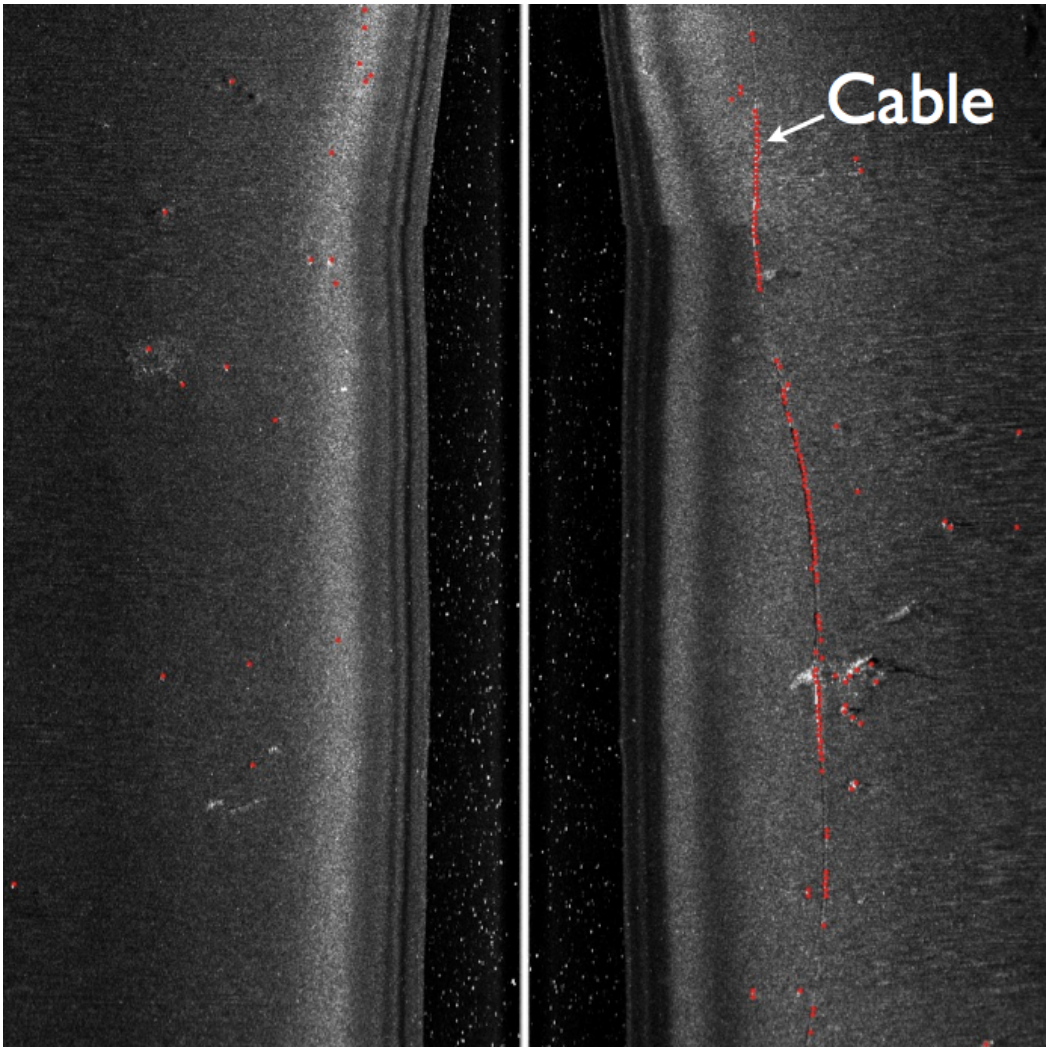

Figure 5.33: Sidescan image of the cable lying on the seabed. The red dots are the result of the detection. The sidescan detector fails to detect the cable through regions of partial burial – in these circumstances, generating a sufficient number of cable contacts to maintain a track leads to a large number of false contacts in each image.

end-to-end survey was completed. The detection probability here is high, but is generated with conservative thresholds so that there are very few false alarms.

The BioSonar system performed well in these trials, but performance could be increased further by more sophisticated detection algorithms. The method

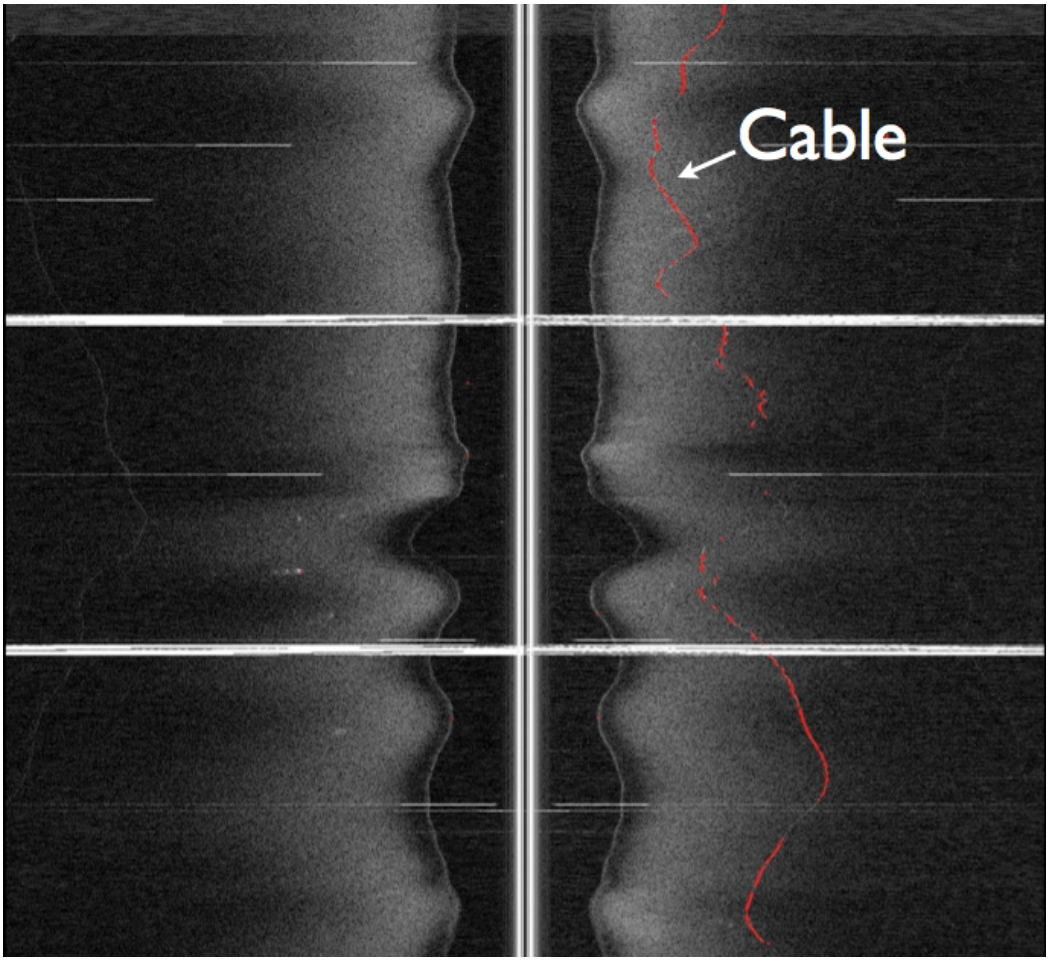

Figure 5.34: Approximately 500 m section of cable showing the BioSonar detections – the cable is detected through regions of shallow burial (red color). There are very few false contacts and this $p(\mathrm{D})/p(\mathrm{FA})$ ratio is sufficient to maintain a continuous unbroken track for the cable survey.

chosen here is simple and exceptionally economical. This is essential to be able to process large quantities of wideband data and pass detection packets to the vehicle network for downstream processing given strictly limited computing power in the current BioSonar bottle. The current package was designed for data acquisition only, so the additional computational load provides a severe challenge. It is intended to upgrade the computing power significantly in a future prototype.

In addition to improving detector performance, the increased resources will enable full spectral processing of contact segments. We have shown in earlier work that there is a sufficient difference in the response of different cable types to provide a positive identification, that is to perform cable recognition. This could be useful, for example, in following a specific cable through cable crossing regions or in discriminating between cable and other contacts to further drive down the false alarm rate.

5.8 Conclusions

In this chapter, we investigate further our understanding of the echo structure and echo formation. By doing so we were able to propose a new approach to sonar: the bio-mimetic sonar. By answering the question: "what makes the dolphin sonar so efficient?", we created new bio-mimetic broadband pulses. We show that by focusing the energy on different part of the spectrum, these bio-mimetic pulses will react differently depending on the target. By analysing the interaction between sound and objects, we identify stable features based on target resonances. We show how these features can be used for identification purposes. The BioSonar prototype has been built according to the dolphin's sonar characteristics. Because the bandwidth is lower than classical imagery sonars and because its wide beamwidth, the BioSonar losses resolution compared to other sonars. But this resolution loss is compensated by the additional information provided by analysing the echo itself. We demonstrated the capabilities of such sensor in real environment for two particular applications: mine countermeasures and cable tracking.

Chapter 6

MIMO Sonar

Tous pour un, un pour tous!
Alexandre Dumas

6.1 Introduction

MIMO stands for Multiple Input Multiple Output. It refers to a structure with spatially spaced transmitters and receivers. It has been widely investigated during the last two decades for wireless communications mainly to overcome the multipath problem in complex environments (principally urban environment). MIMO systems have received a lot of interest in recent years in the radar community (Bliss and Forsythe [2003]; Du [2010]; Fishler et al. [2004, 2006]; Rabideau [2003]). First of all MIMO radar offers better coverage. Radar researchers have then pointed out further multiple advantages of these systems such as diversity gain for target detection (Du et al. [2008]; Fishler et al. [2006]; Lehmann et al. [2007]; Li and Stoica [2009]), angle of arrival (Bekkerman and Tabrikian [2006]; Robey et al. [2004]) and Doppler estimation (Haimovich et al. [2008]; Lehmann et al. [2006a]). Coherent processing also allows super-resolution for target localisation (Lehmann et al. [2006b]).

In this chapter we focus our attention on the detection and the identification problem using MIMO systems. We first present the MIMO formulation for radar

systems. This formulation stipulates the multistatic relation between transmitters and receivers through the channel matrix. The channel matrix models the wave propagation and target scattering. Several models have been proposed for target scattering. We present here how to compute the channel matrix using point scatterer models. The finite scattering point model presents an interesting parallel with the random walk problem. We will explain and explore this close mathematical relationship.

We then explore broadband MIMO sonar systems. The limitation of the MIMO radar formulation is explained and a model based on the target form function more suitable for sonar (and broadband sonar in particular) is proposed. In the previous chapters we presented and developed several models for target backscattering. Taking into account the multistatic aspect of MIMO architecture we propose a new model for cylindrical shell scattering.

Finally we present the detection problem using a MIMO system. Using widely separated transducers, it has been shown that channel matrices are decorrelated from one another, which means that the views of the potential target can be considered as independent. MIMO systems improve the process of classification. We demonstrate that target detection can be enhanced by using time reversal techniques. A pseudo time reversal algorithm is then proposed.

6.2 Reformulation of the broadband MIMO sonar problem

6.2.1 The RADAR formulation

The first formulation for MIMO systems has been made by the radar community. The MIMO system model can usually be expressed by: $\overline{\mathbf{r}} = \overline{\overline{\mathbf{H}}}.\overline{\mathbf{s}} + \overline{\mathbf{n}}$, where $\overline{\mathbf{r}}$ represents the receivers, $\overline{\mathbf{s}}$ the transmitters, $\overline{\mathbf{n}}$ the noise, and $\overline{\overline{\mathbf{H}}}$ the channel matrix. The channel matrix include the wave propagation in the medium from any transmitters to any receivers and the target reflection. At first, targets were represented using the "point target" assumption Skolnik [2002]. Since

then, several target models have been proposed such as rectangular-shape target in Fishler et al. [2006] composed of an infinite number of scatterers. We present here the most popular model for a radar target model which is the finite scatterer model Du et al. [2008]; Haimovich et al. [2008].

In Haimovich et al. [2008] the authors formulate narrowband MIMO radar using a finite point target model. A target is represented here with Q scattering points spatially distributed. Let $\{X_q\}_{q\in[1,Q]}$ be their locations. The reflectivity of each scattering point is represented by the complex random variable ζ_q. All the ζ_q are assumed to be zero-mean, independent and identically distributed with a variance of $\mathbb{E}[|\zeta_q|^2] = 1/Q$. Let Σ be the reflectivity matrix of the target, $\Sigma = \text{diag}(\zeta_1, ..., \zeta_Q)$. By using this notation the average RCS (radar cross section) of the target $\{X_q\}$, $\mathbb{E}[\Sigma\Sigma^T]$, is normalised to 1.

The MIMO system comprises a set of K transmitters and L receivers. Each transmitter k send a pulse $\sqrt{E/K}.s_k(t)$. We assume that all the pulses $s_k(t)$ are normalised. Then E represents the total outcoming energy of the MIMO system. Receiver l receives from transmitter k the signal $z_{lk}(t)$ which can be written as:

$$z_{lk}(t) = \sqrt{\frac{E}{K}} \sum_{q=1}^{Q} h_{lk}^{(q)} s_k \left(t - \tau_{tk}(X_q) - \tau_{rl}(X_q)\right) \tag{6.1}$$

$$\text{with} \quad h_{lk}^{(q)} = \zeta_q \exp\left(-j2\pi f_c[\tau_{tk}(X_q) + \tau_{rl}(X_q)]\right) \tag{6.2}$$

where f_c is carrier frequency, $\tau_{tk}(X_q)$ represents the propagation time delay between the transmitter k and the scattering point X_q, $\tau_{rl}(X_q)$ represents the propagation time delay between the scattering point X_q and the receiver l. Note that $h_{lk}^{(q)}$ represents the total phase shift due to the propagation from the transmitter k to the scattering point X_q, the propagation from the scattering point X_q to the receiver l and the reflection on the scattering point X_q.

Assuming the Q scattering points are close together (*i.e.* within a resolution cell), we can write:

$$\begin{aligned} s_k\left(t-\tau_{tk}(X_q)-\tau_{rl}(X_q)\right) &\approx s_k\left(t-\tau_{tk}(X_0)-\tau_{rl}(X_0)\right) \\ &= s_k^l(t,X_0) \end{aligned} \tag{6.3}$$

where X_0 is the centre of gravity of the target $\{X_q\}$. So Eq.. (6.1) becomes:

$$\begin{aligned} z_{lk}(t) &= \sqrt{\frac{E}{K}}\left(\sum_{q=1}^{Q}\zeta_q \exp\left(-j2\pi f_c[\tau_{tk}(X_q)+\tau_{rl}(X_q)]\right)\right) s_k^l(t,X_0) \\ &= \sqrt{\frac{E}{K}}\left(\sum_{q=1}^{Q} h_{lk}^{(q)}\right) s_k^l(t,X_0) \qquad (6.4) \\ &= \sqrt{\frac{E}{K}}\; h_{lk}\; s_k^l(t,X_0) \qquad (6.5) \end{aligned}$$

using the notation $h_{lk}=\sum_{q=1}^{Q} h_{lk}^{(q)}$.

6.2.2 The random walk analogy

It is interesting to note that the term $\sum_{q=1}^{Q} h_{lk}^{(q)}$ in Eq. (6.4) corresponds by essence to a random walk in the complex plane where each step $h_{lk}^{(q)}$ can be modelled by a random variable. Random walks are often used in physics to model the particle diffusion in gas or liquid. Figure 6.1 draws an example of a random walk in the Euclidian plane. In this example the random walk process is the results of 10^4 random steps in the plane. Each step is the realisation of the random variable described by Eq. (6.6).

Lets assume that the reflectivity coefficients ζ_q can be modelled by the random variable $\frac{1}{\sqrt{Q}}\mathrm{e}^{2i\pi U}$ where $U\in[0,1]$ is the uniform distribution. This hypothesis implies that:

$$h_{lk}^{(q)} = \frac{1}{\sqrt{Q}}\mathrm{e}^{2i\pi U} \tag{6.6}$$

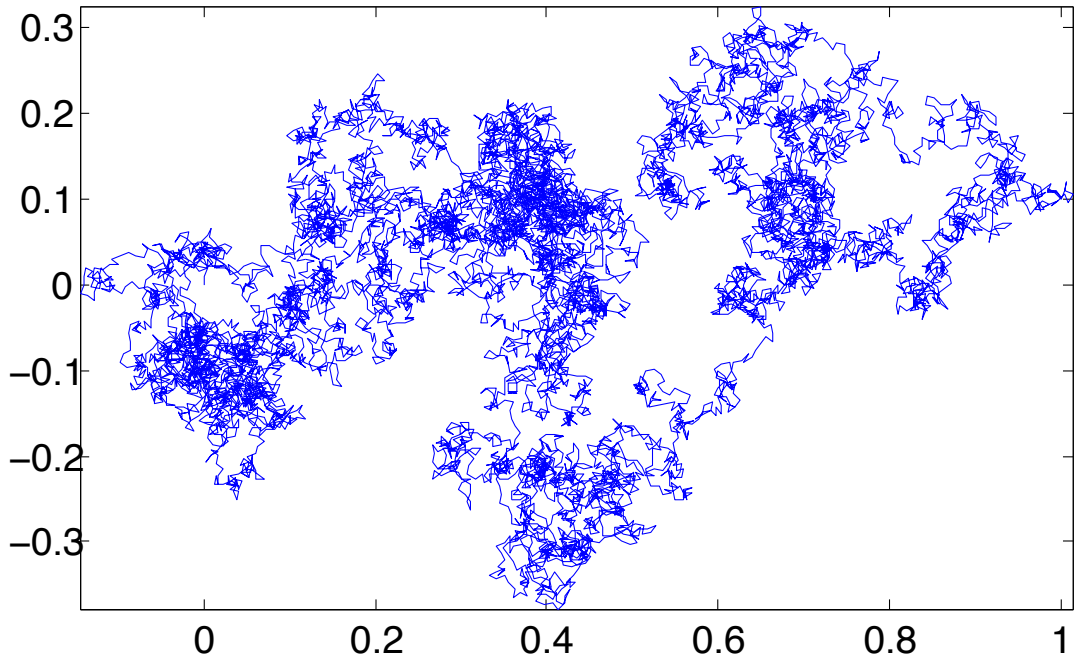

Figure 6.1: Example of a random walk of 10^4 steps in the Euclidian plane.

The independence of each $h_{lk}^{(q)}$ lies in the fact that the antennas are widely spaced and there is no correlation between each transmit $\rightarrow$ scattering point $\rightarrow$ receiver path. Thanks to the central limit theorem we can compute the limit:

$$\lim_{Q\rightarrow+\infty} \sqrt{\left|\sum_{q=1}^{Q} h_{lk}^{(q)}\right|^2} = \text{Rayleigh}(1/\sqrt{2}) \tag{6.7}$$

The central limit theorem gives only the asymptotic behaviour of the random variable. As the number of scattering points becomes large the reflectivity of the target can be modelled by a Rayleigh distribution. This argument justifies the fact that a Rayleigh distribution is often chosen to model speckle noise.

Eq. (6.7) links the expected reflectivity of the target $\{X_q\}$ to the expected diffusion of a particle following the random walk $\sum_{q=1}^{Q} h_{lk}^{(q)}$. It has been proven by Berry [1941] that the convergence of Eq. (6.7) is fast. To demonstrate we use the Moivre-Laplace representation (which consists in essence in comparing the

probability density functions) to visualize the PDF convergence. In figure 6.2 we compute the probability density functions (PDF) of the reflectivity of a Q scattering points target using the model given by Eq. (6.6). As this figure shows, for $Q \geq 5$ the reflectivity PDF matches closely the Rayleigh$(1/\sqrt{2})$ probability distribution. In figure 6.2 we can see that the probability function of the 100 scatterer target and Rayleigh$(1/\sqrt{2})$ are almost indistinguishable.

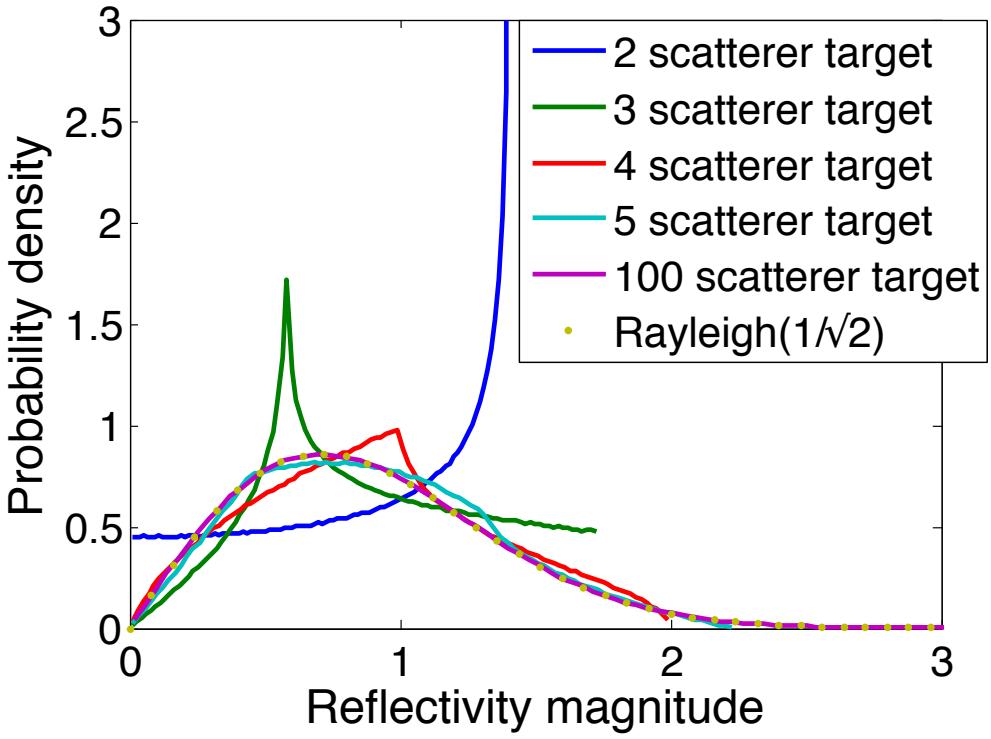

Figure 6.2: Reflectivity probability density functions of a Q scattering points target with $Q = 2, 3, 4, 5$ & 100 using the scatterer reflectivity model from Eq. (6.6). Note that the Rayleigh distribution (in yellow dots) matches almost perfectly the 100 scatterers curve.

We notice in figure 6.2 that while the convergence of the reflectivity distribution function to a Rayleigh distribution is fast the reflectivity of a target with few scattering points ($Q \in [2, 3, 4]$) presents a very characteristic PDF.

6.2.3 The MIMO sonar extension

In this section we propose a reformulation of the Haimovich model presented in section 6.2.1 to suit broadband sonars. We saw in Capus et al. [2007]; Pailhas et al. [2006] that for broadband sonar a formulation in the Fourier domain is more appropriate. Eq. (6.1) becomes:

$$Z_{lk}(\omega) = \sqrt{\frac{E}{K}} \sum_{q=1}^{Q} h_{lk}^{(q)} S_k(\omega) \mathbf{e}^{-j\omega[\tau_{tk}(X_q)+\tau_{rl}(X_q)]} \tag{6.8}$$

Using the following notations:

$$\begin{array}{rcl} \tau_{tk}(X_q) & = & \tau_{tk}(X_0) + \tilde{\tau}_{tk}(X_q) \\ \tau_{rl}(X_q) & = & \tau_{rl}(X_0) + \tilde{\tau}_{tk}(X_q) \end{array} \tag{6.9}$$

and

$$H_{lk}(X_0, \omega) = \sqrt{\frac{E}{K}} . \mathbf{e}^{-j(2\pi f_c+\omega).[\tau_{tk}(X_0)+\tau_{rl}(X_0)]} \tag{6.10}$$

we arrive to:

$$\begin{array}{rl} Z_{lk}(\omega) & = H_{lk}(X_0, \omega) \left(\sum_{q=1}^{Q} \tilde{h}_{lk}^{(q)} \mathbf{e}^{-j\omega[\tilde{\tau}_{tk}(X_q)+\tilde{\tau}_{rl}(X_q)]} \right) S_k(\omega) \\ & = H_{lk}(X_0, \omega) F_\infty(\omega, \theta_l, \phi_k) S_k(\omega) \end{array} \tag{6.11}$$

where θ_l is the angle of view of the target from the transmitter and ϕ_k is the angle of view of the target from the receiver.

Eq. (6.11) can be interpreted as follows: the first term corresponds to the propagation of the wave to and from the target, the second term is the form function of the target, the third term is the transmitted signal.

The main advantage of this formulation is the clear separation between propagation terms and target reflection terms. In our formulation the target form function F_∞ is independent of any particular model. The second advantage of this formulation is that the generalization of Eq. (6.11) including multipath and

attenuation terms is straightforward. Considering P multipaths between the transmitter l and the receiver k Eq. (6.11) becomes:

$$Z_{lk}(\omega) = \sum_{p=1}^{P} A^{(p)}(\omega) H_{lk}^{(p)}(X_0, \omega) F_{\infty}(\omega, \theta_l^{(p)}, \phi_k^{(p)}) S_k(\omega) \tag{6.12}$$

$A^{(p)}(\omega)$ is the attenuation through path p.

6.3 Virtual point scatterers model for a cylindrical shell

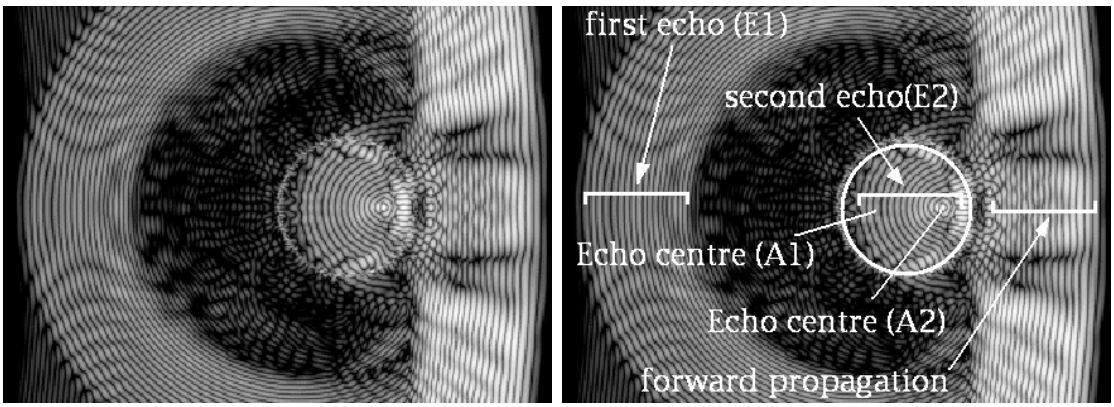

Figure 6.3: Sound interaction between a plane wave and a plastic cylindrical shell.

In this section we present an accurate multi-static model for a low impedance shell cylinder. In section 5.4.4, we demonstrated that the sound scattering of a low impedance shell cylinder is analogous to the reflection by two spherical mirrors (one convex for the front face and one concave for the back face) in geometrical optics. Figure 6.3 shows the echo formation of an acoustic wave reflected by a plastic cylindrical shell. The location of the two echo centres **A1** and **A2** (in figure 6.3) can be computed thanks to the well known formula of reflection by a spherical mirror:

$$\frac{1}{\overline{\mathbf{SA'}}} + \frac{1}{\overline{\mathbf{SA}}} = \frac{2}{\overline{\mathbf{SC}}} \tag{6.13}$$

where **A** and **A′** represent respectively the source and the source image, **C** the centre of the sphere and **SC** the radius of the sphere.

A1 and **A2** are the source images of an incoming plane wave. The two echo centres, **A1** and **A2**, are then exactly in between the centre of the cylinder and respectively the front and the back of the cylinder. In our model **A1** and **A2** will represent the virtual scatterers. They act like point sources, but contrary to scattering points, they emit the received pulse with a delay (positive or negative).

The transmitter k transmits the pulse $s_k(t)$. The acoustic wave is reflected by the cylinder modelled by the virtual scatterers **A1** and **A2** to receiver l. Eq. (6.14) expresses the acoustic field $r_{kl}(t)$ received at receiver l:

$$r_{kl}(t) = s_k\left(t - \tau_{kC} - \frac{3}{2}\frac{SC}{c} - \tau_{A_1 l}\right)\mathbf{e}^{i\phi_1} + s_k\left(t - \tau_{kC} + \frac{3}{2}\frac{SC}{c} - \tau_{A_2 l}\right)\mathbf{e}^{i\phi_2} \tag{6.14}$$

where SC represents the radius of the cylinder, c the speed of sound in water, C the centre of the cylinder and the notation τ_{AB} represents the propagation time between A and B.

The two terms $-\frac{3}{2}\frac{SC}{c}$ and $+\frac{3}{2}\frac{SC}{c}$ represent the negative and positive delays of the virtual scatterers. In figure 6.4 we compare the echo spectra of our virtual scattering point model with the analytic solution given in Doolittle and Uberall [1966]. In this example, the cylindrical shell is made of PVC, its diameter is 32 cm and its thickness is 3 mm. The receiver is placed at 4 metres from the shell at an angle of 30°. An excellent match is found between the theoretical prediction and our model.

6.4 Statistical MIMO

6.4.1 The detection problem with statistical MIMO

The usual approach to the detection problem consists in evaluating the presence of a target of interest in the received signal $\mathbf{r}$. Under the null hypothesis $\mathcal{H}_0$ the

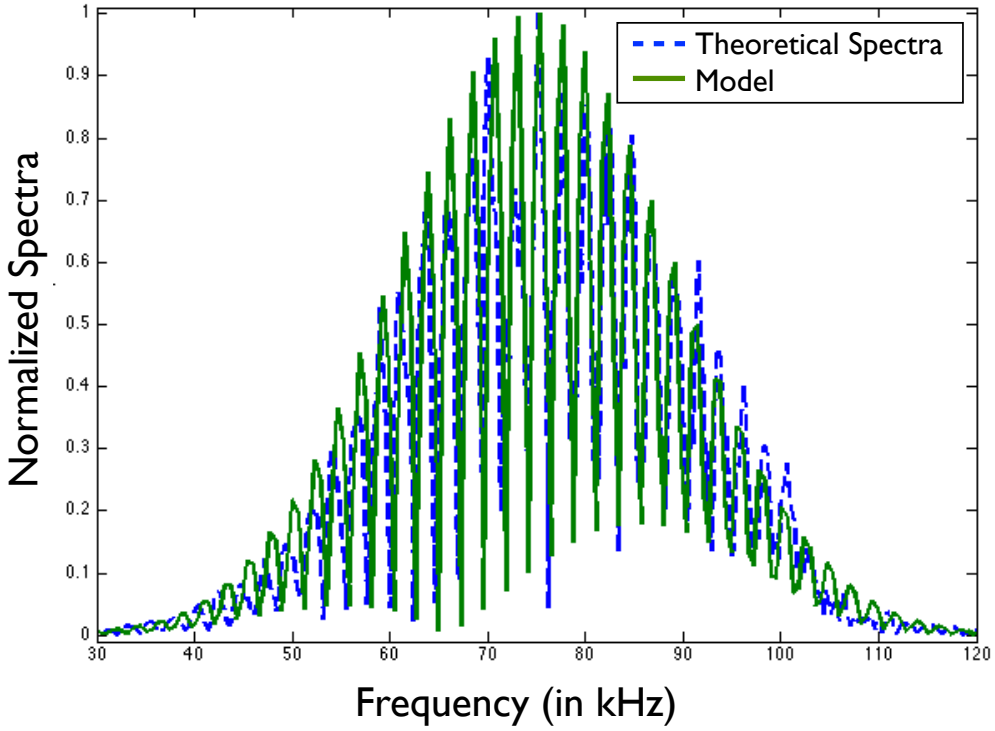

Figure 6.4: Matching between the normalized spectra between the theoretical prediction and our model.

received signal $\mathbf{r}$ contains only the noise $\mathbf{n}$. Under the target presence hypothesis $\mathcal{H}_1$ the received signal contains both the target signal and the noise. A detection rule function $\mathcal{F}(\mathbf{r})$ is compared to a given threshold η. If $\mathcal{F}(\mathbf{r}) < \eta$, the hypothesis $\mathcal{H}_0$ is chosen; if $\mathcal{F}(\mathbf{r}) \geq \eta$, hypothesis $\mathcal{H}_1$ is chosen. We can distinguish two kinds of errors:

- the *false alarm*: the detector detects a target ($\mathcal{F}(\mathbf{r}) \geq \eta$) when no target is present.
- the *missed detection*: the detector misses a target ($\mathcal{F}(\mathbf{r}) < \eta$) when a target is present.

In the rest of this section we compute the detection rule function $\mathcal{F}(\mathbf{r})$ under the hypothesis made in section 6.2.

Let $r_l(t)$ be the total received signal at the receiver l. According to our previous notations we have:

$$r_l(t) = \sum_{k=1}^{K} z_{lk}(t) \tag{6.15}$$

where $z_{lk}(t)$ has been defined in Eq. (6.4). Let $\mathbf{x}$ be the $KL \times 1$ output vector from the filter bank $s_k^*(t)$ with $k \in [1, K]$. Note that $\mathbf{x}$ represents the match-filtered response and is computed as followed:

$$[\mathbf{x}]_{(l-1)L+k} = r_l \star s_k^*(t) \tag{6.16}$$

We assume that all the sending pulses $s_k(t)$ are orthogonal so:

$$s_i \star s_j^*(t) = \delta(i - j) \tag{6.17}$$

where δ denotes the discrete Dirac delta function. So Eq. (6.16) becomes:

$$\begin{aligned} [\mathbf{x}]_{(l-1)L+k} &= r_l \star s_k^*(t) \\ &= \sum_{k=1}^{K} z_{lk} \star s_k^*(t) \\ &= z_{lk} \star s_k^*(t) \\ &= \sum_{q=1}^{Q} h_{lk}^{(q)} \end{aligned} \tag{6.18}$$

We choose the following detection rule:

$$\mathcal{F}(\mathbf{r}) = ||\mathbf{x}||^{\mathbf{2}} = \sum_{\mathbf{l},\mathbf{k}} ||\mathbf{x_{lk}}||^{\mathbf{2}} \tag{6.19}$$

Using the same probability distribution stated in the model presented in section 6.2.2, we deduce that under the $\mathcal{H}_1$ hypothesis, $\mathcal{F}(\mathbf{r})$ follows the following probability distribution:

$$\mathcal{F}(\mathbf{r}) \sim \sum_{\mathbf{n=1}}^{\mathbf{N}} \text{Rayleigh}^{\mathbf{2}}(\sigma) \tag{6.20}$$

where $N = K \times L$ represents the number of independent views provided by the MIMO system. Using the properties of the Rayleigh distribution we can write:

$$\sum_{n=1}^{N} \text{Rayleigh}^2(\sigma) \sim \Gamma(N, 2\sigma^2) \tag{6.21}$$

where Γ is the Gamma distribution. The asymptotic behaviour of the detection rule $\mathcal{F}(\mathbf{r})$ can be deduced from the following identity:

$$\lim_{N \to +\infty} N.\Gamma(Nx, N, 1) = \delta(1 - x) \tag{6.22}$$

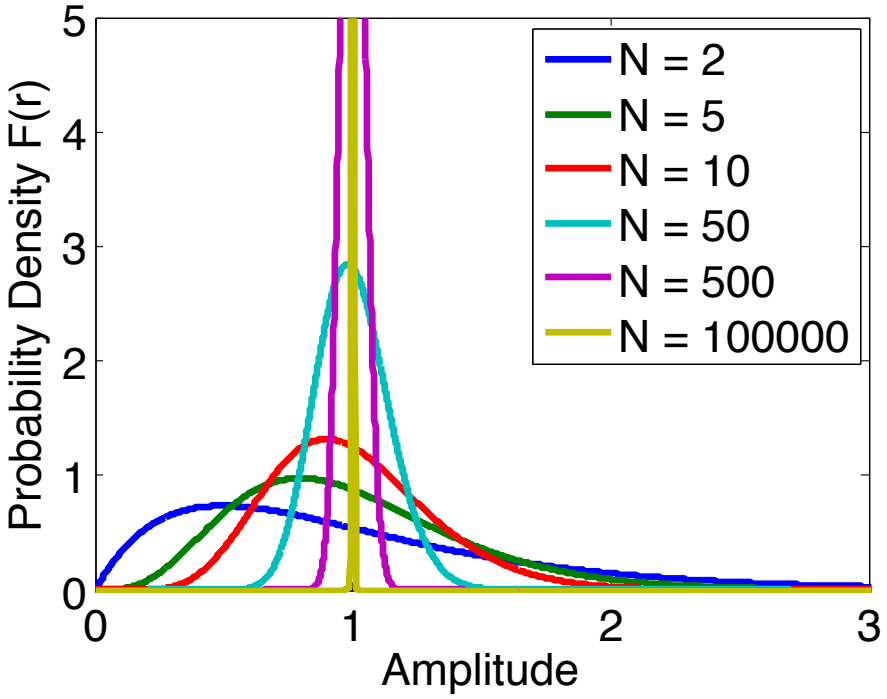

Figure 6.5: Probability density function of $N.\Gamma(Nx, N, 1)$ for several values of N

Note that the proof of Eq. (6.22) is given in Appendix C. Eq. (6.22) has interesting consequences: as the total number of views N offered by the MIMO system increases, the probability density function of the detection rule $\mathcal{F}(\mathbf{r})$ under the $\mathcal{H}_1$ hypothesis tends to a Dirac function. And $\mathcal{F}(\mathbf{r})$ tends to the average RCS defined in 6.2.1. This result can appear counter-intuitive as it seems to be in

disagreement with the results from section 6.2.2. A discussion on this result and its implications are proposed in section 6.4.2. Figure 6.5 shows the convergence speed of Eq. (6.22). Note that the convergence is relatively slow (especially when compared to the convergence speed of Eq. (6.7)). This figure seems to indicate that roughly 100 views are necessary to decorrelate scatterers within one pixel resolution.

6.4.2 Thoughts on the RCS definition and its implications

As has been said in section 6.2.1 Haimovich defines the average radar cross section as $\mathbb{E}[\Sigma\Sigma^T] = 1$. This definition implies that the contribution of all the scatterers sum incoherently. Considering a target contained within a single resolution cell and assuming coherent sensors such radar or sonar the scattering points interact coherently with each other from a signal point of view. The random summation creates constructive and destructive interferences as we explained with the Random Walk analogy in section 6.2.2. We can then define the *effective* RCS as the effective average reflectivity of the target viewed by the sensors. We also demonstrate in the same section that we can very accurately model the *effective* RCS of a target with more than 5 scatterers by:

$$\mathbb{E}\left[\text{Rayleigh}(\sigma)\right] = \sigma\sqrt{\frac{\pi}{2}} \tag{6.23}$$

where $\sigma = 1/\sqrt{2}$. So the *effective* RCS of the target is in fact:

$$\mathbb{E}[\{X_q\}] = \sqrt{\pi}/2 \tag{6.24}$$

It is important to note that $\mathbb{E}[\{X_q\}] < 1$.

For this precise reason the result given by Eq. (6.22) appears counter-intuitive. We would have expected the detection rule function $\mathcal{F}(\mathbf{r})$ to tend to the mean of this Rayleigh distribution *i.e.* $\sqrt{\pi}/2$ which represents the effective RCS defined earlier. The limit given by Eq. (6.22) gives a new insight into the capabilities of MIMO systems. It demonstrates indeed that as the number of independent views increases the MIMO detection system decorrelates the contribution of each

scatterer in the echo signal and suppresses the coherent speckle noise in the target response.

6.4.3 Super-resolution with MIMO systems

Two important results were given in the previous sections:

- it is possible to evaluate the scatterer density of a target if the number of scatterers is low (typically less than 5).
- with a sufficient number of views MIMO systems can decorrelate the scatterers contributions within one pixel resolution.

These elements give us strong leads that super-resolution may be possible using MIMO systems. So far we have not taken into account the geometry of the target. We can reasonably assume that a target has a fixed geometry during the MIMO inspection. The questions we aim to answer here are: is it possible to recover the target geometry? and how?

With the insight of the previous results we know that to achieve super-resolution the following conditions must be respected:

Independent views: the antenna have to be sufficiently spaced to ensure the independence of each view.

Decorrelation: the total number of views has to be large enough to ensure the scatterers decorrelation.

Broadband: in order to achieve the range resolution needed, the MIMO system has to use broadband pulses for range compression.

In the following experiment we aim to demonstrate that we can recover the geometry of a target (*i.e.* the location of its scatterers). The MIMO configuration used here is drawn in figure 6.6. Transmitters are placed in the x-axis, the receivers are on the y-axis. For this experiment we place the transducers an equal spacing along the axis. The number of transmitters and receivers and the

spacing between them is adjustable. The MIMO system will use the frequency band 50 kHz to 150 kHz. We consider a 3 point scatterers target, the scatterers are separated by one wavelength. Note that we are considering the central frequency of the MIMO system (100 kHz). Under this condition one wavelength corresponds to 1.5 cm.

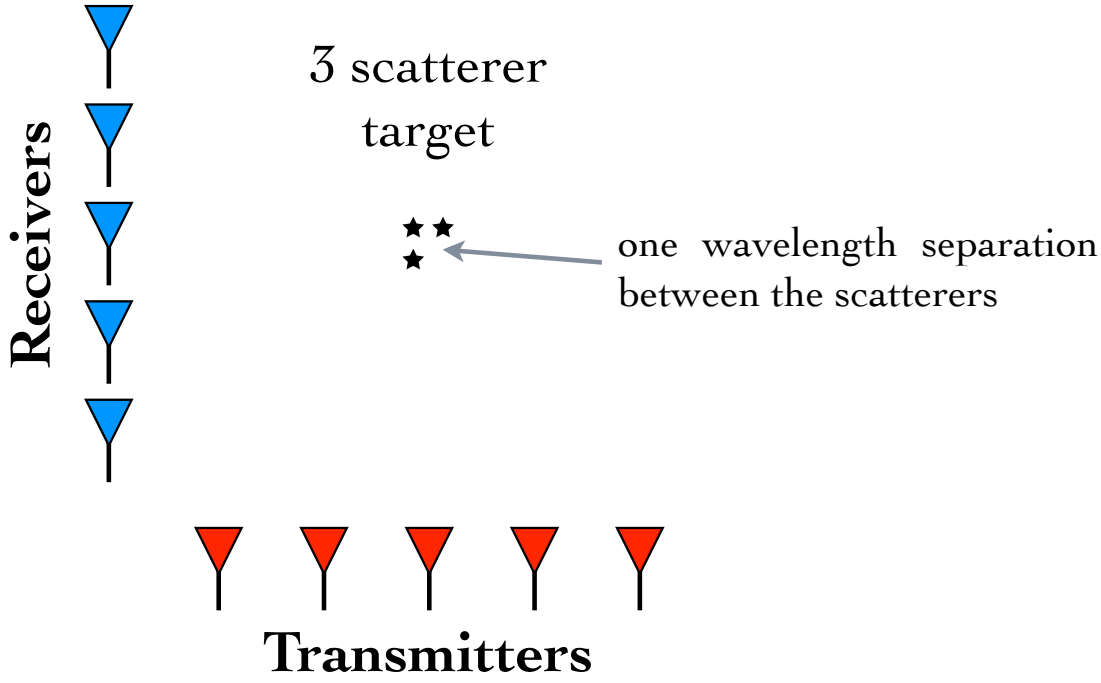

Figure 6.6: MIMO configuration.

In order to image the output of the MIMO system we will use the multi-static back-projection algorithm which is a variant of the bistatic back-projection algorithm developed by the SAR community. Further details can be found in Arikan [1988]; Home and Yates [2002]; N.J.Willis [1991]. In section 4.2.1 we discuss the back-projection algorithm for SAS image formation and we demonstrate that to form the SAS image we integrate the signal along a parabola. In the bistatic case the integration is done along ellipses. For the multi-static scenario the continuous integration is replaced by a finite sum in which each term corresponds to one transmitter/receiver pair contribution. Figure 6.7 shows the principle of the multi-static back-projection algorithm.

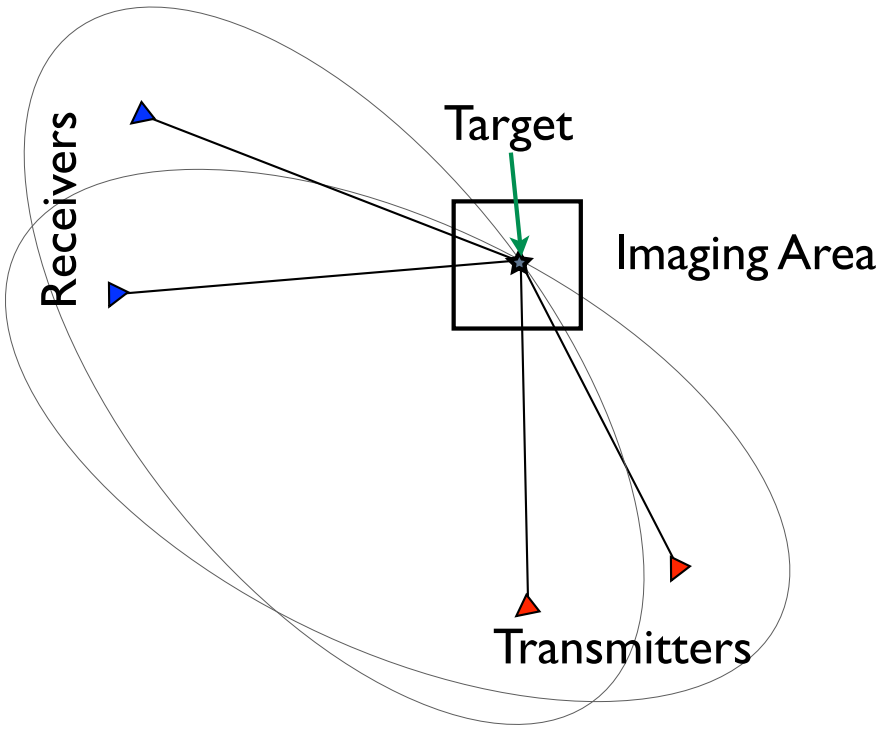

Figure 6.7: Principle of the multi-static back-projection algorithm.

In figure 6.8 we reconstruct the MIMO image using incoherent processing (*i.e.* only the amplitude of the echoes have been used in the multi-static back-

propagation algorithm). This figure represents in essence how the MIMO signal has been treated so far: the detection processing has been done using only the amplitudes of the different views. As expected the 3 scatterer target is represented only as blob of energy. Note that the dimensions of this patch of energy represent the resolution limit of the incoherent system which is approximately 10 cm x 10 cm.

In figure 6.9 we have considered a MIMO system with 10 transmitters and 10 receivers with a spacing of 20 cm. For this scenario the 20 cm spacing breaks the widely spaced antenna assumption and the views are not exactly independent between each other. For this reason we only observe a blob of energy at the target location.

In the next figure 6.10 the MIMO system consists in 5 transmitters and 5 receivers with 3 metres spacing. In this case the spacing between the antennas is several hundreds of wavelengths so the independence of the views is respected. The total number of views however is 5 x 5 = 25 independent views which is relatively low according to the convergence speed of Eq. (6.22). In this scenario the number of views is too low to ensure the decorrelation of the scatterers within the target. For this reason only a blob of energy marks the target location. However by closely inspecting to the central blob it is possible to distinguish a structure.

Finally in figure 6.11 we consider a MIMO system with 10 transmitters and 10 receivers with a spacing of 3 metres. With this configuration we respect the conditions stipulated earlier and we are able to clearly image the 3 scatterer target in so doing achieve super resolution imaging.

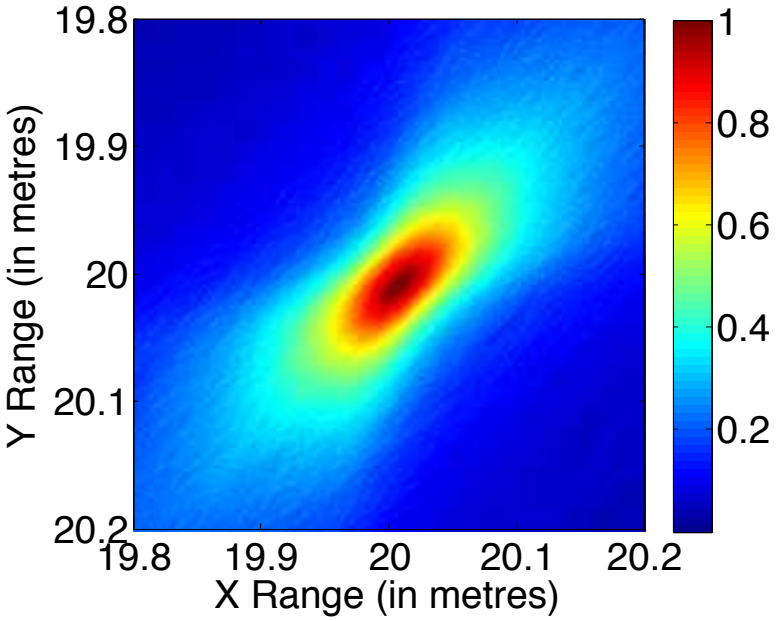

Figure 6.8: Incoherent multistatic image.

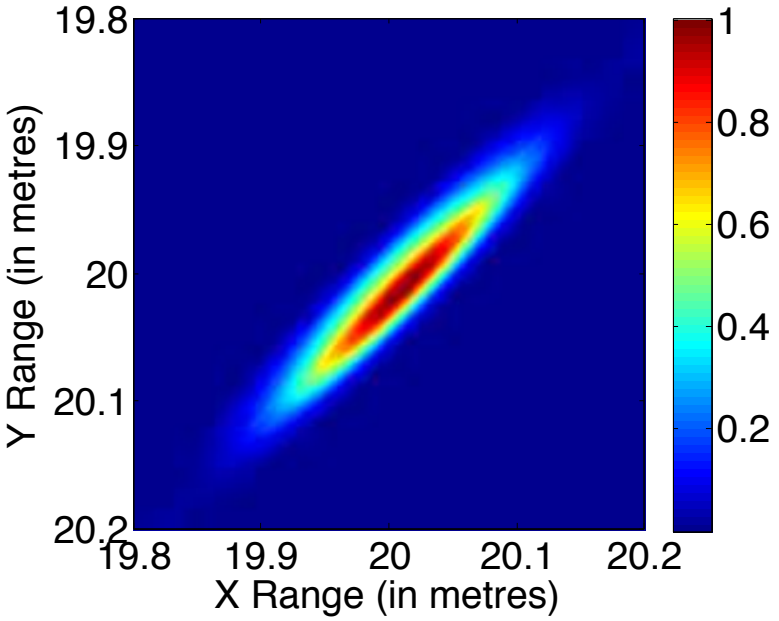

Figure 6.9: 3 scatterers target MIMO image using 10 transmitters and 10 receivers with 20 cm spacing.

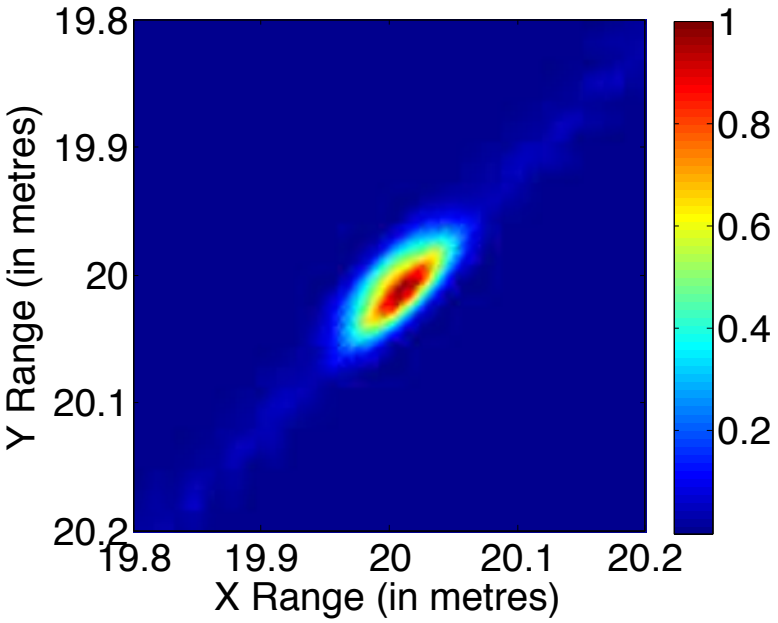

Figure 6.10: 3 scatterers target MIMO image using 5 transmitters and 5 receivers with 3 metres spacing.

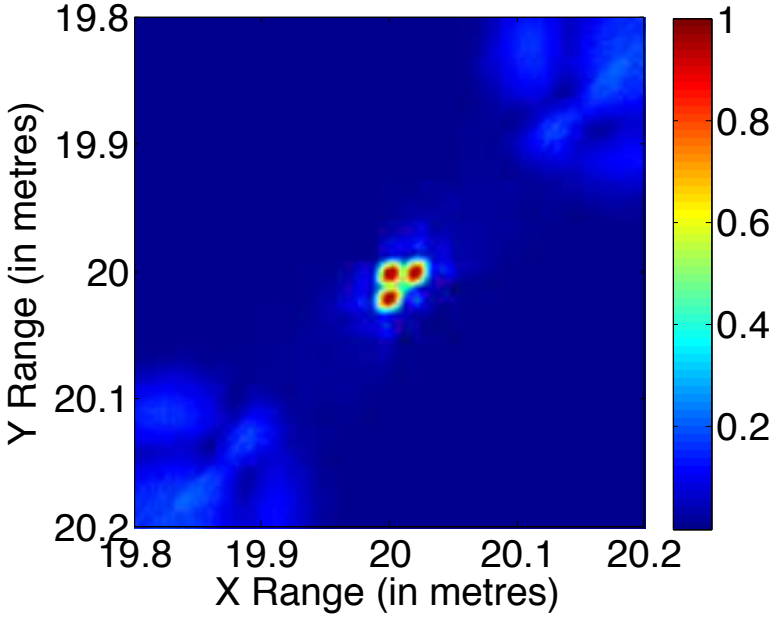

Figure 6.11: 3 scatterers target MIMO image using 10 transmitters and 10 receivers with 3 metres spacing.

6.5 MIMO and Time Reversal

6.5.1 Time reversal

In the previous section we posed the detection problem using statistical MIMO. We demonstrated that the view diversity increases drastically the detection probability and reduces the false alarm rate. In this section we link MIMO systems with time reversal techniques. The main idea behind time reversal is to actively control the outgoing pulses to focus energy on a given region of interest (Folegot et al. [2005]; Prada et al. [1991, 1996]). By focussing the sound on the target the general SNR of the echo is then improved (Folegot et al. [2003]).

Underlying the concept of time reversal is the simple observation that the wave propagation equation (cf. Eq. (6.25)) is not changed by inverting the time:

$$\frac{\partial^2 p}{\partial x^2} - \frac{1}{c}\frac{\partial^2 p}{\partial t^2} = 0 \tag{6.25}$$

In the following example we show the capability of MIMO systems using time reversal techniques to focus sound energy on a specific target. We consider for simplicity a single transmitter, several receivers and a single target in an environment: a so called MISO (Multiple Input Single Output) system. An example configuration is shown in Figure 6.12.

At each ping time, the transmitter projects an acoustical wave. Ignoring any further reflections, this wave is reflected by the target and the echo is recorded through the receivers. By inverting the time, this same process will occur in reverse and this can be achieved by retransmitting the inverted time echoes through the receiver array. In this way, we effectively focus the sound on the target. The images in Figure 6.13 show simulations using a PSTD (pseudo-spectral time domain) model to illustrate the technique. The left column shows the transmit

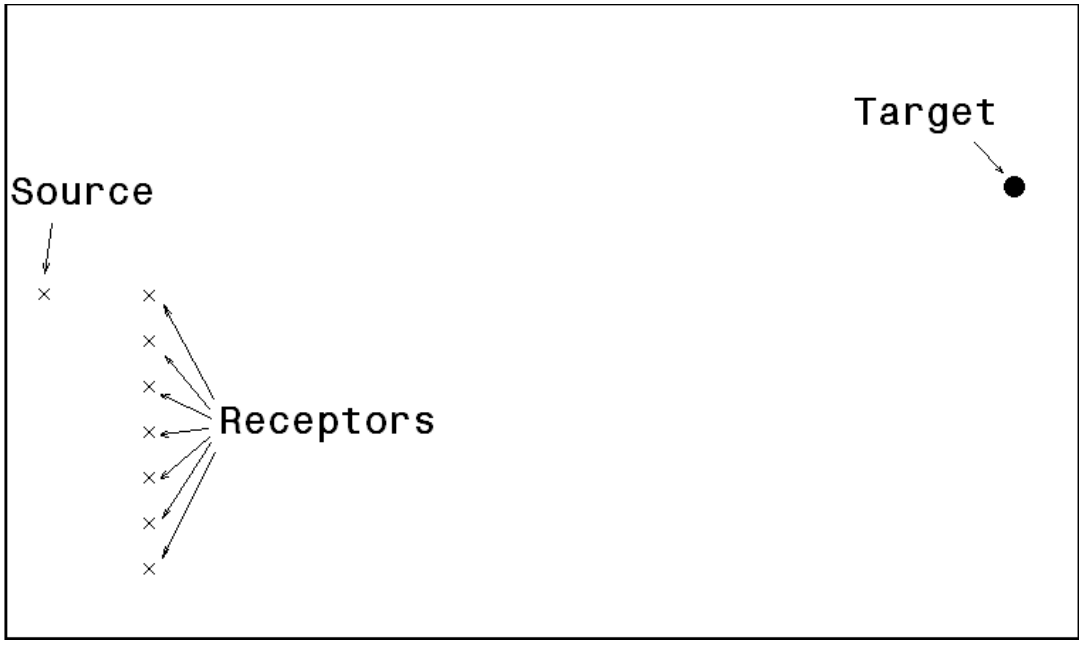

Figure 6.12: Simple MISO installation: multiple receivers coupled with a single transmitter.

pulse, target interaction and scattering. The right column shows the time reversal with the receivers being used to retransmit the received echoes and the ability to focus on the target. Note that the PSTD simulator is able to model the sound propagation exactly by direct solution of the wave equation.

It is interesting to note in this example the parallel between time reversal and adaptive beam forming. The re-transmitting elements of the MIMO system can indeed been seen as the elements of a sparse array. The re-transmitting pulse steers the beam pattern toward the target. Because the spacing between the different transmitters is greater that $\lambda/2$, we can see clear secondary lobes of the beam pattern in the bottom right snapshot of figure 6.13.

Time reversal techniques can also be applied to multi-sensor systems for change detection. A base response is measured for a region. Any changes introduced will affect the response and time reversal is able to focus on the source of the discrepancy, regardless of the complexity of the static environment. Here we consider

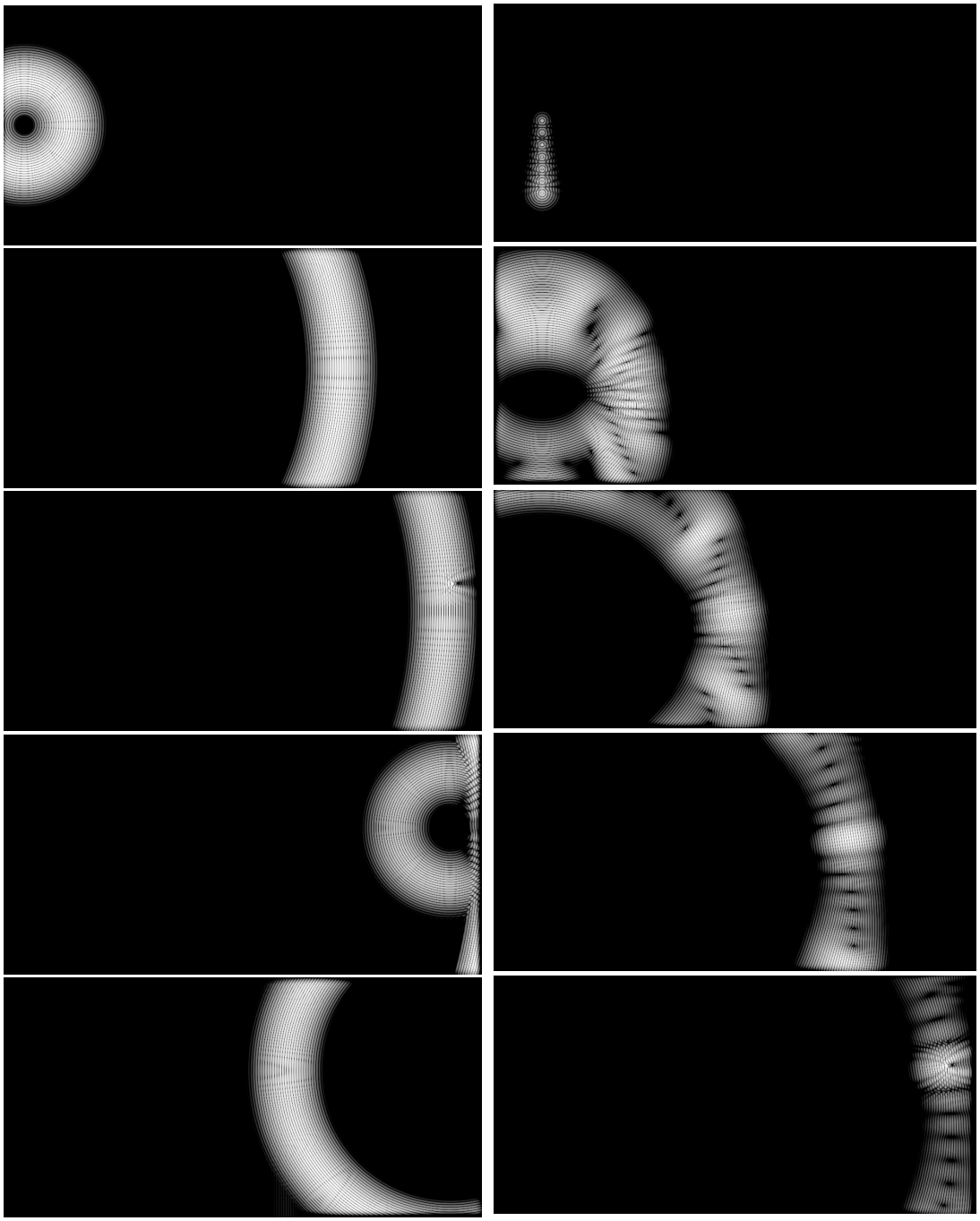

Figure 6.13: Time reversal using MISO setup: (left column) transmission from single source, propagation, target interaction and scattering; (right column) re-tranmission from multiple receivers, retro-propagation and auto-focus on target.

the problem of diver detection in a complex and high risk environment such as a harbour. There are a number of difficulties inherent to such an environment

- Shallow water: this greatly increases multipath phenomena and the noise associated with them.

- Shipping: heavy traffic increases the ambient noise and increases likelihood of false alarms.

- Structured environment: each harbour has its own particular geometry and configuration.

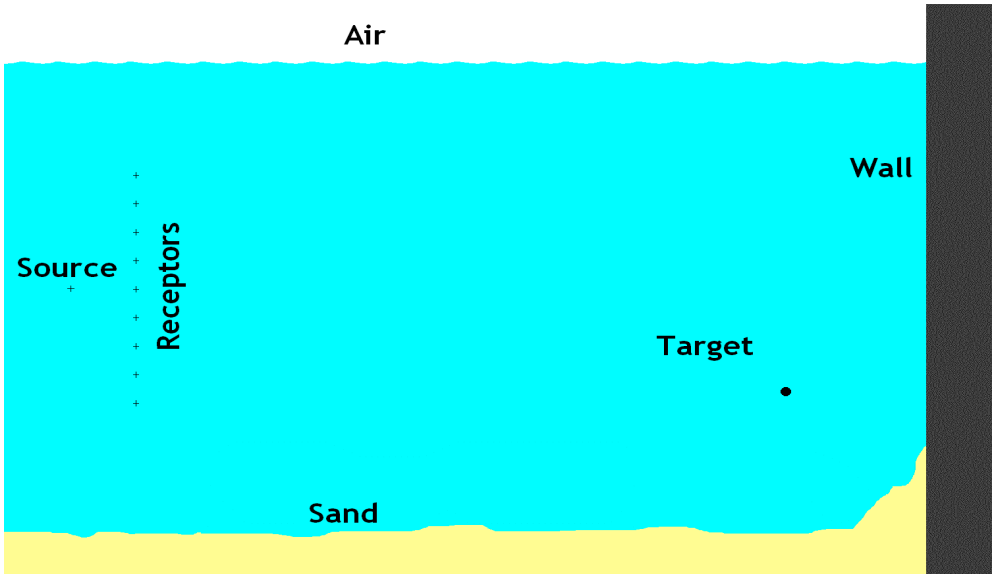

Figure 6.14: MISO installation in a more complex simulation environment.

An application of change detection is depicted in figure 6.14. Here, we consider a similar multi-sensor system with one transmitter, several receivers, and one target, but this time a more complex environment is introduced. Because the environment can be considered as static, the entire system without the target will give a consistent echo, which can be considered as a background noise. If we

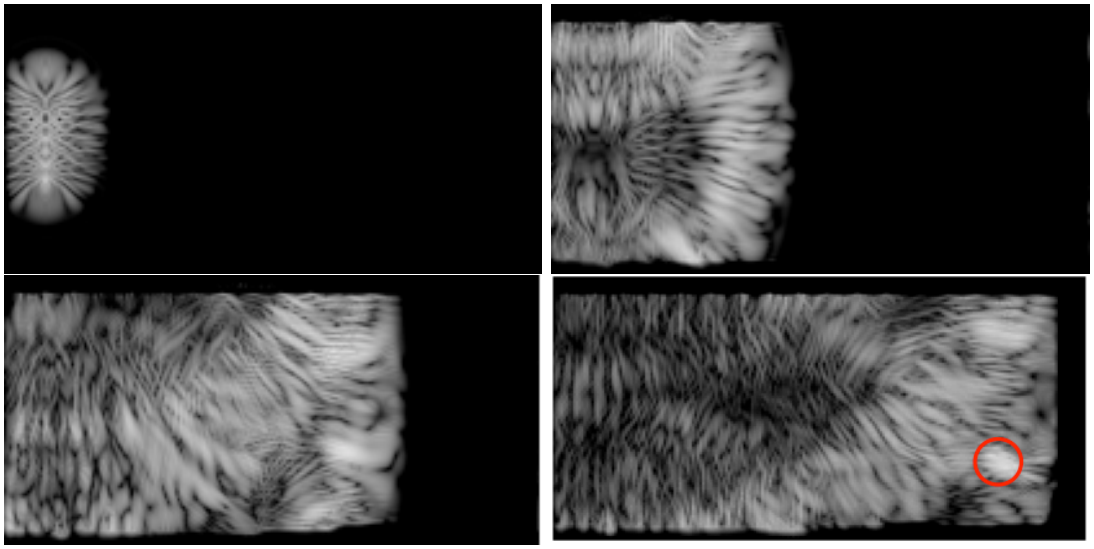

Figure 6.15: Retropropagation of the cleaned target echo. The sound focus on the target is circled in red.

have a target free record of the acoustic response, this can be subtracted from subsequent returns to detect the presence of a target. Retro-propagation of the cleaned echo with the target is shown in figure 6.15, demonstrating that the sound is still focused on the target despite the complex environment.

6.5.2 Pseudo Time Reversal

In MIMO systems, the total signal received at each receiver is the sum over all of the transmissions, *i.e.* $\sum_k z_{kl}(t)$. The classical assumption made in MIMO is the orthogonality of the transmitted pulses $s_k(t)$. So in the detection problem, the total received signal is projected into each transmitted pulse space, in order to recover the channel matrix elements h_{kl}.

We consider here a deep water propagation type, which means no multi-path. By playing with the delay between the transmitted pulses, the combined sound is focused on certain parts of the space. Figure 6.16 displays an example of sound focusing using two transmitters. By knowing the geometry of the transmitters, time delays can be computed to focus on a particular point in space.

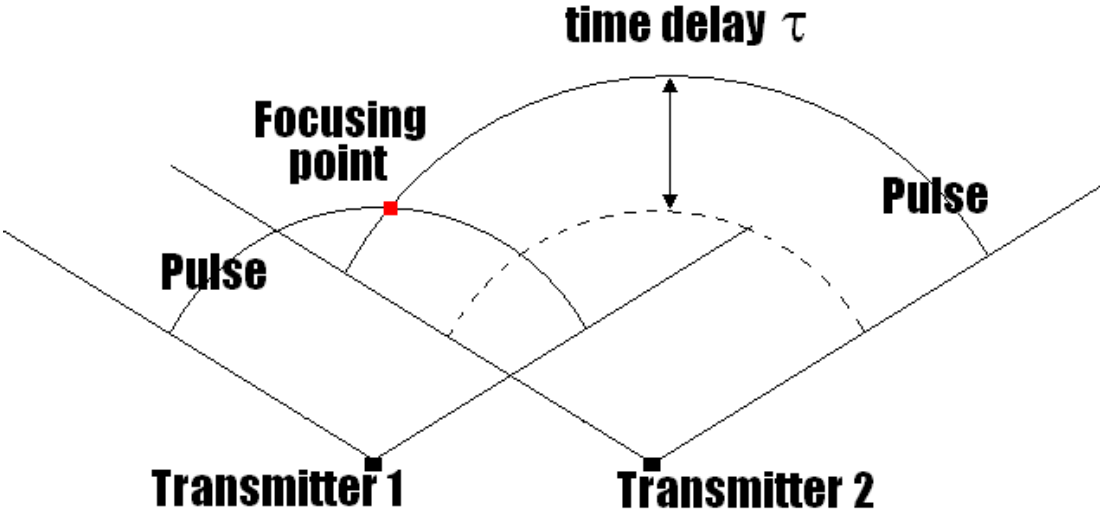

Figure 6.16: Spatial sound focus using two transmitters

The idea of our Pseudo time reversal is to use this combined energy on the target to improve the detection. We want to maximize the total signal from the receiver point of view which means maximizing $\sum_k z_{kl}(t - \tau_k)$ where τ_k is the delay used to focus the beams. Usually the pulses used are coherent (they cover the same frequency band) so the sum term $\sum_k z_{kl}(t-\tau_k)$ is a coherent summation which results in destructive as well as constructive interferences.

Figure 6.17 illustrates the interferences due to the coherence in the summation of the same chirp. If the two chirps do not overlap in frequency, the two pulses do not interfere with each other and no interferences are observed.

By using different frequency bands for each transmitter, the sum $\sum_k z_{kl}(t-\tau_k)$ becomes incoherent, and as a result: $\max(\sum_k z_{kl}(t - \tau_k)) = \sum_k \max(z_{kl}(t))$. Assuming that the K transmitters can emit the same energy in all the frequency band, the SNR increases by a factor of K.

Note that this pseudo time reversal technique can easily be generalised to a more complex scenario (including multipath) by band pass filtering the re-transmitting pulses to insure the incoherent summation at the target location.

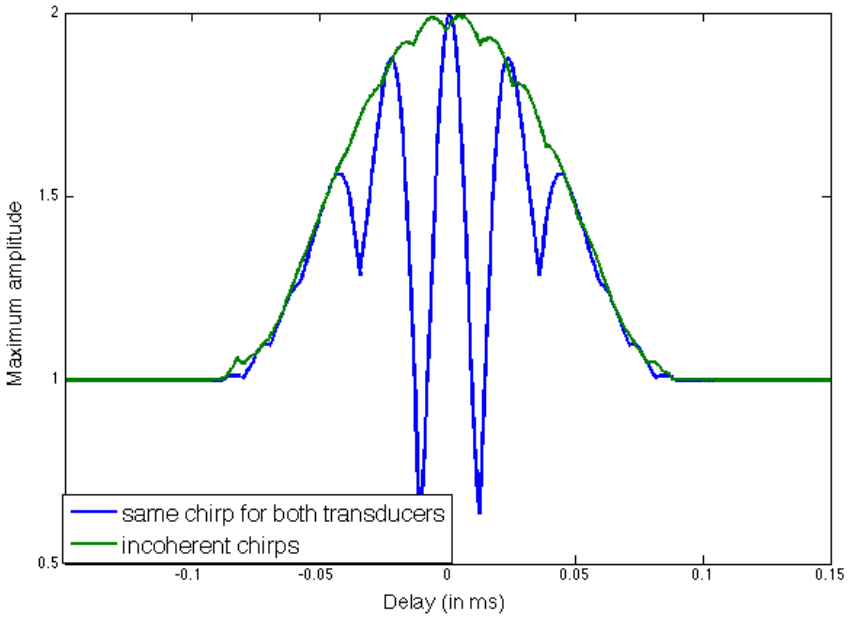

Figure 6.17: Maximum amplitude of the summation of two chirps. The chirps are windowed by a gaussian. The chirp duration is 200μs.

6.6 Conclusion

In this chapter we have posed the fundamental principles for MIMO sonar systems. We propose a new formulation for broadband MIMO sonar systems by separating clearly the terms of propagation and the terms of target reflection. This formulation is more flexible than the one proposed by the radar community for different target model integration. An analogy between the MIMO echo and the random walk problem has been formulated. We were then able to suggest an algorithm to determine the number of scatterers contained in a target. Because MIMO echoes are fundamentally bistatic we update our scattering model developed in the previous chapters using virtual scattering points and propose a new model for cylindrical shell target. Finally a new method of pseudo time reversal has been proposed in order to increase the SNR by a factor of K (where K is the number of transmitters) and improve the detection performance of the system. In future works we propose to demonstrate our Pseudo Time Reversal technique in a real environment .

Chapter 7

Conclusions

There are two mistakes one can make along the road to truth...
not going all the way, and not starting.
Gautama Siddharta (500 BC)

7.1 Summary

In this thesis we explored existing sonar systems as well as concept design sonars for survey, object recognition or inspection.

In chapter 2 we present the sonar equation proposed by Urick [1975]. Despite its simplicity this equation has been used for decades to predict and evaluate sonar performances. For an active sonar for example, it explains in simple terms the history of a pulse sent into the medium, hitting a target and reflected back the to sonar sensor. Each term in the equation explained a step in the sonar process. The source level SL, the directivity index DI and the detection threshold DT are linked to the sonar design for both hardware and software. Both sonar manufacturers and transducer designers aim to improve SL and DT for better sonar performances. DI depends on the sonar applications but for imaging sonars such as sidescan manufacturers aim for narrow beamwidth for greater resolution and low sidelobes to prevent from artefacts. The transmission loss TL, the reverberation level RL and the noise level NL are part of the environmental factor. Those three terms are not yet fully understood and are the subject of many research

projects. The SAX (sediment acoustics experiment) experiments are an example of recent large scale trials and studies for acoustic propagation and acoustic scattering (cf. Richardson et al. [2001]). The target strength TS originally refers to the percentage of the energy reflected back toward the transducer. The core of this thesis is built behind this notion of TS to bring some elements of response to a fundamental question: "How acoustic waves interact with matter?"

In chapter 3 we studied the most used sonar configuration for area survey and target detection: the sidescan sonar configuration. We showed that with only the basic knowledge given by the sonar equation we were able to explain almost entirely a sidescan image from a physical point of view. Taking the problem under another approach and effectively solving each term of the equation we build a realistic sidescan simulator. The simulator can generate a 3D synthetic environment and integrates any 3D trajectory within this environment. Based on a pseudo-raytracing algorithm realistic sonar images are then generated in seconds. The cost both in resources and time to gather real sonar data in real environment makes synthetic images extremely attractive. The second main advantage of synthetic data is the capability to control every parameters independently. One recurrent question in ATR is the precision needed to identify unambiguously a certain object. Thanks to our simulator we were able to change the resolution from tens of centimetres to a single centimetre. We demonstrated the widely accepted idea that processing shadow images is reaching its performance limit using current sidescan resolution (10- 20 centimetres). From an ATR point of view, we have demonstrated that as the sonar resolution increases the information level contained in the shadow stagnates below 10 - 15 cm and that the information level contained in the highlight becomes extractable below 5 cm resolution. In other words image based algorithms need very high resolution sonars.

In chapter 4 we studied the last generation of sonar, the synthetic aperture sonar. Offering a centimetric resolution and a constant resolution over range the resulting SAS images appear visually close to optical images. However objects lying on the seafloor are most likely to be covered in growth in few weeks time, the shape information even using high resolution systems is likely to be extremely

noisy and unreliable. For this reason we focus our study on low frequency SAS systems. We have proposed the design of a LF-SAS system and demonstrated that with such system it is possible to image the inside of complex targets. This approach provide much more stable and consistent features than the object outer shape: the shape of a mine for example can vary drastically depending on the manufacturers, beside hiding a mine in a wooden box will trick any high resolution sonar image based algorithms. However looking at the content and the internal structure of an object tells much more about its purpose: any mine to be functional will need a container to stock the explosive and a dry electronic bottle to control the detonation.

We propose several models and algorithms to synthesise artificial SAS images based on the analytical solution for the backscattering echo of simple targets or using the Kirchhoff model for more complex targets. In parallel we have studied SAS image formation and have proved that the seabed reflection plays an active role during the imaging process. We have demonstrated that the specular echo, the diffracted echo and the backscattered resonances is the result of the direct path contribution. The shape and the texture of the target in a SAS image is however due to the reflection of the seabed. Finally we have proposed a method in order to simulate accurately SAS images of objects lying on the seabed.

Developments have pushed sonar systems towards imaging systems mainly because we are more comfortable in looking at an image than listening to echoes. However we demonstrated that a lot of information is lost in this process. In chapter 5 we took another approach than imaging for recognition and study the content and structure of the echo signal. Thanks to marine mammals such as dolphins or whales we know that the echo contains much more information than its amplitude only. We investigated further our understanding of the echo structure and echo formation. By doing so we were able to propose a new approach to sonar: the bio-mimetic sonar. We therefore proposed and built a biomimetic sonar based on bottlenose dolphin observations. By analysing the interaction between sound and objects, we demonstrated that broadband echoes contain information on the geometry, the structure and the composition of an insonified

object. We identified stable features based on target resonances and showed how these features can be used for identification purposes. Finally we demonstrated the capabilities of such sensor in real environment for two particular applications: mine countermeasures and cable tracking.

Finally in chapter 6 we explored the path of MIMO systems. A broadband MIMO sonar system formulation has been proposed. We showed that this formulation is more flexible than the one proposed by the radar community for different target model integration. Because MIMO echoes are fundamentally bistatic we proposed new scattering model using virtual scattering points and presented a novel model for cylindrical shell target. We then formulated the detection problem for statistical MIMO system and demonstrated the advantages of widely spaced MIMO systems for detection and recognition. By studying the target cross-section for MIMO systems we demonstrated that under certain condition MIMO systems can solve the speckle and therefore produce super-resolution images. Finally a new method of pseudo time reversal has been proposed in order to increase the SNR by a factor of K (where K is the number of transmitters) and improve the detection performance of the system. In future works we propose to demonstrate our Pseudo Time Reversal technique in a real environment .

7.2 Future work

In chapter 4 we demonstrated the capability for LF-SAS systems to image inside a target. So potentially such a system shows the resonances of the full object. As we discuss in this same chapter if SAS is by essence a broadband sonar (the emitting pulse is traditionally a chirp), the frequency band is used exclusively for the range compression in the image formation process. As we saw in chapter 5 the echo spectra can also be used for feature extraction and classification. From this it is easy to imagine a system which can offer imagery and the recognition capability of a broadband sonar. By having a dual system

(sonar image and echo signal) the image based algorithms for target recognition can be greatly improved: the basic detections can then be analysed from an echo point of view decreasing drastically the false alarm rate and providing deeper information of the detected objects.

In chapter 5 we explored some of the biosonar capabilities in particular in object recognition. Because our system is operating at relatively low frequencies a part of the sound propagates inside the insonified objects. Thanks to this it was possible to distinguish between same shape and same dimension objects. Or from another point of view: if we know the target we want to inspect it will be possible to detect small changes or anomalies into the backscattering echo. The applications for such capabilities are immense: by inspecting a pipeline lying on the seabed for example, it will possible to assess its condition (corrosion, crack...) or to detect a blockage such as a hydrate.

In chapter 6 we laid the foundations of broadband MIMO sonar systems. Once again the potential of such systems are wider than this thesis. But we can acknowledge two major directions for future work. Considering a static MIMO installation, the system will be very susceptible to any changes. We can then imagine that this configuration would suit a harbour protection application. Another possible application for MIMO systems will be in telecommunications. Traditional acoustic modems suffer by their extremely slow data rate and unreliability. The wireless community have demonstrated the capability of MIMO for communications. The same could apply to underwater acoustic communications.

Appendix A

Computation of the form function f_∞

Given the form function f_∞ represented by: $\sum_{n=0}^{\infty}(-1)^n\epsilon_n b_n$, we show that f_∞ is well approximated by a truncation of the infinite sum so that: $f_\infty(ka) \simeq \sum_{n=0}^{N}(-1)^n\epsilon_n b_n$ with $ka < N/2$.

We begin by analyzing the b_n term given by Eq. (1). The expression of each term in the determinants in Eq. (1) can be found in Doolittle and Uberall [1966].

$$b_n = \frac{\begin{vmatrix} b_{11} & a_{12} & a_{13} & a_{14} & a_{15} & 0 \\ b_{21} & a_{22} & a_{23} & a_{24} & a_{25} & 0 \\ 0 & a_{32} & a_{33} & a_{34} & a_{35} & 0 \\ 0 & a_{42} & a_{43} & a_{44} & a_{45} & a_{46} \\ 0 & a_{52} & a_{53} & a_{54} & a_{55} & a_{56} \\ 0 & a_{62} & a_{63} & a_{64} & a_{65} & 0 \end{vmatrix}}{\begin{vmatrix} a_{11} & a_{12} & a_{13} & a_{14} & a_{15} & 0 \\ a_{21} & a_{22} & a_{23} & a_{24} & a_{25} & 0 \\ 0 & a_{32} & a_{33} & a_{34} & a_{35} & 0 \\ 0 & a_{42} & a_{43} & a_{44} & a_{45} & a_{46} \\ 0 & a_{52} & a_{53} & a_{54} & a_{55} & a_{56} \\ 0 & a_{62} & a_{63} & a_{64} & a_{65} & 0 \end{vmatrix}} \tag{1}$$

Let $\det(\mathrm{D}) = \det(d_{ij})$, the numerator in Eq. (1). Using a determinant expansion by minor following the columns, we can write:

$$\det(\mathrm{D}) = \sum_{\sigma\in\Omega}(-1)^{i(\sigma)}\prod_{j=1}^{6} d_{\sigma(j)j} \tag{2}$$

where Ω is the set of all the permutations of $[1,6]$, and $i(\sigma)$ is the number of permutation inversions in permutation σ. So,

$$|\det(\mathrm{D})| \leq 6! \max_{\sigma\in\Omega}\left|\prod_{j=1}^{6} d_{\sigma(j)j}\right| \tag{3}$$

The behavior of each column is dominated by a specific Bessel function: the Bessel function of the first kind J_n for columns 1, 2, 4 and 6; and the Bessel function of the second kind N_n for columns 3 and 5. So we would expect the behavior of $\left|\prod_{j=1}^{6} d_{\sigma(j)j}\right|$ to follow the form $J_n^4 N_n^2$.

Given,

$$\begin{aligned} J_n(z) &= \tfrac{1}{2\pi j}\oint \mathrm{e}^{\frac{z}{2}\left(t-\frac{1}{t}\right)} t^{-n-1}\mathrm{d}t \\ &= \tfrac{1}{2\pi}\int_0^{2\pi} \mathrm{e}^{\frac{z}{2}\left(\alpha-\frac{1}{\alpha}\right)(\cos\omega + j\sin\omega)} \tfrac{\mathrm{e}^{-jn\omega}}{\alpha^n}\mathrm{d}\omega \end{aligned}$$

with $\alpha > 0$, we can write,

$$\begin{aligned} |J_n| &\leq \tfrac{1}{2\pi}\int_0^{2\pi} \tfrac{\mathrm{e}^{\frac{z\cos\omega}{2}\left(\alpha-\frac{1}{\alpha}\right)}}{\alpha^n}\mathrm{d}\omega \\ &\leq \tfrac{1}{2\pi}\int_0^{2\pi} \tfrac{\mathrm{e}^{\frac{z\alpha\cos\omega}{2}}}{\alpha^n}\mathrm{d}\omega \\ &\leq \tfrac{\mathrm{e}^{\frac{\alpha z}{2}}}{\alpha^n} = f(\alpha) \end{aligned}$$

We next choose α in order to minimize $f(\alpha)$,

$$\frac{\mathrm{d}f}{\mathrm{d}\alpha} = 0 \Longleftrightarrow \alpha = \frac{2n}{z}$$

and arrive at the majoration:

$$|J_n(z)| \leq \left(\frac{z\mathrm{e}}{2n}\right)^n \tag{4}$$

We can see that for $z \leq n/2$, $|J_n| \to 0$.

The Bessel function of the second kind can be written as follows (Abramowitz and Stegun [1965]):

$$N_n = AJ_n + BJ_n \int \frac{\mathrm{d}x}{xJ_n^2} \tag{5}$$

where A and B are constants, so that:

$$N_n J_n = AJ_n^2 + BJ_n^2 \int \frac{\mathrm{d}x}{xJ_n^2} \tag{6}$$

It can be shown through a series approximation that $J_n^2 \int \frac{\mathrm{d}x}{xJ_n^2} = O(1)$ for $z < n/2$. This implies that the product $J_n^4 N_n^2$ can be bounded by $A\left(\frac{z\mathrm{e}}{2n}\right)^{2n}$. with A constant.

Turning to the denominator in Eq. (1), using the same determinant expansion over the columns, the behavior should follow the characteristic $(J_n N_n)^3$, which remains roughly constant for $z \leq n/2$. Thus, the b_n coefficient can be bounded by $A'\left(\frac{z\mathrm{e}}{2n}\right)^{2n}$. We can verify that the function $\sum_{n=N}^{+\infty}\left(\frac{z\mathrm{e}}{2n}\right)^{2n} \leq \sum_{n=N}^{+\infty}\left(\frac{N\mathrm{e}}{4n}\right)^{2n} = r(N)$ decreases very quickly to 0. For example, with $N = 20$ we find $r(N) \approx 2 \times 10^{-7}$.

Appendix B

Spatial filtering algorithm

The feature extraction algorithm presented in chapter 5 requires a smooth echo spectra. In this section we propose an algorithm to filter the power spectra. The algorithm is simply based on a lowpass filter of the power spectra. Let $p(t)$ be the sonar outcoming pulse and $s(t)$ be the echo of this pulse from a finite number of point scatterers, we can write:

$$s(t) = \sum_{n=1}^{N} p(t - t_n) \tag{7}$$

where $\{t_n\}_{n\in[1,N]}$ are the corresponding timing between the sonar and each individual scatterer. The spectra and the power spectra are given respectively by Eq. (8) and (9).

$$FT[s(t)] = FT[p(t)] \sum_{n=1}^{N} e^{-j\omega t_n} \tag{8}$$

$$\begin{aligned} |FT[s(t)]|^2 &= |FT[p(t)]|^2 \left(\sum_{n=1}^{N} e^{-j\omega t_n} \right) \left(\sum_{n=1}^{N} e^{j\omega t_n} \right) \\ &= |FT[p(t)]|^2 \sum_{n,m=1}^{N} \mathrm{e}^{j\omega(t_n - t_m)} \end{aligned} \tag{9}$$

Eq. (9) shows that the scatterers interfere between them creating oscillations

in the power spectra. By computing the inverse Fourier transform of Eq. (9) and assuming that the pulse $p(t)$ has a Gaussian envelope $G(t, \sigma)$, we arrive at:

$$\begin{aligned} FT^{-1}[|FT[s(t)]|^2] &= FT^{-1}[|FT[p(t)]|^2] \star \sum_{n,m=1}^{N} \delta_{t_n - t_m}(t) \\ &= G(t.2\sigma) \star \sum_{n,m=1}^{N} \delta_{t_n - t_m}(t) \\ &= \sum_{n,m=1}^{N} G(t - (t_n - t_m), 2\sigma) \end{aligned} \tag{10}$$

Eq. (10) tells us that the dual space of the power spectra is the timing density between every pair of pulses. And every peaks of the inverse Fourier transform of the echo power spectra represent the timing difference between two scatterers.

Figure 1 shows an example of an echo of three scatterers with $t_1 = 2$ms, $t_2 = 3$ms and $t_3 = 3.4$ms, and the inverse Fourier transform of its power spectra. The peaks in Figure 1*(b)* represent the timing between scatterers at 0.4ms, 1ms and 1.4ms.

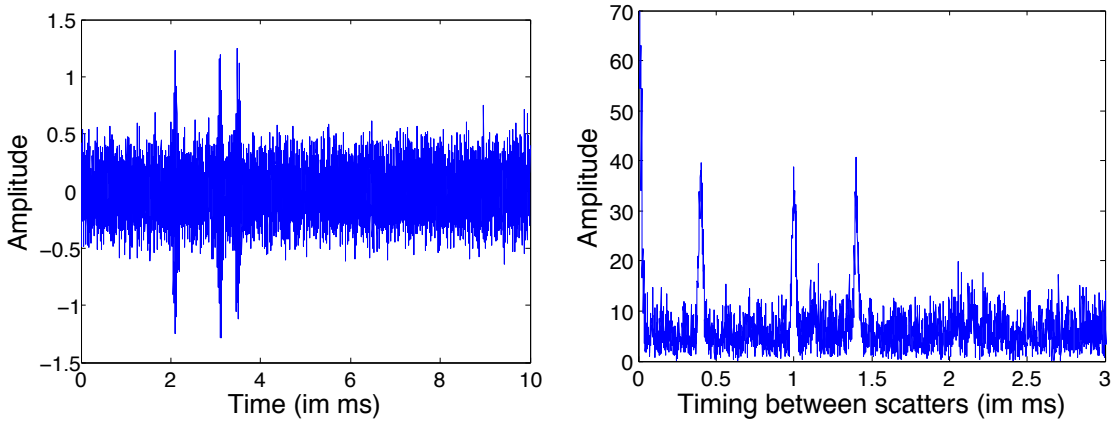

(a) (b)

Figure 1: *(a)* Example of an echo with three scatterers with respective arriving time of 2.10^{-3}s, 3.10^{-3}s and 3.4 10^{-3}s and *(b)* the resulting inverse Fourier transform of its power spectra.

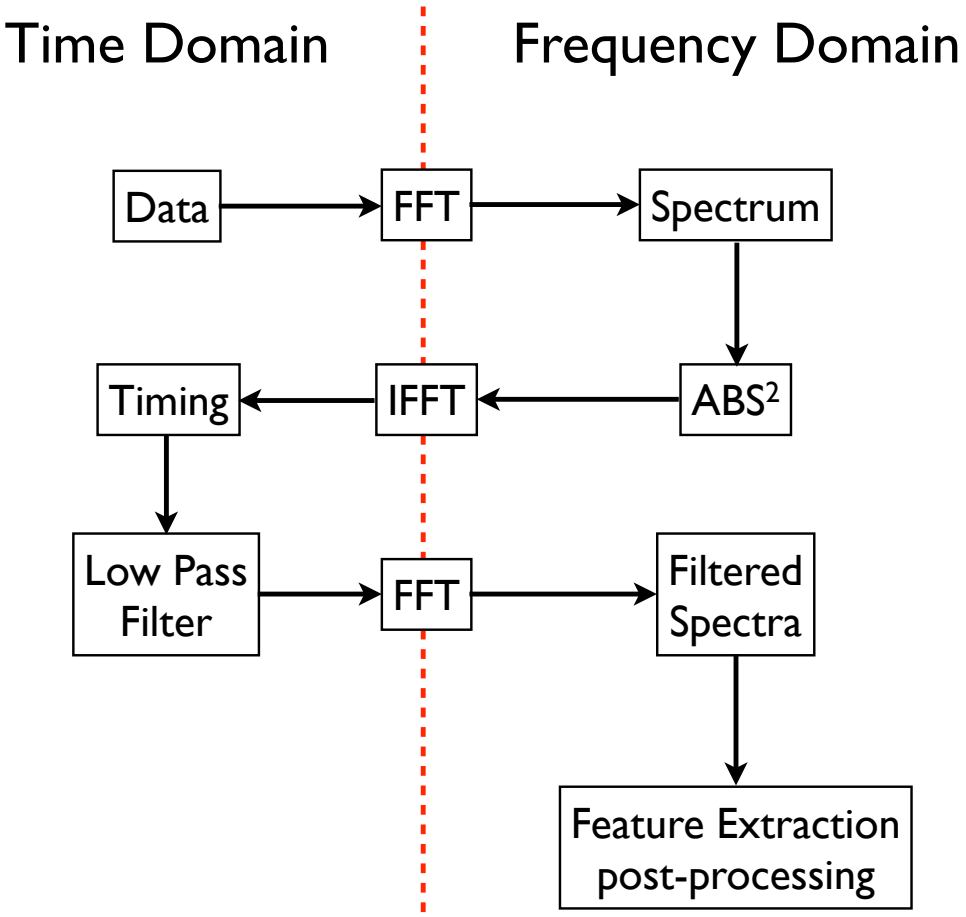

Figure 2: Diagram of the spatial filtering algoritm.

Appendix C

Proof of the convergence of equation 6.22

In this section we demonstrate the result given by equation (6.22) in section 6.5. In equation (6.22) we stipulated that:

$$\lim_{N\to+\infty} N.\Gamma(Nx, N, 1) = \delta(1-x) \tag{11}$$

where $\Gamma(x, k, \theta)$ represents the Gamma distribution function and $\delta(x)$ the Dirac function. The Gamma distribution function is defined as follows:

$$\Gamma(x, k, \theta) = x^{k-1}\frac{\mathrm{e}^{-x/\theta}}{\theta^k\Gamma(k)} \tag{12}$$

with $x \geq 0$ and $k, \theta > 0$ and $\Gamma(k)$ represents the Gamma function. Note that $\Gamma(x, k, \theta) > 0$. In our case we are looking at the convergence of:

$$\begin{aligned} N.\Gamma(Nx, N, 1) &= N(Nx)^{N-1}\frac{\mathrm{e}^{-Nx}}{\Gamma(N)} \\ &= \frac{N^N}{\Gamma(N)\mathrm{e}^N}.\frac{(x\mathrm{e}^{1-x})^N}{x} \\ &= A(N)f(x, N) \end{aligned} \tag{13}$$

where $A(N) = \frac{N^N}{\Gamma(N)\mathrm{e}^N}$ and $f(x, N) = (x\mathrm{e}^{1-x})^N/x$. Note that $A(N)$ represents a normalization factor and for all N:

$$\int_{x=0}^{+\infty} x^{N-1}\mathrm{e}^{N(1-x)}dx = \frac{1}{A(N)} \tag{14}$$

Asymptotic behaviour of $A(N)$

To get the asymptotic behaviour of $A(N)$, we use the Stirling formula:

$$n! \sim \sqrt{2\pi n}\left(\frac{n}{\mathrm{e}}\right)^n \tag{15}$$

$$\begin{aligned} A(N) &= \frac{N^N}{\Gamma(N)\mathrm{e}^N} \\ &\sim \frac{\mathrm{e}^{N-1}}{\sqrt{2\pi(N-1)}(N-1)^{N-1}}\frac{N^N}{\mathrm{e}^N} \\ &\sim \left(\frac{N}{N-1}\right)^{N-1}\frac{1}{\mathrm{e}}\frac{N}{\sqrt{2\pi(N-1)}} \\ &\sim \left(\frac{N}{N-1}\right)^{N-1}\frac{1}{\mathrm{e}}\sqrt{\frac{N}{2\pi}} \end{aligned} \tag{16}$$

By using the following identity:

$$\lim_{n\to+\infty}\left(\frac{n}{n-1}\right)^{n-1} = \mathrm{e} \tag{17}$$

we arrive at:

$$A(N) \sim \sqrt{\frac{N}{2\pi}} \tag{18}$$

It is important to note that $\lim_{N\to+\infty} A(N) = +\infty$.

Study of the $f(x, N)$ function

The $f(x, N)$ function has the following properties:

$$f(x,N) > 0 \quad \text{for all } x, N \geq 0 \tag{19}$$

$$f(0,N) = 0 \quad \text{for } N > 0 \tag{20}$$

$$\lim_{x \to +\infty} f(x,N) = 0 \tag{21}$$

$$f(x,N) \leq f(x_N,N) \quad \text{where } x_N = 1 - \tfrac{1}{N} \tag{22}$$

$$f(x_N,N) = \left(\frac{N-1}{N}\right)^{N-1} \mathrm{e} \to 1 \quad \text{when } N \to +\infty \tag{23}$$

$$f(x,N+1) \leq f(x,N) \tag{24}$$

It is also important to note that $f(x,N)$ is an increasing function from 0 to x_N and a decreasing function from x_N to $+\infty$.

Convergence of the $A(N)f(x,N)$ function

In order to prove that the $A(N)f(x,N)$ function converge to a Dirac function, we need to demonstrate the following properties:

$$\lim_{N \to +\infty} \int_{x=0}^{+\infty} A(N)f(x,N)dx = 1 \tag{25}$$

$$\lim_{N \to +\infty} A(N)f(x,N) = 0 \text{ for } x \neq 1 \tag{26}$$

$$\lim_{N \to +\infty} A(N)f(1,N) = +\infty \tag{27}$$

The property (25) is given by definition: $A(N)f(x,N)$ represents a probability density so for all N we have $\int_{x=0}^{+\infty} A(N)f(x,N)dx = 1$.

Proof of (27)**:** For $x = 1$ we have:

$$\begin{aligned}\lim_{N\to+\infty} A(N)f(1,N) &= \left(\lim_{N\to+\infty} A(N)\right)\left(\lim_{N\to+\infty} f(x_N,N)\right)\\ &= \lim_{N\to+\infty} A(N)\\ &= +\infty \qquad (28)\end{aligned}$$

Proof of (26)**:** For $x \neq 1$ we want to prove that $\lim_{N\to+\infty} A(N)f(x,N) = 0$. In order to demonstrate this we need to proceed using *reductio ad absurdum*.

We suppose that there exists a $x_0 \neq 1$, a $\xi > 0$, a $N_0 \geq 0$ such that for all $N \geq N_0$, $f(x_0, N) > \xi$. We suppose here that $x_0 < 1$. Note that the proof for $x_0 > 1$ is identical and is left to the reader. We can choose N_0 such that $N_0 > \frac{1}{1-x_0}$. And note $\eta = \frac{1-x_0}{2}$.

$$\begin{aligned}\int_{x=0}^{+\infty} A(N)f(x,N)dx &\geq \int_{x=x_0}^{1-\frac{1}{N}} A(N)f(x,N)dx \qquad (29)\\ &\geq A(N)\left(1-\frac{1}{N}-x_0\right)\min_{x\in[x_0,1-\frac{1}{N}]}(f(x,N)) \qquad (30)\\ &\geq A(N).\eta.\xi \qquad (31)\end{aligned}$$

So

$$\begin{aligned}A(N)\eta\xi &\leq 1 \qquad (32)\\ \xi &\leq \frac{1}{\eta A(N)} \text{ for all } N > N_0 \qquad (33)\end{aligned}$$

We deduce from the last equation that because $\lim_{N\to\infty} A(N) = +\infty$, $\xi = 0$ which is in contradiction with the hypothesis.

So for all $x \neq 1$, $\lim_{N\to\infty} A(N)f(x,N) = 0$ ■

References

M. Abramowitz and I.A. Stegun. *Handbook of Mathematical Functions*. Dover Publication, New York, 1965. 70, 206

APL-UW. *High-Frequency Ocean Environmental Acoustic Models Handbook*. Technical Report APL-UW TR 9407, October 1994. 27, 41

0. Arikan. A tomographic formulation of bistatic synthetic aperture radar. In *Procedings of ComCon 88*, 1988. 188

W. Au. *The Sonar of Dolphins*. Springer-Verlag, 1993. 19, 119, 121, 123

M.R. Azimi-Sadjadi, A. Jamshidi, and G.J. Dobeck. Adaptive underwater target classification with multi-aspect decision feedback. Presented at CAD/CAC Conf., Halifax, Novia Scotia, Canada, Nov. 2001. 50, 51, 158

R. Balasubramanian and M. Stevenson. Pattern recognition for underwater mine detection. Presented at CAD/CAC Conf., Halifax, Novia Scotia, Canada, Nov. 2001. 50, 51

I. Bekkerman and J. Tabrikian. Target detection and localization using mimo radars and sonars. *EEE Trans. Signal Processing*, 54:38733883, 2006. 173

E.O. Belcher, H.Q. Dinh, D.C. Lynn, and T.J. Laughlin. Beamforming and imaging with acoustic lenses in small, high-frequency sonars. In *Proceedings of Oceans 99 MTS/IEEE*, volume 3, pages 1495–1499, 1999. 50

J. Bell. *A Model for the Simulation of Sidescan Sonar*. PhD thesis, Heriot-Watt University, August 1995. 40

J. Bell. Application of optical ray tracing techniques to the simulation of sonar images. *Optical Engineering*, 36(6):1806–1813, 1997. 40

A. Belletini and M. Pinto. Design and experimental results of a 300 khz synthetic aperture sonar optimized for shallow water operations. *IEEE J. Oceanic Eng.*, 34:285–293, 2009. 50, 64

A. Belletini and M.A. Pinto. Theoretical accuracy of synthetic aperture sonar micronavigation using a displaced phase-center antenna. *IEEE J. Ocean. Eng.*, 27:780–789, 2002. 66

A. C. Berry. The accuracy of the gaussian approximation to the sum of independent variates. *Trans. Amer. Math. Soc.*, 49:122–136, 1941. 177

M.A. Biot. Theory of propagation of elastic waves in a fluid-saturated porous solid. i. low frequency range. *J. Acoust. Soc. Am.*, 28:168–178, 1956a. 88

M.A. Biot. Theory of propagation of elastic waves in a fluid-saturated porous solid. ii. higher frequency range. *J. Acoust. Soc. Am.*, 28:179–191, 1956b. 88

L. V. Blake. A guide to basic pulse-radar maximum-range calculation. Technical report, Naval Research Laboratory, 1969. 18

D.W. Bliss and K.W. Forsythe. Multiple-input multiple-output (mimo) radar and imaging: Degrees of freedom and resolution. In *Proc. 37th Asilomar Conf. Signals, Systems and Computers*, 2003. 173

K. Brown, C. Capus, Y. Pailhas, Y. Petillot, and D. Lane. The application of bioinspired sonar to cable tracking on the seafloor. *EURASIP Journal on Advances in Signal Processing*, art. Article ID 484619, 2011. doi: 0.1155/2011/484619. 164

A. Bultan. A four-parameter atomic decomposition of chirplets. *IEEE Trans. Signal Process.*, 47:731–745, 1999. 123, 126

P. Burrought. Fractal dimension of landscapes and other environmental data. *Nature*, 294:240–242, 1981. 43

B. Calder. *Bayesian Spatial Models for SONAR Image Interpretation*. PhD thesis, Heriot-Watt University, September 1997. 50, 51

B.R. Calder, L.M. Linnett, and D.R. Carmichael. Spatial stochastic models for seabed object detection. *Proc. SPIE-Int Soc. Opt. Eng.*, 3079, 1997. 50, 51, 157

B.R. Calder, L.M. Linnett, and D.R. Carmichael. Bayesian approach to object detection in sidescan sonar. *IEE Proc-Vis. Image Signal Proc.*, 45(3), 1998. 50, 51, 158

C. Capus and K. Brown. Short-time fractional fourier methods for the time-frequency representation of chirp signals. *J. Acoust. Soc. Am.*, 113(6):3253–3263, 2003. 123, 126

C. Capus, Y. Pailhas, K.E. Brown, D.M. Lane, P. Moore, and D. Houser. Bio-inspired wideband sonar signals based on observations of the bottlenose dolphin (tursiops truncatus). *J. Acoust. Soc. Am.*, 121(1):594–604, 2007. 50, 126, 179

C.M. Ciany and J. Huang. Computer aided detection/computer aided classification and data fusion algorithms for automated detection and classification of underwater mines. *Proc. MTS/IEEE Oceans Conf. and Exhibition*, 1:277–284, 2000. 50, 51, 158

C.M. Ciany and W. Zurawski. Performance of computer aided detection/computer aided classification and data fusion algorithms for automated detection and classification of underwater mines. Presented at CAD/CAC Conf., Halifax, Novia Scotia, Canada, Nov. 2001. 50, 51

D. Clark and Ba-Ngu Vo. Convergence analysis of the gaussian mixture phd filter. *Signal Processing, IEEE Transactions on*, 55(4):1204–1212, 2007. ISSN 1053-587X. doi: 10.1109/TSP.2006.888886. 161

L. Cohen. *Time-Frequency Analysis*. Prentice-Hall, 1995. 123

J. D. Colladon. *Souvenirs et Memoires*. Albert-Schuchardt, 1893. 11

L. Collatz. *The numerical treatment of differential equations*. Springer-Verlag, 1966. 136

P. Courmontagne. A new approach for mine detection in sas imagery. In *OCEANS 2008 - MTS/IEEE Kobe Techno-Ocean*, pages 1 –8, 8-11 2008. doi: 10.1109/OCEANSKOBE.2008.4530974. 68

L. J. Cutrona. Comparison of sonar system performance achievable using synthetic-aperture techniques with the performance achievable with more conventional means. *J. Acoust. Soc. Amer.*, 58:336–348, 1975. 66

L. J. Cutrona. Additional characteristics of synthetic-aperture sonar systems and a further comparison with non synthetic-aperture sonar systems. *J. Acoust. Soc. Amer.*, 61:1213–1217, 1977. 66

A. P. Dempster, N. M. Laird, and D. B. Rubin. Maximum likelihood from incomplete data via the em algorithm. *Journal of the Royal Statistical Society*, 39:1–38, 1977. 161

G.J. Dobeck, J.C. Hyland, and L. Smedley. Automated detection/classification of sea mines in sonar imagery. *Proc. SPIE-Int. Soc. Optics*, 3079:90–110, 1997. 50, 51, 158

R.D. Doolittle and H. Uberall. Sound scattering by elastic cylindrical shells. *J. Acoust. Soc. Am.*, 39(2):272–275, 1966. 69, 130, 181, 204

C. Du. *Performance Evaluation and Waveform Design for MIMO Radar*. PhD thesis, Edinburgh University, 2010. 173

C. Du, Y. Petillot, and J.S. Thompson. Predicted detection performance of mimo radar. *Signal Processing Letters, IEEE*, 15:83–86, 2008. ISSN 1070-9908. doi: 10.1109/LSP.2007.910312. 173, 175

E. Dura, J. Bell, and D. Lane. Superellipse fitting for the recovery and classification of mine-like shapes in sidescan sonar images. *IEEE J. Oceanic Eng.*, 33 (4):434–444, Oct. 2008. ISSN 0364-9059. doi: 10.1109/JOE.2008.2002962. 50, 51, 53, 158

G.R. Elston and J.M. Bell. Pseudospectral time-domain modeling of non-rayleigh reverberation: synthesis and statistical analysis of a sidescan sonar image of sand ripples. *IEEE J. Oceanic Eng.*, 29(2):317–29, 2004. 40

J. J. Faran. Sound scattering by solid cylinders and spheres. *J. Acoust. Soc. Am.*, 23:405–418, 1951. 70

J.A. Fawcett. Image-based classification of side-scan sonar detections. CAD/CAC Conf., Halifax, Novia Scotia, Canada, Nov. 2001. 50, 51, 158

B. Ferguson and R. Wyber. Generalized framework for teal aperture, synthetic aperture and tomographic sonar imaging. *IEEE J. Oceanic Eng.*, 34:225–238, 2009. 50

E. Fishler, A. Haimovich, R. S. Blum, D. Chizhik, L. J. Cimini, and R. A. Valenzuela. Mimo radar: An idea whose time has come. In *Proc. IEEE Int. Conf. Radar*, 2004. 173

E. Fishler, A. Haimovich, R.S. Blum, Jr. Cimini, L.J., D. Chizhik, and R.A. Valenzuela. Spatial diversity in radars-models and detection performance. *Signal Processing, IEEE Transactions on*, 54(3):823–838, March 2006. ISSN 1053-587X. doi: 10.1109/TSP.2005.862813. 173, 175

F. Florin, F. Van Zeebroeck, I. Quidu, and N. Le Bouffant. Classification performance of minehunting sonar: theory, practical, results and operational applications. In *Proceeedings of the UDT Conference*, 2003. 54

T. Folegot, J. de Rosny, C. Prada, and Mathias Fink. Resolution enhancement and separation of reverberation from target echo with the time reversal operator decomposition. *J. Acoust. Soc. Am.*, 113:3155–3160, 2003. 192

T. Folegot, J. de Rosny, C. Prada, and Mathias Fink. Adaptive instant record signals applied to detection with time reversal operator decomposition. *J. Acoust. Soc. Am.*, 117:37573765, 2005. 192

R. E. Francois and G. R. Garrison. Sound absorption based on ocean measurements. part i: Pure water and magnesium sulfate contributions. *J. Acoust. Soc. Am.*, 72:896907, 1982a. 21

R. E. Francois and G. R. Garrison. Sound absorption based on ocean measurements. part ii: Boric acid contribution and equation for total absorption. *J. Acoust. Soc. Am.*, 72:18791890, 1982b. 21

G. Gaunaurd and H.C. Strifors. Frequency- and time-domain analysis of the transient resonance scattering resulting from the interaction of a sound pulse with submerged elastic shells. *IEEE Trans. Signal Process.*, 40(4):313–324, 1993. 69, 133

G. C. Gaunaurd, D. Brill, H. Huang, P. W. B. Moore, and H. C. Strifirs. Signal processing of the echo signatures returned by submerged shells insonified by dolphins 'clicks': Active classification. *J. Acoust. Soc. Am.*, 103(3):1547–1557, 1998. 147

G.C. Gaunaurd and H. Uberall. RST analysis of monostatic and bistatic acoustic echoes from an elastic sphere. *J. Acoust. Soc. Am.*, 73(1):1–12, 1983. 69, 133

A. Goldman and I. Cohen. Anomaly subspace detection based on a multi-scale markov random field model. *Signal Processing*, 2004. 157

A. Goldman and I. Cohen. Anomaly subspace detection based on a multi-scale markov random field model. *Signal Processing*, 85:463–479, 2005. 50, 51

R.R. Goodman and R. Stern. Reflection and transmission of sound by elastic spherical shells. *J. Acoust. Soc. Am.*, 34(3):338–344, 1962. 69, 70

T. N. Grigsby and E. J. Tajchman. Properties of lamb waves relevant to the ultrasonic inspection of thin plates. *IRE Trans. Ultrason. Eng*, UE-8:26–33, 1961. 134

V.A. Del Grosso and C.W. Mader. Sound speed in pure water. *J. Acoust. Soc. A.*, 52:1442–1446, 1972. 19

A.M. Haimovich, R.S. Blum, and L.J. Cimini. Mimo radar with widely separated antennas. *Signal Processing Magazine, IEEE*, 25(1):116–129, 2008. ISSN 1053-5888. doi: 10.1109/MSP.2008.4408448. 173, 175

R.M. Haralick, S. Shanmugan, and I. Dinstein. Textural features for image classification. *IEEE Trans. on Systems, Man and Cybernetics*, 3:610–621, 1973. 94

M.A. Hasan and M.R. Azimi-Sadjadi. A modified block ftf adaptive algorithm with applications to underwater target detection. *IEEE Trans. Signal Process.*, 73(1):1–12, 1996. 69, 133

L-A. Henry, A.J. Davies, and J.M. Roberts. Beta diversity of cold-water coral reef communities off western scotland. *Coral Reefs*, 29:427–436, 2010. 2

R. Hickling. Analysis of echoes from a solid elastic sphere in water. *J. Acoust. Soc. Am.*, 34:1582–1592, 1962. 76, 130

A. Home and G. Yates. Bistatic synthetic aperture radar. *IEEE RADAR 2002*, pages 6–10, 2002. 188

D. Houser, S. Martin, M. Pillips, E. Bauer, T. Herrin, and P. Moore. Signal processing applied to the dolphin-based sonar system. *OCEANS 2003, Proceeding*, 1:297–303, 2003. 142

D. Houser, S. Martin, E. Bauer, M. Phillips, T. Herrin, M. Cross, A. Vidal, and P. Moore. Echolocation characteristics of free-swimming bottlenose dolphins during object detection and identification. *J. Acoust. Soc. Am.*, 117:23082317, 2005. 121

D.S. Houser, D.A. Helweg, and P.W.B. Moore. Classification of dolphin echolocation clicks by energy and frequency distributions. *J. Acoust. Soc. Am.*, 16: 1576–1585, 1999. xxi, 121, 122, 126

A. J. Hunter, M. P. Hayes, and P. T. Gough. Simulation of multiple-receiver, broad- band interferometric sas imagery. In *IEEE OCEANS Conf. Proc.*, 2003. 40

B.D. Huxtable and E.M. Geyer. Motion compensation feasibility for high resolution synthetic aperture sonar. In *Proc. IEEE OCEANS'93*, 1993. 66

D. R. Jackson and M. D. Richardson. *High-Frequency Seafloor Acoustics*. Springer Science, 2007. 87, 88

M. Jonsson, J. Pihl, and M. Aklint. Imaging of buried objects by low frequency sas. In *Oceans 2005 - Europe*, volume 1, pages 669 – 673 Vol. 1, 20-23 2005. doi: 10.1109/OCEANSE.2005.1511794. 68

E. Kamran and R. Chellappa. Discriminant analysis for recognition of human face images. *J. Opt. Soc. Am.*, 14 (8):1724–1733, 1997. 52

S. G. Kargl and P. L. Marston. Observations and modeling of the backscattering of short tone bursts from spherical shell:lamb wave echoes, glory, and axial reverberation. *J. Acoust. Soc. Am.*, 85(3):1014–1028, 1989. 134

D.E. Kerr. *Propagation of Short Radio Waves*, volume 13 of *MIT Radiation Laboratory Series*. McGraw-Hill, 1951. 18, 24

R. Kessel. Estimating the limitations that image resolution and contrast place on target recognition. In *Proc. SPIE*, volume 4726, 2002. 54

G.S. Kino. *Acoustic Waves*. Prentice-Hall Signal Processing Series, 1987. xxi, 131

G. R. Kirchhoff. *Vorlesungen uber Mathematische Physik*. Mechanik. Teubner, Leipzig, 1876. 96

V.O. Knudsen, R.S. Alford, and J.W. Emling. Underwater ambient noise. *Journal of Marine Research*, 7:410–429, 1948. 29

H. Lamb. On waves in an elastic plate. *Proc. R. Soc. London Ser.*, 93:114–128, 1917. 134

N. Lehmann, A.M. Haimovich, R.S. Blum, and L. Cimini. Mimo-radar application to moving target detection in homogenous clutter. In *Adaptive Sensor Array Processing Workshop at MIT Lincoln Laboratory*, 2006a. 173

N.H. Lehmann, A.M. Haimovich, R.S. Blum, and L.J. Cimini. High resolution capabilities of mimo radar. In *Proc. 40th Asilomar Conf. Signals, Systems and Computers*, 2006b. 173

N.H. Lehmann, E. Fishler, A.M. Haimovich, R.S. Blum, D. Chizhik, L.J. Cimini, and R.A. Valenzuela. Evaluation of transmit diversity in mimo-radar direction finding. *Signal Processing, IEEE Transactions on*, 55(5):2215–2225, May 2007. ISSN 1053-587X. doi: 10.1109/TSP.2007.893220. 173

H. Lew. Broadband active sonar: Implications and constraints. Technical report, DSTO-TR-0435, 1996. 120

J. Li and P. Stoica. *MIMO radar signal procesing.* New Jersey: John Wiley & Sons, 2009. 173

M. Lianantonakis and J. Bell. Sonar simulation: Modelling the effect of shear from elastic objects and seabeds. *Internal Report*, 2003. 136

G. Lippman. Principe de la conservation de l'lectricit. *Annales de chimie et de physique*, 24, 1881. 11, 13

S. Lovejoy. Area-perimeter relation for rain and cloud areas. *Science*, 216:185–187, 1982. 43

X. Lurton. Swath bathymetry using phase difference: theoretical analysis of acousitcal measurement precision. *IEEE J. Ocean. Eng.*, 24:4–15, 2000. 66

K.V. Mackenzie. Discussion of sea water sound-speed determinations. *J. Acoust. Soc. Am.*, 70:801–806, 1981. 18

B. Mandelbrot. *The fractal geometry of nature.* W H Freeman & Co, 1982. 43, 89

P. L. Marston. Gtd for backscattering from elastic spheres and cylinders in water and coupling of surface elastic waves with the acoustic field. *J. Acoust. Soc. Am.*, 83:25–37, 1988. 81, 134

S. Martin, M. Phillips, E. Bauer, P. Moore, and D. Houser. Application of the biosonar measurement tool. In *Proc. MTS/IEEE OCEANS 2003*, page 311315, 2003. 121

A.D. Matthews, T.C. Montgomery, D.A. Cook, J.W. Oeschger, and J.S. Stroud. 12.75" synthetic aperture sonar (sas), high resolution and automatic target recognition. In *OCEANS 2006*, pages 1 –7, 18-21 2006. doi: 10.1109/OCEANS.2006.307046. 68

F. Maussang, A. Hetet, and M. Amate. Higher-order statistics for the detection of small objects in a noisy background application on sonar imaging. *EURASIP Journal on Applied Signal Processing*, 2007. 50, 51, 157

R.H. Mellen. Thermal-noise limit in the detection of underwater acoustic signals. *J. Acoust. Soc. Am.*, 24, 1952. 29

M. Mignotte, C. Collet, P. Perez, and P. Bouthemy. Hybrid genetic optimization and statistical model-based approach for the classification of shadow shapes in sonar imagery. *IEEE Trans. Pattern Anal. Machine Intell.*, 22(2):129–141, Feb. 2000. 50, 51, 158

P. Moore, H. Roitblat, R. Penner, and P. Nachtigall. Recognizing successive dolphin echoes with an integrator gateway network. *Neural Networks*, 4:701–709, 1991. 121

V. Myers and M. Pinto. Bounding the performance of sidescan sonar automatic target recognition algorithms using information theory. *IEE Proc.-Radar Sonar Navig.*, 1:266–273, 2007. 54

V. L. Myers. Image segmentation using iteration and fuzzy logic. In *Proc. Conf. Comput.-Aided Classification/Comput.-Aided Design*, 2001. 53

P.E. Nachtigall. Odontocete echolocation performance on object size, shape, and material. *Animal Sonar Systems*, pages 71–95, 1980. 120

A.F. Nayak, E. Trucco, A. Ahmad, and A.M. Wallace. Simbil: appearance-based simulation of burst-illumination laser sequences. *IET Proceedings on Image Processing*, 2:165–174, 2008. 54

N.J.Willis. *Bistatic Radar*. Norwood, MA:ArtechHouse, 1991. 188

Y. Pailhas, C. Capus, and J. Bell. Modelling for obstacle avoidance sonar design. *Proc. IOA*, April 2005. 120

Y. Pailhas, C. Capus, K. Brown, and P. Moore. Measured target responses to bio-inspired sonar pulses. In *Proceedings of the 8th European Conference on Underwater Acoustics, ECUA 06*, 2006. 179

Y. Pailhas, C. Capus, K. Brown, and P. Moore. Analysis and classification of broadband echoes using bio-inspired dolphin pulses. *J. Acoust. Soc. Am.*, 127 (6):3809–3820, 2010. doi: 10.1121/1.3372754. URL `http://link.aip.org/link/?JAS/127/3809/1`. 50, 107

A. P. Pentland. Fractal-based description of natural scenes. *IEEE Trans. Pattern Anal. Machine Intell.*, PAMI-6(6):661–674, Nov. 1984. ISSN 0162-8828. doi: 10.1109/TPAMI.1984.4767591. 43, 89

S. W. Perry. Detection of small man-made targets in multiple range sector scan imagery using neural networks. In *Proc. Conf. Comput.-Aided Classification/Comput.-Aided Design*, 2001. 50, 51, 158

Y. Petillot and F. Maurelli. A tree-based planner for active localisation: Applications to autonomous underwater vehicles. In *ELMAR, 2010 PROCEEDINGS*, pages 479–483, sept. 2010. 158

A. D. Pierce. *Acoustics: An Introduction to Its Physical Principles and Applications*. Acoust. Soc. Am., 1991. 96

M. Pinto. Performance index for shadow classification in minehunting sonar. In *Proceedings of the UDT Conference 1997*, 1997. 54

M. Pinto. Design of synthetic aperture sonar systems for high-resolution seabed imaging. In *OCEANS06 MTS/IEEE Boston*, 2006. 40, 64

M. Pinto and A. Bellettini. Shallow water synthetic aperture sonar: an enabling technology for nato mcm forces. In *UDT Europe, Undersea Defence Technology Europe, Naples, Italy*, 2007. 64

M. Pinto, A. Bellettini, R. Hollett, and L. Wang. Recent advances in synthetic aperture sonar for proud and buried object detection. *J. Acoust. Soc. Am.*, 111 (5):2457–2457, 2002. URL `http://link.aip.org/link/?JAS/111/2457/2`. 68

G. A. Ponomarev and V. P. Yakubov. Kirchhoff's approximation method of geometrical optics in the problem of scattering of waves at an irregular surface. *Radiophysics and Quantum Electronics*, 19(8):849–852, 08 1976. URL `http://dx.doi.org/10.1007/BF01043482`. 104, 113

C. Prada, F. Wu, and M. Fink. The iterative time reversal mirror: A solution to self-focusing in the pulse echo mode. *J. Acoust. Soc. Am.*, 90:11191129, 1991. 192

C. Prada, S. Manneville, D. Spoliansky, and M. Fink. Decomposition of the time reversal operator: Detection and selective focusing on two scatterers. *J. Acoust. Soc. Am.*, 99:20672076, 1996. 192

I. Quidu, Ph. Malkasse, G. Burel, and P. Vilbe. Mine classification based on raw sonar data: An approach combining fourier descriptors, statistical models and genetic algorithms. *OCEANS MTS/IEEE Conf. and Exhibition*, 1:285–290, 2000a. 50, 51

I. Quidu, Ph. Malkasse, G. Burel, and P. Vilbe. Mine classification using a hybrid set of descriptors. *OCEANS MTS/IEEE Conf. and Exhibition*, 1:291–297, 2000b. 50, 51

D. Rabideau. Ubiquitous mimo digital array radar. In *Proc. 37th Asilomar Conf. Signals, Systems, and Computers*, 2003. 173

L. Rayleigh. *The Theory of Sound*. Dover Publications, 1945. 23, 129

S. Reed, Y. Petillot, and J. Bell. An automatic approach to the detection and extraction of mine features in sidescan sonar. *IEEE J. Oceanic Eng.*, 28(1): 90–105, Jan 2003a. ISSN 0364-9059. doi: 10.1109/JOE.2002.808199. 53, 158

S. Reed, Y. Petillot, and J. Bell. An automated approach to the detection and extraction of mine features in sidescan sonar. *IEEE Journal Oceanic Eng.*, 28 (1):90–105, Jan. 2003b. 158

S. Reed, J. Bell, and Y. Petillot. A model based approach to the detection and classification of mines in sidescan sonar. *J. Opt. Soc. Am., Applied Optics*, 43: 237–246, 2004a. 50, 51

S. Reed, Y. Petillot, and J. Bell. An automated approach to the classification of mine-like objects in sidescan sonar using highlight and shadow information. In *IEE Proc.-Radar Sonar Navig.*, 2004b. 50, 51

M. D. Richardson, Briggs Kevin B., L. Dale Bibee, Peter A. Jumars, William B. Sawyer, Daniel B. Albert, Richard H. Bennett, Thomas K. Berger, Michael J. Buckingham, Nicholas P. Chotiros, Peter H. Dahl, Nancy T. Dewitt, Peter Fleischer, Roger Flood, Charles F. Greenlaw, D. Vance Holliday, Matthew H. Hulbert, Michael P. Hutnak, Peter D. Jackson, Jules S. Jaffe, H. Paul Johnson, Dawn L. Lavoie, Anthony P. Lyons, Christopher S. Martens, Duncan E. McGehee, Karl D. Moore, Tim H. Orsi, James N. Piper, Richard I. Ray, Allen H. Reed, Robert. F. Liko Self, Jill L. Schmidt, Stephen G. Schock, Fernando Simonet, Robert D. Stoll, Dajun Tang, David E. Thistle, Eric I. Thorsos, Donald J. Walter, and Robert A. Wheatcroft. Overview of sax99: Environmental considerations. *IEEE J. Oceanic Eng.*, 26:26–53, 2001. 200

J.M. Roberts, A. Wheeler, A. Freiwald, and S.D. Cairns. *Cold-water Corals: The Biology and Geology of Deep-sea Coral Habitats*. Cambridge University Press, 2009. 2

F.C. Robey, S. Coutts, D. Weikle, J.C. McHarg, and K. Cuomo. Mimo radar theory and experimental results. In *38th Asilomar Conference on Signals, Systems and Computers*, 2004. 173

J. Sawas, Y. Petillot, and Y. Pailhas. Cascade of boosted classifiers for rapid detection of underwater objects. In *Proceedings of the European Conference on Underwater Acoustics*, 2010. 164

H. Schmidt. Virtual source approach to scattering from partially buried elastic targets. In *AIP Conf. Proc.*, 728, page 456463, 2004. 96

J.A. Seydel. Ultrasonic synthetic-aperture focusing techniques. In New York: Academic Press, editor, *NDT Research Techniques for Nondestructive Testing*, 1982. 67

G. Shafer. *A mathematical theory of evidence*. Princeton University Press, 1976. 153

L. Sirovich and M. Kirby. Low-dimensional procedure for the characterization of human faces. *J. Opt. Soc. Am.*, pages 519–524, 1987. 52

M. Skolnik. *Introduction to Radar Systems*. Mc-Graw-Hill, 2002. 174

T.K. Stanton. Sound scattering by cylinders of finite length. iii. deformed cylinders. *J. Acoust. Soc. Am.*, 86(2):691–705, 1989. 131

A. Tesei, W. L. J. Fox, A. Maguer, and A. Løvik. A method of target characterization based on the analysis of scholte–stoneley and lamb-type waves scattered by submerged fluid-filled thin-walled shells. *J. Acoust. Soc. Am.*, 103(5):2813–2813, 1998. doi: 10.1121/1.421572. URL `http://link.aip.org/link/?JAS/103/2813/3`. 78

A. Tesei, P. Guerrini, and M. Zampolli. Tank measurements of scattering from a resin-filled fiberglass spherical shell with internal flaws. *J. Acoust. Soc. Am.*, 124(2):827–840, 2008. doi: 10.1121/1.2945701. URL `http://link.aip.org/link/?JAS/124/827/1`. 82

K. Tomiyasu. Tutorial review of synthetic-aperture radar (sar) with applications to imaging of the ocean surface. *IEEE Proc.*, 66(5):563 – 583, may 1978. ISSN 0018-9219. 65

G. Turin. An introduction to matched filters. *Information Theory, IRE Transactions on*, 6(3):311 –329, june 1960. ISSN 0096-1000. doi: 10.1109/TIT.1960.1057571. 67

M. Turk and A. Pentland. Face recognition using eigenfaces. In *Proc. IEEE Conference on Computer Vision and Pattern Recognition*, page pp. 586591, 1991. 56

R. Urick. *Principles of Underwater Sound*. McGraw-Hill, New York, 1975. 2, 16, 27, 199

R. F. Voss. *Random Fractal Forgeries in Fundamental Algorithms for Computer Graphics*. Springer-Verlag, R. A. Earnshaw, 1985. 43

J Wright, Y. Y. Allen, A. Ganesh, S. S. Sastry, and Y. Ma. Robust face recognition via sparse representation. *IEEE Trans. Pattern Anal. Machine Intell.*, 31(2): 210–227, 2009. 52, 54

M. Zampolli, A. Tesei, G. Canepa, and O. A. Godin. Computing the far field scattered or radiated by objects inside layered fluid media using approximate green's functions. *J. Acoust. Soc. Am.*, 123(6):4051–4058, 2008. doi: 10.1121/1.2902139. URL `http://link.aip.org/link/?JAS/123/4051/1`. 96, 98

M. Zampolli, F. B. Jensen, and A. Tesei. Benchmark problems for acoustic scattering from elastic objects in the free field and near the seafloor. *J. Acoust. Soc. Am.*, 125(1):89–98, 2009. doi: 10.1121/1.3027446. URL `http://link.aip.org/link/?JAS/125/89/1`. 96

B. Zerr, E. Bovio, and B. Stage. Automatic mine classification approach based on auv manoeuverability and the cots side scan sonar. In *Autonomous Underwater Vehicle and Ocean Modelling Networks: GOATS 2000 Conf. Proc. CP-46*, pages 315–322. NATO Saclant Undersea Research Centre, 2001. 50, 51, 53, 158